京都産業大学　神山天文台
2019 年度　年報

KYOTO SANGYO UNIVERSITY
KOYAMA ASTRONOMICAL OBSERVATORY

目　次

巻頭言

令和元（2019）年度は、神山天文台が設置されて10年目という節目の年になります。その間、文部科学省の私立大学戦略的研究基盤形成支援事業には二度にわたって採択されており、一度目は平成20（2008）年度～平成24（2012）年度「研究教育用天文台の設置」、二度目が平成26（2014）年度～平成30（2018）年度「赤外線高分散分光天文学研究拠点 Infrared Spectroscopy Laboratory の形成」でした。こうした流れの中で、神山天文台では「赤外線波長」と「高分散分光天文学」というキーワードにリソースを集中し、天体観測装置の国内開発拠点として、現在、目覚ましい成果を挙げています。近赤外線高分散分光器WINEREDを筆頭として、世界最高レベルの機器開発を進めており、これら独自開発機器を使って世界中の他の研究機関が追随できないような様々な観測研究を推進しています。平成28（2016）年度には神山天文台の口径1.3m荒木望遠鏡から海外拠点への拡大に成功し、WINEREDを欧州南天天文台ESOの管理するラ・シヤ観測所（チリ共和国）に置かれた口径3.6m NTT望遠鏡に移設して観測研究が進められており、日本よりはるかに高い晴天率と低い湿度が相まって、日本国内では実現できなかったような、極めて高精度かつ高感度な赤外線高分散分光観測が実現でき、次々に新しい成果が出ています。

以上の成果は、神山天文台のスタッフのみならず、客員研究員等として研究プロジェクトに参加していただいている学外の研究機関・企業の研究者／技術者のみなさん、そして、本学学生のみなさんが、大変な苦労をされた結果です。多種多様で優秀な人材が、学内外を問わず神山天文台を中心に集い、このような目覚ましい成果を挙げているのです。まさに、本学の「むすびわざ」の精神の具現化と言えるでしょう。学祖・荒木俊馬博士の建学の精神を具現化するシンボルとしてスタートした神山天文台は、現在、十分に役目を果たすことが出来るようになったと実感しております。神山天文台は、荒木博士が研究テーマとされたセファイド型変光星や、はくちょう座P星・新星に代表される爆発天体の観測研究を引き継ぎ、世界トップレベルの研究拠点となりました。今後、次の10年を見据え、更に強力に研究を推進してまいります。

神山天文台長

河北　秀世

2021年1月14日

主要な研究成果

タ　イ　ト　ル　：　Fe I Lines in 0.91-1.33 μm Spectra of Red Giants for Measuring the Microturbulence and Metallicities

担　　当　：　Sohei Kondo, Kei Fukue, Noriyuki Matsunaga, Yuji Ikeda, *et al.*

関　連　出　版　：　The Astrophysical Journal, Volume 875, Issue 2, article id. 129, 13 pp. (2019).

関連学会発表等　：

Draft version March 7, 2019
Preprint typeset using LaTeX style emulateapj v. 01/23/15

Fe I LINES IN 0.91–1.33 μm SPECTRA OF RED GIANTS FOR MEASURING THE MICROTURBULENCE AND METALLICITIES

Sohei Kondo[1], Kei Fukue[1], Noriyuki Matsunaga[2,1], Yuji Ikeda[1,3], Daisuke Taniguchi[2], Naoto Kobayashi[1,4,5], Hiroaki Sameshima[1], Satoshi Hamano[1], Akira Arai[1], Hideyo Kawakita[1,6], Chikako Yasui[1,7], Natsuko Izumi[7], Misaki Mizumoto[8], Shogo Otsubo[6], Keiichi Takenaka[6], Ayaka Watase[6], Akira Asano[6], Tomohiro Yoshikawa[9], and Takuji Tsujimoto[7]

Draft version March 7, 2019

ABSTRACT

For a detailed analysis of stellar chemical abundances, high-resolution spectra in the optical have mainly been used, while the development of near-infrared (NIR) spectrograph has opened new wavelength windows. Red giants have a large number of resolved absorption lines in both the optical and NIR wavelengths, but the characteristics of the lines in different wave passbands are not necessarily the same. We present a selection of Fe I lines in the z', Y, and J bands (0.91–1.33 μm). On the basis of two different lists of lines in this range, the Vienna Atomic Line Database (VALD) and the catalog published by Meléndez & Barbuy in 1999 (MB99), we selected sufficiently strong lines that are not severely blended and compiled lists with 107 Fe I lines in total (97 and 75 lines from VALD and MB99, respectively). Combining our lists with high-resolution ($\lambda/\Delta\lambda = 28,000$) and high signal-to-noise (> 500) spectra taken with a NIR spectrograph, WINERED, we present measurements of the iron abundances of two prototype red giants: Arcturus and μ Leo. A bootstrap method for determining the microturbulence and abundance together with their errors is demonstrated. The standard deviations of $\log \epsilon_{\rm Fe}$ values from individual Fe I lines are significantly smaller when we use the lines from MB99 instead of those from VALD. With the MB99 list, we obtained $\xi = 1.20 \pm 0.11$ km s^{-1} and $\log \epsilon_{\rm Fe} = 7.01 \pm 0.05$ dex for Arcturus, and $\xi = 1.54 \pm 0.17$ km s^{-1} and $\log \epsilon_{\rm Fe} = 7.73 \pm 0.07$ dex for μ Leo. These final values show better agreements with previous values in the literature than the corresponding values we obtained with VALD.

Subject headings: stars:abundances, stars:late-type, techniques:spectroscopic, individual (Arcturus, μ Leo)

1. INTRODUCTION

Recent developments in instruments (e.g., multi-object spectrographs) and statistical approaches (e.g., CANNON, Ness et al. 2015; ASPCAP, García Pérez et al. 2016) provide opportunities to measure metallicities of a larger number of stars and/or to higher precision. Among the various methods available for estimating stellar metallicities, the measurement of individual metallic lines in high-resolution spectra is the most direct and fundamental one. Such detailed analyses of high-resolution spectra have mostly been performed with optical spectra, while recently developed instruments now produce near-infrared (NIR) high-resolution spectra that are similarly useful and high in quality. For example, the APOGEE project established fiber-fed multi-object spectrographs to collect hundreds of H-band spectra (1.5–1.7 μm, $\lambda/\Delta\lambda$ = 22,500) simultaneously (Majewski et al. 2017). Several other NIR spectrographs with a single slit have been used for abundance analysis for individual stars, especially those affected by strong interstellar extinction. Such pioneering works include studies of chemical abundances of stars in the Galactic bulge (Carr et al. 2000; Cunha & Smith 2006; Ryde et al. 2009, 2010, 2016) and red supergiants in clusters in the inner disk (Davies et al. 2009a,b; Origlia et al. 2013, 2016).

Since abundance analyses based on NIR spectra have now turned state of the art, they require, e.g., accurate calibration of oscillator strengths of absorption lines in that spectral domain. For example, the APOGEE project has not only measured the abundances of a large number of stars but has also made progress in establishing methodology and fundamental datasets: a list of absorption lines in the H band (Shetrone et al. 2015), a new grid of atmospheric models (Mészáros et al. 2012), a tool to search for the best sets of stellar parameters (García Pérez et al. 2016), and so on. In particular, an accurate line list is essential to perform chemical analysis in stellar atmospheres. The correct identification of lines is mandatory, and estimates of abundances can-

[1] Laboratory of Infrared High-resolution spectroscopy (LiH), Koyama Astronomical Observatory, Kyoto Sangyo University, Motoyama, Kamigamo, Kita-ku, Kyoto 603-8555, Japan:kondosh@cc.kyoto-su.ac.jp
[2] Department of Astronomy, Graduate School of Science, The University of Tokyo, 7-3-1 Hongo, Bunkyo-ku, Tokyo 113-0033, Japan
[3] Photocoding, 460-102 Iwakura-Nakamachi, Sakyo-Ku, Kyoto 606-0025, Japan
[4] Kiso Observatory, Institute of Astronomy, School of Science, the University of Tokyo, 10762-30 Mitake, Kiso-machi, Kiso-gun, Nagano 397-0101, Japan
[5] Institute of Astronomy, Graduate School of Science, the University of Tokyo, 2-21-1 Osawa, Mitaka, Tokyo 181-0015, Japan
[6] Department of Physics, Faculty of Science, Kyoto Sangyo University, Motoyama, Kamigamo, Kita-ku, Kyoto 603-8555, Japan
[7] National Astronomical Observatory of Japan, 2-21-1 Osawa, Mitaka, Tokyo 181-0015, Japan
[8] Centre for Extragalactic Astronomy, Department of Physics, University of Durham, South Road, Durham DH1 3LE, UK
[9] Edechs, 17-203 Iwakura-Minami-Osagi-cho, Sakyo-ku, Kyoto 606-0003, Japan

not be accurately carried out without accurate oscillator strengths. As Ryde et al. (2009) pointed out, many lines in the NIR are not properly identified or lack well-calibrated oscillator strengths. Available line lists with a wide wavelength coverage include Kurucz's database (Kurucz & Bell 1995), Vienna Atomic Line Database (VALD3; Ryabchikova et al. 2015), and the list published by Meléndez & Barbuy (1999; hereinafter referred to as MB99). MB99 compiled absorption lines, which they identified in the solar spectrum, and obtained astrophysical $\log gf$ values[10]. In contrast, Kurucz's database and VALD3 have a significantly larger number of lines including those only theoretically predicted. In this work, we compared results of abundance analysis obtained with lines in the range of 0.91–1.33 μm from VALD3 and the MB99 list, and also compared our measurements with previous results.

In addition to comparing line lists, another goal of this study is to test the determination of the microturbulence, ξ, using NIR high-resolution spectra. In an abundance analysis of stars, ξ is one of the most important parameters, and its uncertainty often remains a major error source for the metallicity. In a classical analysis of optical high-resolution spectra, ξ is estimated by necessitating that $\log \epsilon_{\rm Fe}$, defined as $\log(N_{\rm Fe}/N_{\rm H}) + 12$, from individual lines shows no dependency on line strengths, e.g., equivalent widths (EWs, denoted as W) or reduced EWs (W/λ). This method requires a large number of iron lines with various strengths. For NIR spectra, different methods for estimating ξ have often been used so far. Davies et al. (2009b), for example, obtained it by comparing the molecular bands in synthetic and observed spectra. Sometimes ξ is assumed *a priori*. In an analysis of more than 10^5 stars in the APOGEE project, ξ for giants were estimated from the relationship between the surface gravity and ξ in DR13 and by comparing observed spectra to libraries of theoretical spectra in DR14 (Holtzman et al. 2018)[11]. In contrast, Smith et al. (2013) estimated ξ with H-band spectra in the same manner as the classical method mentioned above. However, the number of iron lines used was small (eight or nine), and the range of their strengths was limited. As shown below, we can identify more lines with a broad range of strengths at 0.91–1.33 μm.

2. OBSERVATION AND DATA REDUCTION

We investigated WINERED spectra of well-studied red giants, Arcturus and μ Leo. The former has a subsolar metallicity, and the latter is significantly metal-rich; previous estimates are summarized in Section 3.1. WINERED has a spectral resolution of $R \equiv \lambda/\Delta\lambda \sim 28,000$. A single exposure covers a wide wavelength range of 0.91–1.35 μm, which includes the z', Y, and J bands (Ikeda et al. 2016). Such a wide coverage is a huge advantage in abundance analysis. A large number of Fe I lines are included, and their strengths range from a severely saturated regime to a very weak regime, thus allowing accurate estimates of ξ.

We observed Arcturus and μ Leo on February 23, 2013 with WINERED mounted on the Nasmyth focus of the 1.3 m Araki Telescope at Koyama Astronomical Observatory, Kyoto Sangyo University, Japan (Table 1). WINERED is a cross-dispersed-type echelle spectrograph using a 1.7 μm cutoff 2048 × 2048 HAWAII-2RG array. The pixel scale is $0\farcs8$ pixel^{-1}, and we used a slit $48''$ in length and $1\farcs6$ in width, providing a spectral resolution of $R \sim 28,000$ (further technical details are described in Ikeda et al. 2016). We also observed HIP 76267 (A1IV) as a telluric standard. The total exposure times were 20, 240, and 600 s for Arcturus, μ Leo, and HIP 76267, respectively. For every object, sky frames without the target or any other visible stars included in the slit were obtained to subtract the background including bias and dark of the detector as well as the sky and ambient radiation.

TABLE 1
Targets and WINERED observations

	Arcturus	μ Leo
Alias	HD 124897, α Boo	HD 85503
$T_{\rm eff}$ (K)†	4286 ± 35	4474 ± 60
$\log g$ (dex)†	1.64 ± 0.06	2.51 ± 0.09
[M/H] (dex)†	-0.52 ± 0.08	0.25 ± 0.15
Date (UT)	2013 Feb 23	2013 Feb 23
Time (UT)	16:23	17:18
Exposures (s)	20 (2 s× 10)	240 (20 s× 12)
S/N‡	1200	900
S/N‡⋆	850	720

† The stellar parameters are adopted from Heiter et al. (2015). For [M/H], we simply use their [Fe/H].
‡ S/N is measured at around the middle of J band. Note that these S/N consider statistical errors measured by comparing multiple integrations.
⋆ After the correction of telluric lines with a spectrum (S/N=1200) of the telluric standard HIP 76267.

All the data were reduced following standard procedures adopted in the WINERED pipeline (Hamano et al., in preparation) that is established using PyRAF,[12] which calls IRAF tasks,[13] including sky subtraction, scattered light subtraction, flat-fielding (using a halogen lamp with an integrating sphere), geometric transformation, aperture extraction, and wavelength calibration based on Th-Ar lamp spectra. The continuum was traced in each echelle order and normalized to unity. After the pipeline reduction, we applied the method described in Sameshima et al. (2018) for the telluric correction. The spectrum of a telluric standard, HIP 76267, with a high signal-to-noise ratio (S/N ∼1200), was used for both Arcturus and μ Leo. The spectra in different echelle orders were then combined by taking the averages at overlapping wavelengths, and thus we obtained the continuum-normalized continuous spectra of Arcturus and μ Leo for the z', Y, and J bands. The wavelength ranges of the three bands, in which the telluric lines can be well corrected, cover 0.91–0.93, 0.96–1.115, and 1.16–1.33 μm,

[10] Here and elsewhere in this paper, we consider the logarithm to base 10.
[11] http://www.sdss.org/dr14/irspec/
[12] PyRAF is a product of the Space Telescope Science Institute, which is operated by AURA for NASA.
[13] IRAF is distributed by the National Optical Astronomy Observatories, which are operated by the Association of Universities for Research in Astronomy, Inc., under cooperative agreement with the National Science Foundation.

respectively. Finally, the stellar redshifts were corrected so that the absorption lines can be directly compared with those in synthetic spectra in rest air wavelength. We estimated the S/N ratios at around 12,500 Å, as given in Table 1, in a manner similar to that described in Fukue et al. (2015). Considering the noise present in the telluric correction, we also calculated the S/N of the spectra after the correction. The reduced spectra of Arcturus and μ Leo are presented in Figure 1.

3. TOOLS AND BASIC DATA

3.1. *Atmosphere models and stellar parameters*

For the abundance analysis, we used SPTOOL developed by Y. Takeda (private communication), which utilizes the ATLAS9/WIDTH9 codes by R. L. Kurucz (Kurucz 1993). This tool synthesizes model spectra using ATLAS9 model atmospheres for a given set of parameters, including effective temperature ($T_{\rm eff}$), surface gravity ($\log g$), and global metallicity ([M/H] or $\log Z/Z_\odot$). In these tools and models, the solar abundance was assumed to be that of Anders & Grevesse (1989). However, in the following discussions, we translate $\log \epsilon_{\rm Fe}$ values into [Fe/H] by adopting 7.45 dex (Grevesse et al. 2007) as the solar $\log \epsilon_{\rm Fe}$ value, which was also adopted in many recent works (Smith et al. 2013; Jofré et al. 2014).

We adopted the basic stellar parameters and their errors of the two targets, as listed in Table 1, from Heiter et al. (2015). We simply use their [Fe/H] values as [M/H] in the atmosphere models. For comparison, Figure 2 plots previous estimates of $T_{\rm eff}$, $\log g$, and [Fe/H], published after 1970, against the publication date. We included only papers with [Fe/H] in which the assumed solar $\log \epsilon_{\rm Fe}$ was clearly given and those with iron abundance given as $\log \epsilon_{\rm Fe}$, and all the [Fe/H] values in Figure 2 are scaled with the solar $\log \epsilon_{\rm Fe}$ of 7.45 dex. The averages of the values published in 2000 or later (18 and 6 papers for Arcturus and μ Leo, respectively) give (with standard deviations in parentheses), $T_{\rm eff}$ = 4279 K (40 K), $\log g$ = 1.60 dex (0.18 dex), and [Fe/H] = −0.51 dex (0.06 dex) for Arcturus, and $T_{\rm eff}$ = 4520 K (43 K), $\log g$ = 2.36 dex (0.22 dex), and [Fe/H] = +0.33 dex (0.06 dex) for μ Leo. These averages agree well with the parameters from Heiter et al. (2015) in Table 1.

3.2. *Line lists of VALD3 and MB99*

VALD3 has a large collection of atomic lines, including more than 10,000 Fe I lines, and molecular lines covering the wavelength range of the z', Y, and J bands. In our spectrum of Arcturus, Ikeda et al. (in preparation) identified the atomic lines of various species, including more than 300 Fe I lines (see a summary in Taniguchi et al. 2018). We also considered the line list of MB99, which includes 363 Fe I lines in the 1.00–1.34 μm range among ∼1000 atomic lines in total. We note that MB99 contains lines at only $\lambda > 1$ μm and does not cover the entire range of WINERED spectra. There are 159 lines in both the list of Ikeda et al. and that of MB99, and there are 475 lines in at least one of the two lists. The wavelength and the excitation potential (EP in eV) of each line are consistent between the two line lists. In contrast, the $\log gf$ values in the two lists are significantly different, as seen below.

Fe II lines are not used in our analysis, although there are more than 10,000 Fe II lines in VALD3 in the same wavelength range. MB99 lists 13 Fe II lines, all of which are also included in VALD3. We have in fact identified a few Fe II lines in Arcturus (to be reported in Ikeda et al.) and/or μ Leo. However, most of them are weaker than 0.01, and none of them is stronger than 0.05 in depth. Therefore, we focus on abundance measurements using only Fe I lines in this paper. We use synthetic spectra for both the selection of Fe I lines and the abundance measurements, and we include all the lines in VALD3 or MB99 (i.e., not only the Fe I lines selected in Ikeda et al.). We use VALD3 for atomic lines when we consider Fe I lines and their parameters given in VALD3, and the same is true for the MB99 lines, in order to avoid mixing the two lists in our spectral analysis. In both cases, we adopt lines of CN, CO, C_2, CH, and OH molecules in VALD3 because MB99 compiled only atomic lines.

4. SELECTION OF FE I LINES

To find good Fe I lines for measuring iron abundances, we started the line selection from the aforementioned 475 Fe I lines. First, we excluded 32 lines in the following three ranges, as they are severely affected by telluric lines: 9,300–9,600 Å, 11,150–11,600 Å, and longer than 13,300 Å. Then, we measured the depths (minima measured from the normalized continuum) and central wavelengths of the lines in the synthetic spectra for the two objects (Arcturus and μ Leo). We applied the line broadening, including both macroturbulent and instrumental broadening, corresponding to $R = 28,000$, for the analysis in this section. If the depth of a line was shallower than 0.05, the line was rejected. We also rejected lines that show no minimum in the synthetic spectra for the two objects within 5 km s^{-1} around the expected wavelength. Such lines with a biased minimum may be strongly blended with other lines. In addition, when two or more Fe I lines were detected within 45 km s^{-1}, we included only the strongest line if its X value was larger than those of the other neighboring Fe I lines by more than 0.5 dex; otherwise, we rejected both lines. The X index is defined as $X \equiv \log gf - {\rm EP} \times \theta_{\rm exc}$, where $\theta_{\rm exc} \equiv 5040/(0.86 \times T_{\rm eff})$. It is a convenient indicator of line strength (Magain 1984; Gratton et al. 2006). In total, 181 (166 in VALD3 and 118 in MB99) lines in VALD3 and/or MB99 met these criteria.

Then, the impact of blending on each line observed for each object was examined and used for further selection. We estimated two EWs, W_1 and W_2, around a target line ($\lambda_{\rm c}$) in a synthetic spectrum, $f_{\rm syn}$:

$$W_i = \int_{\lambda_{\rm c}-\Delta_i/2}^{\lambda_{\rm c}+\Delta_i/2} \{1 - f_{\rm syn}(\lambda)\} d\lambda. \quad (1)$$

For the EW of the target line itself and contaminations of lines in neighboring wavelengths, we consider two different integration ranges, Δ_1 and Δ_2, which correspond to velocities of 30 and 60 km s^{-1}, respectively. Neighboring lines other than the target line can also contribute to these EWs (W_1 and W_2). In addition, to evaluate the contamination, we constructed synthetic spectra, $f^{\dagger}_{\rm syn}$, with the target Fe I line removed from the line lists for each of the two stars. The EW of contaminating lines,

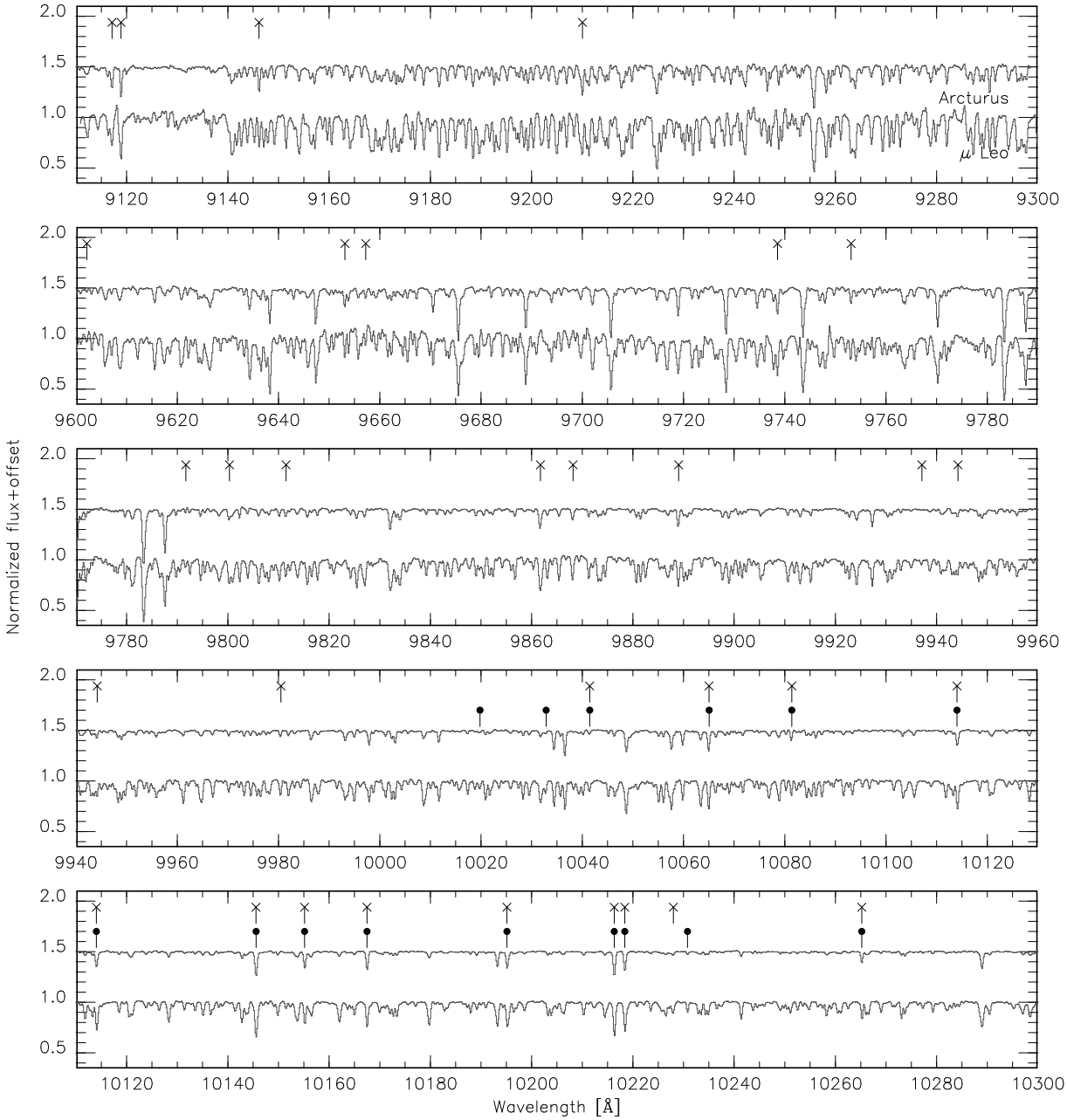

FIG. 1.— Reduced spectra of Arcturus and μ Leo after the telluric correction. The short lines with the cross symbols and the filled circles indicate Fe I lines selected from VALD3 and MB99, respectively, for the metallicity measurements for Arcturus and/or μ Leo.

$W_i^\dagger$, can be estimated by considering Equation (1) but with $f_{\rm syn}$ replaced by $f_{\rm syn}^\dagger$. Combining these EWs, we consider two indices,

$$\beta_1 = W_1^\dagger / W_1, \tag{2}$$

$$\beta_2 = (W_2^\dagger - W_1^\dagger)/W_1, \tag{3}$$

as indicators of blending. The former measures the contamination to the main part of each target line, and the latter measures the contamination mainly to the continuum part around the line. Firstly, we rejected lines for which $f_{\rm syn}^\dagger - f_{\rm syn}$ does not exceed 0.05. The 181 lines were selected because they are deeper than 0.05 in $f_{\rm syn}$ in the previous stage, but we found that a significant number of them are deep because of the contamination. Among the 118 lines in MB99, for example, 53 and 25 were rejected in the cases of Arcturus and μ Leo, respectively, considering the depths in $f_{\rm syn}^\dagger - f_{\rm syn}$. Then, we rejected lines with $\beta_1 > 0.3$ or $\beta_2 > 1$; 8 and 21 lines were rejected in the cases of Arcturus and μ Leo, respectively, although those lines are strong enough. Figure 3 shows examples of Fe I lines with different β_1 and β_2 values. We note that the selection in this section was made on the basis of synthetic spectra, and not observed ones. Some

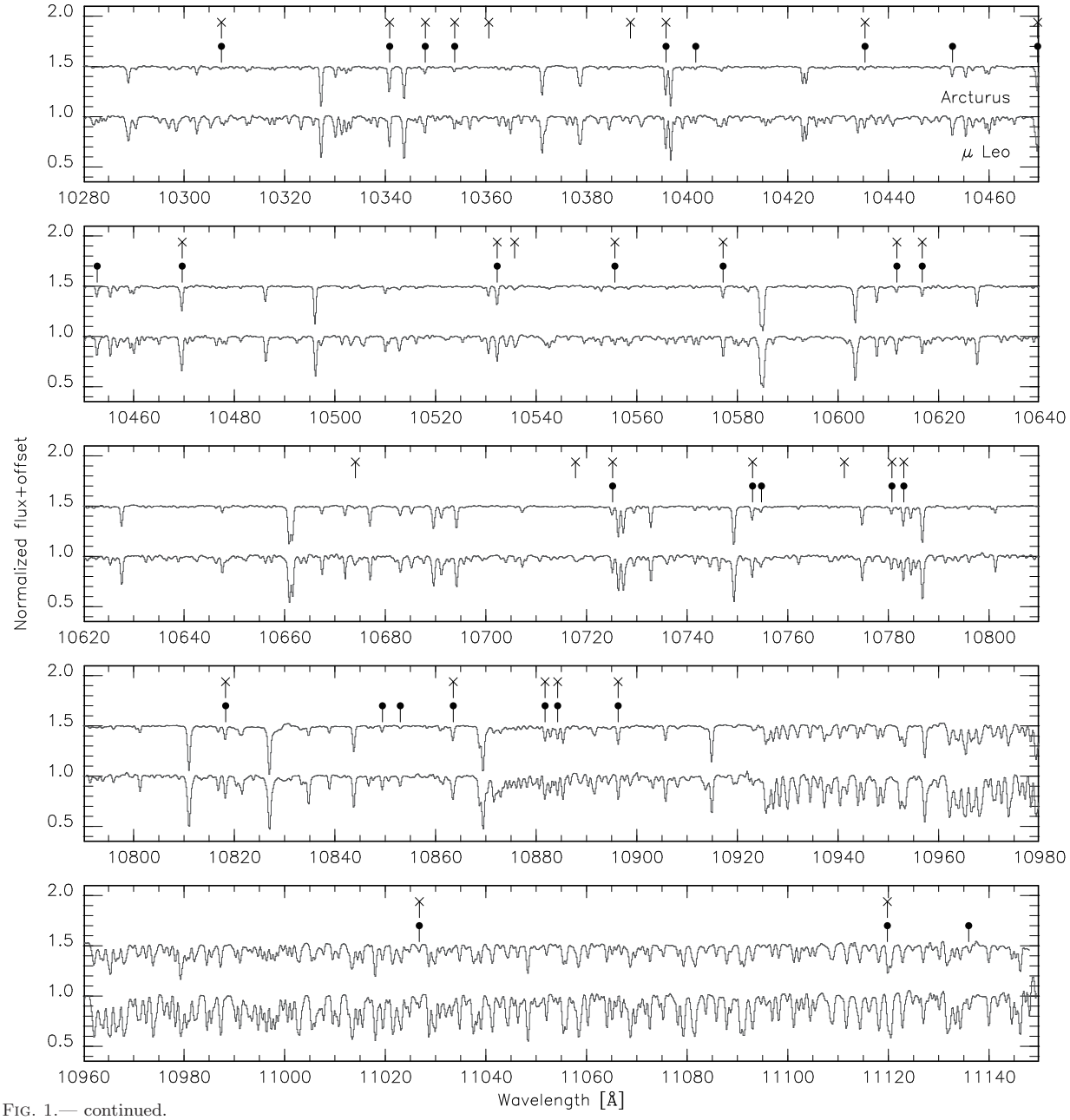

FIG. 1.— continued.

Fe I lines look isolated enough in synthetic spectra but turn out to be severely blended with neighboring strong lines that are not reproduced in the synthetic spectra (see Section 5.1). All of the above mentioned rejections were made independently for each combination of the line list (VALD3 or MB99) and the object (Arcturus or μ Leo).

Tables 2 and 3 list the selected lines, and Table 4 lists the number of the lines, N_1, for each combination of line list and object. Some lines were selected only for one of the two objects owing to the large difference in metallicity. Among the 97 selected lines from VALD3 (Table 2), 24 lines are weak only in Arcturus, while there are no lines, as expected, which are weak in μ Leo but strong enough in Arcturus. In contrast, 6 lines were rejected due to the blending for μ Leo only, and no lines selected for μ Leo show strong blends in Arcturus. The situation is similar for the 75 selected lines from MB99. 18 lines were rejected for Arcturus because they are weak in $f^{\dagger}_{\rm syn} - f_{\rm syn}$, while no line selected for Arcturus is weak in μ Leo. 3 lines were rejected because of blends in μ Leo, but no line selected for μ Leo was rejected owing to blends in Arcturus.

5. MEASUREMENT OF MICROTURBULENCE AND METALLICITY

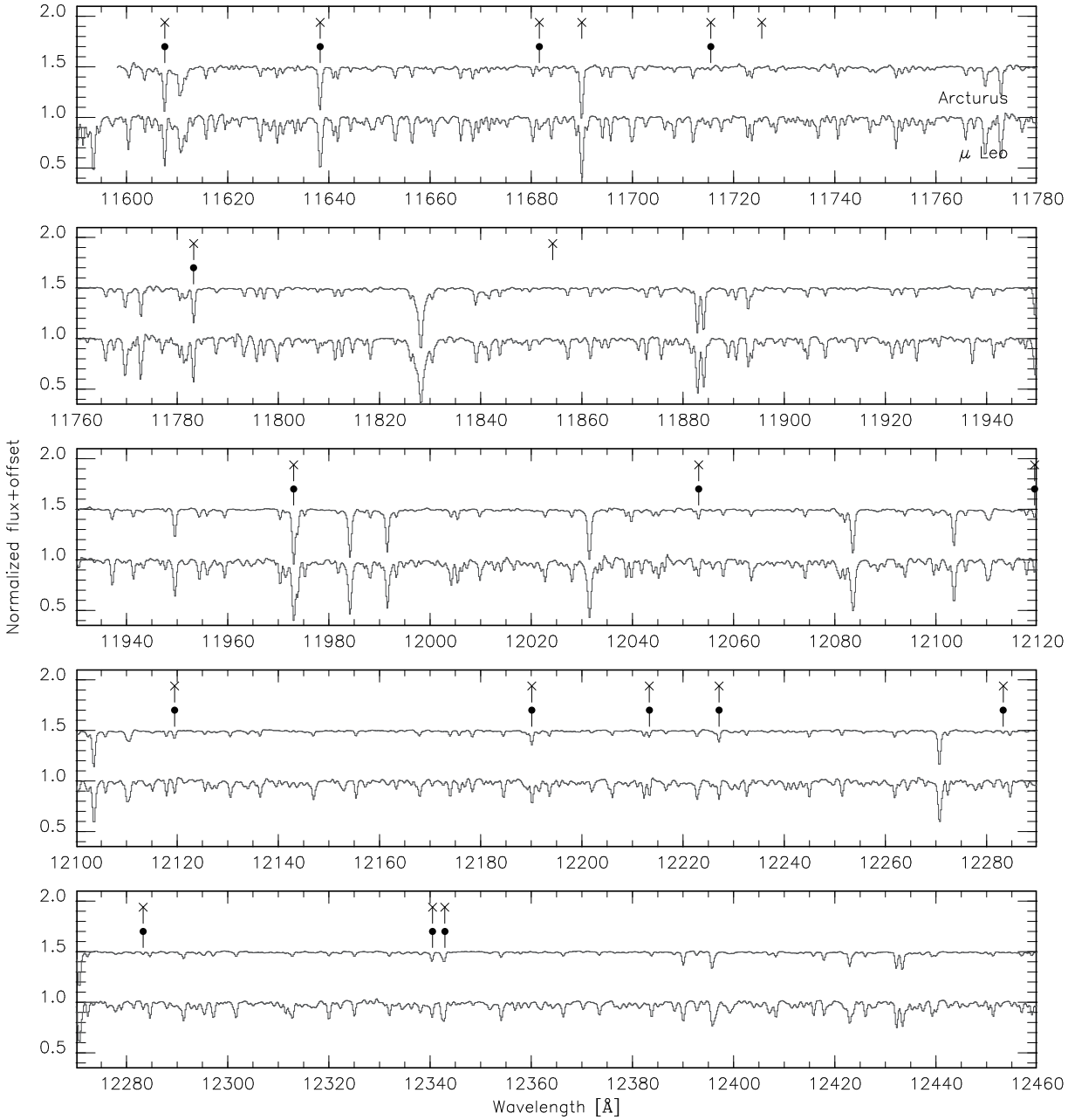

FIG. 1.— continued.

5.1. *Bootstrap method to measure* ξ *and* $\log \epsilon_{\rm Fe}$

We determined the iron abundance ($\log \epsilon_{\rm Fe}$) and the microturbulence (ξ) simultaneously for each combination of object (Arcturus or μ Leo) and line list (VALD3 or MB99) as follows. The basic assumption of the method is that the $\log \epsilon_{\rm Fe}$ values should be independent of line strength, as is often assumed in the classical method of abundance analysis (see the Introduction).

We measured the $\log \epsilon_{\rm Fe}$ of each Fe I line for 21 different ξ values from 0.5 to 2.5 km s^{-1} with a step of 0.1 km s^{-1}. For each combination of line and ξ, $\log \epsilon_{\rm Fe}$ was estimated by a least-squares fit to a small part of the spectrum around the line using MPFIT (Takeda 1995), which is implemented in SPTOOL. Each MPFIT run was performed with a fixed ξ. We used a fitting window, $[\lambda_c - \Delta_2/2 : \lambda_c + \Delta_2/2]$, where λ_c is the central wavelength of each line and Δ_2 is the wavelength shift corresponding to a redshift of 60 km s^{-1}, as Equation (1). MPFIT searches for an optimized solution by treating the following as free parameters: $\log \epsilon_{\rm Fe}$, the width of Gaussian line broadening (including macroturbulence and instrumental broadening), and a small wavelength offset $\Delta\lambda$, which compensates for any remaining errors in the wavelength calibration and in the correction of the redshift of the target. We thus obtained $\log \epsilon_{\rm Fe}$ values for

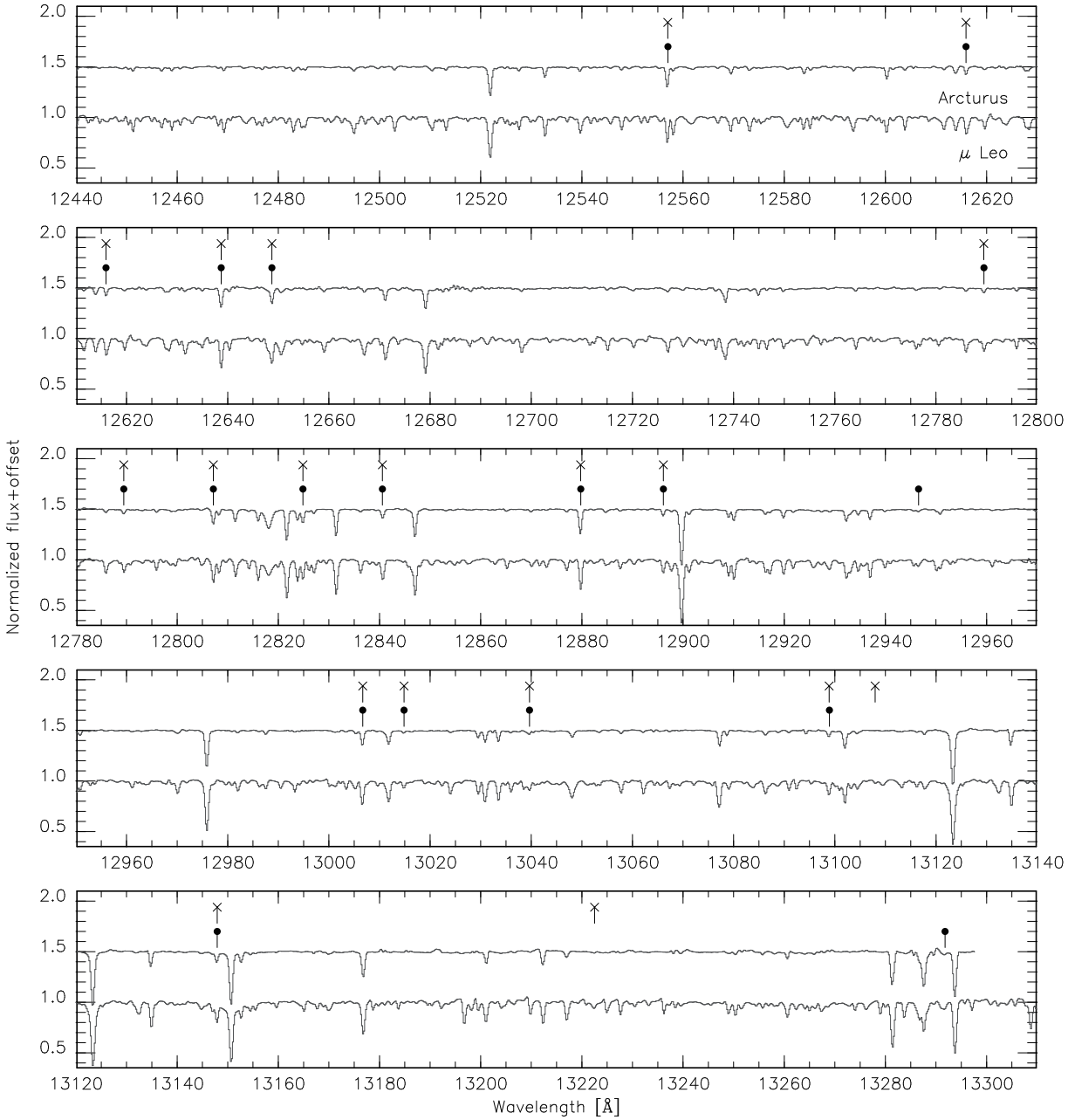

FIG. 1.— continued.

the grid of 21 ξ values for individual Fe I lines. The number of lines measured for each combination of line list and object is given as N_2 in Table 4. Note that MPFIT failed to give a solution for a few lines for μ Leo, namely, Fe I 11026.78, 11053.52, and 11135.96 Å from both line lists, Fe I 9753.09, 9820.24, 13145.07, and 11119.80 Å from VALD3 only, and Fe I 11715.49, and 13291.78 Å from MB99 only. Visual inspection of its observed spectrum around these lines suggests that they are blended by one or two other strong lines. Such cases could have been rejected based on the β_1 and β_2 indices, but the blends around the above lines were not reproduced by the synthetic spectra (on the basis of MB99 and VALD3). Four and three of these lines were rejected for Arcturus when we used VALD3 and MB99, respectively, because they were predicted to be weak, but for the other lines we obtained $\log \epsilon_{\rm Fe}$ of Arcturus. In Tables 2 and 3, we include these lines for which MPFIT failed, marked with an asterisk (*), because they may still be useful in some cases or once the line lists have been improved to reproduce the spectra including the neighboring lines. The Fe I line at 13291.78 Å in the MB99 list was selected for μ Leo; however MPFIT gives completely wrong $\log \epsilon_{\rm Fe}$ values, higher than 10 dex. We found that this line is severely blended in the observed spectrum of μ Leo, but

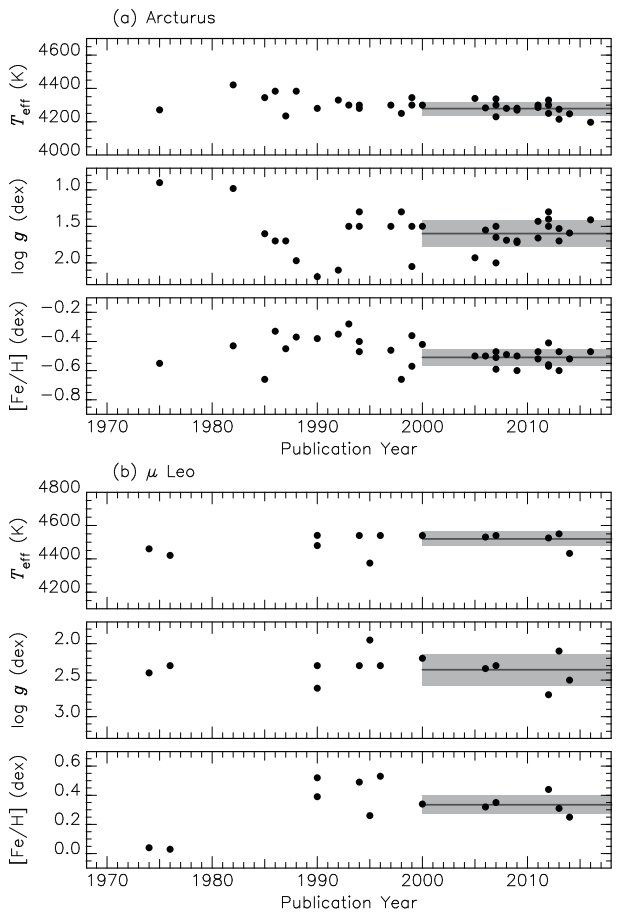

FIG. 2.— Previous measurements of $T_{\rm eff}$, $\log g$, and [Fe/H] in the literature. The upper panels consider 33 papers for Arcturus (Maeckle et al. 1975; Gratton et al. 1982; Bell et al. 1985; Kyrolainen et al. 1986; Leep et al. 1987; Edvardsson 1988; McWilliam 1990; Brown & Wallerstein 1992; Peterson et al. 1993; McWilliam & Rich 1994; Sneden et al. 1994; Hill 1997; Gonzalez & Wallerstein 1998; Tomkin & Lambert 1999; Thévenin & Idiart 1999; Carr et al. 2000; Luck & Heiter 2005; Fulbright et al. 2006; Lecureur et al. 2007; Hekker & Meléndez 2007; Ramírez et al. 2007; Meléndez et al. 2008; Worley et al. 2009; Takeda et al. 2009; Ramírez & Allende Prieto 2011; Bruntt et al. 2011; Sheffield et al. 2012; Britavskiy et al. 2012; Thygesen et al. 2012; Ramírez et al. 2013; Smith et al. 2013; Jofré et al. 2014; Boeche & Grebel 2016). The bottom panels consider 13 papers for μ Leo (Oinas 1974; Peterson 1976; McWilliam 1990; Gratton & Sneden 1990; McWilliam & Rich 1994; Luck & Challener 1995; Castro et al. 1996; Smith & Ruck 2000; Fulbright et al. 2006; Lecureur et al. 2007; Thygesen et al. 2012; Smith et al. 2013; Jofré et al. 2014). The horizontal line and strip in each panel indicate the average and standard deviation of the measurements made in 2000 or later.

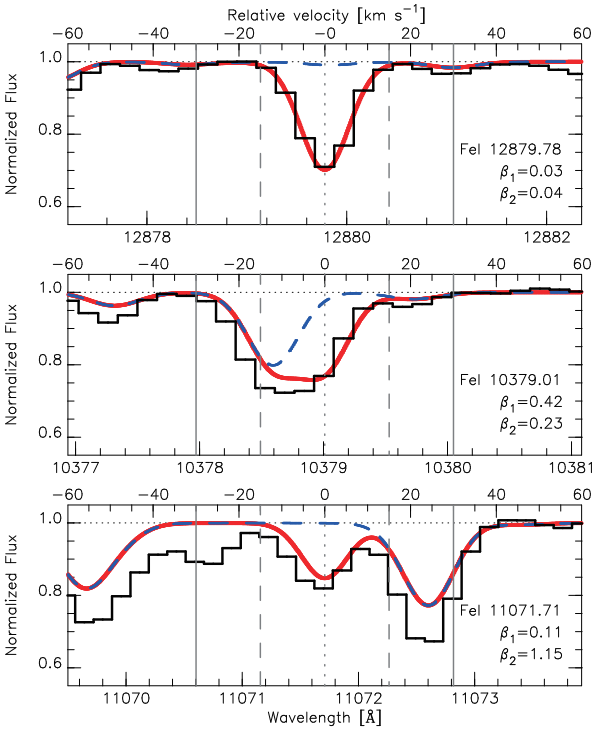

FIG. 3.— Comparisons between the observational spectrum (black) and the two synthetic spectra ($f_{\rm syn}$ by red solid curve and $f^{\dagger}_{\rm syn}$ by blue dashed curve; see text for the details) are illustrated for three Fe I lines seen in μ Leo as examples. The MB99 list was used for atomic lines in those synthetic spectra. The vertical lines indicate the central wavelength and the velocity ranges corresponding to the widths of $\Delta_1 = 30$ and $\Delta_2 = 60$ km s^{-1}. The three Fe I lines have different β_1 and β_2 values from each other, as labeled in the panels, and only the one in the top panel was selected for our abundance analysis according to the selection criteria of $\beta_1 < 0.3$ and $\beta_2 < 1$.

it looks fairly isolated in the synthetic spectrum. This inconsistency probably causes the absurd $\log \epsilon_{\rm Fe}$ values. We, therefore, reject the MPFIT measurements of this line but include the line in Table 3 marked with the asterisk (*). These rejected lines are not included in N_2 in Table 4. Additionally, the lines with $X > -6$ are not used when we estimate the final iron abundances (Section 5.2), and those lines are not included in N_2 in the table.

We then used a bootstrap method to obtain not only the best estimates of ξ and $\log \epsilon_{\rm Fe}$ but also respective errors. We repeatedly extracted N_2 randomly-selected lines among the N_2 lines with $(\xi, \log \epsilon_{\rm Fe})$ available. Note that for each bootstrap sample, each line may be selected more than once and some lines may be excluded.

For a given set of the $(\xi, \log \epsilon_{\rm Fe})$ values for a bootstrap sample, we obtained the best estimates of ξ and $\log \epsilon_{\rm Fe}$ as follows. First, we searched for ξ that leads to no trend of $\log \epsilon_{\rm Fe}$ of individual lines against the line strength. We considered the X value introduced in Section 4 as a proxy of the line strength, and made a simple least-squares fit,

$$\log \epsilon_{\rm Fe} = aX + b, \qquad (4)$$

to calculate the trend, a, for each ξ of the grid. Figure 4 illustrates that lines with different strengths have different responses to ξ. Lines with large X values, but within the range of $X < -6$, tend to give smaller $\log \epsilon_{\rm Fe}$ for larger ξ. This leads to a monotonic decrease in the slope a with increasing ξ. One can, thus, find a ξ that gives $a = 0$ by interpolating two neighboring ξ values where a turns from positive to negative. In Figure 4, a is almost zero at $\xi = 1.2$ km s^{-1} (panel b). The lines at $X > -6$ are biased toward higher $\log \epsilon_{\rm Fe}$ values, and we will discuss their impact on the estimate of ξ and

TABLE 2
List of Fe I lines selected from VALD3 and abundances

Wavelength (Å)	EP (eV)	$\log gf$ (dex)	Arcturus (dex)	μ Leo (dex)
9117.1309	2.8581	−3.454	6.970	7.888
9118.8806	2.8316	−2.115	6.411	8.612
9146.1275	2.5881	−2.804	6.828	6.749
9210.0240	2.8450	−2.404	6.789	7.276
9602.1301	5.0117	−1.744	(w)	7.408
9653.1147	4.7331	−0.684	6.780	7.545
9657.2326	5.0856	−0.780	6.768	7.152
9738.5725	4.9913	+0.150	6.861	7.308
9753.0906	4.7955	−0.782	6.850	(*)
9791.6983	2.9904	−4.223	(w)	7.126
9800.3075	5.0856	−0.453	6.558	7.457
9811.5041	5.0117	−1.362	7.100	7.646
9820.2408	2.4242	−5.073	(w)	(*)
9861.7337	5.0638	−0.142	6.647	(b)
9868.1857	5.0856	−0.979	7.098	8.246
9889.0351	5.0331	−0.446	6.974	7.660
9937.0898	4.5931	−2.442	(w)	7.544
9944.2065	5.0117	−1.338	7.046	7.401
9980.4629	5.0331	−1.379	6.851	7.935
10041.472	5.0117	−1.772	(w)	7.958
10065.045	4.8349	−0.289	6.774	7.618
10081.393	2.4242	−4.537	6.995	7.602
10114.014	2.7586	−3.692	6.918	(b)
10145.561	4.7955	−0.177	6.947	(b)
10155.162	2.1759	−4.226	6.770	7.459

These are the first 25 lines. Lines weaker than the limit 0.05 in depth in synthetic spectra, are flagged as (w), and lines that are blended too much are flagged as (b). The flag (*) indicates lines whose abundance could not be obtained or was rejected. See the details of the line selection in text. The entire list is available as an ASCII file in the online journal.

TABLE 3
List of Fe I lines selected from MB99 and abundances

Wavelength (Å)	EP (eV)	$\log gf$ (dex)	Arcturus (dex)	μ Leo (dex)
10019.79	5.48	−1.44	(w)	7.582
10032.86	5.51	−1.36	(w)	7.522
10041.47	5.01	−1.84	(w)	7.982
10065.05	4.84	−0.57	7.144	7.825
10081.39	2.42	−4.53	6.963	7.459
10114.02	2.76	−3.76	7.010	(b)
10145.57	4.80	−0.41	7.335	8.342
10155.16	2.18	−4.36	6.901	7.438
10167.47	2.20	−4.26	7.071	7.757
10195.11	2.73	−3.63	6.915	7.800
10216.32	4.73	−0.29	7.262	8.006
10218.41	3.07	−2.93	7.092	8.038
10230.78	5.87	−0.70	(w)	7.774
10265.22	2.22	−4.67	6.962	7.416
10307.45	4.59	−2.45	(w)	7.524
10340.89	2.20	−3.65	7.092	7.508
10347.96	5.39	−0.82	6.970	8.024
10353.81	5.39	−1.09	(w)	7.707
10395.80	2.18	−3.42	6.749	7.353
10401.72	3.02	−4.36	(w)	7.583
10435.36	4.73	−2.11	(w)	7.852
10452.75	3.88	−2.30	6.781	7.713
10469.66	3.88	−1.37	6.984	7.908
10532.24	3.93	−1.76	7.151	7.733
10555.65	5.45	−1.39	(w)	7.565

These are the first 25 lines. The entire list is available as an ASCII file in the online journal. The meanings of the flags, (w), (b), and (*), are same as in Table 2.

TABLE 4
Microturbulence and iron abundance

Line list	N_1	N_2	ξ (km s^{-1})	$\log\epsilon_{\rm Fe}$ (dex)	r
			Arcturus		
VALD3	73	67	$1.22^{-0.12}_{+0.12}$	$6.81^{+0.06}_{-0.06}$	−0.946
MB99	57	53	$1.20^{-0.11}_{+0.11}$	$7.01^{+0.04}_{-0.04}$	−0.875
			μ Leo		
VALD3	91	79	$1.16^{-0.24}_{+0.23}$	$7.62^{+0.11}_{-0.10}$	−0.909
MB99	72	63	$1.54^{-0.17}_{+0.17}$	$7.73^{+0.06}_{-0.05}$	−0.828

$\log\epsilon_{\rm Fe}$ in Section 5.3. For the ξ obtained, we calculated $\log\epsilon_{\rm Fe}$ for N_2 individual lines of the bootstrap sample by interpolating the grid points of $(\xi, \log\epsilon_{\rm Fe})$ and took the average of the $\log\epsilon_{\rm Fe}$ values. This gives the best estimate of $(\xi, \log\epsilon_{\rm Fe})$ for the given bootstrap sample. We then took the median and also the 16th and 84th percentiles (as the $\pm1\,\sigma$ range) in each of the histograms of ξ and $\log\epsilon_{\rm Fe}$ values obtained after a large number of bootstrap samples. We repeated this procedure one million times ($N_{\rm b} = 1,000,000$) in this study, and the best estimates of $(\xi, \log\epsilon_{\rm Fe})$ are listed in Table 4 for each combination of the line list and object. We also calculated the correlation coefficient of the two parameters,

$$r = \frac{\sum\left(\xi^i - \langle\xi\rangle\right)\left(\log\epsilon^i_{\rm Fe} - \langle\log\epsilon_{\rm Fe}\rangle\right)}{\sqrt{\sum\left(\xi^i - \langle\xi\rangle\right)^2}\sqrt{\sum\left(\log\epsilon^i_{\rm Fe} - \langle\log\epsilon_{\rm Fe}\rangle\right)^2}} \quad (5)$$

where ξ^i and $\log\epsilon^i_{\rm Fe}$ are the microturbulence and iron abundance obtained for each bootstrap sample, and $\langle\xi\rangle$ and $\langle\log\epsilon_{\rm Fe}\rangle$ are their means (not medians). Each of the summations in Equation (5) takes the integer i for N_b lines, i.e., $1 \le i \le N_{\rm b}$.

The contours in Figure 5 represent the distribution of $(\xi, \log\epsilon_{\rm Fe})$ obtained in the bootstrap simulation. The large $N_{\rm b}$ was used mainly to obtain smooth contours in Figure 5, although we could obtain reasonably stable values including $1\,\sigma$ confidence intervals at around $N_{\rm b} = 10,000$. There is a linear anticorrelation, as expected, between ξ and $\log\epsilon_{\rm Fe}$, which shows that the errors in the two parameters are anticorrelated (see r in Table 4). We do not use r later in this paper, but it is a useful indicator of how much the measured $\log\epsilon_{\rm Fe}$ depends on the ξ estimated. For example, r is expected to vary with the proportion of strong lines. Using more weak lines would reduce the anticorrelation because the $\log\epsilon_{\rm Fe}$ values of weak lines have a smaller dependency on ξ.

Now, we estimate $\log\epsilon_{\rm Fe}$ values of individual lines with the best estimates of ξ that are given in Table 4. For each combination of object and line list, each Fe I line has 21 measurements of $\log\epsilon_{\rm Fe}$ at different ξ values, and we interpolated $\log\epsilon_{\rm Fe}$ values at the two grid points of ξ next to its best estimate. The $\log\epsilon_{\rm Fe}$ values obtained for individual lines are listed in Table 2 for VALD3 and in Table 3 for MB99. In the two tables, lines weaker than the limit are flagged as (w), and lines that are blended

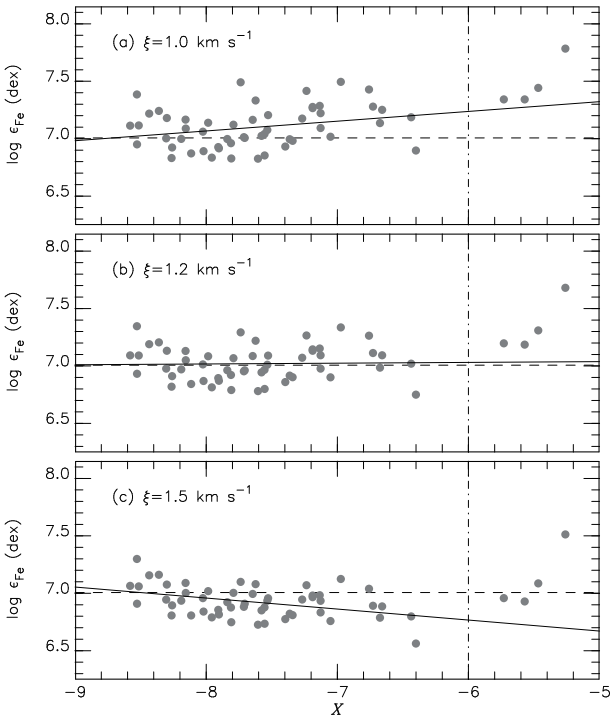

FIG. 4.— Dependency of $\log \epsilon_{\rm Fe}$ on line strength indicated by X at different ξ values, (a) 1.0, (b) 1.2, and (c) 1.5 km s^{-1}. The solid line in each panel shows the linear fit to the $(X, \log \epsilon_{\rm Fe})$ points at $X < -6$. This plot is for the combination of the MB99 line list and Arcturus. The Fe I lines with $X > -6$, indicated by the vertical line in each panel, were not used in the final $(\xi, \log \epsilon_{\rm Fe})$ determination.

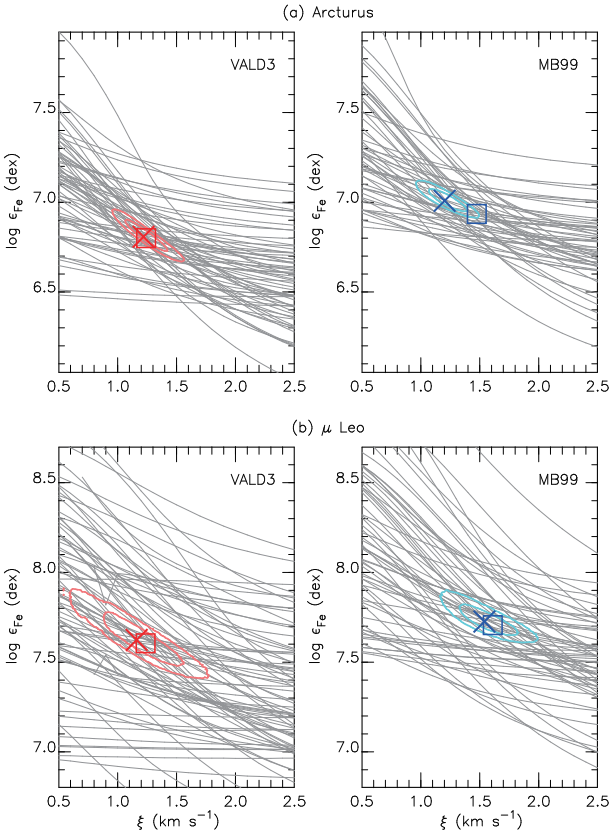

FIG. 5.— Contours for the density distribution of $(\xi, \log \epsilon_{\rm Fe})$ obtained in the bootstrap simulation. The inner and outer contours show the ranges that include 68.26 % ($1\,\sigma$) and 95.44 % ($2\,\sigma$) of the 1,000,000 bootstrap samples. Four panels are given for the combinations of line lists (VALD3 and MB99) and targets (Arcturus and μ Leo). In each panel, gray curves indicate the dependency of $\log \epsilon_{\rm Fe}$ for individual lines. The cross symbol indicates the best estimates that we obtained for each set (Table 4), and the open square indicates the estimates obtained with strong lines with $X > -6$ included (see Section 5.2).

too much are flagged as (b). Lines whose MPFIT measurements were unavailable or rejected were not used for the abundance analysis, but we include them in the tables with the (*) flag. Figure 6 plots the individual $\log \epsilon_{\rm Fe}$ values against the X value and EP. For both objects, the X values of the measured lines are spread over a wide range, approximately between -9 and -5 dex. Such a wide range among the lines in the z', Y, and J bands is advantageous, for example, compared with a narrow range, -8.3 to -7.3 dex, covered by the H-band lines used by Smith et al. (2013). The $\log \epsilon_{\rm Fe}$ shows little dependency on X as demanded in the analysis and also have no clear dependency on EP, indicating that the adopted $T_{\rm eff}$ are reasonable. The scatters of $\log \epsilon_{\rm Fe}$ from individual lines are larger for μ Leo than for Arcturus. This is probably because the spectrum of μ Leo has stronger contaminating lines, especially CN lines, than Arcturus (McWilliam & Rich 1994; Smith et al. 2013), which makes it harder to trace the continuum.

5.2. *Comparison between the two line lists*

There are a few differences between the estimates of $(\xi, \log \epsilon_{\rm Fe})$ obtained with the two line lists.

Firstly, in Table 4, the standard errors for $\log \epsilon_{\rm Fe}$ from the two lists are similar to each other for Arcturus. The number of Fe I lines is larger for VALD3, but the measured $\log \epsilon_{\rm Fe}$ has a slightly larger scatter than for MB99, which is compensated by the larger N_2. For μ Leo, the scatter of $\log \epsilon_{\rm Fe}$ is rather large with VALD3 (Figure 6), and this leads to a larger standard error even with a larger number of Fe I lines.

Secondly, the resultant $\log \epsilon_{\rm Fe}$ values for MB99 are slightly higher than those obtained for VALD3. In fact, there is a systematic offset in the $\log gf$ values between the two line lists (Figure 7). The systematic offset, $\sim$0.2 dex, approximately corresponds to the difference in $\log \epsilon_{\rm Fe}$ for Arcturus obtained with VALD3 and MB99. In contrast, the corresponding difference in the case of μ Leo is smaller. Although the offsets in the $\log gf$ have a direct impact on the $\log \epsilon_{\rm Fe}$ estimation, the different ξ values obtained for μ Leo with the two lists (larger ξ with MB99 than VALD3) partly compensate for this systematic offset.

Finally, the final estimates depend slightly on whether very strong lines with $X > -6$ are used or not. In Figure 7, very strong lines clearly show a systematic tilt. These strong lines have an impact on the slopes, e.g., seen in Figure 4. The lower $\log gf$ values of the stronger lines in MB99 would give higher $\log \epsilon_{\rm Fe}$ values with a fixed ξ, but this would also cause a tilt in Figure 4. A larger ξ is therefore required so that $\log \epsilon_{\rm Fe}$ values of strong and

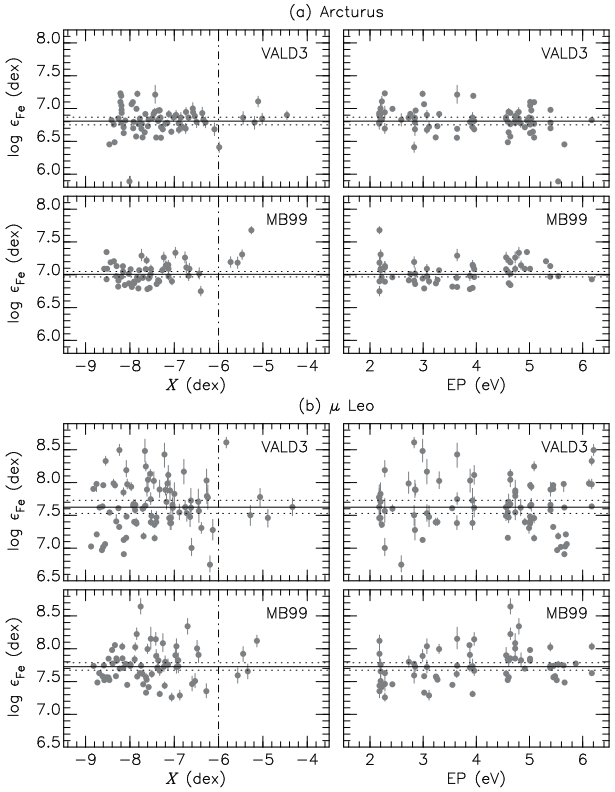

FIG. 6.— The $\log \epsilon_{\rm Fe}$ values obtained for individual Fe I lines are plotted against the line strength indicator, X, on the left-hand side and against the excitation potential, EP, on the right-hand side. For each of the two targets (Arcturus in the upper panels and μ Leo in the lower panels), the results for the two line lists (VALD3 and MB99) are presented. The horizontal solid line and the dashed lines in each panel indicate the best estimate and $1\,\sigma$ confidence intervals for the combination of line list and target. The Fe I lines with $X > -6$, indicated by the vertical line in each panel, were not used in the final $(\xi, \log \epsilon_{\rm Fe})$ determination.

weak lines get balanced. While this is an important difference between the two line lists, generally speaking, it is suggested that using very strong lines often introduces complications such as non-LTE effects into a chemical abundance analysis (e.g., Kovtyukh & Andrievsky 1999; Gratton et al. 2006; Takeda et al. 2013). Based on synthetic spectra, we found that, in case of lines with X $\gtrsim -6$, the line core does not grow any more with increasing metallicity and the damping wing starts to contribute to the EW at around the solar metallicity. If we run the bootstrap method with the same lines but including those with $X > -6$, we obtain moderately different results for the MB99 list, as illustrated in Figure 5. Four lines from MB99 have $X > -6$, and including them leads to higher ξ and lower $\log \epsilon_{\rm Fe}$ values: $(\xi, \log \epsilon_{\rm Fe}) = (1.47 \pm 0.18, 6.94 \mp 0.05)$ for Arcturus and $(1.61 \pm 0.16, 7.71 \mp 0.06)$ for μ Leo. The changes caused by including the strongest lines are marginally significant, 1–2 σ, for the former but are negligible for the latter. Figure 6 shows that one line, Fe I λ 11973.04, with the largest $(X, \log \epsilon_{\rm Fe})$ has a particularly strong impact on the slope in the X versus $\log \epsilon_{\rm Fe}$ diagram for Arcturus with MB99. The same line gives $\log \epsilon_{\rm Fe} \sim 8.10$ dex, which is also higher than the average, for μ Leo. However, the scatter of $\log \epsilon_{\rm Fe}$ from lines within the low-X range is large, which explains the relatively small effect of including the high-X lines for μ Leo. In contrast, six VALD3 lines that we selected have $X > -6$, but including them has a negligible impact on the $(\xi, \log \epsilon_{\rm Fe})$ measurements. For VALD3, the Fe I λ 11973.046 line leads to $\log \epsilon_{\rm Fe}$ values that are very close to the average abundances from other lines for both Arcturus and μ Leo. This line corresponds to the rightmost point in Figure 7 and has a very large difference, 0.8 dex, between the $\log gf$ values in the two line lists. Considering these complications, we decided to adopt the $(\xi, \log \epsilon_{\rm Fe})$ values obtained without the lines at $X > -6$ as our best estimates. Although the $\log \epsilon_{\rm Fe}$ from individual lines depend on ξ as described above, we found that the [Fe/H] obtained in different works are not correlated with ξ (Figure 8). This is probably because systematic differences in previous works, such as differences in line lists and atmosphere models, introduced a scatter larger than the expected correlation between the two parameters.

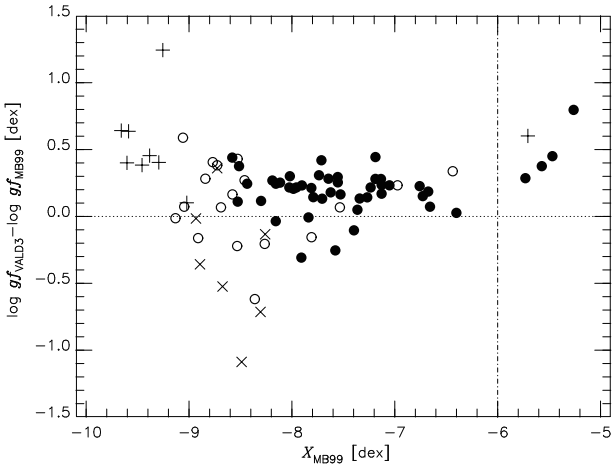

FIG. 7.— Comparison of the $\log gf$ values for the two line lists VALD3 and MB99. The filled circles indicate the lines used for all combinations of line list and target, and the open circles indicate those used for both line lists but for only one of the two targets, Arcturus or μ Leo. The + and × symbols indicate the lines used in only one of the line lists (+ for VALD3 and × for MB99) for both targets. The temperature of Arcturus, $T_{\rm eff} = 4286$ K, and the $\log gf$ values for MB99 are used for calculating the X values (abscissa).

5.3. *Effects of stellar parameters on metallicity*

Here, we estimate how much the uncertainties in the stellar parameters, $T_{\rm eff}$, $\log g$, and [M/H], affect the estimates of $\log \epsilon_{\rm Fe}$. We adopt the errors in these parameters from Heiter et al. (2015), as given in Table 1. To evaluate the effect of changing the three parameters, we added positive and negative offsets to each parameter in the atmosphere models one by one. For each offset, we ran MPFIT and obtained $\log \epsilon_{\rm Fe}$ for the N_2 lines and calculated their means. We did not use the bootstrap method described in Section 5.1 for this step because we need to estimate the effect of a parameter at a fixed ξ. Then, we compared the above means with the counterparts of the mean $\log \epsilon_{\rm Fe}$ with the stellar parameters in Table 1. This gives the offsets in $\log \epsilon_{\rm Fe}$, $\Delta(T_{\rm eff})$, $\Delta(\log g)$, and

Δ([M/H]), as a result of changing the stellar parameters (Table 5).

For both objects and for both line lists, we found that varying the temperature or the gravity gives rather tiny changes in $\log \epsilon_{\rm Fe}$. Synthetic spectra with the same parameters but an offset of 50 K in $T_{\rm eff}$ or an offset of $\pm$ 0.1 dex in $\log g$ do not actually show any noticeable changes in the Fe I lines. The Δ([M/H]) is larger compared with these two. The Δ([M/H]) of Arcturus is smaller than that of μ Leo. We believe that this is simply because the σ[M/H] of Arcturus is smaller than that of μ Leo. We combine the Δ values with the confidence intervals of $\log \epsilon_{\rm Fe}$ estimated by the bootstrap method, the $\Delta_{\rm b}$, in Table 5. Note that the $\Delta_{\rm b}$ correlated with ξ include other errors, e.g., observational errors in the spectra and errors in $\log gf$. Combining the above errors, we can estimate the total error as

$$\Delta_{\rm total} = \sqrt{\Delta_{\rm b}^2 + \Delta(T_{\rm eff})^2 + \Delta(\log g)^2 + \Delta([{\rm M/H}])^2}, \quad (6)$$

which is given in Table 5. Here, we ignored the covariant terms. The previous estimates that we compiled in Figure 2 show no clear correlation between any two of the four parameters, $T_{\rm eff}$, $\log g$, [Fe/H], or ξ.

5.4. *Comparison with previous results*

Figure 8 plots the scaled metallicity [Fe/H], where the solar $\log \epsilon_{\rm Fe}$ is assumed to be 7.45 dex, against ξ. We compared our iron abundances with those in previous papers (an open circle: Smith et al. 2013, a star: Jofré et al. 2014, filled circles: the others) that we compiled in Figure 2 except those without the microturbulence explicitly given. Our total errors are comparable with the errors estimated by Smith et al. (2013) and Jofré et al. (2014). Within the errors and scatters of [Fe/H] in the literature, our metallicities based on the z', Y, and J bands spectra agree very well with previous estimates. The metallicities estimated with MB99 show better agreement with previous estimates than those with VALD3. Considering also that the scatters in Figure 6 are smaller with MB99, we believe that the $\log gf$ values of MB99 are better than those of VALD3 for chemical abundance analyses.

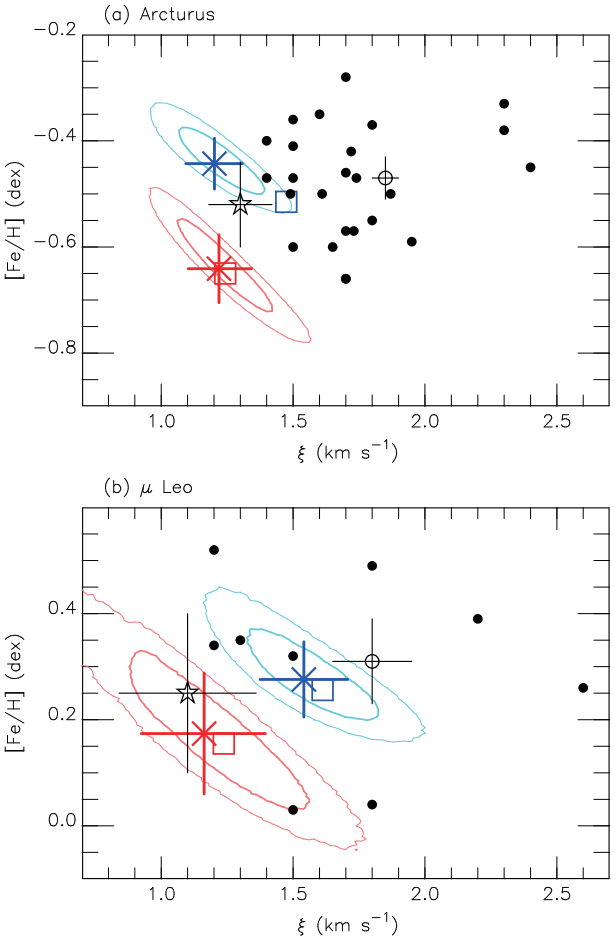

FIG. 8.— Comparison of our estimates of ξ and [Fe/H] with previous estimates. The contours, cross symbols, and open squares are as in Figure 5. The results for VALD3 and MB99 are illustrated in red and blue, respectively. The total errors in Table 5 are added to the crosses. Two recent results in the literature are shown with error bars: Smith et al. (2013) and Jofré et al. (2014) indicated by an open circle and a star symbol, respectively. The filled circles indicate the other previous estimates that we compiled in Figure 2 except those without the microturbulence explicitly given.

6. CONCLUDING REMARKS

We used the $z'YJ$ band high-resolution spectra of Arcturus and μ Leo, obtained with WINERED, to estimate the microturbulence and iron abundance with a precision similar to that of previous results from spectra at different wavelengths. Our lists of Fe I lines in the 0.91–1.33 μm range will be useful for obtaining the precise metallicities of stars obscured by severe interstellar extinction compared with the optical regime, for which the extinction is stronger. For many objects in the Galactic disk found in recent infrared surveys, this new wavelength window may be ideal for detailed abundance analyses. One of the major error sources is the uncertainty in ξ in various studies, including ours, based on spectra at different wavelengths from the optical (e.g., Table 3 of Jofré et al. 2014) to the H-band (e.g., Table 7 of Smith et al. 2013). Furthermore, how to determine the microturbulence and its error is not established or straightforward. The bootstrap method that we demonstrated in this paper can give quantitative estimates of the microturbulence and its error. The error in microturbulence is 0.11–0.24 km s^{-1} for each combination of target and line list. The obtained microturbulences are consistent with those that were estimated or assumed in previous studies on the same targets. Note, however, that using different line lists (or different sets of lines) can result in slightly different microturbulences depending especially on the $\log gf$ values of strong lines used in the analysis. The very strong lines ($X > -6$) were rejected because these lines are likely to introduce problems into a chemical abundance analyses due to severe saturation, non-LTE effects, the contribution of EW from the damping wing, and so on. Considering the comparison of our estimates with previous ones in addition to the scatters of $\log \epsilon_{\rm Fe}$, we adopt the measurements with the Fe I lines selected from MB99 as our best estimates: $(\xi, \log \epsilon_{\rm Fe}) = (1.20 \pm 0.11$ km s^{-1}, 7.01 ± 0.05 dex) and $(1.54 \pm 0.17$ km s^{-1}, 7.73 ± 0.07 dex) for Arcturus and μ Leo, respectively.

TABLE 5
Effects of stellar parameters on iron abundance

Line list	$\sigma T_{\rm eff}$ (K)	$\Delta(T_{\rm eff})$ (dex)	$\sigma \log g$ (dex)	$\Delta(\log g)$ (dex)	σ[M/H] (dex)	Δ([M/H]) (dex)	σ_ξ (km s^{-1})	$\Delta_{\rm b}{}^+$ (dex)	$\Delta_{\rm b}{}^-$ (dex)	$\Delta_{\rm total}$ (dex)
					Arcturus					
VALD3	$\pm$35	$\pm$0.006	$\pm$0.06	$\pm$0.008	$\pm$0.08	$\pm$0.025	$\pm$0.12	$-$0.058	$+$0.059	0.064
MB99	$\pm$35	$\pm$0.007	$\pm$0.06	$\pm$0.009	$\pm$0.08	$\pm$0.021	$\pm$0.11	$-$0.040	$+$0.043	0.048
					μ Leo					
VALD3	$\pm$60	$\mp$0.003	$\pm$0.09	$\pm$0.008	$\pm$0.15	$\pm$0.052	$^{+0.24}_{-0.23}$	$-$0.095	$+$0.106	0.114
MB99	$\pm$60	$\mp$0.004	$\pm$0.09	$\pm$0.017	$\pm$0.15	$\pm$0.040	$\pm$0.17	$-$0.052	$+$0.061	0.071

The σ_p and the $\Delta(p)$ indicate the error of stellar parameter p and its effect on $\log \epsilon_{\rm Fe}$, where p takes $T_{\rm eff}$, $\log g$, or [M/H]. The $\Delta_{\rm b}{}^\pm$ indicate the error of $\log \epsilon_{\rm Fe}$ from the bootstrap method. In the last column, the $\Delta_{\rm total}$ is the total uncertainty (see details in text).

We acknowledge useful comments from the anonymous referee. We are grateful to the staff of Koyama Astronomical Observatory for their support during our observation. We thank Yoichi Takeda for providing us with SPTOOL. This work has made use of the VALD database, operated at Uppsala University, the Institute of Astronomy RAS in Moscow, and the University of Vienna. This study has been financially supported by Grants-in-Aid (numbers 16684001, 20340042, 21840052, 26287028, and 18H01248) from the Japan Society for the Promotion of Science (JSPS) and by Supported Programs for the Strategic Research Foundation at Private Universities (S0801061 and S1411028) from the Ministry of Education, Culture, Sports, Science and Technology (MEXT) of Japan. K.F. is supported by a JSPS Grant-in-Aid for Reseearch Activity Start-up (No. 16H07323). N.K. is supported by JSPS-DST under the Japan-India Science Cooperative Programs during 2013-2015 and 2016-2018.

REFERENCES

Anders, E., & Grevesse, N. 1989, Geochim. Cosmochim. Acta, 53, 197
Bell, R. A., Edvardsson, B., & Gustafsson, B. 1985, MNRAS, 212, 497
Boeche, C., & Grebel, E. K. 2016, A&A, 587, A2
Branch, D., Bonnell, J., & Tomkin, J. 1978, ApJ, 225, 902
Britavskiy, N. E., Andrievsky, S. M., Tsymbal, V. V., et al. 2012, A&A, 542, A104
Brown, J. A., & Wallerstein, G. 1992, AJ, 104, 1818
Bruntt, H., Frandsen, S., & Thygesen, A. O. 2011, A&A, 528, A121
Carr, J. S., Sellgren, K., & Balachandran, S. C. 2000, ApJ, 530, 307
Castro, S., Rich, R. M., McWilliam, A., et al. 1996, AJ, 111, 2439
Cunha, K., & Smith, V. V. 2006, ApJ, 651, 491
Davies, B., Origlia, L., Kudritzki, R.-P., et al. 2009a, ApJ, 694, 46
Davies, B., Origlia, L., Kudritzki, R.-P., et al. 2009b, ApJ, 696, 2014
Edvardsson, B. 1988, A&A, 190, 148
Fukue, K., Matsunaga, N., Yamamoto, R., et al. 2015, ApJ, 812, 64
Fulbright, J. P., McWilliam, A., & Rich, R. M. 2006, ApJ, 636, 821
García Pérez, A. E., Allende Prieto, C., Holtzman, J. A., et al. 2016, AJ, 151, 144
Gratton, L., Gaudenzi, S., Rossi, C., & Gratton, R. G. 1982, MNRAS, 201, 807
Gratton, R., Bragaglia, A., Carretta, E., & Tosi, M. 2006, ApJ, 642, 462
Gratton, R. G., & Sneden, C. 1990, A&A, 234, 366
Gonzalez, G., & Wallerstein, G. 1998, AJ, 116, 765
Grevesse, N., Asplund, M., & Sauval, A. J. 2007, Space Sci. Rev., 130, 105
Heiter, U., Jofré, P., Gustafsson, B., et al. 2015, A&A, 582, A49
Hekker, S., & Meléndez, J. 2007, A&A, 475, 1003
Hill, V. 1997, A&A, 324, 435
Holtzman, J. A., Hasselquist, S., Shetrone, M., et al. 2018, AJ, 156, 125
Ikeda, Y., Kobayashi, N., Kondo, S., et al. 2016, Proc. SPIE, 9908, 99085Z
Jofré, P., Heiter, U., Soubiran, C., et al. 2014, A&A, 564, A133
Kovtyukh, V. V., & Andrievsky, S. M. 1999, A&A, 351, 597
Kurucz, R. L. 1993, Kurucz CD-ROM, Cambridge, MA: Smithsonian Astrophysical Observatory, —c1993, December 4, 1993,
Kurucz, R. L., & Bell, B. 1995, Kurucz CD-ROM, Cambridge, MA: Smithsonian Astrophysical Observatory, —c1995, April 15, 195,
Kyrolainen, J., Tuominen, I., Vilhu, O., & Virtanen, H. 1986, A&AS, 65, 11
Lecureur, A., Hill, V., Zoccali, M., et al. 2007, A&A, 465, 799
Leep, E. M., Wallerstein, G., & Oke, J. B. 1987, AJ, 93, 338
Luck, R. E., & Challener, S. L. 1995, AJ, 110, 2968
Luck, R. E., & Heiter, U. 2005, AJ, 129, 1063
Maeckle, R., Holweger, H., Griffin, R., & Griffin, R. 1975, A&A, 38, 239
Magain, P. 1984, A&A, 134, 189
Majewski, S. R., et al. 2017, AJ, 154, 94
McWilliam, A. 1990, ApJS, 74, 1075
McWilliam, A., & Rich, R. M. 1994, ApJS, 91, 749
Meléndez, J.,Asplund, M., Alves-Brito, A., et al. 2008, A&A, 484, L21
Meléndez, J., & Barbuy, B. 1999, ApJS, 124, 527
Mészáros, S., Allende Prieto, C., Edvardsson, B., et al. 2012, AJ, 144, 120
Ness, M., Hogg, D. W., Rix, H.-W., Ho, A. Y. Q., & Zasowski, G. 2015, ApJ, 808, 16
Oinas, V. 1974, ApJS, 27, 405
Oinas, V. 1977, A&A, 61, 17
Origlia, L., Oliva, E., Maiolino, R., et al. 2013, A&A, 560, A46
Origlia, L., Oliva, E., Sanna, N., et al. 2016, A&A, 585, A14
Peterson, R. 1976, ApJS, 30, 61
Peterson, R. C., Dalle Ore, C. M., & Kurucz, R. L. 1993, ApJ, 404, 333
Ramírez, I., & Allende Prieto, C. 2011, ApJ, 743, 135
Ramírez, I., Allende Prieto, C., & Lambert, D. L. 2007, A&A, 465, 271
Ramírez, I., Allende Prieto, C., & Lambert, D. L. 2013, ApJ, 764, 78
Ryabchikova, T., et al. 2015, Phys. Scripta, 90, 054005
Ryde, N., Edvardsson, B., Gustafsson, B., et al. 2009, A&A, 496, 701
Ryde, N., Gustafsson, B., Edvardsson, B., et al. 2010, A&A, 509, A20
Ryde, N., Schultheis, M., Grieco, V., et al. 2016, AJ, 151, 1
Sameshima, H., Matsunaga, N., Kobayashi, N., et al. 2018, PASP, 130, 074502
Sheffield, A. A., Majewski, S. R., Johnston, K. V., et al. 2012, ApJ, 761, 161
Shetrone, M., Bizyaev, D., Lawler, J. E., et al. 2015, ApJS, 221, 24
Smith, G., & Ruck, M. J. 2000, A&A, 356, 570
Smith, V. V., Cunha, K., Shetrone, M. D., et al. 2013, ApJ, 765, 16
Sneden, C., Kraft, R. P., Langer, G. E., Prosser, C. F., & Shetrone, M. D. 1994, AJ, 107, 1773
Takeda, Y. 1995, PASJ, 47, 287
Takeda, Y., Kaneko, H., Matsumoto, N., et al. 2009, PASJ, 61, 563
Takeda, Y., Kang, D.-I., Han, I., Lee, B.-C., & Kim, K.-M. 2013, MNRAS, 432, 769
Taniguchi, D., et al. 2018, MNRAS, 473, 4993

Thévenin, F., & Idiart, T. P. 1999, ApJ, 521, 753
Thygesen, A. O., Frandsen, S., Bruntt, H., et al. 2012, A&A, 543, A160
Tomkin, J., & Lambert, D. L. 1999, ApJ, 523, 234
Worley, C. C., Cottrell, P. L., Freeman, K. C., & Wylie-de Boer, E. C. 2009, MNRAS, 400, 1039

タ イ ト ル ： FIRST DETECTION OF A-X (0,0) BANDS OF INTERSTELLAR C_2 AND CN

担　　当 ： Satoshi Hamano, Hideyo Kawakita, Naoto Kobayashi, Keiichi Takenaka, Yuji Ikeda, *et al.*

関 連 出 版 ： The Astrophysical Journal, Volume 881, Issue 2, article id. 143, 13 pp. (2019).

関連学会発表等 ： https://www.kyoto-su.ac.jp/news/20190823_859_winered.html

Draft version August 8, 2019
Typeset using LaTeX **twocolumn** style in AASTeX61

FIRST DETECTION OF A–X (0,0) BANDS OF INTERSTELLAR C_2 AND CN

Satoshi Hamano,[1,2] Hideyo Kawakita,[2,3] Naoto Kobayashi,[4,5,2] Keiichi Takenaka,[2,3] Yuji Ikeda,[2,6] Noriyuki Matsunaga,[7,2] Sohei Kondo,[8,2] Hiroaki Sameshima,[9,2] Kei Fukue,[2] Chikako Yasui,[10,2] Misaki Mizumoto,[11] Shogo Otsubo,[2,3] Ayaka Watase,[2,3] Tomohiro Yoshikawa,[12,2] and Hitomi Kobayashi[13]

[1] *National Astronomical Observatory of Japan, 2-21-1 Osawa, Mitaka, Tokyo 181-8588, Japan*
[2] *Laboratory of Infrared High-resolution Spectroscopy (LiH), Koyama Astronomical Observatory, Kyoto Sangyo University, Motoyama, Kamigamo, Kita-ku, Kyoto 603-8555, Japan*
[3] *Department of Astrophysics and Atmospheric Sciences, Faculty of Sciences, Kyoto Sangyo University, Motoyama, Kamigamo, Kita-ku, Kyoto 603-8555, Japan*
[4] *Kiso Observatory, Institute of Astronomy, School of Science,The University of Tokyo, 10762-30 Mitake, Kisomachi, Kisogun, Nagano, 397-0101, Japan*
[5] *Institute of Astronomy, School of Science, University of Tokyo, 2-21-1 Osawa, Mitaka, Tokyo 181-0015, Japan*
[6] *Photocoding, 460-102 Iwakura-Nakamachi, Sakyo-ku, Kyoto, 606-0025, Japan*
[7] *Department of Astronomy, Graduate School of Science, University of Tokyo, Bunkyo-ku, Tokyo 113-0033, Japan*
[8] *Kiso Observatory, Institute of Astronomy, School of Science,The University of Tokyo, 10762-30 Mitake, Kiso-machi, Kiso-gun, Nagano, 397-0101, Japan*
[9] *Institute of Astronomy, School of Science, University of Tokyo,2-21-1 Osawa, Mitaka, Tokyo 181-0015, Japan*
[10] *National Astronomical Observatory of Japan, 2-21-1 Osawa, Mitaka, Tokyo 181-8588*
[11] *Centre for Extragalactic Astronomy, Department of Physics, University of Durham, South Road, Durham DH1 3LE, UK*
[12] *Edechs, 17-203 Iwakura-Minamiosagi-cho, Sakyo-ku, Kyoto 606-0003, Japan*
[13] *Estrista, 9-205 Iwakura-Minamiosagi-cho, Sakyo-ku, Kyoto 606-0003, Japan*

ABSTRACT

We report the first detection of C_2 $A^1\Pi_u$–$X^1\Sigma_g^+$ (0,0) and CN $A^2\Pi_u$–$X^2\Sigma^+$ (0,0) absorption bands in the interstellar medium. The detection was made using the near-infrared (0.91–1.35 μm) high-resolution ($R = 20,000$ and 68,000) spectra of Cygnus OB2 No. 12 collected with the WINERED spectrograph mounted on the 1.3 m Araki telescope. The A–X (1,0) bands of C_2 and CN were detected simultaneously. These near-infrared bands have larger oscillator strengths, compared with the A–X (2,0) bands of C_2 and CN in the optical. In the spectrum of the C_2 (0,0) band with $R = 68,000$, three velocity components in the line of sight could be resolved and the lines were detected up to high rotational levels ($J'' \sim 20$). By analyzing the rotational distribution of C_2, we could estimate the kinetic temperature and gas density of the clouds with high accuracy. Furthermore, we marginally detected weak lines of $^{12}C^{13}C$ for the first time in the interstellar medium. Assuming that the rotational distribution and the oscillator strengths of the relevant transitions of $^{12}C_2$ and $^{12}C^{13}C$ are the same, the carbon isotope ratio was estimated to be $^{12}C/^{13}C = 50$–100, which is consistent with the ratio in the local interstellar medium. We also calculated the oscillator strength ratio of the C_2 (0,0) and (1,0) bands from the observed band strengths. Unfortunately, our result could not discern theoretical and experimental results because of the uncertainties. High-resolution data to resolve the velocity components will be necessary for both bands in order to put stronger constraints on the oscillator strength ratios.

Keywords: dust, extinction — ISM: lines and bands — ISM: molecules

Corresponding author: Satoshi Hamano
satoshi.hamano@nao.ac.jp

1. INTRODUCTION

C_2 and CN are important not only for understanding the chemical evolution of the translucent clouds but also for probing for the physical properties of interstellar clouds (Snow & McCall 2006). Because pure rotational electric dipole transitions of C_2 are forbidden because of the lack of permanent electric dipole moments, C_2 can be rotationally excited to higher levels by the collisions with atoms and molecules, as well as through electronic transitions by the interstellar radiation field. Therefore, the rotational distribution of C_2 can be used for estimating the kinetic temperature and gas density of interstellar clouds (van Dishoeck & Black 1982; Casu & Cecchi-Pestellini 2012). On the other hand, a heteronuclear diatomic molecule of CN has a permanent electric dipole moment (i.e., pure rotational transitions are allowed). The rotational excitation temperature of CN has sometimes been used to estimate the brightness temperature of the cosmic microwave background (CMB Meyer & Jura 1985). Recently, it was suggested that the slight excess of the rotational excitation temperature from the CMB temperature can mainly be attributed to electron collision and thus can be used as a tracer of electron density (Ritchey et al. 2011).

The first detection of interstellar C_2 molecules was reported by Souza & Lutz (1977), who detected the (1,0) band of the C_2 Phillips system ($A^1\Pi_u$–$X^1\Sigma_g^+$) in the line of sight of Cyg OB2 No. 12. C_2 molecules have mainly been investigated with the optical absorption lines of the (2,0) and (3,0) bands at around 8765 and 7720 Å, respectively. The (1,0) and (0,0) Phillips bands located in the near-infrared (NIR) region are not used despite having larger oscillator strengths than the (2,0) and (3,0) bands. This is most likely because it has been difficult to resolve the bands and to detect weak lines at high rotational levels without a high-efficiency and high-resolution NIR spectrograph that has only recently been developed. Moreover, the C_2 (0,0) Phillips band is contaminated by many telluric absorption lines, which make it difficult to detect each individual rotational line. In particular, the C_2 (0,0) Phillips band has never been detected in the interstellar medium. The situation for CN is similar to that of C_2. CN has (1,0) and (0,0) bands of the red system ($A^2\Pi_u$–$X^2\Sigma^+$) in the NIR region. Although these bands are stronger than the (2,0) red band of CN around 7900 Å in the optical region, the lines of the (1,0) and (0,0) bands are contaminated by telluric absorption lines as in the case of the C_2 (0,0) Phillips band. The CN (0,0) red band has also never been detected in the interstellar medium.

In this paper, we report the first detection of the C_2 (0,0) Phillips band and the CN (0,0) red band in the interstellar medium. These bands were detected in the high-resolution NIR spectra (0.91–1.35 μm) of Cyg OB2 No. 12, which is a representative object for the study of the interstellar medium due to its high visual extinction ($A_V \sim 10$ mag) and extreme luminosity (Whittet 2015). The spectra were obtained by the WINERED spectrograph mounted on the 1.3 m Araki telescope. The (1,0) bands of C_2 and CN were also detected with high accuracy in our spectra. Also, we marginally detected the absorption lines of the (0,0) band of $^{12}C^{13}C$. The detection of $^{12}C^{13}C$ in the interstellar medium has never been reported. The rest of this paper is organized as follows. Section 2 describes our observations and data reduction process. Section 3 gives a description of the detected C_2 and CN bands. Section 4 discusses the rotational distribution of the C_2, the constraints on the oscillator strengths of the C_2 bands from our observation, and the carbon isotope ratio. Section 5 gives a summary of this paper. The wavelength of standard air is used throughout this paper.

2. OBSERVATION AND DATA REDUCTION

Data were collected with the high-resolution NIR echelle spectrograph, WINERED (Ikeda et al. 2016), mounted on the F/10 Nasmyth focus of the 1.3 m Araki telescope at Koyama Astronomical Observatory, Kyoto Sangyo University, Japan (Yoshikawa et al. 2012). WINERED uses a 1.7 μm cutoff 2048 × 2048 HAWAII-2RG infrared array with a pixel scale of $0''.8$ pixel^{-1}. WINERED provides three observational modes, WIDE, HIRES-Y, and HIRES-J. The WIDE mode covers 0.91–1.35 μm range with a spectral resolving power of $R \equiv \lambda/\Delta\lambda = 28{,}000$ or $\Delta v = 11$ km s^{-1}. The HIRES-Y and HIRES-J modes cover the whole Y and J bands, respectively, with a spectral resolving power of $R = 68{,}000$ (Otsubo et al. 2016). We already reported the WIDE-mode spectrum of Cyg OB2 No. 12 in Hamano et al. (2016), in which diffuse interstellar bands (DIBs) were investigated.

We obtained the NIR spectra of Cyg OB2 No. 12 using WIDE and HIRES-J modes. Table 1 shows the observational information, as well as the bands of C_2 and CN covered in the observing modes. All of the data were obtained through dithering the telescope by $30''$ (so-called ABBA sequence). For the removal of telluric absorption lines, the telluric standard A-type stars were also observed at airmasses similar to the target airmasses (see Table 1).

The collected data were reduced with our pipeline software (S. Hamano et al. 2019 in preparation). Using this pipeline, the obtained raw images were reduced to one-dimensional spectra. Once the spectra were ob-

tained, we divided the spectra of Cyg OB2 No. 12 with the spectra of the corresponding telluric standard stars. Here, we used the IRAF[1]/telluric task, which can adjust the strength of the telluric absorption lines based on Beer's law with the single layer atmosphere model and the wavelength shift of the standard star's spectrum. See Sameshima et al. (2018) for a full description of our telluric absorption correction method. Then, we fitted a Legendre polynomial function to the continuum regions around the CN and C_2 bands by masking absorption lines of these bands and the region where the telluric transmittance was lower than 0.7. The 5th and 10th order Legendre polynomials were used for fitting continuum regions around the CN and C_2 bands, respectively.

Comparing the WIDE-mode spectra obtained at A and B positions on the slit, broad and shallow spurious features are found to be present in 10130–10150 Å only in the spectra obtained at the A position. The features overlap on a part of the C_2 (1,0) Phillips band. Therefore, we use only the spectra obtained at the B position for the narrow wavelength region of 10130–10150 Å. Because the number of available frames is halved, the signal-to-noise ratio (S/N) becomes lower by a factor of about $\sqrt{2}$ for the wavelength region.

3. RESULTS

3.1. *C_2 Phillips bands*

Figures 1 and 2 show the spectra of C_2 bands obtained with WIDE and HIRES-J modes, respectively. Both the C_2 (0,0) and (1,0) Phillips bands were clearly detected up to the rotational levels of $J'' > 20$ in the ground state for both the WIDE and HIRES-J spectra. The stellar absorption lines and DIBs, with which the C_2 bands are contaminated, are marked in the figures. These DIBs are newly found in this observation and will be reported in another paper (S. Hamano et al. 2019 in preparation). The telluric lines are very weak in the (1,0) band region while the (0,0) band is contaminated with strong telluric absorption lines. The absorption lines of telluric water vapor in the HIRES-J spectrum were particularly strong because the HIRES-J data were obtained in the summer season when the temperature and humidity at the observational site are high. Therefore, as for the HIRES-J data, the wavelength ranges at which the atmospheric transmittance was lower than 0.5 (plotted with gray lines in Figure 2) were not used in the following analysis of the C_2 band.

Figure 3 shows the close-up plots for the $R(0)$ and $P(8)$ lines of the C_2 (0,0) band, which were clearly detected in the HIRES-J spectrum. Three velocity components were resolved with $R = 68,000$. In this paper, the three components are referred to as components 1, 2, and 3 as shown in Figure 3. These three components in the line of sight of Cyg OB2 No. 12 were already recognized by McCall et al. (2002) with the CO and K I absorption spectra. They also detected the C_2 (2,0) Phillips band, but could not detect the absorption lines at the velocity of component 1. Components 1, 2, and 3 could not be resolved in our WIDE spectrum ($\Delta v = 15$ km s^{-1}).

We estimated the line-of-sight velocities, Doppler widths, and column densities of each velocity component using VoigtFit (Krogager 2018), which is a Python package for fitting Voigt profiles to absorption lines. Because the line parameters of C_2 Phillips bands are not included in VoigtFit, we originally calculated the oscillator strengths of each rotational line of C_2 bands. We used the oscillator strengths of $f_{00} = 2.233 \times 10^{-3}$ and $f_{10} = 2.348 \times 10^{-3}$ calculated by Schmidt & Bacskay (2007). The oscillator strengths of each line were calculated from the following relation (Gredel et al. 2001):

$$f_{J'J''} = f_{\rm band} \frac{\nu_{J'J''}}{\nu_{\rm band}} \frac{S_{J'J''}}{2(2J''+1)}, \quad (1)$$

where $f_{\rm band}$ is the oscillator strength of the band (f_{00} or f_{10}), $\nu_{\rm band}$ is the wavenumber of the vibrational band, and $S_{J'J''}$ are Hönl-London factors: $(J''+2)$, $(2J''+1)$, and $(J''-1)$ for the R, Q, and P branches, respectively. The wavelengths of the C_2 (0,0) and (1,0) bands were adopted from Douay et al. (1988) and Chauville et al. (1977), respectively.

The C_2 lines were fitted simultaneously to the HIRES-J spectrum using VoigtFit. The regions contaminated with strong telluric absorption lines were eliminated for the fitting as well as for the estimate of the S/N. The S/N of each pixel was calculated considering the loss of flux by the moderate telluric absorption lines. The C_2 lines blended with other features, such as stellar lines and DIBs, were not included in the fitting.

Table 2 lists the column densities for each velocity component obtained by the fitting. The heliocentric velocities of components 1,2 and 3 were estimated as -15.1, -9.6, and -4.0 km s^{-1}, respectively. The Doppler widths of each velocity component could be estimated in the fitting because the EWs of the strongest P, Q, and R lines in the optically thick regime. The Doppler widths of components 1, 2, and 3 were esti-

[1] IRAF is distributed by the National Optical Astronomy Observatories, which are operated by the Association of Universities for Research in Astronomy, Inc., under cooperative agreement with the National Science Foundation.

Table 1. Observation summary of Cyg OB2 No. 12

Obs. Date	R	Telluric [a]			Int. Time (s)		S/N[b]	C_2[c]	CN[c]
(UT)		Name	Sp. Type	J (mag)	Object	Telluric	Object/Telluric		
2014 Oct 17	20,000	HR 196	A2V	5.291	3600	8400	700	(1,0), (0,0)	(1,0), (0,0)
2016 Jul 23	68,000	29 Vul	A0V	5.153	2400	3600	450	(0,0)	···
2016 Aug 1	68,000	HR 8358	A0V	5.607	2400	7200	420	(0,0)	···

NOTE—

[a] Telluric standard stars used to correct the telluric absorption lines.

[b] The average signal-to-noise ratio per pixel of the spectrum after the division by the telluric standard spectrum.

[c] The bands included in the wavelength coverage of each observation.

mated as 2.39 ± 0.42, 1.47 ± 0.15 and 0.53 ± 0.06 km s^{-1}, respectively. We did not conduct the Voigt profile analysis for the WIDE data because the three velocity components, could not be resolved with $R = 20,000$ ($\Delta v = 15$ km s^{-1}). Therefore, we used $N(J'')$ determined from the HIRES-J data in the following analysis.

According to McCall et al. (2002), who obtained the optical spectrum of Cyg OB2 No. 12 with $R = 200,000$, the FWHMs of the C_2 (2,0) band absorption lines were measured to be 3.0 ± 0.2 and 2.0 ± 0.2 km s^{-1} for components 2 and 3, respectively. Considering the broadening effect by instrumental profiles with $\Delta v = 1.5$ km s^{-1}, the Doppler widths estimated from our fitting, 1.47 ± 0.15 and 0.53 ± 0.06 km s^{-1} for component 2 and 3, correspond to FWHMs of 2.9 ± 0.3 and 1.7 ± 0.1 km s^{-1}, respectively, in the $R = 200,000$ spectrum. These values were consistent with the directly measured FWHMs by McCall et al. (2002).

The column densities obtained by our analysis were compared with those of Gredel et al. (2001) and McCall et al. (2002), both of which analyzed the spectrum of the (2,0) Phillips band of Cyg OB2 No. 12. Gredel et al. (2001) obtained the spectrum with $R = 45,000$ and S/N > 600 and could not resolve the velocity components while McCall et al. (2002) resolved the velocity components with $R = 200,000$ but the S/N[2] was not as good as that of Gredel et al. (2001). Although both of them assumed the optically thin conditions for the calculation of column densities considering the typical Doppler width of $b = 1$ km s^{-1} (Gredel et al. 2001), this assumption is not valid in the case of $b = 0.5$ km s^{-1}. Therefore, we calculated the column densities from the (2,0) band equivalent widths (EWs) by Gredel et al. (2001) and McCall et al. (2002) using the Doppler widths and the velocities estimated from our fitting, and then compared the resultant column densities with those we derived from the (0,0) band. We adopted $f_{20} = 1.424 \times 10^{-3}$ (Schmidt & Bacskay 2007) for the calculation. The ratios of the column densities from the (2,0) band to our values from the (0,0) band were calculated up to $J'' = 8$, below which we could detect the absorption lines of the velocity component 1. The ratios of the column density of Gredel et al. (2001) to our value was 0.94 ± 0.15. The column densities calculated from the data of Gredel et al. (2001) were close to our results but the uncertainties were large. Note that the standard deviation does not include the uncertainties of EWs and Doppler widths. As for McCall et al. (2002), the ratios were calculated to be 0.79 ± 0.07 and 0.74 ± 0.07 for components 2 and 3, respectively, meaning that the EWs of McCall et al. (2002) were lower than those expected from the (0,0) band. Considering the relatively low S/N of the McCall et al. (2002) spectrum, the discrepancy could be attributed to the systematic noise, which could not be estimated in their paper (see the footnote of Table 6 in McCall et al. 2002). Also, the systematic uncertainties due to the continuum normalization could be large because the strong lines in the (2,0) band are detected within the broad stellar lines of H I Paschen 12 and He I. Therefore, the column densities obtained from our (0,0) band data could be more robust than the previous results because of both the high quality of our data and intrinsically large EWs of the (0,0) band.

To measure the EWs of the detected lines independently, we fitted Gaussian curves to the spectrum data. The velocities and widths were fixed in the fit as determined by the VoigtFit analysis for the HIRES-J spectrum. For the partially blended lines, multiple Gaussian curves at the wavelengths of the blended lines were fitted simultaneously. While the EWs of the three velocity

[2] McCall et al. (2002) did not show the value of S/N for their C_2 spectrum of Cyg OB2 No. 12. Judging from the spectrum shown in their paper, the S/N appears to be about 100.

components were measured separately in the HIRES-J spectrum, the total EWs of the three components were measured in the WIDE spectrum. For the EW uncertainties, we included the systematic uncertainties from continuum fitting estimated with the rms shift method (Sembach & Savage 1992) in addition to the statistical uncertainties. Tables 2 and 3 list the EWs measured for the absorption lines identified as C_2 Phillips bands in the spectra obtained with the HIRES-J and WIDE modes, respectively. In the WIDE spectrum, the lower spectral resolution caused the blending of some multiple C_2 lines and it made it difficult to normalize the spectrum using the surrounding continuum regions. We did not list the EWs for those lines, whose systematic uncertainties of EWs were much larger due to the blending. In Table 3, we also list the EWs of the (1,0) band calculated from $N(J'')$ and b determined by HIRES-J data using $f_{10} = 2.348 \times 10^{-3}$ (Schmidt & Bacskay 2007). Comparing the measured and calculated EWs, we discuss the ratio of observationally constrained oscillator strengths of Phillips bands in Section 4.2. Note that the total EWs measured from WIDE and HIRES spectra are consistent within uncertainties for the most lines detected in both spectra.

3.2. *CN red band*

Figure 4 shows the WIDE spectra of the CN (1,0) and (0,0) red bands. The rest-frame wavelengths were adopted from Brooke et al. (2014). As shown in Figure 4, some absorption lines were detected at the wavelengths of CN bands. In particular, the three lines of the (0,0) band around $\lambda = 10990$ Å were clearly detected. As long as we know, this is the first detection of a (0,0) band of the CN red system in the interstellar medium. The lines around 10930Å are overlapped with the broad absorption line of H I Paγ. Within the broad feature of the stellar H I line, narrow dips can be seen at the wavelengths of the CN band. These dips are most likely CN lines, but it is almost impossible to measure their EWs accurately. Table 4 lists the EWs and column densities measured for the lines of the CN (1,0) and (0,0) red bands in the spectrum of Cyg OB2 No. 12. The EWs were measured by fitting a Gaussian curve to the spectrum. Although these CN lines should originate from two major velocity components, components 2 and 3, as well as C_2, they could not be resolved. The measured EWs would be the sum of all velocity components.

Considering the small Doppler widths measured from the C_2 (0,0) band, some detected CN lines are probably optically thick. However, since we could not resolve the velocity components, we could not estimate the Doppler widths of each velocity component. Therefore, we calculated CN column densities based on two assumptions. One is the assumption of the optically thin condition and the other is the assumption that the CN lines that originated from components 1, 2 and 3 and have the same Doppler widths as the C_2 lines. In the latter assumption, the ratios of column densities of each velocity component to the total column densities were assumed as those of the C_2 column densities. The oscillator strengths calculated by Brooke et al. (2014) were adopted. For the blended lines from the $N'' = 1$ level, we calculated the effective oscillator strengths by assuming that the populations of the spin-rotational levels (N'', J'') with the same rotational quantum number N'' are populated according to their statistical weights (Gredel, et al. 2002). Table 4 lists the column densities calculated under two assumptions. As for the $R_1(0)$ line of the CN (0,0) band, which is the strongest detected line, the column density was much different by the assumptions. The column densities of the $N'' = 0$ and 1 levels estimated from each line, $N(N'' = 0)$ and $N(N'' = 1)$, have larger variance than the uncertainties (Table 4). This would be because of the systematic uncertainties due to the surrounding stellar lines, which made it difficult to properly evaluate the appropriate continuum level. Also, both bands were severely contaminated by telluric absorption lines.

The (2,0) and (1,0) bands of the CN red system toward Cyg OB2 No. 12 were also detected by Gredel et al. (2001). As for the (1,0) band, which was also detected in this study, Gredel et al. (2001) showed that the EWs of $Q_2(1) + {}^{Q}P_{21}(1)$ and $R_1(0)$ were 14.3 ± 5Å and 25 ± 5Å, respectively, and the EW upper limits of ${}^{S}R_{21}(0)$ and $R_1(1)$ were < 28Å and < 53Å, respectively. The EWs and upper limits of the (1,0) band measured here were consistent with those reported by Gredel et al. (2001) within uncertainties.

Averaging the column densities calculated with the optically thin condition assumption listed in Table 4, the column densities of the $N'' = 0$ and 1 levels were estimated to be $N(N'' = 0) = (4.7 \pm 0.2) \times 10^{13}$ and $N(N'' = 1) = (3.2 \pm 0.3) \times 10^{13}$ cm^{-2}. The rotational excitation temperature and the CN total column density were estimated to be $T_{10} = 3.7 \pm 0.3$ K and $N(\mathrm{CN}) = (8.2 \pm 0.4) \times 10^{13}$ cm^{-2}. Note that these results are likely to be affected by the systematic uncertainties due to the residual of telluric absorption lines and the stellar lines.

Using only the $R_1(0)$ and $R_1(1)$ lines of the CN (0,0) band, which were clearly detected without the contamination of stellar lines, we estimated the rotational excitation temperature and the CN total column density to be $T_{10} = 3.0 \pm 0.2$ K and $N(\mathrm{CN}) = (1.01 \pm 0.04) \times 10^{14}$ cm^{-2}, respectively, in the optically thick case for the $R_1(0)$ and $R_1(1)$ lines of CN (0,0) band. We suggest

Table 2. Equivalent widths and column densities for the C_2 $(0,0)$ Phillips Bands in the HIRES-J mode spectrum of Cyg OB2 No. 12

				Comp 1		Comp 2		Comp 3		
J''	Branch	λ_{air} (Å)	$f(10^{-3})$	EW (mÅ)	N (10^{12} cm^{-2}) [a]	EW (mÅ)	N (10^{12} cm^{-2}) [a]	EW (mÅ)	N (10^{12} cm^{-2}) [a]	Blending[b]
0	R	12086.244	2.230	3.55 ± 0.40	0.93 ± 0.21	20.55 ± 0.31	7.40 ± 0.24	23.93 ± 0.33	10.83 ± 0.33	
2	R	12078.631	0.894	···	2.94 ± 0.55	···	27.25 ± 0.60	···	39.63 ± 1.66	Telluric
	Q	12092.725	1.120	5.51 ± 0.41		36.13 ± 0.32		36.82 ± 0.34		
	P	12102.141	0.223	2.09 ± 0.40		8.54 ± 0.31		10.81 ± 0.33		
4	R	12073.398	0.745	6.47 ± 0.36	5.75 ± 0.70	24.16 ± 0.28	25.69 ± 0.82	24.01 ± 0.29	30.96 ± 0.74	
	Q	12096.879	1.120	···		···		···		Telluric
	P	12115.742	0.371	2.64 ± 0.41		10.81 ± 0.33		12.56 ± 0.35		
6	R	12070.540	0.688	···	3.52 ± 0.47	15.72 ± 0.32	17.90 ± 0.54	13.91 ± 0.30	20.15 ± 0.47	$R(8)$
	Q	12103.413	1.110	···		···		···		$R(18)$
	P	12131.760	0.428	2.79 ± 0.33		9.72 ± 0.26		10.60 ± 0.28		
8	R	12070.055	0.658	2.47 ± 0.36	3.89 ± 0.40	10.07 ± 0.28	12.46 ± 0.46	···	12.34 ± 0.29	$R(6)$
	Q	12112.335	1.110	6.25 ± 0.40		17.11 ± 0.31		15.29 ± 0.33		
	P	12150.211	0.457	3.03 ± 0.41		7.70 ± 0.31		6.56 ± 0.33		
10	R	12071.943	0.639	···	···	···	9.58 ± 0.40	···	8.19 ± 0.34	Telluric
	Q	12123.652	1.110	···		13.88 ± 0.27		10.52 ± 0.28		
	P	12171.114	0.475	···		5.10 ± 0.22		4.30 ± 0.23		
12	R	12076.208	0.626	5.07 ± 0.35	2.26 ± 0.38	5.61 ± 0.27	7.27 ± 0.39	4.66 ± 0.29	6.18 ± 0.32	
	Q	12137.378	1.110	2.81 ± 0.34		10.20 ± 0.27		7.96 ± 0.29		
	P	12194.491	0.487	···		···		···		DIB
14	R	12082.853	0.616	···	1.70 ± 0.34	···	4.33 ± 0.70	···	3.78 ± 0.29	Telluric
	Q	12153.526	1.110	3.14 ± 0.41		6.52 ± 0.31		5.35 ± 0.33		
	P	12220.370	0.495	···		1.98 ± 0.39		1.72 ± 0.41		
16	R	12091.888	0.609	···	···	2.48 ± 0.33	3.25 ± 0.28	1.32 ± 0.33	2.01 ± 0.25	
	Q	12172.113	1.110	···		4.73 ± 0.22		2.95 ± 0.23		
	P	12248.774	0.501	···		1.82 ± 0.31		1.24 ± 0.34		
18	R	12103.322	0.603	···	1.24 ± 0.33	···	2.78 ± 0.32	···	2.07 ± 0.28	$Q(6)$
	Q	12193.162	1.110	1.73 ± 0.40		4.18 ± 0.30		2.73 ± 0.33		
	P	12279.735	0.505	···		···		···		
20	R	12117.168	0.598	···	···	2.16 ± 0.32	2.72 ± 0.26	2.88 ± 0.33	2.34 ± 0.23	
	Q	12216.696	1.100	···		3.59 ± 0.39		2.08 ± 0.41		
	P	12313.287	0.508	···		2.31 ± 0.22		1.55 ± 0.24		
22	R	12133.443	0.593	···	···	···	1.94 ± 0.34	···	···	
	Q	12242.736	1.100	···		2.75 ± 0.31		···		
	P	12349.467	0.510	···		···		···		
24	R	12152.165	0.589	···	···	···	···	···	···	Telluric
	Q	12271.315	1.100	···		···		···		
	P	12388.311	0.511	···		···		···		
26	R	12173.354	0.586	···	···	1.36 ± 0.22	1.40 ± 0.30	0.78 ± 0.23	1.36 ± 0.27	
	Q	12302.463	1.100	···		1.83 ± 0.22		2.07 ± 0.24		
	P	12429.866	0.512	···		···		···		
28	R	12197.033	0.582	···	···	···	···	1.35 ± 0.33	1.53 ± 0.27	
	Q	12336.214	1.090	···		···		2.06 ± 0.28		
	P	12474.185	0.512	···		···		···		

NOTE—The symbol " ··· " denotes undetected lines.

[a] The column densities of the rotational level J'' estimated from the simultaneous profile fit to the P, Q, and R lines.

[b] The features blended with the lines. "Telluric" means the blending of the strong telluric lines.

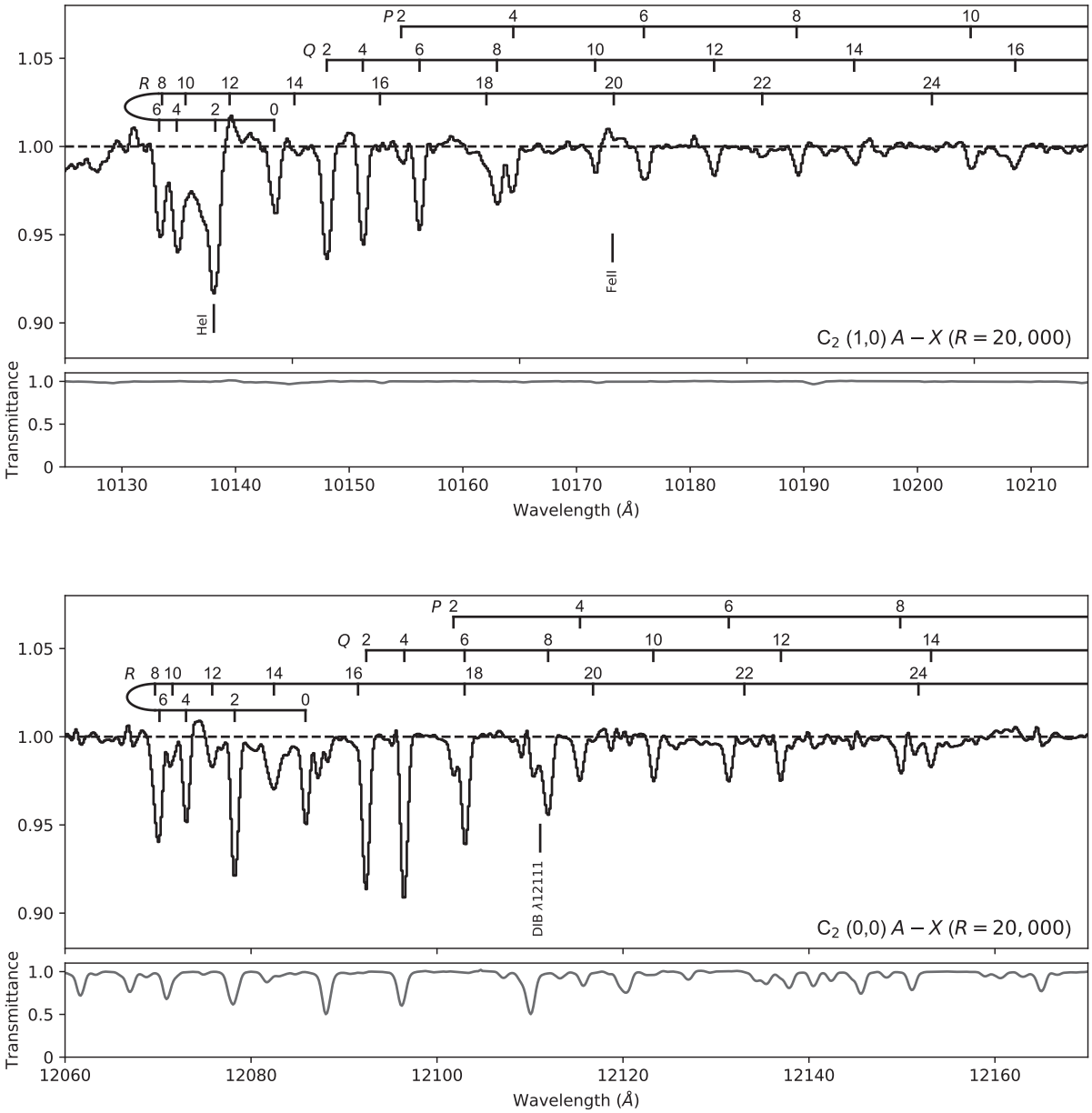

Figure 1. Normalized spectra of the C_2 (1,0) (upper panel) and (0,0) (lower panel) Phillips bands toward Cyg OB2 No 12 obtained with the WIDE mode ($R = 20,000$). The normalized spectra of the telluric standard stars are also shown. The wavelengths of each line of the bands are marked with lines above the spectrum. The positions of stellar lines and DIBs (including its candidates) are also shown with lines below the spectrum. The wavelengths of the (1,0) and (0,0) bands were calculated from the wavenumbers listed in table 2 in Chauville et al. (1977) and table 1 in Douay et al. (1988), respectively.

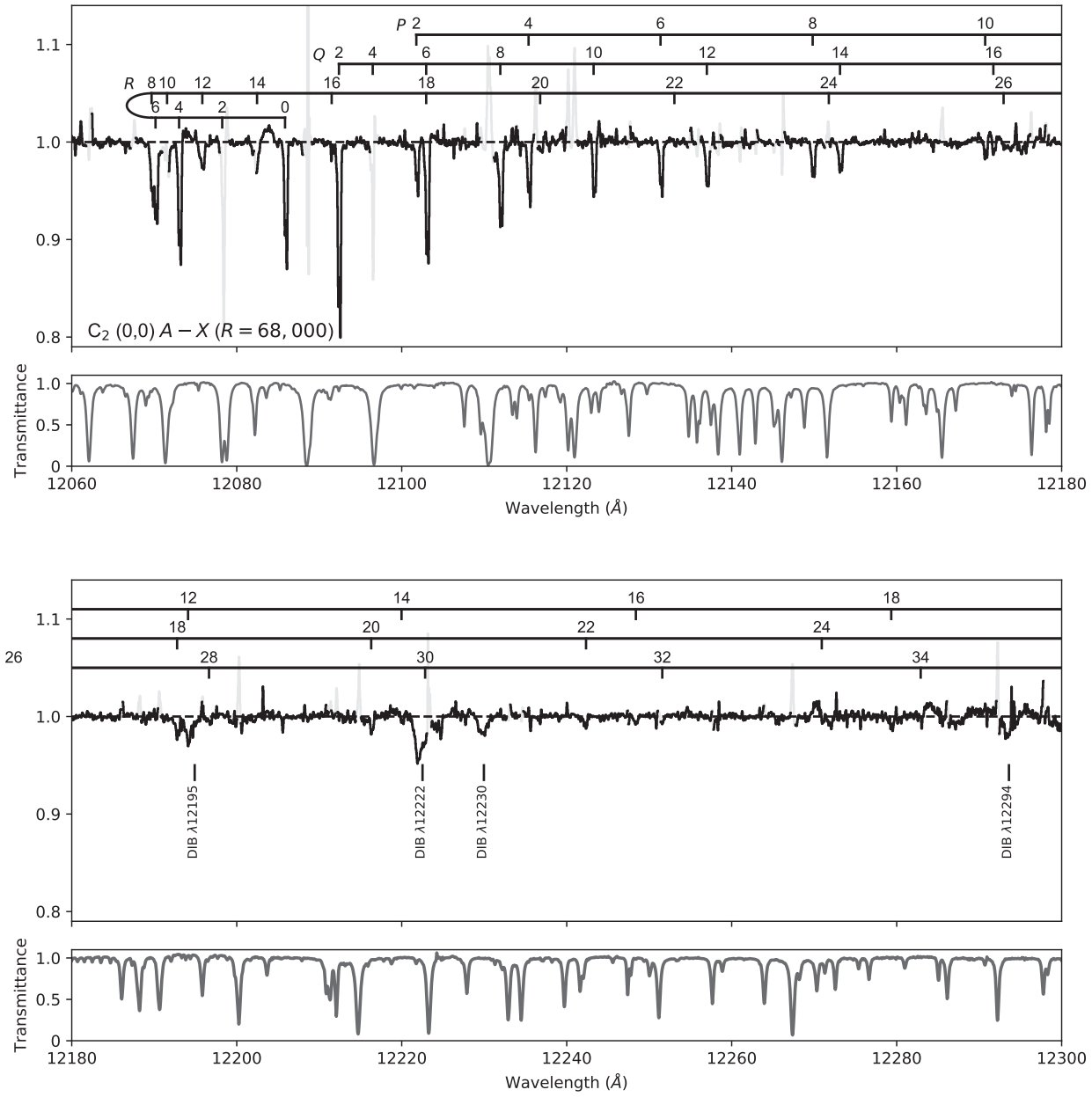

Figure 2. Normalized spectrum of the C_2 (0,0) Phillips band toward Cyg OB2 No. 12 obtained with the HIRES-J mode ($R = 68,000$). The wavelength ranges at which the transmittance was lower than 0.5 are plotted with gray lines. The stellar lines and DIBs are also marked with lines below the spectrum. The normalized spectrum of the telluric standard star is also shown.

Table 3. Equivalent widths for the C_2 (0,0) and (1,0) Phillips Bands in the WIDE-mode spectrum of the Cyg OB2 No. 12

		(0,0)	(1,0)	(1,0) calculation[a]
J''	Branch	EW (mÅ)	EW (mÅ)	EW (mÅ)
0	R	···	35.30 ± 1.49	35.93
2	R	66.36 ± 1.27	···	49.57
	Q	75.55 ± 0.89	60.35 ± 1.50	59.54
	P	19.29 ± 0.94	···	14.09
4	R	···	···	39.39
	Q	···	···	56.16
	P	23.59 ± 1.12	20.49 ± 1.02	20.87
6	R	···	···	25.26
	Q	···	41.35 ± 1.49	39.44
	P	19.78 ± 1.13	17.31 ± 1.18	16.26
8	R	···	···	17.17
	Q	···	27.26 ± 0.95	28.47
	P	17.34 ± 0.97	12.15 ± 1.09	12.23
10	R	···	···	11.14
	Q	22.26 ± 1.13	20.57 ± 1.17	19.17
	P	···	···	8.48
12	R	···	···	9.16
	Q	19.33 ± 1.13	13.57 ± 1.09	16.18
	P	···	6.33 ± 0.98	7.29
14	R	···	···	5.69
	Q	11.97 ± 0.96	···	10.28
	P	···	···	4.67
16	R	···	···	3.45
	Q	···	···	6.34
	P	···	···	2.90
18	R	···	5.05 ± 0.97	3.47
	Q	···	···	6.41
	P	···	···	2.99
20	R	3.53 ± 1.12	···	3.18
	Q	···	···	5.92
	P	···	···	2.78

NOTE—

[a] EWs calculated from $N(J'')$ in Table 2.

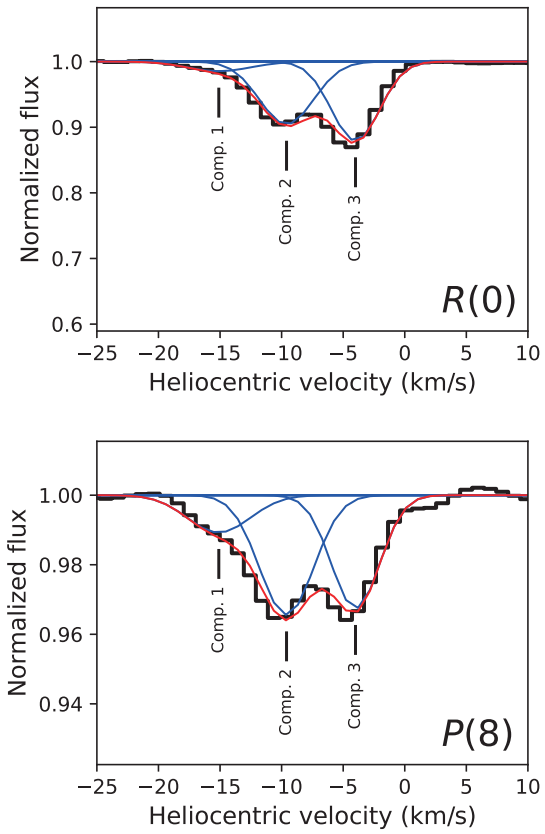

Figure 3. Close-up images of the spectrum of the $R(0)$ and $P(8)$ lines in the C_2 (0,0) band. The black lines show the spectrum of Cyg OB2 No. 12 obtained with the HIRES-J mode. Three components at −15.1, −9.6, and −4.0 km s^{-1} were detected. The blue lines show the Gaussian curves fitted to the spectrum. The red lines show the composite of the Gaussian curves.

that the latter result would be more robust because the rotational temperature is close to the CMB temperature. Gredel et al. (2001) estimated $N(N'' = 0) = 4.4 \times 10^{13}$ and $N(N'' = 1) = 5.5 \times 10^{13}$ cm^{-2} (the oscillator strength was adjusted to the values of Brooke et al. 2014 for comparison). Our result should be more robust than that of Gredel et al. (2001) since the $N(N'' = 1)$ by Gredel et al. (2001) had a large uncertainty and their excitation temperature, $T_{10} = 6.2$ K, was much higher than the CMB temperature. However, there is a systematic uncertainty in our results due to the assumption about the Doppler widths and the CN column density ratios among velocity components. It is necessary to resolve the velocity components with higher resolution and detect more lines to obtain these parameters with high accuracy.

4. DISCUSSION

4.1. *Rotational excitation of C_2*

The gaseous temperature and density of the collision partner (n(H) + $n(H_2)$) can be evaluated from the rotational distribution of C_2 molecules. These parameters are essential for understanding of the interstellar chemical reactions (Gredel et al. 2001). Using the model of van Dishoeck & Black (1982), we estimated the parameters for the three velocity components of Cyg OB2 No. 12 from the column densities of each rotational

Table 4. Equivalent widths and column densities for the CN red bands in the WIDE-mode spectrum of Cyg OB2 No. 12

Band	Transition	N''	J''	$\lambda_{\rm air}$[a] (Å)	$f_{\rm osc}$[a,b] ($\times 10^{-3}$)	EW (mÅ)	$N(N'')$[c] (10^{12} cm^{-2})	$N(N'')$[d] (10^{12} cm^{-2})
(1,0) band	$^{S}R_{21}(0)$	0	1/2	9139.699	0.2646	6 ± 3	31 ± 15	31 ± 15
	$R_2(1) +^{R} Q_{21}(1)$	1	1/2 + 3/2	9142.848	0.4375	12 ± 3	37 ± 9	40 ± 10
	$^{R}Q_{21}(0)$	0	1/2	9144.055	0.6409	17 ± 3	36 ± 6	38 ± 6
	$Q_2(1) +^{Q} P_{21}(1)$	1	1/2 + 3/2	9147.219	0.3203	...	...	...
	$R_1(1)$	1	3/2	9183.230	0.6408	14 ± 3	45 ± 9	46 ± 9
	$R_1(0)$	0	1/2	9186.950	1.0127	21 ± 3	28 ± 4	29 ± 4
	$^{Q}R_{12}(1) + Q_1(1)$	1	1/2 + 3/2	9190.138	0.5851	20 ± 3	46 ± 7	50 ± 8
(0,0) band	$^{S}R_{21}(0)$	0	1/2	10925.147	0.3251	10 ± 2	29 ± 6	29 ± 6
	$R_2(1) +^{R} Q_{21}(1)$	1	1/2 + 3/2	10929.650	0.5386	... [e]	...	...
	$^{R}Q_{21}(0)$	0	1/2	10931.442	0.7892	... [e]	...	...
	$^{Q}P_{21}(1) + Q_2(1)$	1	1/2 + 3/2	10935.970	0.3945	... [e]	...	...
	$R_1(1)$	1	3/2	10987.395	0.7886	17 ± 2	30 ± 3	33 ± 3
	$R_1(0)$	0	1/2	10992.869	1.2461	74 ± 2	55 ± 2	67 ± 3
	$Q_1(1) +^{Q} R_{12}(1)$	1	1/2 + 3/2	10997.445	0.7198	... [f]	...	...

NOTE—

[a] The values were adopted from Brooke et al. (2014).

[b] The effective oscillator strengths are shown for the blended lines.

[c] The column densities calculated with optically thin assumption.

[d] The column densities calculated with the assumption of the cloud parameters from C_2 bands (see the text for details).

[e] Overlapped with the stellar Pa γ line.

[f] Overlapped with the stellar He I line.

level in the ground state. We use the updated value of the absorption rates calculated by van Dishoeck & de Zeeuw (1984). We assumed the scaling factor for the incident radiation field to be $I = 1$. As the recent analysis of interstellar C_2 excitation by Hupe et al. (2012), we adopted the C_2-H_2 collisional cross section as $\sigma_0 = 4 \times 10^{-16}$ cm^{-2}, which is indicated by recent calculations (Lavendy et al. 1991; Robbe et al. 1992; Najar et al. 2008, 2009), rather than the frequently used value of 2×10^{-16} cm^{-2} (van Dishoeck & Black 1982). Although the lines from $J'' > 20$ were detected in our observation, the original model by van Dishoeck & Black (1982) cannot predict the rotational distributions at $J'' > 20$, because they calculated the radiation excitation matrix and the quadruple transition probabilities up to only $J'' = 20$. To extrapolate the model to $J'' > 20$, we estimated the values of the model parameters at $J'' > 20$ levels by fitting power-law functions of J'', which reproduced the values at $J'' \leq 20$ well.

Figure 5 shows the rotational diagrams for each velocity component. The HIRES-J data were used. We could not estimate the parameters for component 1 because of the large uncertainties of column densities. For components 2 and 3, the kinetic temperatures and gas densities (T, n) were estimated as $(30 \pm 5$ K, 100 ± 7 cm$^{-3})$ and $(25 \pm 5$ K, 125 ± 7 cm$^{-3})$, respectively. We compare these results with the previous results of C_2 for Cyg OB2 No. 12 (Gredel et al. 2001; McCall et al. 2002). Because both of the previous papers used the collisional cross section of 2×10^{-16} cm^{-2}, which is the half of our adopted value, their densities were scaled by a factor of about 2 for the comparison in the following. McCall et al. (2002) estimated the parameters to be (40 K , 110 cm^{-3}) and (30 K, 105 cm^{-3}) for components 2 and 3, respectively, but with large uncertainties: $T = 25 - 55$ K and $n = 75 - 300$ cm^{-3} (3σ errors). Gredel et al. (2001) analyzed the rotational distribution summed over the components and estimated the parameters to be $(T, n) = (35$ K, 150 ± 25 cm$^{-3})$. They detected the lines of the C_2 (2,0) band up to $J'' = 18$ but could not resolve the velocity components. In comparison with the previous results, both parameters estimated in this paper are consistent with the previous values within uncertainties. Because of the higher os-

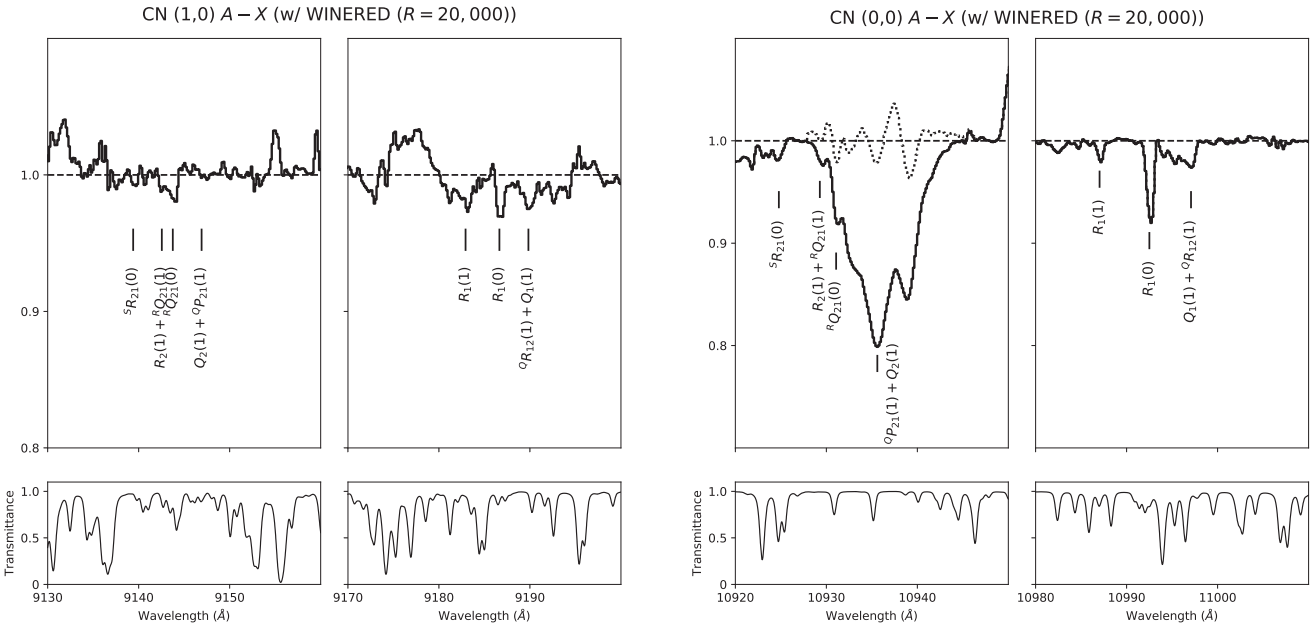

Figure 4. The left two panels and right two panels show the spectra of the CN (1,0) and (0,0) red bands toward Cyg OB2 No. 12, respectively. The transmittance spectrum synthesized using ATRAN (Lord 1992) is also shown, in the lower panels. The wavelengths of the CN red system are adopted from Brooke et al. (2014). The dotted line shows the spectrum after subtracting the Gaussian function arbitrarily fitted to the Pa γ line.

cillator strength of the C_2 (0,0) band than the C_2 (2,0) band, we could estimate the parameters with an accuracy higher than that of previous studies, even those with similar S/Ns.

From the rotational distribution, the C_2 total column densities of components 2 and 3 were estimated to be $(1.29^{+0.16}_{-0.10}) \times 10^{14}$ and $(1.48^{+0.13}_{-0.08}) \times 10^{14}$ cm^{-2}, respectively. By summing up the column densities listed in Table 2, the C_2 total column densities of components 1, 2, and 3 were 2.2×10^{13}, 1.2×10^{14} and 1.4×10^{14} cm^{-2}, respectively. Table 5 summarizes the parameters of the velocity components of Cyg OB2 No. 12 obtained from the C_2 and CN bands.

4.2. *Oscillator strengths*

The oscillator strengths of the C_2 Phillips bands have been investigated experimentally and theoretically. However, the experimental and theoretical results are not in agreement with one another. Astronomical observations of C_2 molecules have put a unique constraint on the oscillator strength ratios of C_2 bands (Lambert et al. 1995). Here, we try to put constraints on the oscillator strength ratios of the C_2 Phillips bands of Cyg OB2 No.12 using the line strengths of (1,0) and (0,0) bands from this study. We use the (0,0) band in HIRES spectrum and the (1,0) band in WIDE spectrum. It is assumed that the column densities of rotational levels J'' in the line of sight of Cyg OB2 No. 12 are constant between our observations with WIDE and HIRES-J modes. From the strength ratios between the detected lines of (1,0) and (0,0) bands from the same lower level J'', the oscillator strength ratio, f_{00}/f_{10}, can be constrained.

Because the strong lines of Cyg OB2 No. 12 are optically thick for both (0,0) and (1,0) bands (§3.1), the oscillator strength ratio cannot be simply calculated from the ratio of the EWs. Therefore, we searched for the oscillator strength ratio that reproduces well the observed EWs with the following procedures. First, we calculated the total EWs of the three velocity components for each rotational lines of the (1,0) band by synthesizing the absorption profiles using the column densities of each rotational level listed in Table 2 and the cloud parameters (the line-of-sight velocities and Doppler widths), which were determined from the (0,0) band (Table 3). By varying the oscillator strength of the (1,0) bands from $f_{10} = 2.348 \times 10^{-3}$ (Schmidt & Bacskay 2007) in the calculation, we searched for the best value of f_{10} reproducing the observed EWs of the (1,0) band. As a result, the f_{00}/f_{10} was estimated to be 0.96 ± 0.05.

The ratios were compared with the experimental results (Davis, et al. 1984; Bauer, et al. 1985) and cal-

Table 5. Summary of parameters

Comp.	v	b	$N_{\rm obs}(C_2)$ [a]	$N_{\rm calc}(C_2)$ [b]	$T_{\rm rot}(C_2)$	$n(C_2)$	$N_{J''=0}(CN)$	$N_{J''=1}(CN)$	$T_{\rm rot}(CN)$	$N(CN)$
	(km s^{-1})	(km s^{-1})	(10^{12} cm^{-2})	(10^{12} cm^{-2})	(K)	(cm^{-3})	(10^{12} cm^{-2})	(10^{12} cm^{-2})	(K)	(10^{12} cm^{-2})
1	-15.1	2.39 ± 0.42	22	...	...	...	...	...	...	...
2	-9.6	1.47 ± 0.15	120	129^{+16}_{-10}	30 ± 5	100 ± 7	...	...	...	...
3	-4.0	0.53 ± 0.06	140	148^{+13}_{-8}	25 ± 5	125 ± 7	...	...	...	...
Sum	...	...	282	...	...	...	67 ± 3 [c]	33 ± 3 [c]	3.0 ± 0.2	101 ± 4

NOTE—The values are in units of 10^{12} cm^{-2}.

[a] The sum of the column densities of all rotational levels that were measured from detected lines.

[b] The C_2 total column densities estimated by fitting the model of van Dishoeck & Black (1982) to the observed rotational population.

[c] The column densities estimated from the EWs of $R_1(0)$ and $R_1(1)$ of CN (0,0) band assuming the cloud parameters measured from C_2 (0,0) bands (see the text for details).

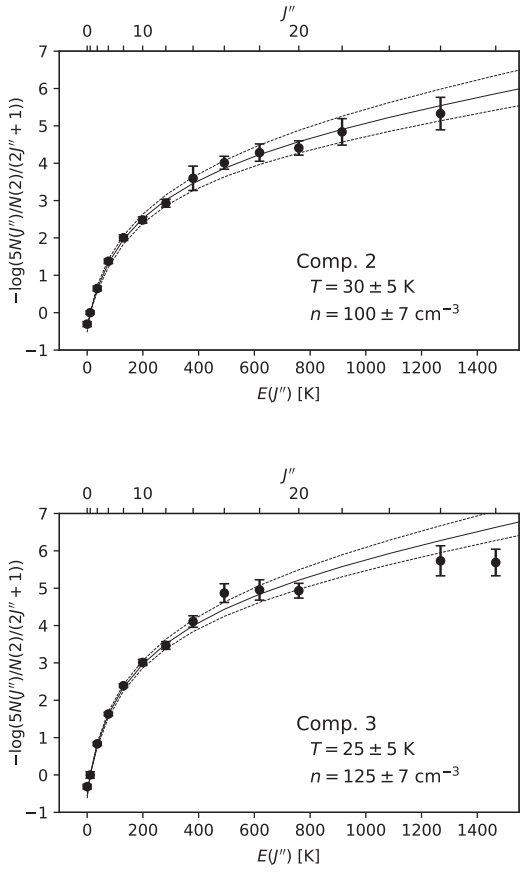

Figure 5. The rotational diagrams for components 2 (upper panel) and 3 (lower panel). Best-fit model lines and its one sigma ranges are plotted with the solid and dashed lines, respectively.

culated values (Schmidt & Bacskay 2007) in Table 6. Although the obtained ratio is closer to the theoretical result than the experimental result, it is consistent with both the experimental and theoretical results within the 1σ uncertainty. High-resolution data that can resolve the velocity components will be necessary for both bands in order to put stronger constraints on the oscillator strength ratios. The oscillator strength constraints from astronomical data can contribute to future improvements of the C_2 estimate (not only for the oscillator strengths of relevant bands of C_2, but also for astrophysical measurements).

4.3. *Marginal detection of* $^{12}C^{13}C$

We searched for the lines of the $^{12}C^{13}C$ (0,0) Phillips band in the HIRES-J spectrum. The wavelengths were based on the wavenumbers measured by Amiot & Verges (1983). $^{12}C^{13}C$ has the rotational levels of both odd and even rotational quantum numbers J'' in the ground state in contrast to $^{12}C_2$, which has only even numbers of J'' due to the homonuclear molecule nature. As the expected strengths of the P lines were too weak to be detected, only the Q and R lines were searched. The wavelengths of the $^{12}C^{13}C$ lines are distributed in the range of almost the same wavelength range of $^{12}C_2$. Although the $^{12}C^{13}C$ (1,0) Phillips band and the $^{13}C^{14}N$ (0,0) and (1,0) red bands covered in the WIDE spectrum were also searched using the line lists from Amiot & Verges (1983) and Sneden et al. (2014), respectively, we could not detect any absorption lines of these bands or put meaningful constraints on the isotope ratio.

As a result, only $Q(3)$ lines were marginally detected at the velocities of components 2 and 3. To date, the $^{12}C^{13}C$ molecule has never been detected in the interstellar medium. Figure 6 shows the spectrum of the $Q(3)$ lines of $^{12}C^{13}C$. Their EWs were 1.0 ± 0.3 and 0.7 ± 0.3

Table 6. Oscillator strengths of C_2 Phillips bands

Reference	Method	$f_{00} \times 10^3$	$f_{10} \times 10^3$	f_{00}/f_{10}
Davis, et al. (1984)	Experiment	1.38 ± 0.14	1.70 ± 0.17	0.81 ± 0.11
Bauer, et al. (1985)	Experiment	1.38	1.56	0.89
Schmidt & Bacskay (2007)	Calculation	2.233	2.348	0.951
This study	Astronomy	···	···	0.96 ± 0.05

mÅ for components 2 and 3, respectively. Although these dips were very weak, the velocities matched with those of components 2 and 3 for the $^{12}C_2$ lines. Other Q and R lines are expected to be weaker or contaminated with telluric absorption lines and $^{12}C_2$ lines; thus, the $Q(3)$ line is the most detectable line in our spectrum of Cyg OB2 No. 12. The multiple line detection for $^{12}C^{13}C$ requires higher S/Ns for this target.

From the EWs of $Q(3)$ lines, we estimated the abundance of $^{12}C^{13}C$ molecules. We assumed that the oscillator strength and the rotational distribution of $^{12}C^{13}C$ in the ground state are the same as $^{12}C_2$. In contrast to $^{12}C_2$, $^{12}C^{13}C$ can have pure rotational electric dipole transitions, which can cool down the rotational populations of $^{12}C^{13}C$, as they have very weak permanent electric dipole moment. We do not have any information regarding the rotational distribution of $^{12}C^{13}C$, and thus we ignore the pure rotational electric dipole transition of $^{12}C^{13}C$. Because the probability is estimated to be very low (Krishna Swamy 1987), the difference of rotational distributions between $^{12}C_2$ and $^{12}C^{13}C$ would not be so large. However, note that Bakker & Lambert (1998), who detected the $^{12}C^{13}C$ absorption band in a circumstellar shell, found that the lower rotational excitation temperature of $^{12}C^{13}C$, compared with that of $^{12}C_2$, is probably due to the radiative cooling of $^{12}C^{13}C$ by the pure rotational electric dipole transition.

On the basis of these assumptions, the $^{12}C_2$ / $^{12}C^{13}C$ ratios for Cyg OB2 No. 12 were estimated to be ~ 25 and ~ 50 for components 2 and 3, respectively. Conversion of these values into carbon isotope ratios results in ^{12}C / $^{13}C \sim 50$ and ~ 100, respectively. Considering the large uncertainties in the EWs, this is roughly consistent with the carbon isotope ratios in the interstellar medium measured by various carbon molecules: 68 ± 15 at the solar galactocentric distance (measurements of CO, CN, and H_2CO in Milam et al. 2005) and 76 ± 2 in the local ISM (CH^+ measurement in Stahl et al. 2008). In addition to the EW uncertainties, the deviation of the $^{12}C^{13}C$ rotational distribution from that of $^{12}C_2$, which was assumed here, can cause additional uncertainties in the resultant carbon isotope ratio. By taking higher-quality spectra and detecting multiple rotational lines (especially those arising from different rotational levels), the carbon isotope ratios of C_2 molecules can be investigated more accurately. Bakker & Lambert (1998) suggested that the isotopic exchange reaction of C_2 molecules is too slow to alter the $^{12}C_2$ / $^{12}C^{13}C$ ratio. The observation of $^{12}C_2$ and $^{12}C^{13}C$ will give us new information about the interstellar carbon isotope ratio and related chemical processes in the regime of translucent clouds.

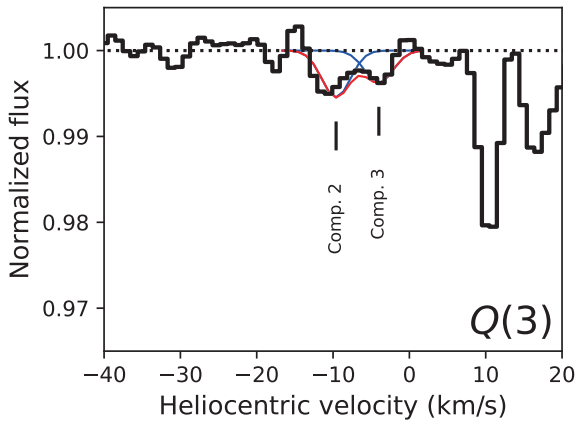

Figure 6. Spectrum of the $^{12}C^{13}C$ $Q(3)$ line. The weak absorption lines were detected at the velocities of components 2 and 3. The absorption lines seen at about +10 and +16 km s^{-1} are the $^{12}C_2$ $R(16)$ lines of the components 2 and 3, respectively.

5. SUMMARY

We reported the first detection of the C_2 (0,0) Phillips band and the CN (0,0) red band in the interstellar medium. We obtained the NIR high-resolution spectrum of Cyg OB2 No. 12 using the WINERED spectrograph mounted on the 1.3 m Araki telescope in Kyoto, Japan. We could detect the (0,0) and (1,0) bands of C_2 and CN with high S/N. In particular, the velocity components were clearly resolved in the C_2 (0,0) band spectrum ($R = 68,000$). Our findings are summarized as follows:

1. The CN column densities at levels of $N'' = 0$ and 1 were estimated to be $(6.7 \pm 0.3) \times 10^{13}$ and $(3.3 \pm 0.3) \times 10^{13}$ cm^{-2}, respectively. From the ratio, the rotational excitation temperature and the CN total column density were calculated as $T_{10} = 3.7 \pm 0.3$ K and $N(CN) = (8.2 \pm 0.4) \times 10^{13}$ $T_{10} = 3.0 \pm 0.2$ K and $N(CN) = (1.01 \pm 0.04) \times 10^{14}$ cm^{-2}, respectively.

2. From the rotational distribution of C_2, the temperatures and densities, (T, n), of components 2 and 3 were estimated to be (30 ± 5 K, 100 ± 7 cm^{-3}) and (25 ± 5 K, 125 ± 7 cm^{-3}), respectively. These essential physical parameters for understanding the interstellar chemistry could be estimated with high accuracy, due to the large oscillator strength of the (0,0) band, which allowed us to detect the rotational lines from high rotational levels for each velocity component.

3. From the line ratios between the C_2 (0,0) and (1,0) Phillips bands, the oscillator strength ratio, f_{00}/f_{10}, of the Phillips bands were constrained. The ratio is estimated to be $f_{00}/f_{10} = 0.96 \pm 0.05$, which is consistent with both theoretical and experimental values within 1σ uncertainties. In order to put stronger constraints on f_{00}/f_{10} from the astronomical observations, it is necessary to obtain high-resolution spectra, in which the velocity components are resolved for both bands.

4. We marginally detected the $Q(3)$ lines of $^{12}C^{13}C$ at the velocities of components 2 and 3. If these lines are real, this is the first detection of $^{12}C^{13}C$ in the interstellar medium. Assuming that the oscillator strength and rotational distributions of $^{12}C^{13}C$ are the same as those of $^{12}C_2$, the carbon isotope ratio was estimated to be 50–100, which is roughly consistent with the values in the local interstellar medium measured from other carbonaceous molecular features.

In this paper, we demonstrated that the absorption bands of C_2 and CN in the NIR region can be used to investigate the physical properties of interstellar clouds. Thanks to the large oscillator strengths of these NIR bands, we could improve the accuracy of the physical parameters estimated from the rotational distributions of both C_2 and CN. On the other hand, the strong telluric absorption lines that overlapped with the NIR bands make the analysis complicated and increase the systematic uncertainties. The removal of telluric absorption lines is critical for analyzing these NIR bands. Along with observational improvements, the updated model of C_2 excitation (Casu & Cecchi-Pestellini 2012) is also important for extracting further information regarding interstellar clouds. In addition to these absorption features of small carbonaceous molecules, many DIBs, which are considered to originate from large carbonaceous molecules such as fullerenes and PAHs, have been found in the Y and J bands covered in our observation (Cox et al. 2014; Hamano et al. 2015, 2016). In particular, the DIBs recently identified as absorption features of C_{60}^+ are located at about 9600Å. In view of the richness of important molecular features, the wavelength range of the Y and J bands is crucial to the study of interstellar carbon chemistry in diffuse clouds. In the future, it will be important to investigate the relationship between DIBs (including C_{60}^+ features), the abundances of C_2 and CN and the physical parameters of interstellar clouds (Elyajouri et al. 2018).

We are grateful to the staff of Koyama Astronomical Observatory for their support during our observation. We also thank the reviewer for a careful reading of the manuscript and helpful comments that improved this paper. This study is financially supported by the JSPS KAKENHI (16684001) Grant-in-Aid for Young Scientists (A), the JSPS KAKENHI (20340042) Grant-in-Aid for Scientific Research (B), the JSPS KAKENHI (26287028) Grant-in-Aid for Scientific Research (B), the JSPS KAKENHI (16K17669) Grant-in-Aid for Young Scientists (B), the JSPS KAKENHI (21840052) Grant-in-Aid for Young Scientists (Start-up), and the MEXT Supported Program for the Strategic Research Foundation at Private Universities, 2008-2012 (No. S0801061) and 2014-2018 (No. S1411028). S.H. is supported by the Grant-in-Aid for JSPS Fellows Grant No. 13J10504. N.K. is supported by JSPS-DST under the Japan-India Science Cooperative Programs during 2013-2015 and 2016-2018. K.F. is supported by the KAKENHI (16H07323) Grant-in-Aid for Research Activity start-up.

REFERENCES

Amiot, C., & Verges, J. 1983, A&AS, 51, 257

Bakker, E. J. & Lambert, D. L. 1998, ApJ, 508, 387.

Bauer, W., Becker, K. H., Hubrich, C., et al. 1985, ApJ, 296, 758.

Brooke, J. S. A., Ram, R. S., Western, C. M., et al. 2014, ApJS, 210, 23
Casu, S., & Cecchi-Pestellini, C. 2012, ApJ, 749, 48
Chauville, J., Maillard, J. P., & Mantz, A. W. 1977, Journal of Molecular Spectroscopy, 68, 399
Cox, N. L. J., Cami, J., Kaper, L., et al. 2014, A&A, 569, A117
Davis, S. P., Pecyner, R., Smith, W. H., et al. 1984, ApJ, 287, 455.
Douay, M., Nietmann, R., & Bernath, P. F. 1988, Journal of Molecular Spectroscopy, 131, 250
Elyajouri, M., Lallement, R., Cox, N. L. J., et al. 2018, A&A, 616, A143
Gredel, R., Black, J. H., & Yan, M. 2001, A&A, 375, 553
Gredel, R., Pineau des Forêts, G. & Federman, S. R. 2002, A&A, 389, 993.
Hamano, S., Kobayashi, N., Kondo, S., et al. 2015, ApJ, 800, 137
Hamano, S., Kobayashi, N., Kondo, S., et al. 2016, ApJ, 821, 42
Hupe, R. C., Sheffer, Y., & Federman, S. R. 2012, ApJ, 761, 38
Ikeda, Y., Kobayashi, N., Kondo, S., et al. 2016, Proc. SPIE, 9908, 99085Z
Krishna Swamy, K. S. 1987, MNRAS, 224, 537.
Krogager, J.-K. 2018, arXiv:1803.01187
Lambert, D. L., Sheffer, Y., & Federman, S. R. 1995, ApJ, 438, 740
Lavendy, H., Robbe, J. M., Chambaud, G., Levy, B., & Roueff, E. 1991, A&A, 251, 365
Lord, S. D. 1992, NASA Technical Memorandum 103957
Meyer, D. M., & Jura, M. 1985, ApJ, 297, 119
McCall, B. J., Hinkle, K. H., Geballe, T. R., et al. 2002, ApJ, 567, 391
Milam, S. N., Savage, C., Brewster, M. A., Ziurys, L. M., & Wyckoff, S. 2005, ApJ, 634, 1126
Najar, F., Ben Abdallah, D., Jaidane, N., & Ben Lakhdar, Z. 2008, Chemical Physics Letters, 460, 31
Najar, F., Ben Abdallah, D., Jaidane, N., et al. 2009, JChPh, 130, 204305
Otsubo, S., Ikeda, Y., Kobayashi, N., et al. 2016, Proc. SPIE, 9908, 990879
Ritchey, A. M., Federman, S. R., & Lambert, D. L. 2011, ApJ, 728, 36
Robbe, J. M., Lavendy, H., Lemoine, D., & Pouilly, B. 1992, A&A, 256, 679
Sameshima, H., Matsunaga, N., Kobayashi, N., et al. 2018, PASP, 130, 074502
Schmidt, T. W., & Bacskay, G. B. 2007, J. Chem. Phys., 127, 234310
Sembach, K. R., & Savage, B. D. 1992, ApJS, 83, 147
Sneden, C., Lucatello, S., Ram, R. S., Brooke, J. S. A., & Bernath, P. 2014, ApJS, 214, 26
Snow, T. P., & McCall, B. J. 2006, ARA&A, 44, 367
Souza, S. P., & Lutz, B. L. 1977, ApJL, 216, L49
Stahl, O., Wade, G., Petit, V., Stober, B., & Schanne, L. 2008, A&A, 487, 323
van Dishoeck, E. F., & Black, J. H. 1982, ApJ, 258, 533
van Dishoeck, E. F., & de Zeeuw, T. 1984, MNRAS, 206, 383
Whittet, D. C. B. 2015, ApJ, 811, 110
Yoshikawa, T., Ikeda, Y., Fujishiro, N., et al. 2012, Proc. SPIE, 8444, 84456

タイトル： Possible progression of mass flow processes around young intermediate-mass stars based on high-resolution near-infrared spectroscopy. I. Taurus

担当： Chikako Yasui, Satoshi Hamano, Kei Fukue, Sohei Kondo, Hiroaki Sameshima, Keiichi Takenaka, *et al.*

関連出版： The Astrophysical Journal, Volume 886, Issue 2, article id. 115, 20 pp. (2019).

関連学会発表等： https://www.kyoto-su.ac.jp/news/20191128_859_winered.html

Draft version September 24, 2019
Typeset using LaTeX **twocolumn** style in AASTeX62

Possible progression of mass flow processes around young intermediate-mass stars based on high-resolution near-infrared spectroscopy. I. Taurus

Chikako Yasui,[1,2] Satoshi Hamano,[2] Kei Fukue,[2] Sohei Kondo,[2] Hiroaki Sameshima,[2] Keiichi Takenaka,[2,3] Noriyuki Matsunaga,[4,2] Yuji Ikeda,[2,5] Hideyo Kawakita,[2,3] Shogo Otsubo,[2,3] Ayaka Watase,[2,3] Daisuke Taniguchi,[4] Misaki Mizumoto,[6] Natsuko Izumi,[1,2] and Naoto Kobayashi[7,8,2]

[1] *National Astronomical Observatory of Japan, 2-21-1 Osawa, Mitaka, Tokyo 181-8588, Japan, 2-21-1 Osawa, Mitaka, Tokyo 181-8588, Japan*

[2] *Laboratory of Infrared High-resolution spectroscopy (LIH), Koyama Astronomical Observatory, Kyoto Sangyo University, Mo-toyama, Kamigamo, Kita-ku, Kyoto 603-8555, Japan*

[3] *Department of Astrophysics and Atmospheric Sciences, Faculty of Sciences, Kyoto Sangyo University, Motoyama, Kamigamo, Kita-ku, Kyoto 603-8555, Japan*

[4] *Department of Astronomy, Graduate School of Science, The University of Tokyo, 7-3-1 Hongo, Bunkyo-ku, Tokyo 113-0033, Japan*

[5] *Photocoding, 460-102 Iwakura-Nakamachi, Sakyo-ku, Kyoto,606-0025, Japan*

[6] *Centre for Extragalactic Astronomy, Department of Physics, University of Durham, South Road, Durham DH1 3LE, UK*

[7] *Institute of Astronomy, University of Tokyo, 2-21-1 Osawa, Mitaka, Tokyo 181-0015, Japan*

[8] *Kiso Observatory, Institute of Astronomy, School of Science, The University of Tokyo, 10762-30, Mitake, Kiso-machi, Kiso-gun, Nagano 397-0101, Japan*

(Accepted 17 Sep 2019)

ABSTRACT

We used the WINERED spectrograph to perform near-infrared high-resolution spectroscopy (resolving power $R = 28{,}000$) of 13 young intermediate-mass stars in the Taurus star-forming region. Based on the presence of near- and mid-infrared continuum emission, young intermediate-mass stars can be classified into three different evolutionary stages: Phases I, II, and III in the order of evolution. Our obtained spectra ($\lambda = 0.91$–$1.35\,\mu$m) depict He I λ10830 and Pβ lines that are sensitive to magnetospheric accretion and winds. We also investigate five sources each for Pβ and He I lines that were obtained from previous studies along with our targets. We observe that the Pβ profile morphologies in Phases I and II corresponded to an extensive variety of emission features; however, these features are not detected in Phase III. We also observe that the He I profile morphologies are mostly broad subcontinuum absorption lines in Phase I, narrow subcontinuum absorption lines in Phase II, and centered subcontinuum absorption features in Phase III. Our results indicate that the profile morphologies exhibit a progression of the dominant mass flow processes: stellar wind and probably magnetospheric accretion in the very early stage, magnetospheric accretion and disk wind in the subsequent stage, and no activities in the final stage. These interpretations further suggest that opacity in protoplanetary disks plays an important role in mass flow processes. Results also indicate that He I absorption features in Phase III sources, associated with chromospheric activities even in such young phases, are characteristics of intermediate-mass stars.

Keywords: accretion, planetary systems: protoplanetary disks — stars: formation — stars: pre-main-sequence — stars: winds, outflows — infrared: stars

1. INTRODUCTION

Stars are formed owing to the gravitationally induced collapse of cold molecular gas. While the molecular clouds are contracted during the collapse, the initial rotation of the star-forming cloud is enormously magnified by the conservation of angular momentum. In this process, the rotating circumstellar disks are formed, and majority of the material of a typical star is accreted through its disk (Hartmann 2009). Although almost all of the angular momentum (>99 %) must be removed

Corresponding author: Chikako Yasui
ck.yasui@nao.ac.jp

to form an observable star, we lack a conclusive theory explaining the mechanics of the angular momentum transfer ("angular momentum problem", Bodenheimer 1995). As one of the most important processes, this study focuses on the mass flow processes occurring very close (radius $r \lesssim 1\,\mathrm{AU}$) to central stars. In this region, a large population of close-in planetary systems has been reported, even around young stellar objects (YSOs) younger than 10 Myr (e.g., Donati et al. 2016). However, the manner in which planets are formed is still being debated (Winn & Fabrycky 2015). Because the interaction between the stars and disks at which planets are formed occurs mainly in the inner disk region, it is essential to investigate the conditions of this region from the planet formation viewpoint.

As for mass flow processes, magnetospheric accretion and outflowing gas have been proposed. Because direct imaging for separations of less than 1 AU is considered to be very difficult using the existing instruments, spectroscopy has been employed. Traditionally, Hα, NaD, Ca II H&K, Mg II h&k lines have been used for conducting diagnostics (e.g., Mundt 1984; Calvet & Hartmann 1992). For mass accretion, these diagnostics have permitted the development of a general picture with respect to various factors, including the mass accretion rate, evolution, geometry, and stellar mass dependence (e.g., Muzerolle et al. 1998b; Hartmann et al. 1998; Muzerolle et al. 2004; Calvet et al. 2004). However, the actual mechanics of outflowing gas have not yet been completely elucidated. There are at least three possible configurations of wind formation: a disk wind (Ustyugova et al. 1995), an X-wind (Shu et al. 1994), and a stellar wind (Hartmann et al. 1982). To distinguish between different theoretical models, constraints on the nature or location of the wind-launching region are very important. However, the aforementioned traditional spectral lines exhibit blueshifted absorption superposed on the broad emission features. This observation signifies the presence of high-velocity wind close to the star (Ardila et al. 2002), yielding little information on the nature or location of the wind-launching region.

Recently, the He I 10,830 Å line has been suggested as a particularly suitable and sensitive probe of both mass accretion and outflow (Edwards et al. 2006). Edwards et al. (2006) exhibited that ∼70 % of their 39 sample classical T-Tauri stars (CTTSs) exhibit a blueshifted subcontinuum absorption that can be assumed to be a probe of outflow. This is in contrast to Hα, for which only ∼10 % of the stars show a similar type of absorption component. Additionally, ∼50 % of their CTTSs show redshifted absorption below the continuum in He I; this can be considered to be a probe of mass accretion. They also highlighted that the direct probes of the outflowing gas launch region can be created only by high-resolution spectroscopy of the He I line. While the targets for Edwards et al. (2006) were primarily low-mass stars, Oudmaijer et al. (2011) and Cauley & Johns-Krull (2014) presented a He I λ10830 profile for Herbig Ae/Be stars (HAeBes), which are intermediate-mass pre-main sequence stars. The calculated He I model profile (e.g., Kwan et al. 2007, Fischer et al. 2008, Kurosawa et al. 2011, Kurosawa & Romanova 2012) suggests that the mass flow processes occurring in the inner part of the protoplanetary disks (disk wind, stellar wind, and magnetospheric accretion) can be distinguished based on the He I profile morphologies. Further, the hydrogen Paschen series can also serve as diagnostics for magnetospheric accretion. Because these series lines are of lower opacity when compared to the Hα lines, they depict signatures of infall of accreting material in a magnetospheric funnel flow more clearly, whereas Hα often do not show such signatures (Muzerolle et al. 2001). Folha & Emerson (1999, 2001) presented the Pβ line profiles for 49 T Tauri stars and observed that inverse P Cygni profile features, indicating the magnetospheric mass accretion, can be observed at a relatively high frequency even though the blueshifted absorption features are absent. Edwards et al. (2006) also presented the Pγ line profiles for 48 T Tauri stars. The calculated model profiles of the Paschen lines (e.g., Kurosawa et al. 2011, Kurosawa & Romanova 2012) suggest that the existence or absence of magnetospheric accretion can be determined based on the line morphology; however, these lines cannot serve as diagnostics for winds.

The progression of the dominant mass flow processes through stellar evolution should also impose constraints on the mechanistic theories. Edwards et al. (2006) proposed a progression involving veilings, which are considered to be correlated with the mass accretion rate (e.g., Beristain et al. 2001). In particular, these authors suggested that the emission equivalent width of Pγ decreases with decreasing veiling. Based on He I profiles, Kwan et al. (2007) used a comparison of their theoretical line profiles with the profiles observed by Edwards et al. (2006) to suggest that the wind signatures of stars with high disk accretion rates are more likely to indicate stellar wind than disk wind. Further, although a moderate trend is evident in these factors, this pattern does not seem to be valid for all the stellar sources. This inconsistency may be attributed to an extensive variety of disk properties that have been revealed by recent observational studies, e.g., mass accretion rate, disk lifetime, and disk mass. The median disk lifetime has been estimated to be approximately

3 Myr even though the lifetimes vary from less than 1 Myr to a maximum of 10 Myr. The mass accretion rate and disk mass also exhibit large dispersions, $\sim\pm1$ dex (for the mass accretion rate, see Figs. 2 and 3 in Hartmann 2008; for the disk mass, see Fig. 5 in Williams & Cieza 2011 and Fig. 7 in Ansdell et al. 2017). Furthermore, because the entirety of dust and gas in the inner and outer disks is dispersed almost simultaneously; at 0.5 Myr (Williams & Cieza 2011), there appear to be no clear indicators of the protoplanetary disk evolutionary stages. However, this picture is obtained from low-mass stars ($\lesssim1\,M_\odot$), which constitute the majority in the solar neighborhood. Recent observations suggest that the protoplanetary disks surrounding the intermediate-mass stars show different evolutionary stages; for the intermediate-mass stars ($\gtrsim1.5\,M_\odot$), only the innermost disk regions that are traced with the near-infrared (NIR) K-band ($r\sim0.3$ AU) disperse at a very early time as compared to the outer disks by $\sim$3 to 4 Myr (Yasui et al. 2014). Therefore, based on the presence of innermost and outer disks, the intermediate-mass stars can be categorized into three phases; further, the intermediate-mass stars should be appropriate targets for investigating the time variation of dominant mass flow processes. Based on the He I line profiles, Cauley & Johns-Krull (2014) suggested that HAe stars exhibit signatures of magnetospheric accretion and stellar wind even though they do not exhibit disk wind. Although these authors have suggested that these processes are characteristic of the intermediate-mass stars, this may only be valid for the Phase I sources to which the HAe stars are comparable. To bridge this gap, it is necessary to observe young intermediate-mass stars in all the evolutionary phases.

In this study, we present the results of a census of He I λ10830 and Pβ in 13 young intermediate-mass stars in the Taurus star-forming region, which is one of the nearest active star-forming regions (distance of $D=140$ pc; Kenyon et al. 2008). Given its proximity, this region can be investigated using X-ray to radio wavelengths, and the members of Taurus have been more comprehensively identified (from early type stars to brown dwarfs) than those of any other star-forming region. Given the young age of the Taurus complex ($\sim$1.5 Myr (Barrado y Navascués & Martín 2003)), most members are still surrounded by circumstellar materials. Therefore, Taurus is the best target for conducting our first star-formation study with WINERED (Warm INfrared Echelle spectrograph for REalizing Decent infrared high-resolution spectroscopy). WINERED is a spectrograph of high sensitivity and high resolution (with two resolution modes of $R=28{,}000$ and $R=70{,}000$), specifically customized for short NIR bands at 0.9 to 1.35 μm (Yasui et al. 2008). WINERED received its first light in 2012 May at the Araki 1.3 m telescope and is now attached to the New Technology Telescope (NTT) (Ikeda et al. 2018); further, it is planned to attach WINERED to the Magellan Telescope. We are continuing to investigate YSOs in the target star-forming regions, including Tr 37 and NGC 7160. By considering that the lifetime of the protoplanetary disks is approximately 10 Myr (e.g., Hernández et al. 2008), these regions are considered to be in different evolutionary phases than Taurus. Tr 37 ($\sim$4 Myr) is in the middle phase, while NGC 7160 ($\sim$10 Myr) is in the final phase. Our results for the other regions will be provided in a future work.

This study can be organized as follows. In Section 2, we discuss the target selection, observations, and data reduction. In Section 3, we present the obtained spectra of the Paschen series and He I λ10830 and determine the excess continuum emission and residual profiles. We further discuss the properties of the Pβ and He I λ10830 lines. In Section 4, we discuss the statistics of the line profile morphologies and present an interpretation of the profile morphology of Pβ and He I λ10830 in different evolutionary phases of the protoplanetary disks in combination with other intermediate-mass stars that have been observed in previous studies. We further discuss the possible progression of dominant mass flow processes in the evolution of protoplanetary disks. After comparing the results with those of the previous studies, we finally discuss the implications for theories of mass flow processes.

2. TARGET SELECTION, OBSERVATION AND DATA REDUCTION

2.1. *Selection and evolutionary phase of targets*

We selected target intermediate-mass stars in the Taurus star-forming region. We defined stars within the mass range of 1.5–7 $M_\odot$ as intermediate-mass stars (Yasui et al. 2014). The intermediate-mass stars were selected in a similar manner to that of Yasui et al. (2014); assuming a typical age of the Taurus star-forming region, $\sim$1.5 Myr (Barrado y Navascués & Martín 2003), we obtained the spectral types of cluster members from the literature. For the lower mass limit, we used a spectral type of K5 corresponding to 1.5 $M_\odot$. Although Yasui et al. (2014) set the upper limit mass at 7 $M_\odot$ (spectral type B3), even the most massive stars in Taurus possess masses of $\sim$4 $M_\odot$ (spectral type B9), which is substantially lower than the upper mass limit. Among the candidates selected above, the final targets are limited to stars with J-band magnitudes of less than 9 mag in the Two Micron All Sky Survey (2MASS) Point Source Catalog (PSC; Skrutskie et al. 2006). This criterion is

required by the limited sensitivity of the Araki 1.3 m telescope's implementation of WINERED, with which this study's spectra can be obtained (see Section 2.2). Therefore, 13 target intermediate-mass stars were selected. The properties of the selected target stars are summarized in Table 1.

In a previous study (Yasui et al. 2014), we derived the intermediate-mass disk fraction in the near-infrared *JHK* photometric bands and in the mid-infrared (MIR) bands for young clusters in the age range of 0 to ∼10 Myr. Yasui et al. (2014) have defined the region to the right of the border line[1] (region highlighted in orange region in Fig. 1) as the disk excess region on $H-K$ vs. $J-H$ color—color diagram (Fig. 1); stars located on the disk excess region are recognized as stars traced by NIR excess emissions. MIR disk fraction is derived using *Spitzer* IRAC [3.6]–[8] photometric bands. The stars that have SED slope with the MIR bands ($\alpha = d\ln\lambda F\lambda/d\ln\lambda$) of >-2.2 are recognized as stars traced by MIR excess emissions (Kennedy & Kenyon 2009). In the case of 2.5 $M_\odot$-stars, NIR and MIR continuum emissions trace innermost dust disk ($r \sim 0.3$ AU) and outer dust disk ($r \gtrsim 5$ AU), respectively. Yasui et al. (2014) have suggested that in the very early phase, the intermediate-mass stars disperse only their innermost dust disks. They further disperse their outer dust disks with a time lag of ∼3 to 4 Myr. Therefore, the presence of innermost disks and outer disks surrounding the intermediate-mass stars can be a clear evolutionary indicator. Hereafter, we will refer to the three evolutionary phases of "Phase I" that contains stars with both innermost and outer disks, "Phase II" that contains stars without innermost disks but with outer disks, and "Phase III" that contains stars without innermost and outer disks.

The photometric data for 13 target intermediate-mass stars selected above are shown in Table 1. The data of NIR bands are obtained from the 2MASS PSC for targets, whose all *JHK* band photometric quality flags are denoted as "A" (signal-to-noise ≤10 for all *JHK* bands). Because AB Aur does not satisfy the condition, we used NIR data reported by Kenyon & Hartmann (1995). We plotted our target sources on $H-K$ vs. $J-H$ diagram in Fig. 1. Only four sources (V892 Tau, AB Aur, IRAS 04101+3103, and T Tau) are located in the disk excess region, suggesting that they have innermost dust disks. For MIR data, because IRAC photometric data for most target stars could not be obtained from the IRAC observations of the Taurus star-forming region (e.g., Hartmann et al. 2005), we adopted α values derived using Spitzer IRS within λ = 6–13 μm. Nine sources (V892 Tau, AB Aur, IRAS 04101+3103, RY Tau, SU Aur, T Tau, RW Aur, V773 Tau, and UX Tau) have α values of ≥ -2.2, suggesting that they have outer dust disks. Therefore, the selected targets cover all the evolutionary phases of the protoplanetary disks, with four Phase I sources, five Phase II sources, and four Phase III sources. Four sources (V892 Tau, AB Aur, IRAS 04101+3103, and T Tau) are categorized into Phase I, five sources (RY Tau, SU Aur, T Tau, RW Aur, V773 Tau, and UX Tau) are categorized into Phase II, and four sources (HP Tau/G2, HD 283572, HBC 388, and V410 Tau) are categorized into Phase III. Table 2 summarizes basic disk properties for all the targets, showing classification, mass accretion rate, and disk mass. Notably, no clear distinctive properties are observed between Phase I and II sources except for aforementioned NIR K-band excesses.

We indicate that disks around the intermediate-mass stars necessarily evolve from Phase I to Phase II and, subsequently, to Phase III, while the disks around the low-mass stars evolve from Phase I to Phase III, spending a considerably short time in Phase II (Yasui et al. 2014). It should be noted that HAeBes are categorized into Phase I sources because they are confirmed to contain NIR K-band excesses. Fig. 1 plots HAe stars in a sample used by Cauley & Johns-Krull (2014), whose mass range is roughly comparable to that of our target intermediate-mass stars and whose He I profile morphologies will be later compared with those of our targets (Sections 3.4, 3.4, 4.6); the stars are shown with gray squares. We used NIR data from 2MASS PSC and rejected four sources (V1578 Cyg, HD 17081, HD 37490, and Z CMa), which do not have an "A" photometric quality flag for at least one band in the catalog. Thus, we confirmed that all sources, except one source, are located in the disk excess region having large color excesses. The exception is HD 141569 ($(J-H, H-K) = (0.01, 0.04)$), which Cauley & Johns-Krull (2014) categorized into potentially misclassified objects and did not include in their final discussion by indicating that it may not be a HAe star. Fig. 1 also shows the intermediate-mass stars in samples reported by Folha & Emerson (2001) and Edwards et al. (2006) that satisfy the conditions for selecting intermediate-mass stars in Taurus, but are excluded from the sample used in this study due to the limited instrumental sensitivities. They are six sources and their properties are summarized in Table 3. Four of these sources (CW Tau, GM Aur, DR Tau, and DS Tau) are included in both the previous studies, while

[1] The border line (the dot-dashed line) passes through the point of $(H-K_S, J-H) = (0.2, 0)$ and is parallel to the reddening vector (shown with gray arrow in Fig. 1).

HP Tau and HN Tau are included in only one of these references (Folha & Emerson 2001 and Edwards et al. 2006). CW Tau, HP Tau, DR Tau, and HN Tau are categorized into Phase I based on their NIR and MIR excesses, while GM Aur and DS Tau are categorized into Phase II. For reference, CTTSs and weak T-Tauri stars (WTTSs) are almost comparable to Phase I and Phase III, respectively, in case of low-mass stars (Yasui et al. 2014).

2.2. *WINERED spectroscopy and data reduction*

We obtained the spectra of selected targets using the near-infrared (NIR) spectrograph WINERED (Kondo et al. 2015; Ikeda et al. 2016) attached to the Araki 1.3 m-telescope at Koyama Astronomical Observatory, Kyoto-Sangyo University, Japan (Yoshikawa et al. 2012). WINERED has a 1.7 μm cutoff 2048 × 2048 HAWAII-2RG infrared array with a pixel scale of $0''.8\,\mathrm{pixel}^{-1}$, simultaneously covering the wavelength range of 0.91–1.35 μm. We used a 1.65″-width slit, corresponding to 2 pixels, which proves a spectral resolving power of $R = 28,300$ or $11\,\mathrm{km\,s^{-1}}$. Observations were performed during the following three periods: February to March 2013; November 2013 to January 2014; and September to October 2014. Seeing was typically ∼5″. To avoid saturation in the emission lines, the exposure time for each frame was set to a duration ranging from 300 to 1200 s. Four to twelve sets of data were obtained for each target, resulting in a total exposure time of 1200 to 7200 s for each target. As the telluric standard stars, the spectra of bright stars with spectral types of late B to early A (B9–A2) at similar airmass ($\Delta \sec z \lesssim 0.2$) were obtained in a similar fashion within 2 hours of target data acquisition on the same night. As the sole exception, the spectra of an M1III spectral type star, HD 1041, as the telluric standard star were obtained for HP Tau/G2. We summarize the details of the observation in Table 4.

All the data were reduced by following the standard procedures using IRAF, including nodding sky subtraction, dome flat-fielding, and aperture extraction. The argon lamp spectra that were obtained at the end of the observing night were used for performing vacuum wavelength calibration. Each target spectrum was divided by the spectrum of the standard star to rectify for atmospheric absorption and instrumental response after the photospheric features of the standard spectrum were eliminated (Sameshima et al. 2018). For each echelle order, the spectra were normalized to 1.0. For the continuum level at $\lambda \sim 12700$ Å, where there are no strong photospheric features in synthetic spectra (see Section 3.2) for all the targets, the estimated signal to noise ratios (S/N) were ∼30 to 110 (see Table 4 for each target). The spectra around Pδ, Pγ, Pβ, and He I (orders of $m = 56, 51, 44$, and 52, respectively), reduced by following the above procedure, are depicted for all the targets with respect to the stellar velocities in Figure 2. The spectra are sorted by spectral type from the early to late type.

3. RESULTS

The obtained spectra depict several lines, including those of hydrogen (Paschen series), He I, and metals (e.g., Fe I, Si I, Mg I). We focus on hydrogen lines and He I λ10830 in this study because these are very sensitive to magnetospheric mass accretion and winds.

3.1. *Hydrogen Paschen series*

The WINERED wavelength range ($\lambda = 0.91$–$1.35\,\mu$m) covers four hydrogen lines: Pϵ ($\lambda = 9549$ Å), Pδ ($\lambda = 10052$ Å), Pγ ($\lambda = 10941$ Å), and Pβ ($\lambda = 12822$ Å), where the numbers in parentheses refer to the vacuum wavelengths. The spectra of Pδ, Pγ, and Pβ are depicted in Figure 2 (panels a, b, and d, respectively). Although each spectrum appears to show similar features across various targets, the S/Ns of the spectra are higher at longer wavelengths, resulting in the features of those spectra becoming more prominent. These tendencies are clearly observed in, e.g., RY Tau, SU Aur, UX Tau, and HP Tau/G2. Consider UX Tau as an example. Although the Pγ spectrum shown in Edwards et al. (2006) exhibits no features, the Paβ spectrum in Figure 2 depicts significant features, including double peaks with centered subcontinuum absorption, thereby making the diagnostics of magnetospheric accretion possible. Therefore, we focus on the spectra of Pβ among four lines in the hydrogen Paschen series in this study. This approach can help us to detect the possible characteristics of profile morphologies in different evolutionary phases.

3.2. *Removal of photospheric features: Estimation of line broadening, radial velocities, and veilings*

The observed spectra comprise circumstellar and photospheric features. To extract the circumstellar features, it is necessary to eliminate the photospheric features. The photospheric features are broadened (line broadening, v_{broad}), and shifted because of radial velocities (RVs); further, they also exhibit continuum excesses. The excess can be referred to as "veiling," which is defined as the ratio of the excess emission to the underlying stellar photosphere (see Hartigan et al. 1989). We eliminate the photospheric features using the following procedure. First, by comparing the observed spectra

with the synthetic spectra, the stellar properties, line broadenings, radial velocities RVs, and veilings can be obtained. We further obtain the circumstellar features by subtracting the synthetic spectra from the observed spectra by considering the aforementioned stellar properties.

For each object, we constructed the synthetic spectra using the analysis program SPTOOL (Takeda 1995; Takeda & Kawanomoto 2005), which is based on the ATLAS9 programs from Kurucz (1993). We adopted the metal line list in Meléndez & Barbuy (1999) and the molecular lines from the Vienna Atomic Line Database (VALD3; Ryabchikova et al. 2015). Further, we assumed solar abundance and spectral type from the literature (see Table 1). The adopted parameters for the synthetic spectra, effective temperature ($T_{\rm eff}$), surface gravity ($\log g$), and microturbulent velocity are provided below. The effective temperatures were adopted from Gray (2005) (Table B.1. in Appendix B). In a case that the spectral types for targets were not listed in Gray (2005), close spectral types were used (see Table 5, column 2). The $\log g$ was calculated with $T_{\rm eff}$, stellar mass (M_*), and stellar luminosity (L_*). Because the model dependence of $\log g$ is considered to be very small (Takagi et al. 2011), we used the values of $T_{\rm eff}$, M_*, and L_* from a PMS isochrone model, Siess et al. (2000), by considering the age of Taurus (1.5 Myr old). The obtained $\log g$ values are 4.1 for spectral type B8, 3.5 for spectral type K0, and 3.7 for spectral types K3–K5. We adopted the values of 4.1 for late B to early A type stars (V892 Tau, AB Aur, and IRAS 04101+3103), 3.5 for G0–K1 type stars (HP Tau/G2, RY Tau, SU Aur, HD 283572, T Tau, and HBC 388), and 3.7 for K3–K5 type stars (RW Aur, V773 Tau, V410 Tau, and UX Tau). For microturbulent velocity, we adopted $2\,{\rm km\,s^{-1}}$ according to Gray et al. (2001), who observed a tight correlation between microturbulence and $\log g$ in the spectral range of late A- to early G-type (see Fig. 7 in Gray et al. 2001).

We derived line broadening $v_{\rm broad}$, radial velocity RV, and Y- and J-band veilings (γ_Y and γ_J, respectively) for each target by fitting the obtained synthetic spectra with the observed spectra. First, we roughly estimated $v_{\rm broad}$[2] and RV by fitting the obtained synthetic spectra with the observed spectra using the automatic profile-fitting program MPFIT (Takeda 1995) included in SPTOOL. Note that the veilings are not yet considered at this stage. Among the spectra shown in Fig.2 ($m = 56$, 52, 51, and 44), our fitting procedure used spectra with interference order $m = 52$, which included He I λ10830, because these spectra show a large number of relatively deep lines, with normalized counts of less than 0.7 in normalized synthetic spectra at $v_{\rm broad} = 0\,{\rm km\,s^{-1}}$. The deep lines used for the fitting, in the wavelength ranges of λ = 10710–10815 Å and 10855–10875 Å, are not affected by the He I λ10830 features and do not include data with very low S/N due to the edges of the spectra. The lines used for the stars with spectral types G–K2 were Si I (λ10730.3, 10752.3, 10787.5, 10789.8, 10871.8, 10872.5), Mg I λ10814.1, and C I λ10732.5. For stars with spectral type of K3 or later, the Fe I lines (λ10756.0, 10786.0) were used in addition to the above lines; however, C I was not used because it was weak in case of later-type stars. We further derived $v_{\rm broad}$, RVs, and γ_Y by comparing several synthetic spectra. The best fit was determined using the minimum chi-squared value by varying the three parameters of $v_{\rm broad}$, RV, and γ_Y. The synthetic spectra were constructed using the following limits on each parameter: (1) $v_{\rm broad}$ values around initially estimated values with $5\,{\rm km\,s^{-1}}$ step; (2) γ_Y values in the range of 0.0 to 2.0 with 0.1 step; and (3) observed spectra with wavelength shifts for RVs with 0.1 Å step. For the fitting, the same wavelength range was used as was used in the initial estimate of $v_{\rm broad}$. When estimating $v_{\rm broad}$ and RV, we also estimated γ_J using spectra with order $m = 44$ in the same way as the derivation of γ_Y but in the spectral range of λ = 12620 to 12700 using lines of Fe I λ12642.2, Fe I λ12652.2, and Na I λ12682.7. The obtained properties ($v_{\rm broad}$, RV, γ_Y, and γ_J) are summarized in Table 5. Finally, we obtained residual profiles of Pβ and He I by subtracting synthetic spectra considering the obtained properties from observed spectra. The profiles relative to the stellar rest velocities are shown in Figure 3.

We note that we could not estimate $v_{\rm broad}$, RV, and veilings using the above procedure for three early-type stars with spectral types of late B–early A: V892 Tau, AB Aur, and IRAS 0401+3103. This was due to a lack of prominent photospheric features in their spectra except for H I. There are only a small number of photospheric features in the spectra for such early-type stars, and even the existing features become quite broadened and very shallow due to the large rotation velocities (e.g., $v \sin i = 116\,{\rm km\,s^{-1}}$ for AB Aur; $100\,{\rm km\,s^{-1}}$ for V897 Tau). Instead, we used synthetic spectra assuming $v_{\rm broad}$ and RV values from the literature, without considering veilings ($\gamma_Y = 0$,$\gamma_J = 0$), for the subtraction of photospheric features from the observed spectra. As for $v_{\rm broad}$ of AB Aur, only the projected rotation ve-

[2] Here, $v_{\rm broad}$ is parameterized by FWHM. However, because the output velocity in MPFIT is a convolution of $v_{\rm broad}$ and the instrumental broadening, and is parameterized by the e-folding half width, it is converted to $v_{\rm broad}$ according to Takeda et al. (2008).

locity ($v \sin i$) was provided by the literature (Alecian et al. 2013), $v \sin i = 100\,\mathrm{km\,s^{-1}}$. Nonetheless, we had to input $v_{\rm broad}$, using combinations of $v \sin i$ and macroturbulence velocity ($v_{\rm mac}$), when making synthetic spectra with SPTOOL. Alecian et al. (2013) assumed a $v_{\rm mac}$ of $2\,\mathrm{km\,s^{-1}}$, and suggested that in the case that $v \sin i$ is larger than $40\,\mathrm{km\,s^{-1}}$, $v_{\rm mac}$ is not a significant parameter. Therefore, we adopted their $v \sin i$ values for $v_{\rm broad}$. Also, for the $v_{\rm broad}$ value for V892 Tau, only $v \sin i$ ($116\,\mathrm{km\,s^{-1}}$) was provided by the literature (Mooley et al. 2013). Although we could not find the adopted value of $v_{\rm mac}$, it should be negligible for $v_{\rm broad}$, considering the large $v \sin i$ value. Therefore, we adopted this value as $v_{\rm broad}$. However, we could not find any literature references for the $v_{\rm broad}$ and RV values for IRAS 04101+3103. We adopted the average value of RVs for all target objects in this paper (Table 1 Col. (9)) that all exist in the Taurus star-forming region, $\sim$20 $\mathrm{km\,s^{-1}}$. For $v_{\rm broad}$, we assumed a value of $100\,\mathrm{km\,s^{-1}}$, similar to those for AB Aur and V892 Tau, considering that their spectral types are almost the same and their disks evolutionary phases are the same (Phase I). As for veilings, we could not find any references about veilings for these three sources. Because the photospheric He I lines show prominent features only in very early-type stars, $\sim$B5 and earlier (Cauley & Johns-Krull 2014), which are not included in our targets, variations of synthetic spectra have little impact on our residual profiles. However, because photospheric Pβ lines show very prominent absorption features in late B- and early A-type stars (our early-type targets), differences between photospheric features in assumed synthetic spectra and those in actual spectra may have a great impact on the residual profiles in normalization. We discuss the possible impact of assuming zero veilings on obtained residual profiles in Section 3.3.

Estimated $v_{\rm broad}$, RV, γ_Y, and γ_J values for each target are summarized in Table 5. WTTSs, comparable to Phase III objects in this paper, are known to show no veiling (e.g., Edwards et al. 2006), while correlation between mass accretion rate and veiling for CTTSs is suggested (e.g., Beristain et al. 2001). For all four Phase III objects (HP Tau/G2, HD 283572, HBC 388, and V410 Tau), γ_Y and γ_J are estimated to be almost zero although some estimated values are nonzero ($\gamma_Y = \gamma_J = 0.1$ for HP Tau/G2; $\gamma_J = 0.1$ for HD 283572). Therefore, taking all results of Phase III objects into an account, estimated veilings are $\leq$0.1, suggesting that veilings are accurately estimated with uncertainties of $\sim$0.1.

3.3. *Pβ line profiles*

Paschen line emissions are thought to arise primarily in the magnetospheric accretion column (Hartmann et al. 2016). Although profiles of Paschen lines in obtained spectra (Pϵ, Pγ, Pδ, and Pβ) show similar morphologies, we discuss those of Pβ that show the most prominent features, as discussed in § 3.1. In this section, we focus on the properties of Pβ emission for each source. We discuss the implications for the profile morphology in Section 4.

We detected Pβ in 8 of our 13 targets (all Phase I sources, and all Phase II sources except V773 Tau), while these lines are not detected in 5 sources (V773 Tau and all Phase III sources). The detection rates for Phase I, II, and III objects are 100 % (4/4), 80 % (4/5), and 0 % (0/4), respectively. In Table 6, we summarize the Pβ profile parameters obtained from the residual profiles (Figure 3), showing object name in column 1, profile type in column 2, the maximum blueshifted and redshifted line velocities ($V_{\rm max}^{\rm blue}$ and $V_{\rm max}^{\rm red}$) in columns 3 and 4, the velocity of peak emission and absorption ($V_{\rm peak}^{\rm em}$ and $V_{\rm peak}^{\rm abs}$) in columns 5 and 6, the line fluxes relative to the continuum at the peak emission and absorption velocities ($F_{\rm peak}^{\rm em}$ and $F_{\rm peak}^{\rm abs}$) in columns 7 and 8, emission and absorption equivalent widths (Em. W_λ and Ab. W_λ) in columns 9 and 10, and the type of subcontinuum absorption in column 11. In column 2, we categorize residual spectra into morphology groups based on the classification scheme of Cauley & Johns-Krull (2014). They divided the line profiles into six groups: (1) P-Cygni (PC), (2) inverse P-Cygni (IPC), (3) pure absorption (A), (4) single-peaked emission (E), (5) double-peaked emission (DP), and (6) featureless (F). We added a new category, a profile with both blueshifted and redshifted subcontinuum absorption but with zero or one emission peak (hereafter, "BR"). Reipurth et al. (1996) has reported another well-known classification. The groups E, PC, and IPC in the classification by Cauley & Johns-Krull (2014) correspond to type I, type IV B, and type IV R in the classification of Reipurth et al. (1996), respectively, and that group DP by Cauley & Johns-Krull (2014) comprises type II and type III of Reipurth et al. (1996).

The Pβ profiles for the targets are categorized into the following four groups; group E, group DP, group IPC, and group F. The profiles of all the four Phase I sources (V892 Tau, AB Aur, IRAS 04101+3103, and T Tau) are categorized into group E. They all exhibit approximately symmetric and broad features with $|V_{\rm peak}^{\rm em}| \leq 20\,\mathrm{km\,s^{-1}}$ for all the sources, and $|V_{\rm max}^{\rm blue}|$ and $|V_{\rm max}^{\rm red}|$ of $\gtrsim$300 $\mathrm{km\,s^{-1}}$ except for T Tau ($|V_{\rm max}| \sim 250\,\mathrm{km\,s^{-1}}$). They have slightly redward absorption features judging from $|V_{\rm max}^{\rm blue}|$ values exceeding $|V_{\rm max}^{\rm red}|$ by $\sim$50 $\mathrm{km\,s^{-1}}$. In

addition, the profiles of three of the sources (RY Tau, SU Aur, and UX Tau) are categorized into group DP. All the sources in this group have influence from redward absorption, judging from $V_{\rm peak}^{\rm em} < 0$. The profile for UX Tau shows subcontinuum absorption centered on the stellar rest velocity. The profile of RW Aur is categorized into group IPC, which has a very slight subcontinuum feature with $F_{\rm peak}^{\rm abs} = 0.96$. Finally, the profiles of the remaining five sources (V773 Tau, HP Tau/G2, HD 283572, HBC 388, and V410 Tau) are categorized into group F.

We note the possibility that photospheric features in Pβ profiles for A- and B-type stars (V892 Tau, AB Aur, and IRAS 04101+3103) are not completely removed in residual profiles shown in Fig. 3 because there is no information on veilings for the early type stars and we tentatively adopted synthetic spectra assuming zero veilings as photospheric features (Section 3.2). We checked the variation of obtained residual profiles assuming the extreme case of high veilings, 2.0, as shown in Table 6 in parentheses. As a result, we found that variations are $\sim$100 km s^{-1}. Although the variations are very large, their impacts are negligible because the interpretation of the profile is only based on line morphology and not line width or intensity (Section 4.2).

3.4. *He I λ10830 line profiles*

He I λ10830 line emissions are thought to have a composite origin, including contributions from wind, from the funnel flow, and from an accretion shock (Edwards et al. 2006). In this section, we focus on the properties of He I emission for each source. We discuss the implication of the profile morphology in Section 4.

We detect He I λ10830 features with absorption below the continuum in all of our targets. The detection rates of He I lines for Phase I, II, and III objects are 100 % (4/4), 100 % (5/5), and 100 % (4/4), respectively. In Table 7, we summarize the He I profile parameters that are obtained from residual profiles in Fig. 3, in the same manner as for Pβ profile parameters in Section 3.3. In column 2, we categorize He I residual spectra into morphology groups in Section 3.3.

The He I profiles for the targets are categorized into five groups, group IPC, group PC, group DP, group BR, and group A. The profiles of two sources (V892 Tau and RW Aur) are categorized into group IPC; both exhibit broad features with $|V_{\rm max}^{\rm blue}|$ and $|V_{\rm max}^{\rm red}|$ of $\gtrsim$250 km s^{-1}. The profiles of three of the sources (AB Aur, T Tau, and V773 Tau) are categorized into group PC; the profiles of AB Aur and T Tau exhibit broad features with $|V_{\rm max}^{\rm blue}|$ and $|V_{\rm max}^{\rm red}| \gtrsim 250$ km s^{-1}, while that of V773 Tau has relatively narrow features with $|V_{\rm max}^{\rm blue}|$ and $|V_{\rm max}^{\rm red}| \lesssim 250$ km s^{-1}. The profiles of three of the sources (IRAS 04101+3101, RY Tau, and UX Aur) are categorized into group DP; they exhibit broad features with $|V_{\rm max}^{\rm blue}|$ and $|V_{\rm max}^{\rm red}|$ of $\gtrsim$250 km s^{-1}. The profiles of all the four Phase III sources (HP Tau/G2, HD 283572, HBC 388, and V410 Tau) are considered to be group A; they demonstrate centered subcontinuum and exhibit narrow profiles with $|V_{\rm max}^{\rm blue}|$ and $|V_{\rm max}^{\rm red}|$ of $\lesssim$150 km s^{-1}. The profile of SU Aur is assigned to a new category, group BR; it exhibits redshifted and blueshifted subcontinuum absorption, which is relatively narrow feature with $|V_{\rm max}^{\rm blue}|$ and $|V_{\rm max}^{\rm red}| \lesssim 250$ km s^{-1}.

4. DISCUSSION

Our WINERED data present a variety of profile morphologies in Pβ and He I λ10830 lines. In this section, 13 sources observed in this study and the six sources observed in previous studies (among them five sources each for Pβ and He I; Folha & Emerson 2001, Edwards et al. 2006; see Section 2.1) are considered in combination for obtaining improved statistical accuracy. The statistics of the categorized line profile morphologies (Section 4.1) and the manner in which the profile morphology for each target provides an insight into magnetospheric accretion and inner winds (Section 4.2), and the possible progression of dominant processes thorough the disk evolutionary phases (Section 4.3) are discussed herein. The suggested progression is compared with previous studies (Section 4.4). The chromospheric activities in Phase III sources from He I profile morphologies are also evaluated (Section 4.5). Finally, the implications of the results are considered for the theories of mass flow processes (Section 4.6).

4.1. *Profile morphologies*

4.1.1. *Pβ line profile morphologies*

Among the six additional stars, Folha & Emerson (2001) presented the Pβ profiles for five of them (CW Tau, HP Tau, GM Aur, DR Tau, and DS Tau). The Pβ line profile morphologies for 18 intermediate-mass stars (the 13 targets observed in the present study and the five additional targets observed in previous studies) are considered in combination. Based on the classification scheme in Section 3.3, they are categorized into two groups: two (CW Tau and DR Tau) in group DP and three (HP Tau, GM Aur, and DS Tau) in group IPC (see Table 3).

The statistics of the Pβ line profile morphologies for 18 intermediate-mass stars for each evolutionary phase are summarized in Table 8. The Pβ line profiles for Phase I sources are categorized into three groups: four (V892 Tau, AB Aur, IRAS 04101+3103, and T Tau) in group

E; two (CW Tau and DR Tau) in group DP; and one (HP Tau) in group IPC. The Pβ line profiles for Phase II sources are categorized into three groups: three (RY Tau, SU Aur, and UX Tau) in group DP; three (RW Aur, GM Aur, and DS Tau) in group IPC; and one (V773 Tau) in group F. Finally, the Pβ line profiles of all of the Phase III sources are categorized into group F. The statistics of Phase III are clearly different from those of Phase I and II, while those of Phase I and Phase II do not appear to differ significantly, except for the fact that a large fraction of Phase I sources but none of the Phase II sources are present in group E. Edwards et al. (2006) reported the Pγ profiles for five sources (CW Tau, GM Aur, DR Tau, DS Tau, and HN Tau) among the six additional sources noted in Section 2.1. The trends observed in this profiles are similar to those in the Pβ profiles although the Pγ profile features are sometimes weaker than the Pβ features (Section 3.1): of the Phase I sources, among which two are in group E and one is in group IPC, and of the Phase II sources, among which one is in group F and one is in group IPC. However, it should be noted that the profile types are not necessarily the same for each source between Pβ profiles presented by Folha & Emerson (2001) and Pγ profiles presented by Edwards et al. 2006. Considering that the spectra of Pγ and Pβ show similar features across various targets in the same observation period (see Section 3.1), the differences of the profile types can be attributed to the differences in the observation period; this will be further discussed in Section 4.3.

We compared Pβ profile morphologies for intermediate-mass stars and those from previous Paschen line spectroscopic observations of YSOs with high spectral resolution (Folha & Emerson 2001; Edwards et al. 2006). These studies' targets were primarily low-mass[3] T Tauri stars. Folha & Emerson (2001) presented Pβ line profiles for 49 T Tauri stars (44 CTTSs, four WTTSs, and one variable star between CTTS and WTTS). Among them, 45 sources (41 CTTSs, three WTTSs, and one variable star between CTTS and WTTS) with sufficient S/Ns are counted later in this paper[4]. Edwards et al. (2006) presented Pγ line profiles for 48 T Tauri stars (39 CTTSs, 6 WTTSs, and three Class I sources). Although the observations by Edwards et al. (2006) were not for Pβ, the Pγ morphology of the profile is known to be reminiscent of the Pβ profile (Edwards et al. 2006). Folha & Emerson (2001) detected Pβ emission in 38 of 41 CTTSs in their sample, while Edwards et al. (2006) detected Pγ emission in 38 of 39 CTTSs in their sample. For profiles of low-mass stars from previous studies, redshifted absorption features are common, while none shows blueshifted absorption features. This is the case with obtained profiles for intermediate-mass stars in our sample. For comparison, we show the statistics of profile morphology of Paschen lines for CTTSs by Folha & Emerson (2001) and Edwards et al. (2006) in Table 8. For both samples, the occurrence rate of group E is highest ($\sim$50 to 70 %). This tendency is similar to that for Phase I sources in the intermediate-mass star sample. Considering that CTTSs are comparable to Phase I (Section 2.1), this tendency seems to be a natural consequence. The occurrence rate of group IPC sources is the second highest for CTTSs in previous studies conducted by Folha & Emerson (2001) and Edwards et al. (2006), $\sim$20 to 30 %. This is not inconsistent with those for Phase I and II sources in the intermediate-mass star sample. Meanwhile, group DP sources are very rare in CTTSs ($\lesssim$10 %), as suggested by Folha & Emerson (2001), while occurrence rate is relatively high for Phase I and II sources in the intermediate-mass star sample ($\sim$30–40 %). This may be characteristics for intermediate-mass stars. However, the statistics of CTTSs do not appear to differ significantly from those of Phase I and II sources in the intermediate-mass star sample. Lastly, we also show the statistics of profile morphology of Paschen lines for WTTSs, which are comparable to low-mass stars in Phase III, by Folha & Emerson (2001) (Pβ) and Edwards et al. (2006) (Pγ) in Table 8. Paschen lines are undetected in almost all WTTSs, both in Folha & Emerson (2001) and in Edwards et al. (2006), prompting a classification in group F. This result is consistent with those for our target intermediate-mass stars in Phase III.

4.1.2. *He I line profile morphologies*

Among the six additional stars, Edwards et al. (2006) reported the He I profiles for five of them (CW Tau, GM Aur, DR Tau, DS Tau, and HN Tau). In this section, the He I line profile morphologies for 18 intermediate-mass stars (the 13 targets observed in the present study and the five additional targets observed in previous studies are considered. The sources are categorized into four groups based on the classification scheme in Section 3.3: two (CW Tau and HN Tau) are assigned to group DP, one (GM Aur) is assigned to group F, one (DR Tau) is

[3] Some of the targets by Folha & Emerson (2001) and Edwards et al. (2006) are the same as ours: V773 Tau, RY Tau, T Tau, SU Aur, and RW Aur in Folha & Emerson (2001); SU Aur, RW Aur, and UX Tau in Edwards et al. (2006).

[4] Folha & Emerson (2001) pointed out that for some sources Pβ lines are too noisy to allow a reliable classification of their profiles: three CTTSs (DQ Tau, FX Tau and GH Tau), and one WTTS (DI Tau).

assigned to group PC, and one (DS Tau) is assigned to group BR (see Table 3).

The statistics of the He I line profile morphologies for the 18 intermediate-mass stars for each evolutionary phase are shown in Table 9. The line profiles of Phase I sources are categorized into three groups: three (AB Aur, T Tau, and DR Tau) are categorized into group PC, three (IRAS 04101+3103, CW Tau, and HN Tau) are in group DP, and one (V892 Tau) is in group IPC. The Phase II sources are categorized into five groups: two (RY Tau and UX Tau) in group DP, two (SU Aur and DS Tau) in group BR, one (RW Aur) in group IPC, one (V773 Tau) in group PC, and one (GM Aur) in group F. Finally, all the Phase III sources are categorized into group A. Based on these statistics, the He I profiles of the sources in Phase I and II are similar to each other but the profiles of the Phase III sources are clearly different (all in group A) from those in the remaining phases. However, in terms of broadness of spectral features, there seem to be clear differences between Phase I and II sources: all four Phase I sources show broad features with $|V_{\rm max}^{\rm blue}|$ or $|V_{\rm max}^{\rm red}|$ of $\gtrsim$250 km s^{-1}, while some Phase II sources (SU Aur and V773 Tau) show narrow features with $|V_{\rm max}^{\rm blue}|$ or $|V_{\rm max}^{\rm red}|$ of $\lesssim$250 km s^{-1}.

We compare He I λ10830 profile morphologies for intermediate-mass stars with those from previous He I spectroscopic observations of YSOs with high spectral resolution. For these comparisons, we reference Oudmaijer et al. (2011) and Cauley & Johns-Krull (2014) for HAeBes (corresponding to intermediate-mass stars in Phase I) and Edwards et al. (2006) mainly for low-mass T Tauri stars. As for intermediate-mass stars, Oudmaijer et al. (2011) detected He I features in 79 out of 90 of their sample HAeBes. Although all of their spectra are not shown in their paper, the partially shown observed spectra (not residual profiles) show group PC, IPC, or DP profiles. Cauley & Johns-Krull (2014) observed 56 HAeBes, 28 HAe stars and 28 HBe stars. For HAe stars, whose mass range is roughly comparable to that of our targets in this paper, they detected He I features in 26 stars. We summarize statistics of profile morphology for their targets in Table 9 based on their Fig. 4. As a result, the occurrence frequencies of groups PC and IPC are relatively higher compared to those of the other types. The statistics of HAe stars are not inconsistent with those of Phase I and Phase II sources in the intermediate-mass star sample in this study. Cauley & Johns-Krull (2014) pointed out that narrow blueshifted absorption features are not seen in HAe stars in their sample while broad blueshifted absorption features are common. This tendency is also seen in our Phase I sources. Considering that narrow blueshifted absorption features are seen only in some Phase II objects in the sample of intermediate-mass stars (RY Tau, SU Aur, V773 Tau, and DS Tau), these features may be characteristics for Phase II objects.

As for low-mass stars, Edwards et al. (2006) detected He I features in 38 of 39 CTTSs in their sample. We show the statistics of He I profile morphology for low-mass stars from Edwards et al. (2006) in Table 9. CTTSs are categorized into almost all profile types. The occurrence frequency of group PC is highest, while that of group BR is second highest. Group PC sources are observed among both Phase I and II sources in the intermediate-mass star sample, but group BR sources are only observed among Phase II sources. However, the statistics of CTTSs do not appear to differ significantly from those of Phase I and II sources in the intermediate-mass star sample. Edwards et al. (2006) suggested that broad P Cygni-like profiles are more common among stars of high veilings ($\gamma_Y \geq 0.5$), while narrow emission coupled with both blueshifted and redshifted absorption is more common among stars with low veilings ($\gamma_Y \leq 0.2$). This tendency aligns with the results of the intermediate-mass samples for He I profiles: group PC sources are more common in Phase I, while some sources with narrow emission and redshifted and blueshifted absorption features are seen only in Phase II. On the contrary, we also show the statistics of He I profile morphology for WTTSs by Edwards et al. (2006), which are comparable to low-mass stars in Phase III, in Table 9. The highest occurrence frequency belongs to group F (featureless) for four sources, and the second highest is group E (pure emission) for two sources. This result is not consistent with those for our target intermediate-mass stars in Phase III, which will be discussed later (Section 4.2.3).

4.2. *Interpretation of Pβ and He I line profile morphologies*

Paschen lines exhibit a centered emission peak and a redshifted absorption that can be used as diagnostics for magnetospheric accretion, while He I profiles show both blueshifted and redshifted absorptions that can be used as diagnostics for magnetospheric accretion flows and inner winds, respectively (Hartmann et al. 2016). We largely based our interpretations on profile morphology of Pβ and He I line profile rather than line width or intensity.

4.2.1. *Magnetospheric accretion*

Both Pβ and He I line profiles show redshifted absorptions that can be used as diagnostics for magnetospheric accretion (e.g., Folha & Emerson 2001, Edwards

et al. 2006, Fischer et al. 2008, Kurosawa et al. 2011). First, we diagnose the sources in which sources magnetospheric accretions are functioning using the Pβ line profiles. The line profiles for RW Aur, HP Tau, GM Aur, and DS Tau show redshifted subcontinuum features, displaying a clear magnetospheric accretion signature. For nine sources (V892 Tau, AB Aur, IRAS 04101+3103, T Tau, RY Tau, SU Aur, UX Tau, CW Tau, and DR Tau), the observed line profiles show emission features but do not show redshifted subcontinuum features. Among them, four sources (V892 Tau, AB Aur, IRAS 04101+3103, and T Tau) are categorized into group E (pure emission), whereas five sources (RY Tau, SU Aur, UX Tau, CW Tau, and DR Tau) are categorized into group DP (double-peaked emission). Considering the sources in group E have $|V_{\rm max}^{\rm blue}| > |V_{\rm max}^{\rm red}|$ and that the sources in group DP, except for CW Tau, have $V_{\rm peak}^{\rm em} < 0$, they show slight influence from redward absorption features, suggesting that magnetospheric accretion activities are functioning. The model Brγ line profiles[5] for sources with magnetospheric accretion calculated by Muzerolle et al. (1998a) also show a redward absorption feature (not subcontinuum features) at inclination angles of $\lesssim$60° (see their Fig. 5). Therefore, the Pβ observed line profiles suggest that magnetospheric accretion processes are functioning in the eight sources that exhibit emission features but not redshifted subcontinuum features, except for CW Tau, in addition to four sources that do exhibit redshifted subcontinuum features.

He I can also be used as diagnostics for magnetospheric accretion. The observed line profiles for five sources (V892 Tau, SU Aur, RW Aur, UX Tau, and DS Tau) show redshifted subcontinuum features, displaying a clear magnetospheric accretion signature. For the other sources in Phase I and II, except for GM Aur, the line profiles show He I emissions but do not show the redshifted subcontinuum features. This seems to suggest that the activities of magnetospheric accretion are not functioning. However, Kurosawa et al. (2011) indicated that wind-related He I emissions are relatively minor, whereas the magnetosphere is a main emission contributor (see Fig. 12 in Kurosawa et al. 2011). The line profiles for three sources (RY Tau, CW Tau, and HN Tau), which are categorized into group DP, also show redward absorption features, judging from $V_{\rm peak}^{\rm em} < 0$, suggesting magnetospheric accretion activities. Therefore, He I profiles for all Phase I and II sources, except for GM Aur, suggest magnetospheric activities.

[5] Brγ line profiles are known to show very similar features to Pβ line profiles (Folha & Emerson 2001).

In summary, all Phase I and II sources suggest magnetospheric activities from the observed line profiles of Pβ and He I although the profile for approximately half of them (V892 Tau, SU Aur, RW Aur, UX Tau, HP Tau, GM Aur, and DS Tau) show redshifted subcontinuum features in Pβ and/or He I lines, which are clear magnetospheric accretion signatures.

4.2.2. *Inner winds*

He I profiles show both blueshifted and redshifted absorptions that can be used as diagnostics for magnetospheric accretion flows and inner winds, respectively (Hartmann et al. 2016). Kwan et al. (2007) modeled blueshifted absorption at He I λ10830 in CTTS via scattering of the stellar and veiling continua as a probe of inner winds, while Kurosawa et al. (2011) presented multidimensional non-local thermodynamic equilibrium radiative transfer models of hydrogen and helium line profiles formed in the magnetospherical accretion and inner winds of CTTSs, including He I λ10830 and Pβ. Both models are consistent with the scenario in which the narrow blueshifted absorption component of He I λ10830 seen in observations is caused by a disk wind, and the wider blueshifted absorption component (the terminal velocity of the wind up to 400 km s^{-1}) is caused by stellar wind.

In the sample of intermediate-mass stars, the line profiles for seven sources (AB Aur, RY Tau, SU Aur, T Tau, V773 Tau, DR Tau, and DS Tau) have blueshifted subcontinuum absorption features. Among them, the line profiles for AB Aur, T Tau, and DR Tau are categorized into group PC with broad blueshifted subcontinuum absorption ($V_{\rm max}^{\rm blue} \sim -300$–$-400$ km s^{-1}). They are consistent with the stellar wind case. The line profiles for RY Tau, SU Aur, V773 Tau, and DS Tau show narrow blueshifted subcontinuum absorption features, with terminal wind volocities of $\lesssim$150 km s^{-1}. They are consistent with the disk wind case. The stellar wind is suggested to be functioning in AB Aur, T Tau, and DR Tau, whereas the disk wind is suggested to be functioning in RY Tau, SU Aur, V773 Tau, and DS Tau.

4.2.3. *Phase III sources*

The observed Pβ profiles show group F features (featureless), while the observed He I profiles for all Phase III sources show group A features (pure absorption) with centered subcontinuum absorption. These features are not expected in model profiles in the case of disk wind, or stellar wind (e.g., Kurosawa et al. 2011). This suggests that these sources have no such activities. Moreover, because absorption features in He I are broader for sources with larger $v_{\rm broad}$, the lines are more likely to be stellar intrinsic features than circumstellar features.

4.3. *Progression of dominant processes with evolution of protoplanetary disks*

In Section 4.2, observed Pβ and He I profiles for each source were interpreted. In Phase I, three sources (AB Aur, T Tau, and DR Tau) show features of stellar wind, while the other four sources (V892 Tau, IRAS 04101+3103, CW Tau, and HN Tau) show no features of inner winds. For magnetospheric accretion, only V892 Tau and HP Tau show clear features, while the other sources show features suggesting the activity. In Phase II, four sources (RY Tau, SU Aur, V773 Tau, and DS Tau) show features of disk wind, while the other three sources (RW Aur, UX Tau, and GM Aur) show no features of inner winds. For magnetospheric accretion, five sources (SU Aur, RW Aur, UX Tau, GM Aur, and DS Tau) show clear features, while the other two sources show the feature suggesting the activities. In Phase III, no targets show activities of mass accretion, disk winds, or stellar winds. This suggests that dominant processes in different evolutionary phases are different, particularly for inner winds. This finding indicates a progression of dominant mass flow processes with disk evolution: stellar wind and probably magnetospheric accretion in Phase I, magnetospheric accretion and disk wind in Phase II, and no activities in Phase III. In particular, progression is observed for inner winds. The statistics of the blueshifted absorption types for He I lines, broad or narrow, which are used for diagnostics of dominant inner winds, are summarized in Table 9.

However, some points still need to be considered. i) YSOs tend to be variable, which can make line profiles differ among observation periods (Bouvier et al. 2003). Previous studies suggest that the general features of the observed line profiles do not change between periods although the lines can show $\sim$10 % variabilities (e.g., Kurosawa et al. 2005, Edwards et al. 2006). However, the times between observations were not very long (a year at longest in the study conducted by Edwards et al. (2006)). On the contrary, the Pβ line profile morphologies reported by Folha & Emerson (2001) and the Pγ line profile morphologies reported by Edwards et al. (2006) for the same sources show clear difference (e.g., those of CW Tau and DR Tau; see Table 3). Considering that the Pγ morphology of the profile is known to be reminiscent of the Pβ profile (Edwards et al. 2006, see also Section 3.1), the line profiles can vary by approximately seven rears, reported for the Paschen series, which has a long time separation (1994–1995 by Folha & Emerson 2001 and 2001–2002 by Edwards et al. 2006). Therefore, continuous observation of He I is necessary in the future. ii) The targets in this study are limited to only 19 sources. 11 sources are excluded due to limited instrumental sensitivities but they satisfy other conditions for selecting the target intermediate-mass stars (Section 2.1). A large fraction of the excluded sources are of the latest spectral type, K5, according to the criteria for selecting the intermediate-mass stars. Because each spectral type corresponds to a certain range of star masses and ages, the sources should have marginal masses between low mass and intermediate mass (Yasui et al. 2014). Thus, the exclusion may not be necessarily bad to avoid contaminating the sample of low-mass stars. However, because the excluded sources may alter the statistics, more observations are necessary in the future. To investigate the universality of the suggested progression, YSOs of a wide variety of ages and masses should be observed. iii) The spectral types of Phase I targets appear earlier (three A- or B- type and five K- type stars) than those of Phase II and III targets (G–K type stars). This bias may impact observed profiles, influencing our interpretation of dominant activities in each source and phase. However, such tendencies are not necessarily true for all intermediate-mass sources observed in this study, e.g., the later spectral type of T Tau (K0) than those of HP Tau/G2 (G0), RY Tau (G1), SU Aur (G1), and HD 283572 (G5). Also, such tendencies are not seen in the six intermediate-mass stars in the samples of Folha & Emerson (2001) and Edwards et al. (2006) (see Section 2.1). Therefore, the differences in spectral type should not generate a systematic bias. iv) From Tables 2 and 5, Phase I sources appear to have larger mass accretion rates. We plotted Pβ and He I equivalent widths vs. mass accretion rate for our intermediate-mass targets with measured mass accretion rate in Fig. 4. Sources of Phase I and II are indicated in red and blue, respectively. Pβ emission equivalent width are shown in the left panel. The figure suggests that Pβ emission equivalent widths are moderately correlated with mass accretion rate ($p = 0.66$), as suggested in Folha & Emerson (2001), and that Phase I sources seem to have larger mass accretion. This may suggest that mass accretion rate determines dominant activities of inner winds. However, such tendencies are not necessarily true for all sources, e.g., T Tau (Phase I) has a smaller mass accretion rate than that of RY Tau (Phase II) for the targets observed in the present study, and the mass accretion rates of HP Tau and DS Tau (Phase I) are smaller or comparable to those for Phase II sources. This is also discussed in Section 4.4 in the context of previous studies (e.g., Edwards et al. 2006). For reference, we also plotted the sum of absolute values of emission and absorption of He I equivalent widths, which is introduced by Edwards et al. (2006), vs. mass accretion rate (Fig. 4, right panel). This shows that the equivalent val-

ues of He I are also correlated with mass accretion rate ($p = 0.75$), which Edwards et al. (2006) specified using their sample CTTSs. v) Finally, the weakening of stellar wind signatures and strengthening of disk wind signatures in Phase II may be due solely to an overall weakening in stellar wind activities through disk evolution. Kwan et al. (2007) indicated that excitation conditions for He I λ10830 are more favorable in stellar wind than in disk wind. In any case, the suggested progression does not change significantly: stellar winds (and possibly disk winds as well) are active at first, and then disk winds become relatively active. However, further quantitative approaches using the fitting of observed profiles with model profiles are necessary in future work.

4.4. *Comparison of suggested progression of dominant processes with previous studies*

Although we could not find previous results for high-resolution spectroscopy of young intermediate-mass stars with both He I and Pβ, the He I profiles for HAeBes are presented in Cauley & Johns-Krull (2014). For HAe stars, whose mass range is roughly comparable to that of our targets, the statistics of their Pβ and He I line profile morphologies are not significantly different from those of Phase I and II sources, as discussed in Section 4.1. Cauley & Johns-Krull (2014) pointed out that in HAe stars, disk winds (evidenced by narrow blueshifted absorption features) are not functioning, while stellar winds (evidenced by commonly broad blueshifted absorption features) are functioning. A summary of the statistics of the He I blueshifted subcontinuum absorption features for the HAe stars is presented in Table 9. These results are consistent with our results for Phase I sources. Admittedly, our data set has a small sample size (seven Phase I sources). But the agreement between the results of their large sample (28 HAe stars) and those of our smaller sample reinforces the suggestion that dominant processes for Phase I are stellar wind and probably magnetospheric accretion.

Previous authors have posited alternative mechanisms for the progression of dominant processes. Edwards et al. (2006) mainly focused on veilings as an indicator of disk evolutionary phases, since veilings are suggested to be correlated with mass accretion rate. Kwan et al. (2007) used a comparison of their theoretical line profiles with observed profiles from Edwards et al. (2006). They identified 11 and 15 CTTSs having blueshifted absorption features that resemble the disk wind models and stellar wind models, respectively. A summary of the statistics of the He I absorption features for CTTSs is presented in Table 9. Edwards et al. (2006) suggested that stars with high disk accretion rates are more likely to have stellar wind signatures than disk wind signatures. However, note that CTTSs in all veiling groups show morphological features of group PC, with broad with broad redshifted absorption suggesting stellar wind, even with the lowest observed veiling, $\gamma_Y \leq 0.2$. In addition, all groups show profiles with narrow absorption features suggesting disk wind, even with the highest observed veiling, $\gamma_Y \geq 0.5$ (see Fig. 10 in Edwards et al. 2006). This set of observations suggests that the trend is not so significant. We find this unsurprising, since the veiling, and thus the mass accretion rate, will not necessarily be a clear indicator of disk evolution as discussed in Section 2.1. As a result, a clear progression of profile morphologies with veilings is not observed.

4.5. *Chromospheric activities in Phase III sources*

In Section 4.2.3, Phase III sources were suggested to show no activities for mass accretion or inner winds. This is consistent with WTTSs reported in Edwards et al. (2006). WTTSs are known to exhibit high levels of chromospheric and coronal features (Stelzer et al. 2013), which persist at the age of $\sim$50 to 100 Myr (Stauffer et al. 1994). The chromospheric profile has often been observed as emission lines in X-ray and optical lines such as Hα, Hβ, Ca II, and Na I lines. Chromospheric activities are also recognized from He I λ10830 absorption lines (e.g., Vaughan & Zirin 1968), and are suggested to persist for star ages as advanced as those of Pop II stars (Takeda & Takada-Hidai 2011). We suggest that He I absorption features detected here are most likely to be chromospheric features, considering that Phase III sources are almost comparable to WTTSs (Yasui et al. 2014) and that the observed He I features in this paper are suggested to be stellar intrinsic features (see Section 4.2.3). Note that the centered subcontinuum absorption features are not necessarily indicative of the chromospheric activities. When the features are accompanied by emissions, the profiles are categorized into group DP (e.g., IRAS 04101+3103). Cauley & Johns-Krull (2014) suggested that the profiles are most likely to be formed because of Keplerian rotation very close to the stellar surface. Also, it should be noted that the photospheric features have little impact on the He I residual profiles. Fig. 5 shows synthetic spectra, observed spectra, and residual profiles for all four Phase III sources. Three photospheric features are observed in the spectral region, Mg I λ10814.1 and Si I (λ10830.1 and λ10846.8); among them, only Si I λ10830.1 profiles appear to cover He I profile. However, the line is very shallow for HP Tau/G2, HD 283572, and V410 Tau due to the large $v_{\rm broad}$, $\sim$100 km s^{-1}, while the line barely covers the He I

profile for HBC 388 due to the small $v_{\rm broad}$, 25 km s^{-1}. Fig. 5 suggests that the photospheric features are moderately removed by subtracting synthetic spectra from observed spectra (Section 3.2).

The He I line is a transition between lower metastable level of 2^3S and the upper level of 2^3P. Two mechanism have been proposed for populating the upper levels of He I: photoionization-recombination (PR) mechanism via EUV and X-ray radiations (Goldberg 1939) and electron collisions from the ground level (Andretta & Jones 1997). The existence or nonexistence of correlation between He I absorption and X-ray luminosity can discern which process is dominant (Zarro & Zirin 1986); the correlation exists when PR mechanism is dominant, while the correlation is absent when collisional excitation is dominant. We show fractional X-ray luminosities ($L_{\rm X}/L_{\rm bol}$) vs. He I absorption equivalent widths (EWs) for all Phase III sources in Fig. 6. EWs are obtained from Table 7, whereas $L_{\rm X}/L_{\rm bol}$ is obtained from previous studies (Güdel et al. 2007, Wichmann et al. 1996). All Phase III sources have $L_{\rm X}/L_{\rm bol}$ in the very small range of -3.4–-3.5, whereas EWs span within $\sim$0.5–1.5. For comparison, we also show the results from Zarro & Zirin (1986) in Fig. 6, who presented the correlation in dwarfs and giants. Thus, EW and $L_{\rm X}/L_{\rm bol}$ are not correlated in Phase III sources, suggesting that the dominant mechanism for these sources is electron collisions rather than PR mechanism. Phase I and II sources are plotted in Fig. 6 for reference although we could not find any literature references for the value of IRAS 04101+3103.

The He I absorption features associated with chromospheric activities had not been previously reported for YSOs, to our knowledge. In Edwards et al. (2006), no WTTSs show He I absorption features although He I line profiles for two WTTSs show emission features (see Section 3.4) and these authors surmised that these features arise in active chromosphere or very weak accretion. We suggest that the features detected even in such young phases are characteristics of intermediate-mass stars, considering that these authors' targets were primarily low-mass stars and that all of our intermediate-mass star targets in Phase III show the He I absorption features. This pattern may be due solely to a positive correlation between stellar mass and X-ray luminosities (Güdel et al. 2007), which can be correlated with chromospheric activities. We show $L_{\rm X}/L_{\rm bol}$ values of the WTTSs in Edwards et al. (2006) in Fig. 6 (gray squares). The $L_{\rm X}/L_{\rm bol}$ values for the WTTSs (-3.4–-2.9; Güdel et al. 2007, Bertout et al. 2007, Yang et al. 2012, Kastner et al. 2016, Kastner et al. 2004), which are comparable to those of our Phase III sources. Therefore, the reason for the detection of He I chromospheric absorption features only in our intermediate-mass targets in Phase III is not likely the correlation between stellar mass and X-ray luminosities.

Correlations of chromospheric and higher-temperature features with stellar age, magnetic field, and rotation period properties have been previously reported (Linsky 2017). For the first factor, the He I absorption features are not seen in the sample WTTSs of Edwards et al. (2006), which are also the sources in the same star forming-region as our targets, i.e., the Taurus star-forming region. Therefore, the stellar age does not seem to be the cause for the He I detection in Phase III sources. For the second factor, although there are only limited number of derivation of magnetic fields, there seem to be no significant differences between those for our Phase III sources and WTTSs reported in Edwards et al. (2006): $\sim$0.5–1.5 kG for HBC 388 and V410 Tau (Basri et al. 1992, Skelly et al. 2010), $\sim$0.5–2 kG for LkCa 4, V891 Tau, and V827 Tau (Donati et al. 2014, Donati et al. 2015, Giardino et al. 2006). Therefore, the magnetic field may not likely to be the cause for the He I detection in Phase III sources. For the last factor, i.e., rotation, Phase III sources generally have large $v \sin i$, $\sim$100 km s^{-1} (Table 5), while WTTSs in the sample of Edwards et al. (2006) generally have small $v \sin i$ values, $<$20 km s^{-1} (Rebull et al. 2004). Most theoretical models of stellar magnetic dynamos predict increasing magnetic flux emerging through stellar photospheres with larger rotation velocities (Linsky 2017). This suggests that the larger rotation velocities may be the possible cause for the detection of He I absorptions in Phase III sources.

4.6. *Implication to theories of mass flow processes*

Although configurations of mass flow processes around central stars have been proposed, we do not yet have a conclusive theory explaining angular momentum transport in the star formation process. From the suggested progression of dominant mass flow processes with evolution of protoplanetary disks in Section 4.3, we discuss what factors determine which processes dominate, or in which physical conditions one dominates the other. These connections may help put useful constraints on current theories.

Before launching into this discussion, it is necessary to pay attention to whether intermediate-mass stars can be regarded as simply massive T Tauri stars. Cauley & Johns-Krull (2014) presented high-resolution He I observations of HAeBes, which correspond to intermediate-mass stars in Phase I. They suggested that HAe stars, whose mass range is roughly comparable to that of our

targets, cannot be regarded as massive CTTSs because they do not show signatures of magnetospheric accretion and inner winds in the same manner as CTTSs: HAe stars show signatures of magnetospheric accretion and stellar winds but do not show signatures of disk winds[6]. They pointed out the possibility that the magnetospheres might be smaller, based on the paucity of detected magnetic fields for HAeBes, compared to CTTSs. They confirmed small magnetospheres from their results that maximum absorption velocities in the redshifted absorption profiles in their sample are a smaller fraction of the system escape velocity than in CTTSs. They suggested that the small magnetospheres may be less efficient at driving disk winds compared to CTTS magnetospheres. The similar trends are also suggested for CTTSs by Kwan et al. (2007): stars with the highest disk accretion rates are less likely to have redshifted absorption from magnetospheric funnel flows. They suggested that their disks have small magnetospheres, which may set up favorable conditions for stellar wind rather than disk wind. The maximum redshifted absorption velocities in all obtained He I line profiles of both Phase I and II sources in our intermediate-mass targets having redshifted absorption features are estimated to be as small as those of HAe stars, $\leq$400 km s^{-1}. Assuming stellar radii of our targets (stellar mass of $\gtrsim$1.5 $M_{\odot}$) based on the isochrone model at the age of 1.5 Myr by Siess et al. (2000), escape velocities of our targets are calculated to be $\gtrsim$500km s^{-1}. The fraction of the system escape velocity estimated with the above velocities (i.e., the maximum redshifted absorption velocities and escape velocities) for our targets is smaller than for CTTSs, corresponding to ballistic infall from distances of $<2\,R_{\odot}$ toward central stars. This is again consistent with that for HAe stars (see Fig. 5 in Cauley & Johns-Krull 2014). This suggests that magnetospheres of intermediate-mass stars are generally smaller than those of CTTSs. Nonetheless, signatures of disk winds are seen in Phase II sources although the same trends (signatures of stellar winds) as seen in HAe stars are seen in Phase I sources. This suggests that the lack of disk wind signatures in HAe stars is not a characteristic for intermediate-mass stars, but only for HAe stars, or Phase I sources. Further, there should be another factor that functions more effectively than magnetosphere size for determining dominant mass flow processes.

The inner part of a protoplanetary disk in Phase II has low opacity and is where most dust settling/growth is expected to be occurring. In contrast, the inner disk in Phase I has high opacity but without substantial dust settling/growth (Yasui et al. 2014). Due to the low opacity in Phase II, radiation from central stars can penetrate deeply into disks, and thus the ionization fraction should be higher. This may be the reason why disk winds are active in Phase II. This interpretation is consistent with the theory of disk wind in which a sufficient magnetic field and ionization fraction launch magneto-centrifugal winds over a significant range of radii in the disk, from an inner truncation radius out to several AU (Ouyed & Pudritz 1997). In addition, Phase III stars, having already lost their entire dust disks, show profiles with no signature of accretion or of inner winds. The absence of these signatures in Phase III, along with the presence of these signatures in Phase I and II, is consistent with the previous suggestion that inner winds (stellar winds and disk winds) are accretion-driven.

[6] Cauley & Johns-Krull (2014) suggested that HBe stars, in general, do not show signatures of magnetospheric accretion and disk winds, whereas show signatures of stellar winds.

5. CONCLUSION

We performed near-infrared high-resolution (R = 28,000) spectroscopy of 13 young intermediate-mass stars in the Taurus star-forming region with WINERED. Our obtained spectra (λ = 0.91–1.35 μm) depict He I λ10830 and Pβ lines that are sensitive to magnetospheric accretion and winds. We investigate five sources each for Pβ and He I lines from previous studies, in addition to the 13 targets observed in this study. Based on the presence of near- and mid-infrared continuum emission, young intermediate-mass stars can be classified into three different evolutionary stages: Phases I, II, and III in the order of evolution.

1. Phase I and II sources exhibit a variety of profile morphologies in Pβ, while all Phase III sources are in group F (i.e., they are featureless). The statistics of the Pβ profile morphologies for Phase I and Phase II sources are not significantly different except that almost half of Phase I sources show group E features, while none of Phase II sources exhibit the features. The statistics of Phase I and II sources are not inconsistent with those of low-mass CTTSs. Furthermore, the morphology statistics for Phase III sources are consistent with those of low-mass WTTSs.

2. Phase I and II sources also show variety of He I profile morphologies. The profile morphologies of Phase I and Phase II sources are mostly broad subcontinuum absorption lines and narrow subcontinuum absorption lines, respectively; however, the statistics of these profile morphologies are not significntly different and are comparable to those

of low-mass CTTSs. On the contrary, all Phase III sources are in group A (i.e., they exhibit pure absorption) with centered subcontinuum absorption features, inconsistent with the characteristics of low-mass WTTSs.

3. By comparing observed Pβ and He I line profiles with model profiles, dominant mass flow processes are suggested to be stellar wind and probably magnetospheric accretion in Phase I; magnetospheric accretion and disk wind in Phase II; and no activities in Phase III.

4. The different dominant processes in different phases indicate a clear progression of dominant mass flow processes with disk evolution. However, because this study may not contain a statistically significant number of sources, more statistical studies are necessary to draw a firm conclusion.

5. The mass flow processes in HAe stars are consistent with Phase I, with stellar wind as the dominant process. As for the progression of mass flow processes, the trends in veilings found by other authors do not seem so significant compared to that suggested in this paper based on disk evolutionary phase. Although the absence of activities in Phase III is consistent with previous studies for low-mass WTTSs, we note that He I line profiles do show chromospheric activities in these sources.

6. Disk wind signatures are seen in Phase II sources, despite their smaller magnetospheres, which was suggested to be the reason for the absence of the signature in HAe stars by other authors. Alternatively, we suggest that opacity in protoplanetary disks plays an important role in determining dominant mass flow processes.

We thank an anonymous referee for helpful comments that improved the manuscript. This work has made use of the VALD database, operated at Uppsala University, the Institute of Astronomy RAS in Moscow, and the University of Vienna.

REFERENCES

Akeson, R. L., Ciardi, D. R., van Belle, G. T., & Creech-Eakman, M. J. 2002, ApJ, 566, 1124

Alecian, E., Wade, G. A., Catala, C., et al. 2013, MNRAS, 429, 1001

Andretta, V., & Jones, H. P. 1997, ApJ, 489, 375

Andrews, S. M., & Williams, J. P. 2005, ApJ, 631, 1134

Andrews, S. M., Wilner, D. J., Espaillat, C., et al. 2011, ApJ, 732, 42

Ansdell, M., Williams, J. P., Manara, C. F., et al. 2017, AJ, 153, 240

Ardila, D. R., Basri, G., Walter, F. M., Valenti, J. A., & Johns-Krull, C. M. 2002, ApJ, 566, 1100

Barrado y Navascués, D., & Martín, E. L. 2003, AJ, 126, 2997

Basri, G., Marcy, G. W., & Valenti, J. A. 1992, ApJ, 390, 622

Beristain, G., Edwards, S., & Kwan, J. 2001, ApJ, 551, 1037

Bertout, C., & Genova, F. 2006, A&A, 460, 499

Bertout, C., Siess, L., & Cabrit, S. 2007, A&A, 473, L21

Bessell, M. S., & Brett, J. M. 1988, PASP, 100, 1134

Bodenheimer, P. 1995, ARA&A, 33, 199

Bouvier, J., Covino, E., Kovo, O., et al. 1995, A&A, 299, 89

Bouvier, J., Grankin, K. N., Alencar, S. H. P., et al. 2003, A&A, 409, 169

Calvet, N., & Hartmann, L. 1992, ApJ, 386, 239

Calvet, N., Muzerolle, J., Briceño, C., et al. 2004, AJ, 128, 1294

Cauley, P. W., & Johns-Krull, C. M. 2014, ApJ, 797, 112

Corder, S., Eisner, J., & Sargent, A. 2005, ApJL, 622, L133

Donati, J.-F., Hébrard, E., Hussain, G., et al. 2014, MNRAS, 444, 3220

Donati, J.-F., Hébrard, E., Hussain, G. A. J., et al. 2015, MNRAS, 453, 3706

Donati, J. F., Moutou, C., Malo, L., et al. 2016, Nature, 534, 662

Donehew, B., & Brittain, S. 2011, AJ, 141, 46

Dong, R., Najita, J. R., & Brittain, S. 2018, ApJ, 862, 103

Edwards, S., Fischer, W., Hillenbrand, L., & Kwan, J. 2006, ApJ, 646, 319

Espaillat, C., D'Alessio, P., Hernández, J., et al. 2010, ApJ, 717, 441

Fischer, W., Kwan, J., Edwards, S., & Hillenbrand, L. 2008, ApJ, 687, 1117-1144

Folha, D. F. M., & Emerson, J. P. 1999, A&A, 352, 517

Folha, D. F. M., & Emerson, J. P. 2001, A&A, 365, 90

Furlan, E., Hartmann, L., Calvet, N., et al. 2006, ApJS, 165, 568

Furlan, E., Luhman, K. L., Espaillat, C., et al. 2011, ApJS, 195, 3

Garcia Lopez, R., Natta, A., Testi, L., & Habart, E. 2006, A&A, 459, 837

Giardino, G., Favata, F., Silva, B., et al. 2006, A&A, 453, 241
Goldberg, L. 1939, ApJ, 89, 673
Grady, C. A., Woodgate, B., Bruhweiler, F. C., et al. 1999, ApJL, 523, L151
Gray, D. F. 2005, The Observation and Analysis of Stellar Photospheres, 3rd ed. (Cambridge: Cambridge Univ. Press)
Gray, R. O., Graham, P. W., & Hoyt, S. R. 2001, AJ, 121, 2159
Güdel, M., Briggs, K. R., Arzner, K., et al. 2007, A&A, 468, 353
Hamidouche, M. 2010, ApJ, 722, 204
Hartigan, P., Hartmann, L., Kenyon, S., Hewett, R., & Stauffer, J. 1989, ApJS, 70, 899
Hartmann, L. 2008, Physica Scripta Volume T, 130, 014012
Hartmann, L. 2009, Accretion Processes in Star Formation, 2nd edition, by Lee Hartmann. Cambridge, UK: Cambridge University Press, 2009. ISBN-13: 9780521531993,
Hartmann, L., Avrett, E., & Edwards, S. 1982, ApJ, 261, 279
Hartmann, L., Calvet, N., Gullbring, E., & D'Alessio, P. 1998, ApJ, 495, 385
Hartmann, L., Herczeg, G., & Calvet, N. 2016, ARA&A, 54, 135
Hartmann, L., Megeath, S. T., Allen, L., et al. 2005, ApJ, 629, 881
Hatzes, A. P. 1995, ApJ, 451, 784
Herbst, W. 1989, AJ, 98, 2268
Herbst, T. M., Robberto, M., & Beckwith, S. V. W. 1997, AJ, 114, 744
Hernández, J., Hartmann, L., Calvet, N., et al. 2008, ApJ, 686, 1195-1208
Ingleby, L., Calvet, N., Herczeg, G., et al. 2013, ApJ, 767, 112
Ikeda, Y., Kobayashi, N., Kondo, S., et al. 2016, Proc. SPIE, 9908, 99085Z
Ikeda, Y., Kobayashi, N., Kondo, S., et al. 2018, Society of Photo-Optical Instrumentation Engineers (SPIE) Conference Series, 10702, 107025U
Isella, A., Carpenter, J. M., & Sargent, A. I. 2010, ApJ, 714, 1746
Johns-Krull, C. M., & Gafford, A. D. 2002, ApJ, 573, 685
Joncour, I., Bertout, C., & Bouvier, J. 1994a, A&A, 291, L19
Joncour, I., Bertout, C., & Menard, F. 1994b, A&A, 285,
Kastner, J. H., Huenemoerder, D. P., Schulz, N. S., et al. 2004, ApJL, 605, L49
Kastner, J. H., Principe, D. A., Punzi, K., et al. 2016, AJ, 152, 3
Kennedy, G. M., & Kenyon, S. J. 2009, ApJ, 695, 1210
Kenyon, S. J., Gómez, M., & Whitney, B. A. 2008, Handbook of Star Forming Regions, Volume I, 4, 405
Kenyon, S. J., & Hartmann, L. 1995, ApJS, 101, 117
Kondo, S., Ikeda, Y., Kobayashi, N., et al. 2015, arXiv:1501.03403
Kurosawa, R., Harries, T. J., & Symington, N. H. 2005, MNRAS, 358, 671
Kurosawa, R., & Romanova, M. M. 2012, MNRAS, 426, 2901
Kurosawa, R., Romanova, M. M., & Harries, T. J. 2011, MNRAS, 416, 2623
Kurucz, R. 1993, Diatomic Molecular Data for Opacity Calculations. Kurucz CD-ROM No. 15. Cambridge, Mass.: Smithsonian Astrophysical Observatory, 1993., 15,
Kwan, J., Edwards, S., & Fischer, W. 2007, ApJ, 657, 897
Linsky, J. L. 2017, ARA&A, 55, 159
Liu, T., Zhang, H., Wu, Y., Qin, S.-L., & Miller, M. 2011, ApJ, 734, 22
Meléndez, J., & Barbuy, B. 1999, ApJS, 124, 527
Monnier, J. D., Tannirkulam, A., Tuthill, P. G., et al. 2008, ApJL, 681, L97
Mooley, K., Hillenbrand, L., Rebull, L., Padgett, D., & Knapp, G. 2013, ApJ, 771, 110
Mundt, R. 1984, ApJ, 280, 749
Muzerolle, J., Calvet, N., & Hartmann, L. 1998a, ApJ, 492, 743
Muzerolle, J., Calvet, N., & Hartmann, L. 2001, ApJ, 550, 944
Muzerolle, J., Calvet, N., Hartmann, L., & D'Alessio, P. 2003, ApJL, 597, L149
Muzerolle, J., D'Alessio, P., Calvet, N., & Hartmann, L. 2004, ApJ, 617, 406
Muzerolle, J., Hartmann, L., & Calvet, N. 1998b, AJ, 116, 2965
Oudmaijer, R. D., van den Ancker, M. E., Baines, D., et al. 2011, Astronomische Nachrichten, 332, 238
Ouyed, R., & Pudritz, R. E. 1997, ApJ, 482, 712
Rebull, L. M., Wolff, S. C., & Strom, S. E. 2004, AJ, 127, 1029
Reipurth, B., Pedrosa, A., & Lago, M. T. V. T. 1996, A&AS, 120, 229
Rice, J. B., & Strassmeier, K. G. 1996, A&A, 316, 164
Rieke, G. H., & Lebofsky, M. J. 1985, ApJ, 288, 618
Ryabchikova, T, Piskunov, N., Kurucz, R., et al. 2015, PhyS, 90, 054005
Sameshima, H., Matsunaga, N., & Kobayashi, N., et al. 2018, accepted to PASP

Sanz-Forcada, J., & Dupree, A. K. 2008, A&A, 488, 715
Shu, F., Najita, J., Ostriker, E., Wilkin, F., Ruden, S., & Lizano, S. 1994, ApJ, 429, 781
Siess, L., Dufour, E., & Forestini, M. 2000, A&A, 358, 593
Simon, M. N., Pascucci, I., Edwards, S., et al. 2016, ApJ, 831, 169
Skrutskie, M. F., Cutri, R. M., Stiening, R., et al. 2006, AJ, 131, 1163
Skelly, M. B., Donati, J.-F., Bouvier, J., et al. 2010, MNRAS, 403, 159
Stauffer, J. R., Caillault, J.-P., Gagne, M., Prosser, C. F., & Hartmann, L. W. 1994, ApJS, 91, 625
Stelzer, B., Frasca, A., Alcalá, J. M., et al. 2013, A&A, 558, A141
Strassmeier, K. G. 1994, A&A, 281, 395
Strassmeier, K. G., Bartus, J., Kovari, Z., Weber, M., & Washuettl, A. 1998, A&A, 336, 587
Takagi, Y., Itoh, Y., Oasa, Y., & Sugitani, K. 2011, PASJ, 63, 677
Takeda, Y. 1995, PASJ, 47, 287
Takeda, Y., & Kawanomoto, S. 2005, PASJ, 57, 45
Takeda, Y., Sato, B., & Murata, D. 2008, PASJ, 60, 781
Takeda, Y., & Takada-Hidai, M. 2011, PASJ, 63, 547
Tang, Y.-W., Guilloteau, S., Piétu, V., et al. 2012, A&A, 547, A84
Ustyugova, G. V., Koldoba, A. V., Romanova, M. M., Chechetkin, V. M., & Lovelace, R. V. E. 1995, ApJL, 439, L39
Vaughan, A. H., Jr., & Zirin, H. 1968, ApJ, 152, 123
Weaver, W. B. 1987, ApJL, 319, L89
White, R. J., & Ghez, A. M. 2001, ApJ, 556, 265
Wichmann, R., Krautter, J., Schmitt, J. H. M. M., et al. 1996, A&A, 312, 439
Williams, J. P., & Cieza, L. A. 2011, ARA&A, 49, 67
Winn, J. N., & Fabrycky, D. C. 2015, ARA&A, 53, 409
Wittkowski, M., Schöller, M., Hubrig, S., Posselt, B., & von der Lühe, O. 2002, Astronomische Nachrichten, 323, 241
Yang, H., Herczeg, G. J., Linsky, J. L., et al. 2012, ApJ, 744, 121
Yasui, C., Kobayashi, N., Tokunaga, A. T., & Saito, M. 2014, MNRAS, 442, 2543
Yasui, C., Kondo, S., Ikeda, Y., et al. 2008, Proc. SPIE, 7014, 701433
Yoshikawa, T., Ikeda, Y., Fujishiro, N., et al. 2012, Proc. SPIE, 8444, 84446G
Zarro, D. M., & Zirin, H. 1986, ApJ, 304, 365

Table 1. Target list and photometric data.

Object	R.A. (J2000.0)	Decl. (J2000.0)	SpT	J (mag)	H (mag)	K_S (mag)	$\alpha_{\rm MIR}$
(1)	(2)	(3)	(4)	(5)	(6)	(7)	(8)
V892 Tau	04:18:40.62	+28:19:15.5	B9	8.5	6.6	6.2	1.75
AB Aur	04:55:45.85	+30:33:04.3	A0	6.3*	5.5*	4.5*	−0.79
IRAS 04101+3103	04:13:20.02	+31:10:47.3	A1	9.2	8.7	8.1	0.97
HP Tau/G2	04:35:54.15	+22:54:13.6	G0	8.1	7.5	7.2	−0.43
RY Tau	04:21:57.41	+28:26:35.6	G1	7.2	6.1	5.4	−0.16
SU Aur	04:55:59.38	+30:34:01.5	G1	7.2	6.6	6.0	−0.32
HD 283572	04:21:58.84	+28:18:06.5	G5	7.4	7.0	6.9	−2.85
T Tau	04:21:59.43	+19:32:06.4	K0	7.2	6.2	5.3	−0.56
HBC 388	04:27:10.57	+17:50:42.6	K1	8.8	8.4	8.3	−2.78
RW Aur	05:07:49.57	+30:24:05.2	K3	8.4	7.6	7.0	−0.67
V773 Tau	04:14:12.92	+28:12:12.3	K3	7.5	6.6	6.2	−1.10
V410 Tau	04:18:31.11	+28:27:16.1	K3	8.4	7.8	7.6	−2.78
UX Tau	04:30:03.99	+18:13:49.4	K5	8.6	8.0	7.6	−1.99

Notes.
Col. (4) Spectral types from Furlan et al. (2006, 2011). Cols. (5)–(7) NIR magnitude from the 2MASS Point Source Catalog, J-band (Col. 5), H-band (Col. 6), and K_S-band magnitude (Col. 7). Magnitudes for AB Aur are obtained from a study reported by Kenyon & Hartmann (1995), shown with *. Col. (8) SED slope ($\alpha = d\ln\lambda F\lambda/d\ln\lambda$) with Spitzer IRS 6–13 μm presented in Furlan et al. (2006).

Table 2. Disk properties of target YSOs.

Object	Phase	SED	C/WTTS	i (deg.)	$\dot{M}$ ($10^{-8}\ M_\odot\ {\rm yr}^{-1}$)	$M_{\rm disk}$ ($M_\odot$)
(1)	(2)	(3)	(4)	(5)	(6)	(7)
V892 Tau	I	II	W	60 (Mo08), 59 (Ha10)	10.5 (DNB18), 7.2 (Liu11)	0.009
AB Aur	I	II	C	<45 (Gr99), 22 (Co05), 40 (Ta12)	14.1 (GNTH06), 1.8 (DB11), 39 (DNB18)	0.004
IRAS 04101+3103	I	II	C	...	...	...
HP Tau/G2	III	III	W	50 (We87), 67 (Bo95)	...	...
RY Tau	II	II	C	86 (Mu03), 66 (Is10)	6.4–9.2 (Ca04)	0.02
SU Aur	II	II	C	62 (Ak02), 86 (Mu03)	0.5–0.6 (Ca04)	0.0009
HD 283572	III	III	W	35 (St98), 48 (Wi02), 60 (JBB94)	...	<0.0004
T Tau	I	II	C	19 (HRB97), 20 (Ar02)	3.1–5.7 (Ca04), 3.2 (WG01)	0.008
HBC 388	III	III	W	45 (Ar02)	<0.9 (WG01)	<0.0003
RW Aur	II	II	C	40 (Ar02)	2.0 (In13)	0.004
V773 Tau	II	II	W	34 (Si16)	0.15 (Si16)	0.0005
V410 Tau	III	III	W	54 (Ha95), 70 (JBM94, St94, RS96), 80 (He89), 90 (Bo95)	<0.16 (WG01)	<0.0004
UX Tau	II	II	C	35 (An11)	1.1 (Es10)	0.005

Notes.
Col. (2) Phase of dust disk (Phase I/II/III) from Yasui et al. (2014) (see Section 2.1). Col. (3) SED classification type (Class I/II/III). Col. (4) Accretion-based classification type (CTTS or WTTS). Col. (5) Inclination angles. Note that the angles for Phase III sources are often estimated with stellar rotation periods and stellar rotational velocities, while those for Phase I and II sources are estimated from observations of their disks. Col. (6) Mass accretion rate. Col. (7) Dust disk masses derived by Andrews & Williams (2005).

References.
Mo08: Monnier et al. (2008), Ha10: Hamidouche (2010), DNB18: Dong et al. (2018), Liu11: Liu et al. 2011, Gr99: Grady et al. (1999), Co05: Corder et al. (2005), Ta12: Tang et al. (2012), GNTH06: Garcia Lopez et al. (2006), DB11: Donehew & Brittain (2011), We87: Weaver (1987), Bo95: Bouvier et al. (1995), Mu03: Muzerolle et al. (2003), Is10: Isella et al. (2010), Ca04: Calvet et al. (2004), Ak02: Akeson et al. (2002), St98: Strassmeier et al. (1998), Wi02: Wittkowski et al. (2002), JBB94: Joncour et al. (1994a), HRB97: Herbst et al. (1997), Ar02: Ardila et al. (2002), WG01: White & Ghez (2001), In13: Ingleby et al. (2013), Si16: Simon et al. (2016), Ha95: Hatzes (1995), JBM94: Joncour et al. (1994b), St94: Strassmeier (1994), RS96: Rice & Strassmeier (1996), He89: Herbst (1989), An11: Andrews et al. (2011), Es10: Espaillat et al. (2010).

Table 3. Intermediate-mass stars in the samples of previous studies (Folha & Emerson 2001; Edwards et al. 2006) and their properties.

Object	SpT	Phase	Pβ (Pγ)			He I		
			Data	Group	Abs. Type	Data	Group	Abs. Type
(1)	(2)	(3)	(4)	(5)	(6)	(7)	(8)	(9)
CW Tau	K3	I	✓(✓)	DP (E)	... (...)	✓	DP	...
HP Tau	K3	I	✓	IPC	r			
GM Aur	K3	II	✓(✓)	IPC (F)	r (...)	✓	F	...
DR Tau	K5	I	✓(✓)	DP (IPC)	... (r)	✓	PC	b
DS Tau	K5	II	✓(✓)	IPC (IPC)	r (r)	✓	BR	b, r
HN Tau	K5	I	(✓)	(E)	(...)	✓	DP	...

Notes.
Col. (2): Spectral types from Furlan et al. (2006, 2011). Col. (3): Phase of dust disk (Phase I/II/III) from Yasui et al. (2014) (see Section 2.1). Cols. (4)–(6): Properties of the Pβ line profiles with those of Pγ profiles (shown in parenthes). The tick marks in Col. 4 mean that the corresponding spectra are available in Folha & Emerson (2001) for Pβ and Edwards et al. (2006) for Pγ. Col. (5): Morphology groups based on the classification scheme in Section 3.3. Col. (6): Type of subcontinuum absorption (blue, red, or centered subcontinuum absorption, denoted by b, r, and c, respectively). Cols. (7)–(9): Properties of He I line profiles; the tick marks in Col. 7 indicate that the corresponding spectra are available in Edwards et al. (2006). Col. (8): Morphology groups based on the classification scheme in Section 3.3. Col. (9): Type of subcontinuum absorption (blue, red, or centered subcontinuum absorption, denoted by b, r, and c, respectively).

Table 4. Summary of WINERED Observations.

Object	Obs date (YYYY/MM/DD)	Airmass (sec z)	Exp time (s)	S/N[a]	Standard[b]
V892 Tau	2013/12/08	1.0–1.1	4800 (600 × 8)	58	HR 104 (A2Vs)
AB Aur	2013/02/22	1.2	1200 (300 × 4)	82	HIP53910 (A1V)
IRAS 04101+3103	2014/09/28	1.1–1.2	3000 (300 × 10)	59	HR 196 (A2Vs)
HP Tau/G2	2013/12/04	1.0	2400 (600 × 4)	54	HD 1041 (M1III)
RY Tau	2013/02/23	1.3–1.4	1200 (300 × 4)	43	HIP58001 (A0Ve+K2V)
	2013/02/23	1.5–1.8	1200 (300 × 4)		HIP23179 (A1V)
SU Aur	2013/03/03	1.8-2.5	1800 (300 × 6)	34	HIP76267 (A0V)
HD 283572	2013/11/30	1.0	2400 (600 × 4)	113	omi Aur (A2Vp)
T Tau	2013/12/02	1.2-1.3	7200 (1200 × 6)	94	HR 196 (A2Vs)
HBC 388	2014/10/15	1.2-1.3	2400 (600 × 4)	84	HR 922 (B9V)
RW Aur	2013/12/03	1.0	4800 (600 × 8)	55	HR1736 (A2V)
V773 Tau	2013/11/28	1.0-1.1	5400 (600 × 9)	74	50 Cas (A2V)
V410 Tau	2013/12/08	1.1–1.3	3600 (600 × 6)	33	HR 104 (A2Vs)
UX Tau	2013/12/12	1.3	7200 (600 × 12)	37	50 Cas (A2V)

Notes.
[a]The pixel-to-pixel S/N of the continuum level at $\lambda \sim 12700$ Å. For RY Tau, the value (43) is from combined spectra of all 8 frames.
[b]Standard stars used for telluric correction. The spectral type for each standard star is shown in parentheses.

Table 5. Obtained properties from the fit of the synthetic spectra.

Object	SpT	$v_{\rm broad}$ (km s^{-1})	RV (km s^{-1})	γ_Y	γ_J
(1)	(2)	(3)	(4)	(5)	(6)
V892 Tau	A0 (B9)	(100[a])	(16.0[b])	...	...
AB Aur	A0 (A0)	(116[c])	(24.7[c])	...	...
IRAS 04101+3103	A0 (A1)	(100)	(20)	...	...
HP Tau/G2	G0 (G0)	120	15.1	0.1	0.1
RY Tau	G0 (G1)	65	22.9	0.4	0.3
SU Aur	G0 (G1)	85	23.9	0.3	0.2
HD 283572	G5 (G5)	105	17.9	0.0	0.1
T Tau	K0 (K0)	35	21.8	0.9	0.5
HBC 388	K0 (K1)	25	15.7	0.0	0.0
RW Aur	K3 (K3)	35	13.5	1.0	0.2
V773 Tau	K3 (K3)	60	5.6	0.4	0.3
V410 Tau	K3 (K3)	130	26.2	0.0	0.0
UX Tau	K5 (K5)	25	12.5	0.6	1.0

Notes.
Col. (2) Spectral types of target objects used for synthetic spectra. Spectral types from the literature are shown in parentheses. Col. (3) Line broadening measured in velocity units. For V892 Tau and AB Aur, values from the literature are assumed, shown in parentheses. For IRAS 04101+3103, 100 km s^{-1} is assumed, shown in parenthesis (see more detail in the main text). Col. (4) Radial velocities. For V892 Tau and AB Aur, values from the literature are assumed. For IRAS 04101+3103, the average RV value for all targets, 20 km s^{-1}, is assumed (see more detail in the main text). Col. (5) Y-band veiling. Col. (6) J-band veiling.

References.
[a]Mooley et al. (2013), [b]Bertout & Genova (2006), [c]Alecian et al. (2013).

Table 6. Pβ profile parameters.

Object	Profile type	$V_{\rm max}^{\rm blue}$ (km s^{-1})	$V_{\rm max}^{\rm red}$ (km s^{-1})	$V_{\rm peak}^{\rm em}$ (km s^{-1})	$V_{\rm peak}^{\rm abs}$ (km s^{-1})	$F_{\rm peak}^{\rm em}$	$F_{\rm peak}^{\rm abs}$	Em. W_λ (Å)	Ab. W_λ (Å)	Ab. Type
(1)	(2)	(3)	(4)	(5)	(6)	(7)	(8)	(9)	(10)	(11)
V892 Tau	E	−350 (−250)	250 (200)	−20	...	2.01 (1.64)	...	8.93 (5.74)	...	...
AB Aur	E	−400 (−350)	400 (300)	−20	...	3.39 (2.69)	...	19.0 (13.1)	...	...
IRAS 04101+3103	E	−500 (−350)	400 (350)	5	...	1.98 (1.57)	...	12.2 (7.2)	...	...
HP Tau/G2	F	...	...	...	...	...	...	...	...	...
RY Tau	DP	−400	300	−100	...	1.27	...	4.00	...	...
SU Aur	DP	−300	250	−100	...	1.22	...	2.29	...	...
HD 283572	F	...	...	...	...	...	...	...	...	...
T Tau	E	−250	250	−15	...	2.56	...	9.15	...	...
HBC 388	F	...	...	...	...	...	...	...	...	...
RW Aur	IPC	−400	450	−50	305	1.99	0.96	10.36	0.20	r
V773 Tau	F	...	...	...	...	...	...	...	...	...
V410 Tau	F	...	...	...	...	...	...	...	...	...
UX Tau	DP	−250	250	−35	...	1.29	...	1.68	...	...

Notes.
Col. (2) Profile type based on classification scheme in Section 3.3 (see main text in the detail). Cols. (3) and (4): The maximum blueshifted and redshifted line velocities. For V892 Tau, AB Aur, and IRAS 04101+3103, estimated values assuming $\gamma_Y = \gamma_J = 0.0$ are shown, while those assuming $\gamma_Y = 2.0$, $\gamma_J = 2.0$ are shown in parentheses. Cols. (5) and (6): The velocity of peak emission and absorption. Cols. (7) and (8): The line fluxes relative to the continuum at the peak emission and absorption velocities. Cols. (9) and (10): Emission and absorption equivalent widths. Col. (11): The type of subcontinuum absorption: blue, red, or centered subcontinuum absorption are marked by the letter b, r, and c, respectively.

Table 7. He I Profile parameters.

Object	Profile type	$V_{\rm max}^{\rm blue}$ (km s^{-1})	$V_{\rm max}^{\rm red}$ (km s^{-1})	$V_{\rm peak}^{\rm em}$ (km s^{-1})	$V_{\rm peak}^{\rm abs}$ (km s^{-1})	$F_{\rm peak}^{\rm em}$	$F_{\rm peak}^{\rm abs}$	Em. W (Å)	Ab. W (Å)	Ab. Type
(1)	(2)	(3)	(4)	(5)	(6)	(7)	(8)	(9)	(10)	(11)
V892 Tau	IPC	−250	200	−155	80	1.19	0.88	0.18	0.09	r
AB Aur	PC	−400	400	45	−225	1.29	0.79	2.71	0.98	b
IRAS 04101+3103	DP	−450	350	−230	0	1.16	0.85	1.12	0.48	c
HP Tau/G2	A	−150	150	...	∼0	...	0.75	...	1.50	c
RY Tau	DP	−400	300	−155	−40	1.41	0.79	3.03	0.32	b
SU Aur	BR	−200	250	...	−95	...	0.47	...	2.32	b, r
HD 283572	A	−100	100	...	∼0	...	0.83	...	0.82	c
T Tau	PC	−300	400	−10	−185	2.31	0.13	7.47	3.98	b
HBC 388	A	−100	50	...	0	...	0.78	...	0.51	c
RW Aur	IPC	−400	350	−140	60	1.81	0.76	4.32	1.73	r
V773 Tau	PC	−100	250	30	−15	1.49	0.70	1.32	0.44	b
V410 Tau	A	−160	120	...	∼0	...	0.69	...	1.06	c
UX Tau	DP	−300	250	−85	50	1.71	0.74	3.69	0.33	r

Notes.
Col. (1): Object name. Col. (2): Profile type based on classification scheme in Section 3.3 (see main text in the detail). Cols. (3) and (4): The maximum blueshifted and redshifted line velocities. Cols. (5) and (6): the velocity of peak emission and absorption. Cols. (7) and (8): The line fluxes relative to the continuum at the peak emission and absorption velocities. Cols. (9) and (10): Emission and absorption equivalent widths. Col. (11): The type of subcontinuum absorption: blue, red, or centered subcontinuum absorption are marked by the letter b, r, and c, respectively.

Table 8. Statistics summary of Pβ features.

	E	DP	PC	IPC	A	F	BR	Reference
Intermediate-mass stars								
Phase I	57 % (4/7)	29 % (2/7)	0 % (0/7)	14 % (1/7)	0 % (0/7)	0 % (0/7)	0 % (0/7)	This study, FE01
Phase II	0 % (0/7)	43 % (3/7)	0 % (0/7)	43 % (3/7)	0 % (0/7)	14 % (1/7)	0 % (0/7)	This study, FE01
Phase III	0 % (0/4)	0 % (0/4)	0 % (0/4)	0 % (0/4)	0 % (0/4)	100 % (4/4)	0 % (0/4)	This study, FE01
Low-mass stars								
CTTS[a]	49 % (20/41)	12 % (5/41)	0 % (0/41)	32 % (13/41)	0 % (0/41)	7 % (3/41)	0 % (0/41)	FE01
WTTS	0 % (0/3)	0 % (0/3)	0 % (0/3)	0 % (0/3)	0 % (0/3)	100 % (3/3)	0 % (0/3)	FE01
CTTS (Pγ)[b]	69 % (27/39)	3 % (1/39)	0 % (0/39)	21 % (8/39)	0 % (0/39)	8 % (3/39)	0 % (0/39)	Ed06
WTTS (Pγ)[c]	17 % (1/6)	0 % (0/6)	0 % (0/6)	0 % (0/6)	0 % (0/6)	83 % (5/6)	0 % (0/6)	Ed06

Notes.
[a]The line profiles for 41 CTTSs in a sample of Folha & Emerson (2001) with sufficient S/Ns were used (see main text in detail).
[b]The Pβ line profiles for all CTTSs except for 12 sources (DR Tau, RW Aur A, DS Tau, YY Ori, AA Tau, GI Tau, CI Tau, BM And, RW Aur B, SU Aur, UX Tau, and GM Aur) are categorized into group E. The line profiles for the 12 sources are as follows: group DP: SU Aur; group IPC: DR Tau, RW Aur A, DS Tau, YY Ori, AA Tau, GI Tau, BM And, and RW Aur B; Group F: CI Tau, UX Tau, and GM Aur.
[c]The Pβ line profiles for all WTTSs except for V826 Tau are categorized into group F. Although classification is difficult for V826 Tau due to very subtle features ($W_\lambda < 0.3$ Å), we categorize it into group E.
References.
FE01: Folha & Emerson (2001), Ed06: Edwards et al. (2006).

Table 9. Statistics summary of He I features and blueshifted absorption types.

	Spectral type							Blue abs. type		Reference
	E	DP	PC	IPC	A	F	BR	Broad	Narrow	
Intermediate-mass stars										
Phase I	0 % (0/7)	43 % (3/7)	43 % (3/7)	14 % (1/7)	0 % (0/7)	0 % (0/7)	0 % (0/7)	43 % (3/7)	0 % (0/7)	This study, Ed06
Phase II	0 % (0/7)	29 % (2/7)	14 % (1/7)	14 % (1/7)	0 % (0/7)	14 % (1/7)	29 % (2/7)	0 % (0/7)	57 % (4/7)	This study, Ed06
Phase III	0 % (0/4)	0 % (0/4)	0 % (0/4)	0 % (0/4)	100 % (4/4)	0 % (0/4)	0 % (0/4)	0 % (0/4)	0 % (0/4)	This study
HAe	7 % (2/28)	11 % (3/28)	36 % (10/28)	32 % (9/28)	7 % (2/28)	7 % (2/28)	0 % (0/28)	36 (10/28)	0 (0/28)	CJ14
Low-mass stars										
CTTS[a]	3 % (1/39)	21 % (8/39)	36 % (14/39)	13 % (5/39)	0 % (0/39)	3 % (1/39)	26 % (10/39)	38 (15/39)	28 (11/39)	Ed06
WTTS[b]	33 % (2/6)	0 % (0/6)	0 % (0/6)	0 % (0/6)	0 % (0/6)	67 % (4/6)	0 % (0/6)	0 (0/6)	0 (0/6)	Ed06

Notes.
[a]The line profiles for CTTSs are categorized as follows: group E: BP Tau; group DP: CW Tau, RW Aur A, HN Tau, DS Tau, GK Tau, UZ Tau E, V836 Tau, UX Tau; group PC: DR Tau, AS 353A, DL Tau, HL Tau, DG Tau, DF Tau, DO Tau, GG Tau, GW Ori, DE Tau, DD Tau, DQ Tau, TW Hya, XZ Tau; group IPC: AA Tau, BM And, RW Aur B, LkCa8, DN Tau; group F: GM Aur; group BR: DK Tau, HK Tau, UY Aur, YY Ori, CI Tau, CY Tau, FP Tau, GI Tau, UZ Tau W, SU Aur
[b]The line profiles for all WTTSs except for V826 Tau and TWA 14 are categorized into group F, while those for V826 Tau and TWA 14 are categorized into group E.
Reference:
CJ14: Cauley & Johns-Krull (2014); Ed06: Edwards et al. (2006)

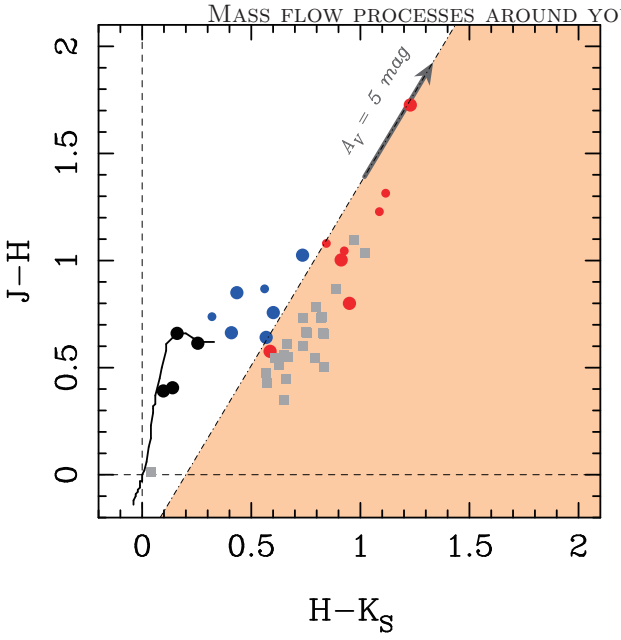

Figure 1. $H - K_S$ vs. $J - H$ color–color diagram. The dwarf track (Bessell & Brett 1988) is shown with a black line, while the reddening vector (Rieke & Lebofsky 1985) for $A_V = 5$ mag is shown with the gray arrow. The border line, which is parallel to the reddening vector and distinguishes HAeBe stars from other objects, is shown with a dot-dashed line. The region to the right of the border line (orange color) is defined as the "excess region" for intermediate-mass stars (Yasui et al. 2014). Target intermediate-mass stars in this paper are shown with filled circles: Phase I, II, and III sources are shown with red, blue, and black, respectively. Six additional intermediate-mass stars in the samples of Folha & Emerson (2001) and Edwards et al. (2006) are denoted by small symbols with the same colors as the targets observed in the present study. HAe stars in a sample of Cauley & Johns-Krull (2014) are shown with gray filled squares.

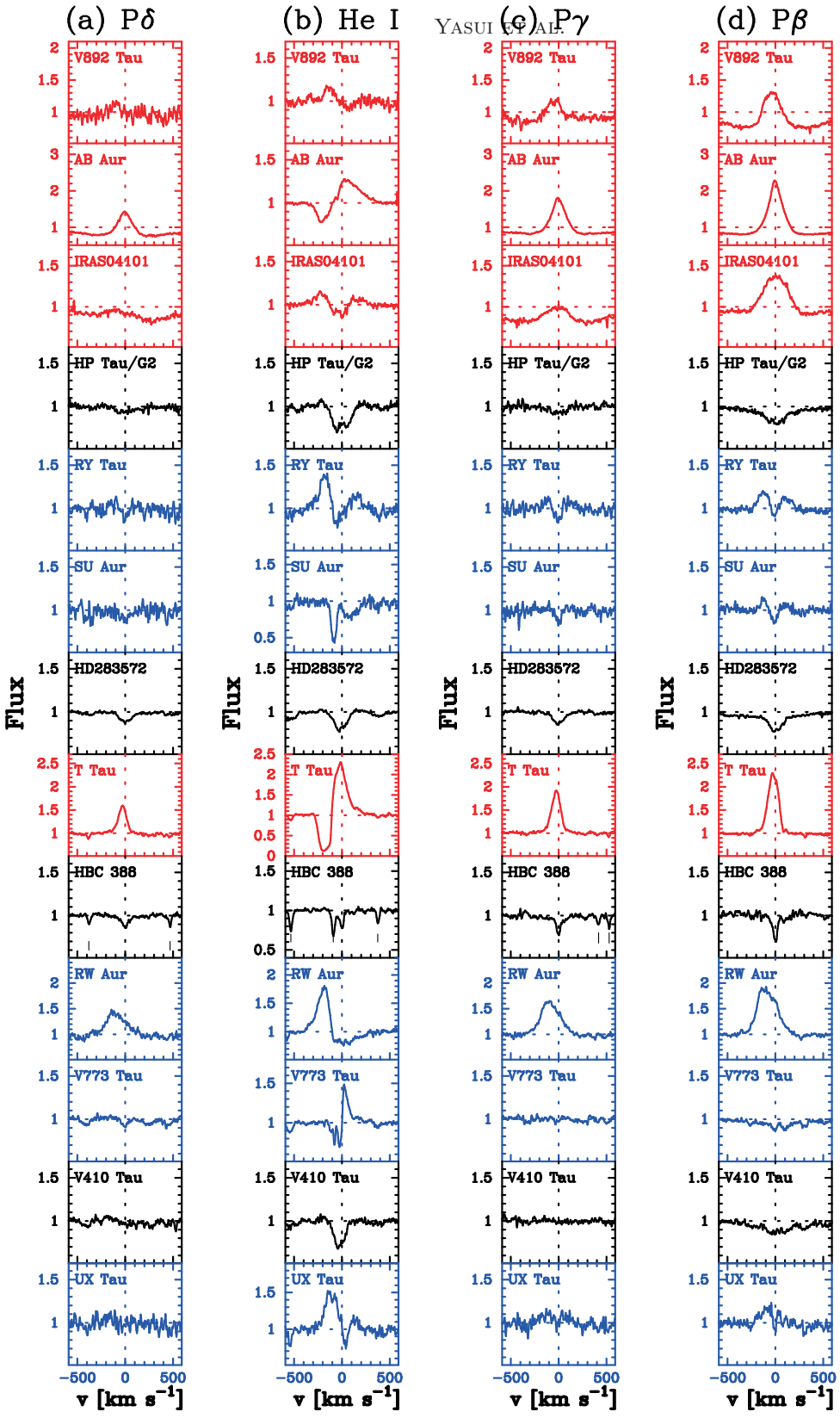

Figure 2. Spectral regions of Pδ (a), He I λ10830 (b), Pγ (c), and Pβ (d). Fluxes are normalized to the continuum. Velocities are relative to the stellar rest velocities. The spectra are sorted by spectral type, from early to late type. Spectra for Phase I, II, and III sources are shown with red, blue, and black, respectively. Photospheric features are marked with vertical lines in the panels for HBC 388. Note that the plot range has been widened for some objects with strong features.

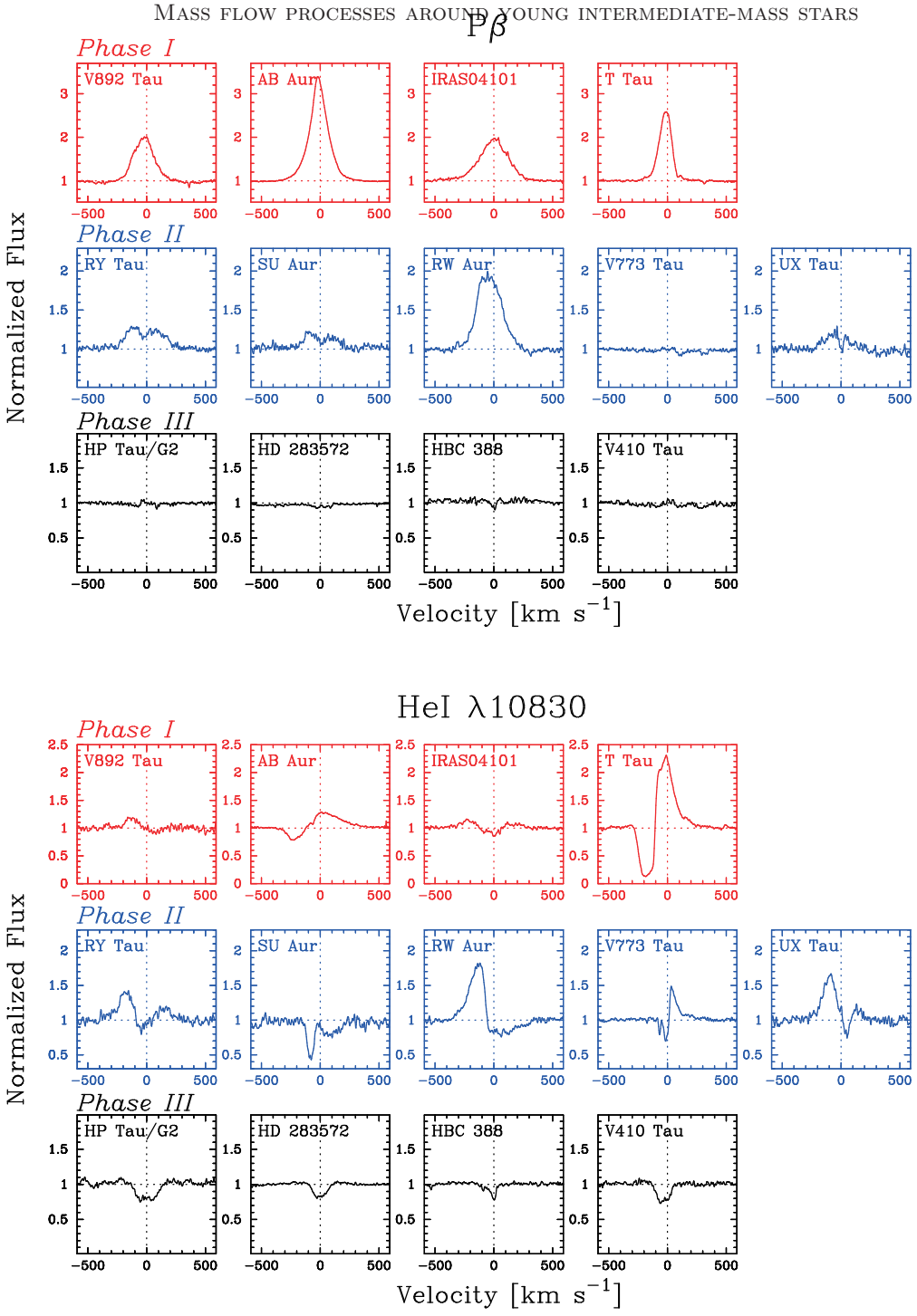

Figure 3. Residual Pβ profiles (top) and He I profiles (bottom). Velocities are relative to the stellar rest velocities. Spectra for Phase I, II, and III sources are shown in top, middle and bottom panels, respectively.

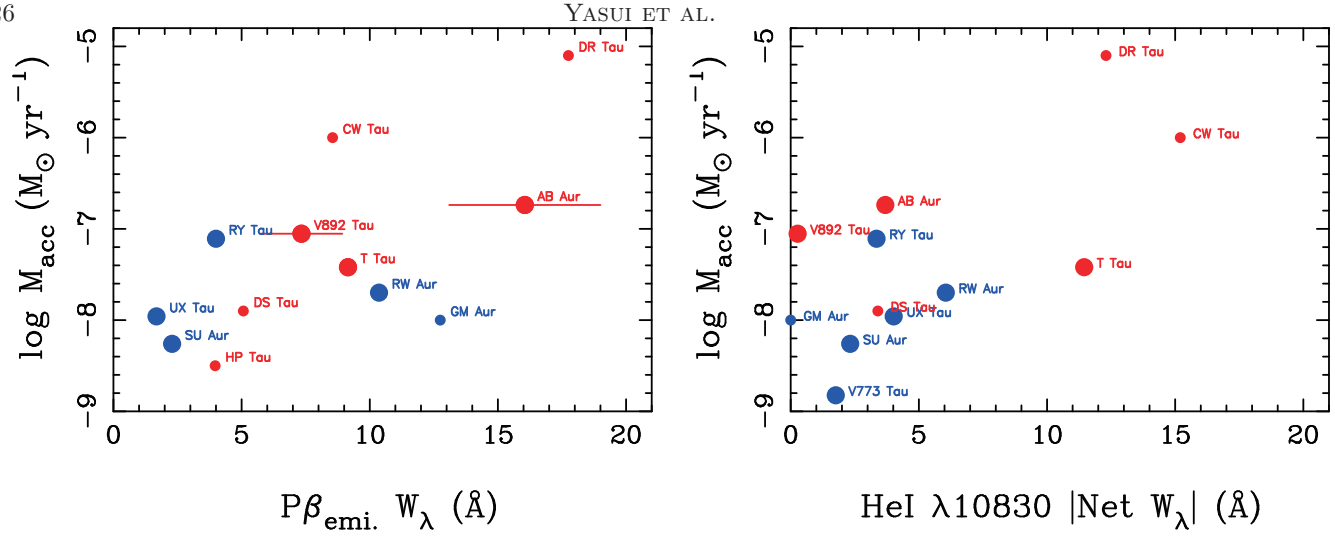

Figure 4. Equivalent width vs. mass accretion rate. The target intermediate-mass stars in this study are presented by large filled circles. Phase I, II, and III sources are shown with red, blue, and black, respectively. Six additional intermediate-mass stars in the samples of Folha & Emerson (2001) and Edwards et al. (2006) are denoted by small symbols with the same colors as that of the targets observed in the present study. The mass accretion rates for the targets observed in the present study are shown in Table 2, that for HP Tau is reported by Johns-Krull, & Gafford (2002), and those for the five remaining additional sources are reported by Edwards et al. (2006). Left: Pβ emission equivalent width and mass accretion rate. Equivalent widths for the targets observed in the present study are shown in Table 6. The error bars of Phase I sources are for V892 Tau and AB Aur, showing the equivalent widths in the case of $\gamma = 0.0$ and 2.0 (Section 3.3). The equivalent widths for the additional sources are from Folha & Emerson (2001); those for HP Tau, GM Aur, and DS Tau (showing PC profiles) are obtained from Table 6 in that article and those for CW Tau and DR Tau are roughly estimated from Figure 1 in that article. Right: Sum of absolute values of emission plus absorption He I equivalent widths vs. mass accretion rate. The equivalent widths for the targets observed in the present study are shown in Table 7 and those for the additional sources are from Table 1 of the study by Edwards et al. (2006).

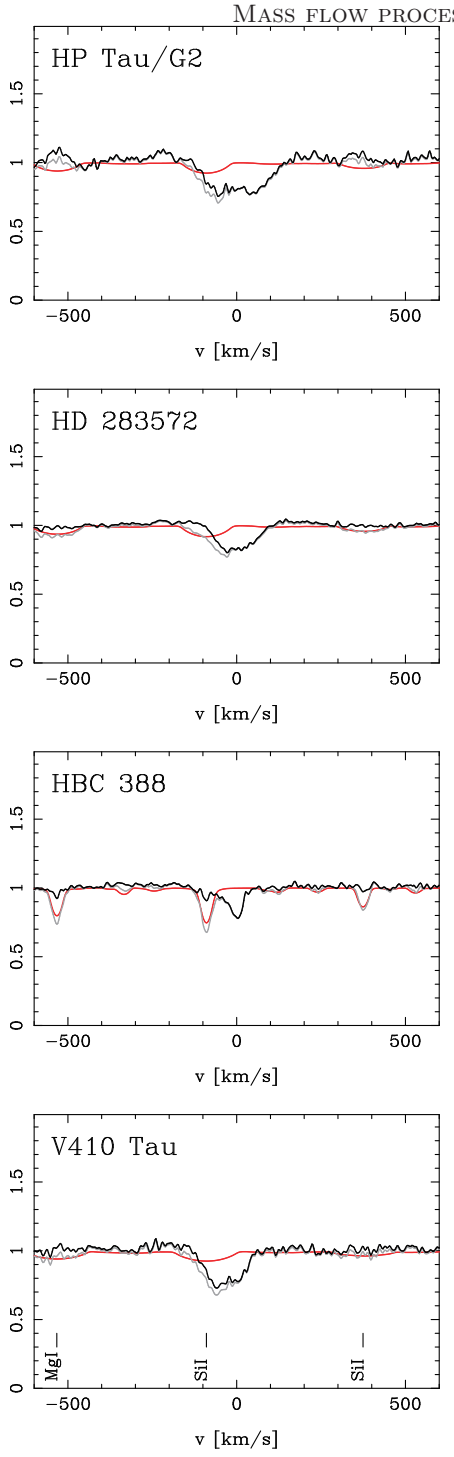

Figure 5. He I λ10830 spectra for Phase III sources. The synthetic spectra, observed spectra, and residual profiles are shown with red, gray, and black lines, respectively. Photospheric features, Mg I λ10814.1 and Si I (λ10830.1 and λ10846.8), are marked with vertical lines in the panel of V410 Tau (bottom).

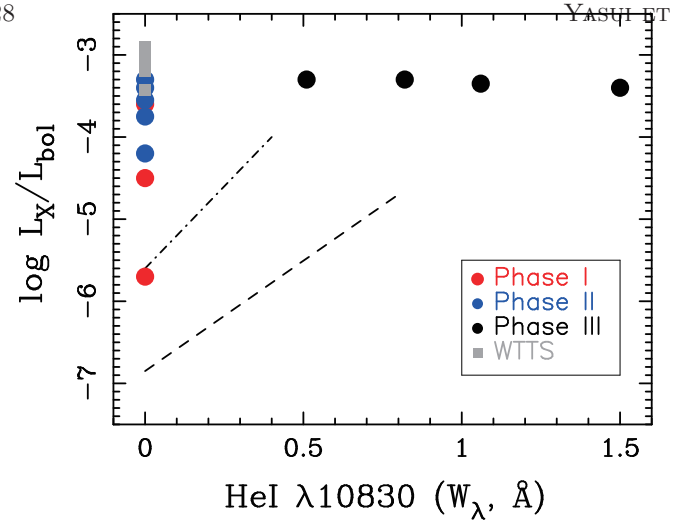

Figure 6. The fractional X-ray luminosities (L_X/L_{bol}) vs. He I absorption equivalent widths. Phase I, II, and III sources are shown by red, blue, and black circles, respectively, while WTTSs in a sample of Edwards et al. (2006) are shown by gray squares. The lines show linear fits to sample stars in Zarro & Zirin (1986) by Sanz-Forcada & Dupree (2008); the dot-dashed line is for dwarfs and subgiants, and the dashed line is for all giants.

タ イ ト ル ： Identification of Absorption Lines of Heavy Metals in the Wavelength Range 0.97-1.32 μm

担　　当 ： Noriyuki Matsunaga, Daisuke Taniguchi, Mingjie Jian, Yuji Ikeda, Kei Fukue, *et al.*

関 連 出 版 ： The Astrophysical Journal Supplement Series, Volume 246, Issue 1, article id. 10, 14 pp. (2020).

関連学会発表等 ： https://www.kyoto-su.ac.jp/news/20200109_859_winered.html

Draft version November 27, 2019
Typeset using LaTeX **twocolumn** style in AASTeX62

Identification of Absorption Lines of Heavy Metals in the Wavelength Range 0.97–1.32 μm

Noriyuki Matsunaga,[1,2] Daisuke Taniguchi,[1] Mingjie Jian,[1] Yuji Ikeda,[3,2] Kei Fukue,[2] Sohei Kondo,[4,2] Satoshi Hamano,[5] Hideyo Kawakita,[2,6] Naoto Kobayashi,[4,7,2] Shogo Otsubo,[2] Hiroaki Sameshima,[7] Keiichi Takenaka,[6] Takuji Tsujimoto,[5] Ayaka Watase,[6] Chikako Yasui,[5,2] and Tomohiro Yoshikawa[8]

[1] *Department of Astronomy, School of Science, The University of Tokyo, 7-3-1 Hongo, Bunkyo-ku, Tokyo 113-0033, Japan*
[2] *Laboratory of Infrared High-resolution spectroscopy (LiH), Koyama Astronomical Observatory, Kyoto Sangyo University, Motoyama, Kamigamo, Kita-ku, Kyoto 603-8555, Japan*
[3] *Photocoding, 460-102 Iwakura-Nakamachi, Sakyo-ku, Kyoto 606-0025, Japan*
[4] *Kiso Observatory, Institute of Astronomy, School of Science, The University of Tokyo, 10762-30 Mitake, Kiso-machi, Kiso-gun, Nagano 397-0101, Japan*
[5] *National Astronomical Observatory of Japan, 2-21-1 Osawa, Mitaka, Tokyo 181-8588, Japan*
[6] *Department of Physics, Faculty of Science, Kyoto Sangyo University, Motoyama, Kamigamo, Kita-ku, Kyoto 603-8555, Japan*
[7] *Institute of Astronomy, School of Science, The University of Tokyo, 2-21-1 Osawa, Mitaka, Tokyo 181-0015*
[8] *Edechs, 17203 Iwakura-Minami-Osagi-cho, Sakyo-ku, Kyoto 606-0003, Japan*

(Received October 20, 2019; Revised November 25, 2019; Accepted November 25, 2019)

Submitted to ApJS

ABSTRACT

Stellar absorption lines of heavy elements can give us various insights into the chemical evolution of the Galaxy and nearby galaxies. Recently developed spectrographs for the near-infrared wavelengths are becoming more and more powerful for producing a large number of high-quality spectra, but identification and characterization of the absorption lines in the infrared range remain to be fulfilled. We searched for lines of the elements heavier than the iron group, i.e., those heavier than Ni, in the Y (9760–11100 Å) and J (11600–13200 Å) bands. We considered the lines in three catalogs, i.e., Vienna Atomic Line Database (VALD), the compilation by R. Kurucz, and the list published in 1999 by Meléndez & Barbuy. Candidate lines were selected based on synthetic spectra and the confirmation was done by using WINERED spectra of 13 supergiants and giants within FGK spectral types (spanning 4000–7200 K in the effective temperature). We have detected lines of Zn I, Sr II, Y II, Zr I, Ba II, Sm II, Eu II, and Dy II, in the order of atomic number. Although the number of the lines is small, 23 in total, they are potentially useful diagnostic lines of the Galactic chemical evolution, especially in the regions for which interstellar extinction hampers detailed chemical analyses with spectra in shorter wavelengths. We also report the detection of lines whose presence was not predicted by the synthetic spectra created with the above three line lists.

Keywords: line: identification — techniques: spectroscopic — stars: abundances — supergiants — infrared: stars

1. INTRODUCTION

The identification of stellar absorption lines in the near-infrared range is not complete compared to the established lists of lines in the optical (see, e.g., Andreasen et al. 2016). In this work, we focus on the elements with the atomic number $Z \geq 29$, i.e., those heavier than the iron group elements of which the heaviest is Ni. Those heavy elements are useful for studying the detailed chemical evolution of the Galaxy (McWilliam 1997; Sneden et al. 2008; Delgado Mena et al. 2017), although their absorption lines are rather limited. The so-called neutron-capture (n-capture) elements usually stand for the elements with $Z \geq 31$ (e.g., Sneden et al. 2008), and they are mostly synthesized in the presence of excessive neutrons. Depending on the density of

Corresponding author: Noriyuki Matsunaga
matsunaga@astron.s.u-tokyo.ac.jp

neutrons and the resultant time scale of the n-capture process, compared with the time scale of the β decay, the n-capture nucleosynthesis has two main modes, s-process (slow) and r-process (rapid), and they occur at different astronomical sites. In contrast, Cu ($Z = 29$) and Zn ($Z = 30$) are often included in the "iron peak" elements and not in the n-capture elements; the origins of these two elements are, however, considered to be multiplex and complicated (Delgado Mena et al. 2017). We will further discuss, in the Discussion (Section 4.1), the groups of the heavy elements and the insights that can be yielded by the elements with absorption lines confirmed in this study.

We here investigate the absorption lines that appear in near-infrared spectra of FGK-type stars, in particular, supergiants. We have two main reasons for considering supergiants: (i) many absorption lines are expected to be strong in stars with low surface gravity as we see below, and (ii) their high luminosities are advantageous as stellar tracers of the Galaxy and nearby galaxies. In particular, Cepheid variable stars are supergiants within the range of FGK types, aged at 10–300 Myr, and they are useful for studying the Galactic disk because their distances and ages can be accurately estimated (see, e.g., the review by Matsunaga et al. 2018). For example, da Silva et al. (2016) investigated abundances of five n-capture elements (Y, La, Ce, Nd, and Eu) in hundreds of Cepheids, of which 73 were observed by the authors themselves. They used optical high-resolution spectra for measuring six Y II, six La II, three Ce II, six Nd II, and two Eu II lines which are located between 4500 and 8000 Å (see also Lemasle et al. 2013). In addition, measurements of the heavy elements in Cepheids and supergiants, based on the line list of Kovtyukh & Andrievsky (1999), are found in a series of papers by Luck and collaborators (Luck et al. 2011; Luck, & Lambert 2011; Luck 2018, and references therein). The number of the lines used in the previous studies is not so large, and yet they provide us with valuable information on the chemical enrichment of the Galactic disk. Identification and characterization are less advanced for absorption lines in the infrared range, but many efforts have gradually increased the lines available for measuring stellar abundances.

Meléndez & Barbuy (1999; hereinafter referred to as MB99) used the solar spectrum (Kitt Peak Solar Atlas; Wallace et al. 1996, and references therein) to compile the oscillator strengths, $\log gf$, and other parameters of the 978 lines that they identified between 10000 and 13400 Å, a part of the YJ bands, in addition to the 1240 lines in the H band. We use this MB99 line list as a starting point of our line selection in addition to Vienna Atomic Line Database (VALD; Ryabchikova et al. 2015) and the compilation by R. Kurucz (KURZ; updated at his web site[1]). The latter two give more general compilations of absorption lines including those purely based on theoretical calculations.

In the recent decade, high-resolution spectrographs covering infrared wavelengths have been used to explore absorption lines including weak ones. For example, dozens of absorption lines of the heavy elements ($Z \geq 29$) have been found (e.g., Hasselquist et al. 2016; Cunha et al. 2017; Afşar et al. 2018; Böcek Topcu et al. 2019; Chojnowski et al. 2019) with high-quality spectra from the APOGEE survey (Majewski et al. 2017) and IGRINS (Park et al. 2014), although they do not cover the YJ bands of our interest. In contrast, GIANO (Oliva et al. 2012) covers the YJ bands in addition to H and K. Origlia et al. (2013, 2016) measured Sr abundances using one or two lines with GIANO Y-band spectra. These two studies by Origlia et al. targeted red supergiants in stellar clusters. In contrast, Caffau et al. (2016) investigated GIANO spectra of FG-type dwarfs and found three Sr I lines in the Y band. Some warmer stars provide us with unique data useful for identifying various absorption lines. Hubrig et al. (2012) reported one Sr II line and one Dy II line in the Y band in one or more peculiar A-type stars by investigating the spectra from CRIRES (Kaeufl et al. 2004).

The studies mentioned in the preceding paragraph mark important progress in the identification and characterization of absorption lines in the near infrared, but the current list of confirmed lines is clearly incomplete. In this paper, we investigate the lines of the heavy elements with $Z \geq 29$ seen in the observed spectra, covering the YJ bands, collected with the near-infrared spectrograph, WINERED.[2] It is a high-resolution echelle spectrograph covering the wavelength range of 0.90–1.35 μm with the resolving power of 28000 or higher (Ikeda et al. 2016; Otsubo et al. 2016). We use WINERED spectra of supergiants and giants with various effective temperatures, $T_{\rm eff}$, between 4000 and 7200 K. The dependency on the temperature varies from line to line, and the set of the WINERED spectra enables us to check whether the absorption at the wavelength of each candidate line depends on $T_{\rm eff}$ as expected for the particular line. The purpose of this study is to confirm the absorption lines of the heavy elements that are seen in the YJ-band spectra of FGK-type stars.

2. SPECTRAL DATA

[1] http://kurucz.harvard.edu/linelists/gfnew/
[2] http://merlot.kyoto-su.ac.jp/LIH/WINERED/

2.1. *Observational spectra*

We investigate YJ-band spectra of 13 stars, supergiants and giants. Their spectra were obtained in 2015 and 2016 with WINERED attached to the 1.3 m Araki Telescope at Koyama Astronomical Observatory in Kyoto, Japan. The spectral resolution of WINERED with the setting of the WIDE mode and the 100 μm slit is around 28000 (Ikeda et al. 2016). We observed dozens of supergiants, giants, and dwarfs whose temperatures were derived making use of the line-depth ratios by Kovtyukh et al. (2003, 2006) and Kovtyukh (2007). The entire set of the spectra for these objects will be considered for discussing the line-depth ratios (Jian et al., in preparation), but a part of the spectra of supergiants and giants are used in this study (Table 1). We use the stellar parameters, including $T_{\rm eff}$, taken from Luck (2014) and Hekker & Meléndez (2007) because they obtained the four necessary parameters, i.e., $T_{\rm eff}$, $\log g$, [Fe/H], and the microturbulence (ξ), altogether. Their measurements are based on high-resolution spectra ($R \geq 40000$), and the obtained parameters are precise enough for our purpose; in fact, the spectra synthesized with the given parameters reproduce the observed spectra at around the 1 % level as we see below. Figure 1 presents the distribution of the 13 objects on the $(T_{\rm eff}, \log g)$ plane.

All the observed spectra were reduced by following the standard procedure adopted in the WINERED pipeline (Hamano et al., in preparation) that was established using PyRAF,[3] which calls IRAF tasks[4] from Python scripts. The reduction steps include sky subtraction, scattered light subtraction, flat-fielding (using a halogen lamp with an integrating sphere), geometric transformation, aperture extraction, and wavelength calibration based on Th–Ar lamp spectra. In addition, small wavelength shifts[5] between individual exposures were corrected, if necessary, before they were combined to give an averaged one-dimensional spectrum for each target. Throughout this paper, we use air wavelengths rather than vacuum wavelengths. Then, the one-dimensional spectrum was normalized at the continuum level, and the telluric correction was performed as described in Sameshima et al. (2018a) using the WINERED spectrum of an A0 V star taken at the same night.

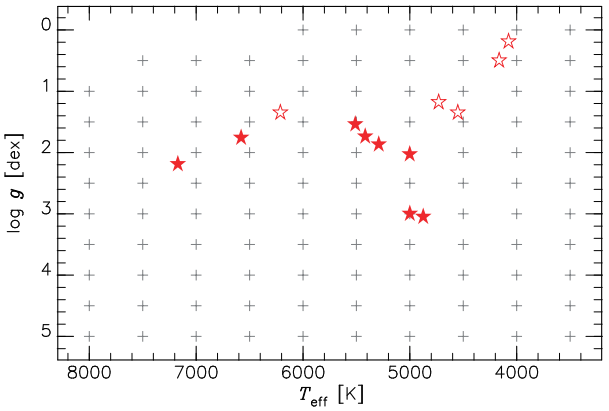

Figure 1. Stellar parameters used for spectral synthesis. The effective temperatures, $T_{\rm eff}$, and the surface gravities, $\log g$, of our targets (Table 1) are indicated by star symbols, the open symbol for those with $\log g < 1.5$ and the filled symbol for those with $\log g > 1.5$. The gray '+' symbol indicates the grid of $(T_{\rm eff}, \log g)$ used for a set of synthetic spectra (Section 2.2).

It is worthwhile to add remarks on some objects. Because they are bright, there were studies with optical spectra dating back decades ago, e.g., Steel (1945) for HD 20902 (α Per). In particular, HD 194093 (or γ Cyg) is an interesting supergiant. Since the early discovery by Adams & Joy (1926, 1927), it is known that the spectrum of γ Cyg is rich in rare-earth lines, e.g., Eu and Dy (see, also, Roach 1942). The star γ Cyg is located close to the so-called γ-Cygni supernova remnant, but Johnson (1975) found that they are not connected with each other.

2.2. *Synthetic spectra*

We used MOOG (the version released in February 2017 Sneden et al. 2012) to create synthetic spectra for selecting and confirming absorption lines of the heavy elements. We adopted the 1D plane-parallel atmosphere models compiled by R. Kurucz.[6] The local thermal equilibrium (LTE) is assumed in the models we used and any part of the spectral synthesis. We considered two sets of stellar parameters. Those for the first set are listed in Table 1 and used for making direct comparisons between the synthetic and observed spectra. We estimated the broadening of individual objects ($v_{\rm b}$, in the full width at half maximum) including the instrumental resolution

[3] PyRAF is a product of the Space Telescope Science Institute, which is operated by AURA for NASA.

[4] IRAF is distributed by the National Optical Astronomy Observatories, which are operated by the Association of Universities for Research in Astronomy, Inc., under cooperative agreement with the National Science Foundation.

[5] The wavelength shifts are, at least partly, due to the instability of the instrument caused by varying ambient temperature, and we made an instrumental upgrade to minimize such shifts in late 2016.

[6] We adopted the files named amXX.dat or apXX.dat where XX is to be replaced by two digits indicating the abundances, not the original ones available in Kurucz (1993), from http://kurucz.harvard.edu/grids/.

Table 1. Observed objects and their parameters

HD	Name	Sp. Type	$T_{\rm eff}$ (K)	$\log g$ (dex)	[Fe/H] (dex)	ξ ($\rm km\,s^{-1}$)	Ref.	Obs. Date (UT)	$v_{\rm b}$ ($\rm km\,s^{-1}$)	γ
25291	HR 1242	F0 II	7171	2.19	+0.03	1.67	1	2015.10.28	12.65	1.103
20902	α Per	F5 Ib	6579	1.76	+0.15	3.65	1	2015.10.26	25.61	1.694
194093	γ Cyg	F8 Ib	6212	1.35	+0.05	4.02	1	2015.10.26	16.64	1.386
204867	β Aqr	G0 Ib	5511	1.54	+0.03	3.39	1	2015.10.26	17.60	1.535
26630	μ Per	G0 Ib	5418	1.74	+0.09	3.02	1	2015.10.28	17.93	1.362
159181	β Dra	G2 Ib–IIa	5291	1.87	+0.15	2.72	1	2016.02.03	18.10	1.198
77912	HR 3612	G7 IIa	5001	2.03	+0.12	2.16	1	2016.03.21	14.27	1.012
27697	δ Tau	G9.5 III	5000	3.00	+0.08	1.50	2	2015.10.25	12.31	0.957
19787	δ Ari	G9.5 IIIb	4875	3.05	+0.09	1.68	2	2016.03.11	12.07	0.917
208606	HR 8374	G8 Ib	4731	1.18	+0.25	3.49	1	2015.10.31	17.05	0.896
9900	HR 461	K0 II	4552	1.35	+0.19	2.46	1	2015.10.31	13.51	0.815
206778	ϵ Peg	K2 Ib–II	4165	0.50	−0.01	2.96	1	2015.10.31	14.73	1.409
52005	HR 2615	K3 Ib	4077	0.19	−0.07	2.76	1	2015.10.28	14.18	1.557

NOTE—Parameters of each target are taken from one of the two references, Ref. 1=Luck (2014) and Ref. 2=Hekker & Meléndez (2007). In the last two columns, $v_{\rm b}$ indicates the broadening width including the instrumental profile which corresponds to $\sim$10.7 $\rm km\,s^{-1}$, and γ indicates the factor we used to convert the depths (see Section 3.2). Spectral types are taken from the SIMBAD database.

based on several isolated lines in the observed spectra. For the second set, we used the $T_{\rm eff}$ and $\log g$ values on the grid indicated by the '+' points in Figure 1 together with the following parameters fixed: the microturbulence $\xi = 2\,\rm km\,s^{-1}$, the broadening $v_{\rm b} = 10.7\,\rm km\,s^{-1}$, and the chemical abundances to be solar (Asplund et al. 2009). The fixed microturbulence and broadening are not optimal for stars with broad ranges of $T_{\rm eff}$ and $\log g$. The ξ of $2\,\rm km\,s^{-1}$ is typical for red giants, but ξ tends to be larger for stars with higher luminosity (Gray et al. 2001). The macroturbulence ($v_{\rm mac}$), or broadening in general, also shows the dependency on the luminosity class (Gray & Toner 1986). Likewise, both ξ and $v_{\rm mac}$ depend on $T_{\rm eff}$ (e.g., Ryabchikova et al. 2016). This infers that the predicted line strengths in the second set of the synthetic spectra may be biased especially for dwarfs and supergiants. Nevertheless, those synthetic spectra useful to predict where absorption lines in question get significant or deep in the parameter space of $(T_{\rm eff}, \log g)$. Incidentally, the absorption lines we discuss here are mostly shallow and not strongly saturated; therefore, ξ does not affect our predictions so much.

For both of the sets mentioned above, we assumed the solar abundance ratios of Asplund et al. (2009), $\log \epsilon_{\rm Fe,\odot} = 7.50$ dex for [Fe/H] = 0 and other 'Photosphere' abundances listed in their Table 1, except the carbon abundance. We changed [C/H] by some amounts, between −0.31 and 0.28 dex, in order to get better agreements of CN lines between the synthetic and observed spectra. The observed spectra in the lower temperature range show many CN lines, and those lines are not well reproduced by the synthetic spectra of many stars without the changes. This may be caused by the surface abundance ratios modified by the first dredge-up (Luck, & Lambert 1985; Takeda et al. 2013; Lyubimkov et al. 2015). The purpose of this adjustment is merely to get the synthetic spectra that match better with the observed ones. The [C/H] values we used are not necessarily accurate estimates of the carbon abundances; therefore, we do not give the [C/H] used for individual objects. In contrast, [C/H] is fixed to be solar in the second set of synthetic spectra for the grid of $(T_{\rm eff}, \log g)$.

In order to assess the absorption of target lines even if they are contaminated by other lines, we consider four kinds of synthetic spectra: (i) normal ones with all lines included, (ii) those with lines of only one species (i.e., each atom or atomic ion) included, (iii) those with only one target line included, and (iv) those with the target lines excluded. We consider the $\log gf$ values and other parameters of a given target line in each of the three lists. For other atomic lines, we adopted the lines and their parameters in KURZ when we considered target lines in the KURZ list, but we used the VALD line list for considering target lines in VALD or those in MB99. The KURZ list we used is the version compiled

on 2017 Oct 8, while we downloaded the VALD3 list to use on 2019 August 27. For molecular lines, we used those listed in VALD, in which lines of C_2, CH, CN, CO, and OH molecules are included within the wavelength range of our interest. Only CN lines appear significant in the temperature ranges we investigate. In addition, we adopted FeH lines compiled by Plez (private communication; see also Önehag et al. 2012). We adopted the FeH's dissociation energy of 1.59 eV, at 273.15 K, from Schultz & Armentrout (1991). The FeH lines appear only in a few objects with the lowest temperatures.

In comparing the observed and synthetic spectra of the 13 objects, we noticed dozens of absorption lines which are well visible in the observed spectra but not predicted in the synthetic ones. We list such lines and discuss their characteristics in Appendix B.

3. DETECTION OF ABSORPTION LINES

3.1. *Line selection*

We searched for absorption lines of elements heavier than the iron group elements in the three line lists, KURZ, VALD, and MB99. Combining the three lists, our target elements are from Cu to Th, i.e., $29 \leq Z \leq 90$, with some gaps. We limited ourselves to the ionization states between I (neutral) and III (doubly ionized). We also limited the wavelength ranges to 9760–11100 and 11600–13200 Å, corresponding to the orders of 51–57 th (Y band) and 43–48 th (J band) of WINERED.

In the given wavelength ranges, MB99 lists 19 lines of 6 species in total, i.e., Zn I, Ge I, Sr II, Y II, La II, and Eu II. MB99 covers the wavelengths longer than 10000 Å only. MB99 actually lists 20 lines of our target species between 10000 and 13400 Å, but one of the lines, Ge I 11125.12, falls within the gap of the target in the wavelength range. There is dense and strong telluric absorption around the Ge I line (see, e.g., Fig. 4 in Sameshima et al. 2018a), and we neglected this line. We consider the 19 lines in MB99 in the next selection step.

In contrast to MB99, VALD and KURZ list large numbers of absorption lines for various elements between Cu and Th. Hundreds of lines are listed for some elements, but we cannot expect to see so many lines of these heavy elements in real stellar spectra as we confirm below. Before we compare the observed spectra with the synthetic ones, we limited the number of candidate lines for each species using the synthetic spectra. We considered the spectra for the grid of $(T_{\rm eff}, \log g)$ with lines of only one species included at each time (see Section 2.2). We picked up lines that become deeper than 0.02 in depth in at least one of the synthetic spectra at all the grid points. 67 lines of 9 species in KURZ and 63 lines of 14 species in VALD were found to be candidates.

There are many overlaps between the lines selected with the three line lists, and there are 108 different lines of 14 species in total; 40, 35, and 5 lines are listed only in KURZ, VALD, and MB99, respectively. All of the 5 lines selected from MB99 only are of Ge I. In the following, we consider whether these lines appear significant in the observed spectra or not and, if detected, examine their temperature dependence in comparison with the synthetic spectra.

3.2. *Measurements*

A significant fraction of the lines we investigate are expected to be blended with other absorption lines even if they exist, and it is difficult to measure the equivalent widths. We therefore consider depths, i.e., $d \equiv 1 - f(\lambda_{\rm c})$, where $f(\lambda_{\rm c})$ is the flux at the line center, $\lambda_{\rm c}$, in normalized spectra.

In order to make direct comparisons between the depths in the observed and synthetic spectra, we perform the normalization to adjust the continuum levels of the two kinds of spectra. The reduction performed by the standard pipeline software for WINERED includes the continuum normalization (see, e.g., Section 3.1 in Taniguchi et al. 2018). Although the synthetic spectra we created for individual objects show reasonable agreements between the observed and synthetic spectra, there are noticeable deviations especially within absorption lines. Such deviations can be attributed to inaccurate $\log gf$ values (Andreasen et al. 2016; Kondo et al. 2019) and maybe to inaccurate abundances assumed. Moreover, narrow flat parts outside apparent absorption lines are found to be lower than the unity in some spectral regions of the synthetic spectra, but the normal continuum procedure applied to the observed spectra adjusts such regions to be around 1. We therefore match the continuum levels of the observed and synthetic spectra around each target line as follows.

First, we searched for velocity offsets to fix small offsets in the wavelength scale, if any, by minimizing the residuals between the observed and synthetic spectra. For each target line at the wavelength of $\lambda_{\rm c}$, the residuals were calculated for spectral parts around the line center. We used the width of $\pm 300\,{\rm km\,s^{-1}}$ for the objects with $T_{\rm eff} < 5200$ K and the width of $\pm 1000\,{\rm km\,s^{-1}}$ for the others for this wavelength adjustment. The large width for the warmer stars was necessary to accommodate many absorption lines which enable us to estimate the offset precisely. When we compare the observed and synthetic spectra, the synthetic spectra were pixelized to match the pixels of the observed spectra by integrat-

ing the normalized flux within the wavelength range of each pixel of the latter, and $f_{\rm syn}$ indicates the counts of thus digitized spectra. We corrected the observed spectra produced by the pipeline for the velocity offsets; $f_{\rm obs,0}$ indicates the counts of the observed spectra after this correction.

Second, we considered the pixel-by-pixel ratio between each observed spectrum and the corresponding synthetic one, $r_{\rm org} \equiv f_{\rm obs,0}/f_{\rm syn}$, for adjusting the continuum level of the former to that of the latter. For the normalization around each target line, we used the adjacent parts on both sides of the line, i.e., $\lambda_{\rm c} - \Lambda_2 < \lambda < \lambda_{\rm c} - \Lambda_1$ and $\lambda_{\rm c} + \Lambda_1 < \lambda < \lambda_{\rm c} + \Lambda_2$, where Λ_1 and Λ_2 are the wavelength steps corresponding to the velocity of $15\,{\rm km\,s^{-1}}$ and $100\,{\rm km\,s^{-1}}$, at around $\lambda_{\rm c}$, respectively. The ratio shows deviations from 1 caused by various errors including the offset and slope in the pre-normalized continuum level of $f_{\rm obs,0}$ and imperfect reproduction of the stellar spectrum in $f_{\rm syn}$. The ratio, as a function of pixel, of the adjacent parts around each target line was fitted as a linear trend, $a(\lambda - \lambda_{\rm c}) + b$, by minimizing

$$\chi^2 = \sum_{\lambda_i} w_f w_\lambda \left\{ r_{\rm org}(\lambda_i) - a(\lambda_i - \lambda_{\rm c}) - b \right\}^2 , \quad (1)$$

where the summation is taken over the pixels, λ_i, within the adjacent ranges mentioned above. The pixels within $\pm 15\,{\rm km\,s^{-1}}$around the center were not included. We introduced two weight terms, w_f and w_λ,

$$w_f = [f_{\rm syn}(\lambda_i)]^2, \quad (2)$$

$$w_\lambda = \exp\left(-\frac{|\lambda_i - \lambda_c|}{\Lambda_2} \right) . \quad (3)$$

The former depends on the count of $f_{\rm syn}$; the pixels with flux closer to the continuum are more weighted than the pixels within strong absorption. The latter, w_λ, gives higher weights to the pixels closer to the target line in wavelength than to those more separated. Admittedly, we have no solid mathematical background to use the weights as given in Equations (2) and (3). Nevertheless, after some experiments, we found that they tend to give reasonable results even if the observed spectra show deviations from the synthetic one such as lines with clearly different depths. Next, we divided the original observed spectra by the fitted linear trend to obtain the re-normalized spectra, $f_{\rm obs}(\lambda) = f_{\rm obs,0}(\lambda)/[a(\lambda - \lambda_{\rm c}) + b]$. We also calculated the weighted standard deviation of the residual between the observed and synthetic spectra,

$$e = \sqrt{ \frac{\sum \left\{ w_f w_\lambda \left[f_{\rm obs}(\lambda_i) - f_{\rm syn}(\lambda_i) \right]^2 \right\}}{\sum w_f w_\lambda} } . \quad (4)$$

This e serves as the error in depth when we compare the depths of the line in the observed and synthetic spectra. The residual is attributed to various factors including pixel-to-pixel errors in the observed spectra, the inconsistency between the observed and synthetic spectra, and the error in the normalization. The median of the e values calculated for individual ranges around the target lines is $\sim$0.01 or smaller for most of the 13 objects. For the two objects with $T_{\rm eff} < 4200\,{\rm K}$, however, the median e values are nearly 0.02. We note that the error estimates described here do not include the uncertainty concerning the target lines themselves because the normalization and the calculations of e were done without considering the pixels within $\Lambda_1 = 15\,{\rm km\,s^{-1}}$ around the lines. The residuals at the target wavelengths, if significant, would tell us the inconsistency between the depths observed and those predicted with the line lists.

Then, we measured the depths, d, at the line wavelength, λ_c, by linearly interpolating the two adjacent pixels, λ_i and λ_{i+1}, with $\lambda_i \le \lambda_c < \lambda_{i+1}$; $d_{\rm obs}$ and $d_{\rm syn}$ indicate the depths measured with $f_{\rm obs}$ and $f_{\rm syn}$, respectively. While the two depths of each target line can be directly compared with each other for each object, the depths for different objects are affected by differences in various stellar parameters. Here we consider the indicator, $d^* = \gamma d$, i.e., the depths multiplied by the factor γ which compensates the effects of stellar metallicity and line width,

$$\gamma \equiv 10^{-[{\rm Fe/H}]} \left(\frac{v_{\rm b}}{v_{\rm inst}} \right) , \quad (5)$$

where the first term compensates the metallicity effect and the second term converts the depths in spectra broadened by the width of $v_{\rm b}$ ($\simeq \sqrt{v_{\rm mac}^2 + v_{\rm inst}^2}$) into those in the spectra merely broadened by the instrumental line width, $v_{\rm inst} = 10.7\,{\rm km\,s^{-1}}$, of the WIDE mode of WINERED (i.e., with the broadening by macroturbulence, $v_{\rm mac}$, ignored). The γ factor for each target is listed in Table 1. It should be noted that d^* does not necessarily agree with the depth of a line in the spectrum of a star with [Fe/H] = 0 dex broadened by the instrumental width if the line is blended with other lines. Nevertheless, the conversion from d to d^* makes it easier to compare the depths of 13 targets directly and examine the dependence on $T_{\rm eff}$. The d^* may still be affected by $\log g$ and ξ. We will take into account the effect of $\log g$ by considering the depths in the synthetic spectra obtained for the grid of $(T_{\rm eff}, \log g)$ that was described in Section 2.2. On the other hand, ξ has little impact on shallow lines for which we need precise measurements for confirming the line identification.

Finally, we evaluate the indicator that measures the absorption of the target lines themselves. As mentioned in Section 2.2, we synthesized the spectra with the target lines excluded. Their depths at the wavelengths in question are also measured and denoted as $d_{\rm syn\dagger}$. They are expected to be zero if there is no blending line, but they are often not zero. By subtracting $d_{\rm syn\dagger}$ from the normal depth, we can estimate the contribution of a target line to absorption. We calculated this indicator, α, for the depths in both observed and synthetic spectra; $\alpha_{\rm obs} \equiv d_{\rm obs} - d_{\rm syn\dagger}$ and $\alpha_{\rm syn} \equiv d_{\rm syn} - d_{\rm syn\dagger}$. If $\alpha_{\rm obs}$ is large with respect to e, the absorption by the target line is suggested to be significant. When we compare the measurements for the 13 objects, we consider the conversion by considering the effects of metallicity and broadening, $\alpha^* \equiv d^* - d^*_{\rm syn\dagger} = \gamma(d - d_{\rm syn\dagger})$, where α^* and d^* are considered for both the observed and synthetic spectra. In addition, we use $\beta \equiv d_{\rm syn\dagger}/d_{\rm syn}$ as the estimate of the blend; β varies from 0 (no blend) to 1 (fully contaminated). We define $\beta = 1$ when $d_{\rm syn} = 0$, but we are not interested in such cases because our purpose is to confirm or reject predicted lines.

3.3. *Results*

We measured the depths, $d_{\rm obs}$ and $d_{\rm syn}$, and also the errors, e, for the 108 candidate lines, selected in Section 3.1, in the spectra of the 13 objects. While many lines were not seen, there are dozens of lines showing large $\alpha_{\rm obs}/e$ values. We considered the lines with $\alpha_{\rm obs}/e > 2$ to be significant unless they are affected by spurious noises too much. Then, we examined the d^*, α^*, and β plotted against $T_{\rm eff}$ (Figure 2) and checked if the dependence on $T_{\rm eff}$ is consistent with the expectation from the synthetic spectra. For some lines, the gravity effect on the depths measured for the targets with different $\log g$ is significant, and we took it into account by comparing the $T_{\rm eff}$ trends expected for the two $\log g$ values, 0.5 and 2.5, illustrated in Figure 2. In addition, we checked the appearance of the spectra, comparing the synthetic spectra with the target lines removed with the observed spectra (see Figure 3), as well as how the telluric absorption could have left noises after the correction.

Among the 108 lines we examined in the observed spectra (Section 3.1), we detected 23 lines (Table 2). Figure 3 presents the spectra of some stars with the line detected. We here summarize the characteristics of the lines we identified, but more details on the lines of individual species are given in Appendix A. We detected two Zn I, three Sr II, and five Y II lines listed in all the three lists, KURZ, VALD, and MB99, but no other lines of these species were confirmed. We also detected one MB99 line of Eu II (10019.52 Å) together

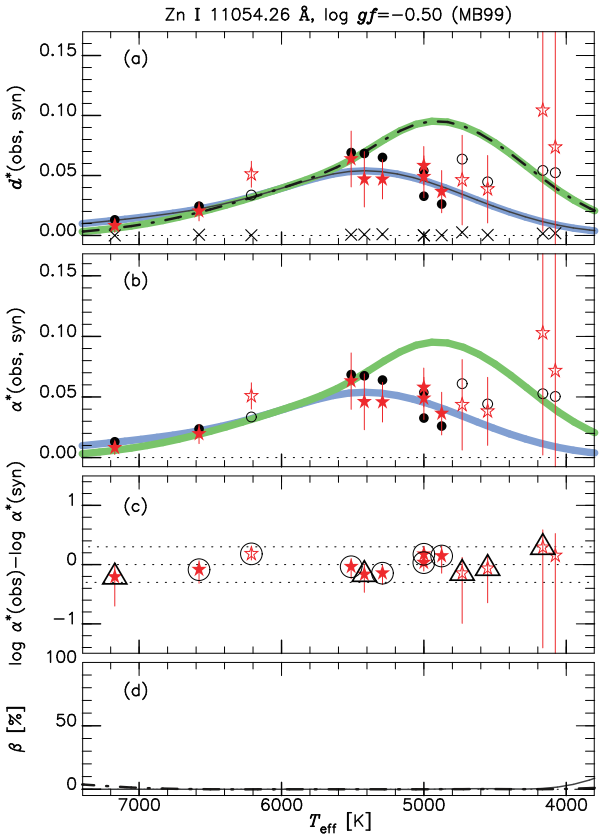

Figure 2. The temperature dependency of the line depths and blends. The species and wavelength of the line together with the $\log gf$ and its source (KURZ, VALD, or MB99) are labeled at the top. The top two panels plot the depths, d^*, and the contribution of the target lines themselves, α^*, against $T_{\rm eff}$. Both d^* and α^* are after the correction of metallicity and broadening (see Section 3.2). Star symbols indicate the measurements with the observed spectra of 13 objects; the open symbol for those with $\log g < 1.5$ and the filled symbol for those with $\log g > 1.5$. Open and filled circles indicate the values obtained with the synthetic spectra for the objects with $\log g < 1.5$ (open) and those with $\log g > 1.5$ (filled). The '×' symbol in the top panel indicates the depths in the synthetic spectra with the target lines excluded. The green and blue curves in the panels (a) and (b) indicate the $T_{\rm eff}$ trend of the target line itself expected for stars with 0.5 and 2.5, respectively, in $\log g$, while the dot–dashed and solid curves in the panel (a) indicate the corresponding trends of the depth including blends. In the third panel, we plot $\log \alpha^*_{\rm obs} - \log \alpha^*_{\rm syn} \simeq 0$ and the error against $T_{\rm eff}$ for the 13 objects. The star symbols in the panel (c) are accompanied by circles or triangles if we found significant ($\alpha_{\rm obs}/e > 2$) or marginal ($1 < \alpha_{\rm obs}/e < 2$) detection. The last panel shows the blends, β, for the synthetic spectra of stars with $\log g = 0.5$ (dot–dashed) and 2.5 (solid). The complete figure set (23 images) is available in the online journal.

with Eu II 9898.27 and 10165.56 that are not included in MB99. In addition, among the candidate lines which are not in MB99, we identified four Zr I, one Ba II, two Ce II, two Sm II, and one Dy II lines.

A few lines have been already reported in previous papers, besides MB99, based on high-resolution spectra. Although the temperature of the object is different from ours, Sameshima et al. (2018b) identified the two Sr II lines at 10327.31 and 10914.89 Å in a WINERED spectrum of an A0 V-type star. The same lines were used for measuring abundances of red supergiants by Origlia et al. (2013), and the one at 10914.89 Å was also identified by Hubrig et al. (2012) in peculiar A-type stars. In addition to these Sr II lines, we also confirmed the one at 10036.65 Å (a strong line listed in MB99). The Dy II line at 10835.94 Å reported by Hubrig et al. (2012) with spectra of peculiar A-type stars was not confirmed in any of our targets.

The 85 lines We could not confirm 85 candidate lines in the observed spectra. They include some lines listed in MB99: Zn I 13196.62, La II 11874.19, and six Ge I lines (see the notes on the individual elements in the Appendix). We found that there may be absorption by some of the unconfirmed lines, but rejected them either because the lines are not deep enough to be confirmed ($\alpha_{\rm obs}/e < 2$; e.g., Ce II 9774.63) or the telluric absorption seems to leave spurious noises (e.g., Sm II 9788.96). In addition, we found quite strong absorption at the wavelength of Dy II 10305.36, but did not conclude that the line was confirmed because the observed $T_{\rm eff}$ trend is not consistent with the prediction. The Dy II line, if exists, is at least contaminated by an unidentified line.

We examined $\log \alpha^*_{\rm obs} - \log \alpha^*_{\rm syn}$ and judged if the $\log gf$ values given in the line lists reproduce the depths of significant lines ($\log \alpha^*_{\rm obs} - \log \alpha^*_{\rm syn} \simeq 0$) or not. The superscript c in Table 2 indicates that the measured depths differ from those predicted with the given $\log gf$ by ∼0.3 dex or more. We note, however, that our conclusions on the $\log gf$ cannot be final because we only made comparisons with the synthetic spectra created with the solar [X/Fe] values assumed.

Table 2. Absorption lines identified in the observed spectra

Species	$\lambda_{\rm air}$	EP	$\log gf$ (dex)		
	(Å)	(eV)	KURZ	VALD	MB99
Zn I	11054.26	5.796	−0.20	−0.30	−0.50
Zn I	13053.60[a]	6.655	+0.39	+0.34	+0.13
Sr II	10036.65	1.805	−1.22	−1.31	−1.10
Sr II	10327.31	1.839	−0.25	−0.35	−0.40
Sr II	10914.89	1.805	−0.57	−0.64	−0.59
Y II	10105.52	1.721	−1.63	−1.89	−1.89
Y II	10186.46	1.839	−2.65[c]	−2.65[c]	−1.97
Y II	10245.22	1.738	−1.82	−1.82	−1.91
Y II	10329.70	1.748	−1.51	−1.76	−1.71
Y II	10605.15	1.738	−1.71	−1.96	−1.89
Zr I	9822.56	0.623	−1.44	−1.20	—
Zr I	10654.18	1.582	−1.32	—	—
Zr I	11612.67	1.366	−0.88	—	—
Zr I	11658.07	1.396	−0.56	—	—
Ba II	13057.72[b]	5.251	+0.34[c]	+0.34[c]	—
Ce II	9805.49	0.322	—	−3.23[c]	—
Ce II	9853.11	0.704	—	−2.49[c]	—
Sm II	9850.67	1.971	—	−0.46[c]	—
Sm II	9936.51	1.890	—	−0.61	—
Eu II	9898.30	2.108	−0.76[c]	−0.07	—
Eu II	10019.52	2.091	−0.66[c]	−0.66[c]	−0.30
Eu II	10165.56	2.108	−0.78	−0.78	—
Dy II	10523.39	1.946	—	−0.45	—

[a] The wavelength in the KURZ list, 13053.559 Å, is slightly different from the counterparts in the VALD, 13053.627 Å, and the MB99, 13053.64 Å.

[b] The wavelength in the KURZ list, 13057.716 Å, is shorter than the counterpart in the VALD, 13058.015 Å.

[c] The measured depths differ from those predicted with the given $\log gf$ by ∼0.3 dex or more.

4. DISCUSSION

4.1. *Astronomical implications*

In the following, we discuss the implications that individual elements with the detected line(s) may give to the chemical evolution of the Galaxy and nearby galaxies. We here focus on the chemical imprints one would find in Galactic-disk stars of around the solar metallicity. For stars with different metallicities or those in different systems, some elements may be explained by different origins. For example, Ba is an *s*-process element at around the solar metallicity but the contribution of the *r*-process gets stronger at the low-metallicity range (Burris et al. 2000). Moreover, there are proposed *n*-capture processes that show patterns different from those of the main *s*- and *r*-processes (e.g., Burris et al. 2009; Hampel et al. 2016). Our main targets, supergiants, are young and expected to be relatively metal rich, and previous explanations on the origins of the heavy elements in the Sun and the Solar system (Burris et al. 2000; Sneden et al. 2008) gives at least an approximate idea on the origins of individual elements in the supergiants.

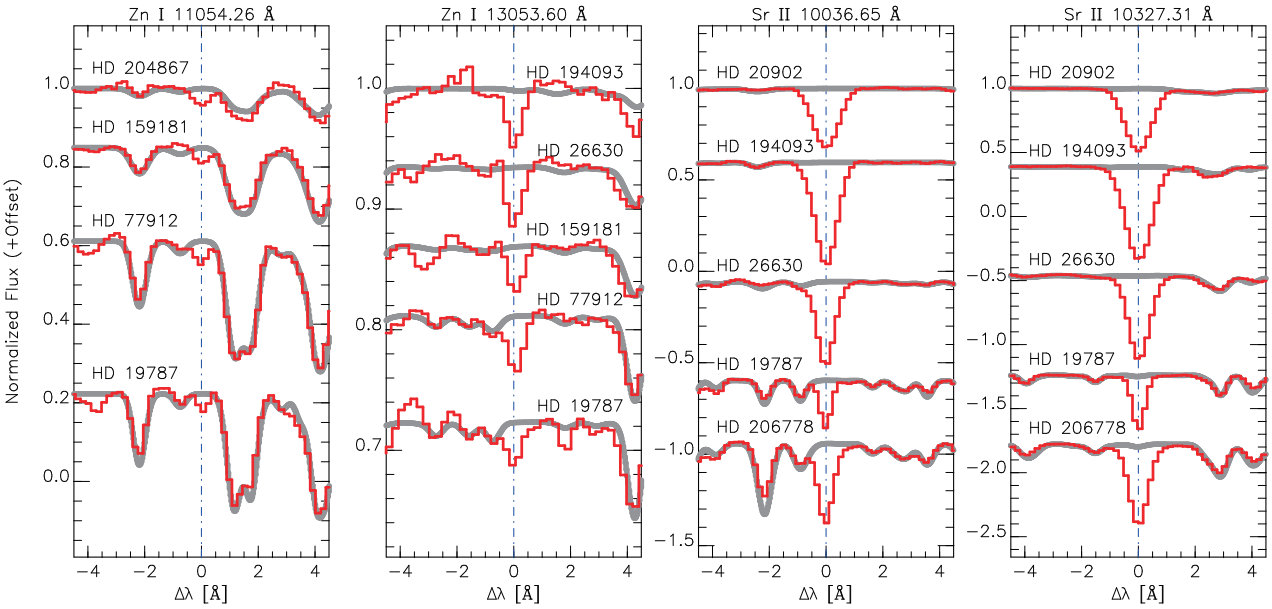

Figure 3. Spectra around the absorption lines detected. The species and the air wavelength, indicated by the vertical line, of each line are labeled at the top of each panel. The red and gray curves respectively indicate the observed spectra and the spectra synthesized without the target line included. The complete figure set (23 panels) is available in the online journal.

Zn is often included in the iron peak elements and considered as the heaviest one of this group. In fact, in a broad range of the metallicity down to [Fe/H] $\simeq -2$ dex, Zn in stars in the solar neighborhood shows a concentration around [Zn/Fe]$= 0$ and thus seems to be created along with Fe and other iron peak elements (Sneden et al. 1991). However, it has become clear that systematic differences in the [Zn/Fe] trends are found in different systems (thin and thick disks, bulge, halo, and dwarf galaxies) thanks to the efforts of various authors (Duffau et al. 2017; Ji & Frebel 2018; Hirai et al. 2018, and references therein). The origins of Zn remain still elusive and its implication to the Galactic chemical evolution may be unique compared with other better-understood elements (see, e.g., Tsujimoto & Nishimura 2018).

The s-process elements are created mainly in low- and intermediate-mass Asymptotic Giant Branch (AGB) stars. Good reviews on the process are found, e.g., in Busso et al. (1999) and Karakas, & Lattanzio (2014). Sr, Y, and Zr are grouped as light s-process elements, although they show slightly different trends from each other in disk stars (Delgado Mena et al. 2017). Ba and Ce are often called heavy s-process elements together with Nd. The abundance trends of the three heavy s-process elements are, however, not necessarily common. For example, Andrievsky et al. (2013, 2014) reported that the radial gradient of Ba has a negligible slope, while Lemasle et al. (2013) and da Silva et al. (2016) found significant slopes of the gradient for the other heavy s-process elements, Ce and Nd, as well as for Y and Zr, i.e., light s-process elements. As noted by Andrievsky et al. (2014) and Luck (2014), only strong Ba lines were used with non-LTE calculations, which may leave significant uncertainties. Readers are referred to other studies such as D'Orazi et al. (2009), Bensby et al. (2014), and references therein concerning the Ba abundances by using the strong lines in the optical, but their targets are dwarfs and giants. Ba II 13058.01 found in this study is, in contrast, expected to be weak; therefore, this line may add an important constraint on the Ba abundances. On the other hand, the three Sr II lines in the Y band are very strong and the same problem of the non-LTE effect may prevent us from obtaining accurate Sr abundances.

Eu is representative of r-process elements. Sm and Dy are considered to be mainly formed through the r-process around the solar metallicity (Burris et al. 2000). The contribution of the s-process to Sm can be larger, especially for some isotopes, but the trend of Sm seen in the disk stars with about the solar metallicity is similar to that of Eu (Battistini, & Bensby 2016). After the discovery of the gravitational wave and the electromagnetic counterpart of GW 170817 (Abbott et al. 2017), it has become more evident that the neutron star mergers accompanied by kilonovae are major contributors to r-process elements (Smartt et al. 2017; Tanaka et al. 2017). However, explaining the chemical evolution of r-process abundances seen in disk stars requires further investigations concerning some complications due, e.g.,

to the delay-time distributions of the neutron star mergers (Hotokezaka et al. 2018), the initial mass functions (Tsujimoto, & Baba 2019), and potential contribution from other origins (Siegel et al. 2019). New observational constraints on the r-process enrichment can be expected if the near-infrared diagnostic lines of Eu and Dy are used for measuring the abundances of stars in unexplored regions of the Galactic disk behind severe interstellar extinction.

4.2. *Expected targets*

The lines we report here will be useful diagnostic lines of detailed chemical abundances available in the YJ bands. In order to give a rough idea on the $(T_{\rm eff}, \log g)$ range in which the detected lines are seen, we present in Figure 4 the contours of $\alpha_{\rm syn} = d_{\rm syn} - d_{\rm syn\dagger}$ based on the synthetic spectra obtained for the $(T_{\rm eff}, \log g)$ grid (see Figure 1). Some lines are blended and may be difficult to measure the abundances even if α gets significant. Also, note that the depths refer to those expected for the spectra with the WINERED resolution, $R = 28000$, for stars with the solar metallicity, [Fe/H] = 0 dex, and sufficiently small broadening. Nevertheless, the contours will be useful, e.g., for selecting the targets to study the abundances discussed in this paper and making the observational plans to achieve the detection of the lines.

Only two species (Zn I and Zr I) among the 9 with the lines detected are neutral. In contrast, the others are singly ionized. The first ionization potentials of the elements with the detected lines are low, 5.2–6.2 eV, compared to Zn (9.4 eV) and Zr (6.6 eV). The lines of the ionized species are sensitive to $\log g$ and strong in low-gravity stars as expected. Furthermore, Figure 4 indicates that supergiants with $T_{\rm eff} \sim 5000$ K and $\log g \lesssim 1.5$ dex show the strongest absorption of the lines of Sr II, Y II, Ba II, Sm II, Eu II, and Dy II. The contours of Zn I are similar to those of the above species to some extent, the peak being around 5000 K and stronger towards the lower surface gravity, but the sensitivity to the gravity is not so high as the ionized species. In contrast, the lines of Ce II require both low temperature, $T_{\rm eff} < 4000$ K, and low surface gravity, $\log g < 1$, to be significant. In the case of Zr I, the line strengths grow rapidly towards low $T_{\rm eff}$ but are insensitive to surface gravity.

Cepheids have intermediate temperatures, 4500–6500 K, and low surface gravities, $\log g \lesssim 1.5$ dex (see, e.g., Genovali et al. 2014). Their locations on the Hertzsprung-Russell diagram (HRD) thus agree with the peaks of the strengths for most of the lines reported in this paper, although Zr I may be seen only in Cepheids with the lowest $T_{\rm eff}$ among this group of pulsating stars in the Cepheid instability strip. Therefore, YJ-band spectra of Cepheids would allow us to measure various heavy elements including both s- and r-process elements and also those with mixed origins such as Zn.

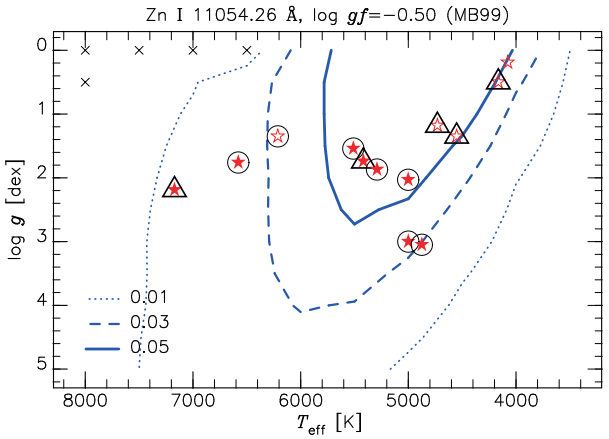

Figure 4. Contours of the predicted depths of the lines we detected. The species and wavelength of the line together with the $\log gf$ and its source (KURZ, VALD, or MB99) are labeled in the top of each panel. The contours of $\alpha_{\rm syn}$ for the levels indicated within each panel are created based on the synthetic spectra with the solar abundance and the broadening $v_{\rm b} = 10.7\,{\rm km\,s^{-1}}$ for the grid of $(T_{\rm eff}, \log g)$ illustrated in Figure 1. We note that the grid lacks the points indicated by the '×' symbol. The star symbols (open if $\log g < 1.5$ and filled if $\log g > 1.5$) indicate the observed targets in this study, and they are accompanied by circles or triangles if we found significant ($\alpha_{\rm obs}/e > 2$) or marginal ($1 < \alpha_{\rm obs}/e < 2$) detection of the line. The complete figure set (23 images) is available in the online journal.

Cepheids are young, 10–300 Myr old, and provide valuable information on chemical abundances of the present Galaxy. It is known that their metallicities are anti-correlated with the distances from the Galactic center ($R_{\rm GC}$), known as the abundance gradient (Genovali et al. 2014). Observing Cepheids in a wide range of $R_{\rm GC}$ thus allows investigating the abundance patterns from the metal-rich end ([Fe/H]$\sim +0.2$ at $R_{\rm GC} \leq 6$ kpc) to the metal-poor end ([Fe/H]$\lesssim -0.3$ at $R_{\rm GC} \geq 14$ kpc) of the current Galactic disk. The youth of Cepheids offers a crucial advantage in studying the disk chemical evolution. The radial migration of the disk (Sellwood & Binney 2002) affects the current abundance distribution of various elements for stars in the disk (e.g., see a recent study on the r-process abundance in the solar neighborhood by Tsujimoto, & Baba 2019). Cepheids are, however, considered to be located almost at their birth positions in terms of $R_{\rm GC}$ and tell us, at least approximately, the current abundances of star-forming gas. Recent large-scale surveys have

found a large number of new Cepheids spread in a large range of $R_{\rm GC}$ (Udalski et al. 2018; Chen et al. 2019; Dékány et al. 2019; Skowron et al. 2019), and some of them are heavily reddened in the Galactic disk. Near-infrared spectroscopic observations are desired to obtain their abundances.

Bright red giants, roughly $T_{\rm eff} \lesssim 5000\,{\rm K}$ and $1 \lesssim \log g \lesssim 2\,{\rm dex}$, are often targeted for investigating the heavy elements in nearby dwarf galaxies (e.g., McWilliam et al. 2013; Ji et al. 2016; Ji & Frebel 2018). Sr II and Zr I lines are expected to be strong, while Y II lines are probably weak, $\lesssim 0.05$ in depth. Some Eu II lines may also be seen but the abundance measurements would require high signal-to-noise ratios with the typical depths expected to be around $\sim$0.02 or smaller. Observing the lines of other heavy elements would be even more challenging. Bright red giants are important because they are usually the easiest targets in stellar systems like the Galactic bulge and dwarf galaxies which are dominated by old stars. Measuring their Eu abundances, if possible, would be very useful for studying the chemical evolution of those systems together with the s-process abundances traced with Sr and Zr.

At the lower parts of the Hertzsprung-Russell diagram, $\log g \lesssim 3$, only a small fraction of the lines reported in this study are expected to be visible. The three Sr II lines are expected to be still strong, $\gtrsim 0.2$, for a wide range of $T_{\rm eff}$. In fact, Caffau et al. (2016) detected the three lines and estimated the abundances by taking into account the non-LTE effect. The two Zn I lines may be seen in stars with intermediate temperatures around 5500 K, while Zr I 9822.56 is expected to be visible only in late-type stars with $T_{\rm eff} < 5000\,{\rm K}$. None of the other species is probably significant unless the abundances are highly enhanced.

5. SUMMARY

We identified 23 lines of 9 elements heavier than the iron group elements, i.e., Zn, Sr, Y, Zr, Ba, Ce, Sm, Eu, and Dy, using the YJ-band WINERED spectra of 13 supergiants and giants. Besides the lines we detected, significantly more lines of the targeted heavy elements were selected based on KURZ and/or VALD but not detected. We also found lines that are clearly present in the observed spectra but are not predicted in the synthetic counterparts (Appendix B). It is vital to establish the list of lines of various elements in the infrared range.

Although we have identified the absorption lines of rare heavy elements, including newly detected lines, there remains a lot to be done. Further searches for new lines should be performed. Our search was done by using WINERED spectra with the resolution of 28000 with the typical S/N around 200–300. It would be useful to make a more complete survey of the relevant absorption lines by using spectra with higher resolution and/or higher quality, although the resolution of 28000 is high enough to resolve the intrinsic line profiles of many supergiants. Solid estimates of $\log gf$ values are also important for abundance measurements with these lines especially because the numbers of lines are small. For this purpose, our targets and dataset are not optimal. For example, relatively metal-poor stars with enhanced abundances of s-process or r-process elements (e.g., Sneden et al. 2008; Bisterzo et al. 2011) would be good calibrators because the lines of the enhanced elements can be measured with reduced line contamination.

We thank Andy McWilliam for useful comments on the analysis and the manuscript. We are grateful to the staff of the Koyama Astronomical Observatory for their support during our observation. This study is financially supported by JSPS KAKENHI (grant No. 16684001, 20340042, 21840052, 26287028, and 18H01248) and the MEXT Supported Program for the Strategic Research Foundation at Private Universities, 2008–2012 (No. S0801061) and 2014–2018 (No. S1411028). HS acknowledges the JSPS grant No. 19K03917. This study has made use of the SIMBAD database, operated at CDS, Strasbourg, France, and also the VALD database, operated at Uppsala University, the Institute of Astronomy RAS in Moscow, and the University of Vienna. We thank the referee, Prof. Robert Kurucz, for comments that helped us to improve this paper.

Software: WINERED pipeline (Hamano et al., in preparation), IRAF (Tody 1986, 1993), PyRAF (Science Software Branch at STScI 2012), MOOG (February 2017 version; Sneden et al. 2012).

APPENDIX

A. IDENTIFICATION OF LINES OF INDIVIDUAL ELEMENTS

Here we describe the identification (or the failure of confirmation) of the lines of the heavy elements using the WINERED spectra of 13 objects (Table 1). We examined 108 lines of 14 species in total. Table 2 lists the 23 detected lines.

- Zn (Zinc, $Z = 30$) — We investigated four Zn I lines using the observed spectra. The line at 13150.5 Å (13150.464 Å in KURZ and 13150.533 Å in VALD) is not included in MB99, but the other three are included. We clearly detected two lines at 11054.26 and 13053.60 Å, which are free from blends at most of the $T_{\rm eff}$ range we investigated. For each line of them, the $\log gf$ values in KURZ and VALD are consistent within 0.1 dex, but the $\log gf$ in MB99 is different by 0.15–0.3 dex. The $\log gf$ values in MB99 seem to give better agreements between the predicted and measured depths for both of the lines although the differences between the three lists are not large. Among the two lines that were not confirmed, Zn I 13150.5 is dominated by the strong blending line, Al I 13150.75. The other one, Zn I 13196.6, also suffers from significant blends especially at lower $T_{\rm eff}$, if exists, and it tends to be affected by telluric lines too. KURZ and VALD list slightly different wavelengths, within 0.1 Å, for the two undetected lines but these lines are not detected in the observed spectra in any case.

- Ga (Gallium, $Z = 31$) — We investigated two Ga I lines, included in both KURZ and VALD, using the observed spectra. Neither of them is included in MB99 although their wavelengths are longer than 10000 Å. They were predicted to be significant, $\gtrsim 0.02$, only at the lowest temperatures, $T_{\rm eff} \lesssim 4000$ K. Moreover, both of them are strongly blended with other lines ($\gtrsim 80$ %), and we could confirm none of the Ga I lines. Around the wavelength of Ga I 11949.23, Ti I 11949.55 gives strong absorption at lower $T_{\rm eff}$ and Ca II 11949.74 gives strong absorption at higher $T_{\rm eff}$. Around Ga I 12109.85, Si I 12110.66 gets stronger towards the lower $T_{\rm eff}$.

- Ge (Germanium, $Z = 32$) — We investigated eight Ge I lines using the observed spectra. All of them are located at longer than 10000 Å. One line at 11714.75 Å is listed in all the three lists. In addition, three lines are listed only in KURZ and VALD, while four lines only in MB99. The Ge I lines are expected to get strongest at around 4500 K, but most of the lines we investigated do not reach 0.05 in $\alpha^*_{\rm syn}$ according to the $\log gf$ values available in the lists. Some lines are expected to be strongly blended while others are not, but we could not confirm any of the Ge I lines. The $\alpha^*_{\rm obs}$ we obtained are consistent with zero for almost all of the objects expected to show the Ga absorption, which indicates that the $\log gf$ values are at least smaller than expected.

- Sr (Strontium, $Z = 38$) — We investigated nine Sr II lines using the observed spectra. Three of them (10036.65, 10327.31, and 10914.89 Å) are listed in all the three line lists. These lines are strong and there are almost no blends. The $\log gf$ values in the three lists are more-or-less consistent with each other, within 0.2 dex, and they give reasonable agreements between the observed and synthetic spectra. We note that these three lines are very deep and the departures from the predicted depths may well be caused by the factors, other than inaccurate $\log gf$ values, that were not taken into account in our simple spectral synthesis (e.g., the non-LTE effect). In contrast, we could confirm no other Sr II lines. The reduced spectra of a couple of objects present a hint of Sr II 12974.38, but telluric absorption lines around this wavelength seem to give spurious noise on the spectra. We also found non-zero $\alpha_{\rm obs}/e$ for Sr II 12013.96 in a few objects, but the dependency of the depth on $T_{\rm eff}$ and $\log g$ is not consistent with predicted for this line. There is one Fe I line at 12013.88 Å, and the $\alpha_{\rm obs}$ we measured could be explained by the error in oscillator strength of this line with a $\log gf$ larger than listed. For Sr II 13121.96, two entries with different $\log gf$ values, 0.692 and -0.609 dex, are listed in VALD with the same wavelength and the same excitation potential (EP). Including or excluding the shallower one with $\log gf = -0.609$ does not change the synthetic spectra significantly and, in any case, the absorption was not confirmed in the observed spectra.

- Y (Yttrium, $Z = 39$) — We investigated two Y I and five Y II lines using the observed spectra. The Y I lines are not included in MB99, while it lists all the Y II lines. The Y I lines were predicted to be visible at very low temperatures, around 3500 K, but still shallow, $\sim$0.03; we could not confirm them in the observed spectra. In contrast, we detected all the five Y II lines. All of them except Y II 10605.15 are significantly blended at least at $T_{\rm eff} \lesssim 5000$ K, but the Y II lines are expected to get deepest at 5000–5500 K and this dependency on $T_{\rm eff}$ can be well traced with our measurements. The $\log gf$ values in MB99 reproduce the observed depths better for Y II 10186.46, while the $\log gf$ values in the three lists are at least roughly consistent with each other and they predict reasonable depths for the other four lines.

- Zr (Zirconium, $Z = 40$) — We investigated 40 Zr I lines using the observed spectra. Two lines are listed in both KURZ and VALD, while the other 38 lines are found in KURZ only. None of them is listed in MB99. We confirmed four lines in a few objects at low $T_{\rm eff}$ without significant blends. One of them is listed in both KURZ and VALD, while the others are given in KURZ only. The $\log gf$ values in the KURZ list give reasonable

predictions of the depths observed where the detection is significant. We note that the observed and synthetic spectra show poor agreements around Zr I 10654.18 (see the online material for Figure 3). The absorption line observed at around 10657.4 Å is listed as an unknown one in Table 3. In addition, the observed spectra show broad and stronger absorption than the synthetic ones at around 10652 Å, which indicates that more than one lines contribute to the observed absorption but the line lists used for the synthetic spectra give too low $\log gf$ values or completely miss necessary lines. A part of the inconsistency can be explained by the low $\log gf$ values, approximately −2.8 dex, of Fe I 10652.24 (EP=5.478 eV) in KURZ and VALD, whose $\log gf$ in MB99 is significantly higher, −1.79 dex. At least one other line is necessary to explain the wide absorption observed, and CN 10651.796 but with $\log gf$ higher than given in VALD would probably explain the absorption in combination with the Fe I line.

- Ba (Barium, $Z = 56$) — We investigated one Ba II line using the observed spectra. This line is listed in KURZ and VALD but not in MB99. The wavelengths in the former two catalogs are slightly different, 13057.716 Å in KURZ and 13058.015 Å in VALD. Synthetic spectra indicate: (i) The line gets deepest at around 5300 K. (ii) It becomes shallower and shallower with increasing $\log g$, and the d^* never reaches 0.01 at $\log g \gtrsim 2.5$ dex. (iii) There are strong blends throughout the temperature range from 4000 to 8000 K; 30 % or higher (reaching almost 100 %) at $\lesssim 4,500$ K and $\log g = 0.5$ dex, and 50 % or higher at $\log g = 2.5$ dex. The absorption by this Ba II line is supported by the observed spectra of a few objects with $T_{\rm eff} > 5000$ K where the blends are moderate. The overall result indicates that the detection of this line is solid, but the confirmation based on more spectra is desirable. The observed depths, where significant, are larger than predicted based on the synthetic spectra by a factor of ∼3, although this may be because we assumed the solar abundance ratio of Ba to the metallicity, i.e., [Ba/Fe]= 0.

- La (Lanthanum, $Z = 57$) — We investigated one La II line, 11874.19 Å, using the observed spectra. This line is included in both VALD and MB99 but not in KURZ. Based on the synthetic spectra, the line is expected to be as deep as 0.05 in many objects at $T_{\rm eff} \lesssim 6000$ K and reach ∼0.2 in depth in the two lowest-$T_{\rm eff}$ objects. However, the depths we measured are consistent with zero for most objects and we could not confirm this line in any of the observed spectra.

- Ce (Cerium, $Z = 58$) — We investigated 22 Ce II lines using the observed spectra. All of these are at $\lambda < 10000$ Å and listed in VALD, but not included in KURZ or MB99. Most of the lines are expected to be significantly blended with other lines. We detected two lines at 9805.49 Å and 9853.11 Å; they are also blended with other lines, but clearly appear in the shoulders of the contaminating lines. The observed depths of the two lines, where significant, are larger than predicted based on the synthetic spectra by a factor of ∼5. There may be a couple of other Ce II lines visible in the observed spectra, although we could not conclude that they are real. In the case of Ce II 9774.63, the spectra of the two objects with the lowest $T_{\rm eff}$ show absorption, but their $\alpha_{\rm obs}/e$ values, 1.5–1.8, suggest that the detection is marginal. While no significant blend of stellar lines is expected, the telluric absorption may disturb the observed spectra at around this line. The $\alpha_{\rm obs}/e$ values for Ce II 9889.47 are significant for a couple of objects with low $T_{\rm eff}$, but strong blending lines, Fe I 9889.035 and CN 9890.1513, prevent us from confirming it. There seems to be an absorption line at the wavelength of Ce II 9949.45 in a few objects, but it looks more significant in stars with intermediate $T_{\rm eff}$, 5000–6500 K. Such $T_{\rm eff}$ dependency is inconsistent with the $T_{\rm eff}$ trend of the Ce II line predicted with the synthetic spectra.

- Sm (Samarium, $Z = 62$) — We investigated four Sm II lines using the observed spectra. They are listed in VALD, but KURZ includes none. One of them is at $\lambda > 10000$ Å but not listed in MB99. We found that all the four lines may be present but it is not easy to make firm conclusions. The predicted depths of these lines are rather small; α is expected to be smaller than ∼0.03 in our objects except the two with the lowest $T_{\rm eff}$, ∼4100 K. In the low-$T_{\rm eff}$ objects, however, larger depths are predicted to be accompanied by severe blends, and we could not confirm any Sm II line significantly. In contrast, we made significant and marginal detections of some lines in warmer objects. For Sm II 9850.67 and 9936.51 (included in Table 2), the significant absorption was found in two objects for the former and in three objects for the latter in addition to marginal detections in a few more objects. The $\alpha_{\rm obs}/e$ for Sm II 10083.34 was ∼2.5 for the coolest objects, HD 52005, and marginal, 1–2, in a few objects. However, this line is significantly blended with Cr I 10083.18, and the $T_{\rm eff}$ trend of the $\alpha_{\rm obs}$ is similar to that of the contaminating line. We could not confirm the presence of this Sm II line. We also found that $\alpha_{\rm obs}/e$

for Sm II 9788.96 is not zero for some objects; larger than 2 for HD 20902 and 1–2 for HD 194093 and HD 204867. In this case, however, the dependency of the absorption on $T_{\rm eff}$ and $\log g$ is inconsistent with the prediction based on the synthetic spectra. In addition, this line is located where the telluric absorption is relatively strong (Sameshima et al. 2018a). In this paper, we conclude that we detected the two lines, Sm II 9850.67 and 9936.51, but further confirmation and characterization based on spectra of higher resolution and/or higher quality are desired for all the four candidate lines.

- Eu (Europium, $Z = 63$) — We investigated five Eu II lines using the observed spectra. The one at 10019.52 Å is listed in MB99. We detected this line in addition to two new lines at 9898.30 and 10165.56 Å. For all of them, the detection is clearest in HD 194093, which is enhanced in rare-earth elements as mentioned in Section 2.1. We also found that the three lines are significant or at least marginally significant in HD 204867, while they were marginally detected in a few more objects. For Eu II 10019.52, $\alpha_{\rm obs}/e$ are approximately 8 and 4 for HD 194093 and HD 204867, respectively. The $\log gf$ in MB99 seems to predict the observed depths slightly better than the values in KURZ and VALD. The synthetic spectra predict that Fe I 11019.79 and Si I 10020.07 similarly contaminate the Eu II line for the two objects. While the Fe I line is included in both VALD and MB99 and its EP and $\log gf$ are consistent in the two lists, the Si I line is not included in MB99. The latter is much weaker than suggested with the VALD list even if it exists, and this explains the inconsistency between the observed and synthetic spectra presented in Figure 3 (see the panel for Eu II 10019.52 available as the online material). For the other two lines detected, 9898.30 and 10165.56 Å, there are telluric lines that may disturb the detection of the Eu II lines. We examined the spectra before and after the telluric correction together with the telluric spectra and also the target spectra of individual exposures, and they suggest that the Eu II lines are real. The other two lines at 10034.22 and 10142.99 Å were not detected.

- Dy (Dysprosium, $Z = 66$) — We investigated four Dy II lines, listed in VALD only, using the observed spectra. None of them are found in MB99 although three are located at $\lambda > 10000$ Å. The KURZ list does not include those lines either. We clearly detected the line at 10523.39 Å in several objects although the overall fits between the observed and synthetic spectra tend to be poor in the surrounding wavelength range. For this line, the $\log gf$ in VALD predicts reasonable depths that are comparable with the measured. We found clear absorption at the wavelength of Dy II 10305.36 in many objects. The absorption line looks reasonably isolated except the objects with the lowest $T_{\rm eff}$. However, the measured depths are significantly larger than predicted by ∼0.8 dex in the logarithm of depth. Moreover, the temperature dependency of the depths does not follow the prediction well. In fact, the trend of $\alpha^*_{\rm obs}$ is similar to some of the unidentified lines, discussed in Section B, that get stronger towards the lower temperature, while Dy II should get strongest at around 5000 K. Although this Dy II line may exist, there seems to be an unidentified line, at almost the same wavelength, which makes it hard to confirm the Dy II line. We cannot include this line in the list of confirmed lines. The other two lines, Dy II 9763.05 and 10835.94, were not detected.

- Er (Erbium, $Z = 68$) — We investigated one Er II line using the observed spectra. This line at 11059.56 Å is not listed in KURZ or MB99. According to the prediction based on the synthetic spectra, the line is shallow across the temperature range we investigated. The depth may be as deep as ∼0.03 only in stars with $T_{\rm eff} \sim 5000$ K and $\log g \lesssim 0.5$, but such objects were not included in this study and we could not detect this line in any object.

B. DETECTION OF UNIDENTIFIED LINES

Some lines are clearly significant in the observed spectra but not found in the synthetic spectra. Table 3 lists such unidentified lines whose depths are sufficiently large, ∼0.05 or more, at least in a few objects and show systematic trends with $T_{\rm eff}$. Spectra of five objects, regardless of the significance in each object, around the wavelengths of the unidentified lines are presented in Figure 5 with which one can trace the $T_{\rm eff}$ trend of each line between 4000 and 7200 K. The KURZ list was used for the synthetic spectra in Figure 5, but none of the KURZ, VALD, and MB lists has the unidentified lines. Many of the lines get deeper towards the lower (or higher) end of the $T_{\rm eff}$ range we investigated, but some lines show a peak within the temperature range of our targets or a rather flat trend (e.g., 9994.9 and 12571.1 Å).

Table 3. Absorption lines not predicted by the synthetic spectra

$\lambda_{\rm air}$ (Å)	Comments
	Y band
9994.9	Blended at $T_{\rm eff} \lesssim 5000$ K by a couple of CN lines (the strongest is at 9995.10 Å), but there is an unknown line which gets strongest at around 5500 K.
10071.8	Stronger towards the lower temperature.
10133.5	Stronger towards the lower temperature. Maybe this is the Fe I line listed in both KURZ and VALD at a different wavelength, 10134.21 Å, that has no counterpart in the observed spectra (see text).
10163.6	Synthetic spectra have almost no absorption at around 4500–5000 K, but a clear line was detected. Fe II 10163.606 may be present in some objects, but it is expected to be significant only at > 5000 K.
10185.5	Stronger towards the lower temperature.
10243.7	Stronger towards the lower temperature.
10271.2	Stronger towards the lower temperature.
10273.1	Stronger towards the lower temperature. There are two lines, CN 10272.93 Å and Ca I 10273.68 Å, blending with this unknown line, but they cannot explain the absorption detected.
10277.3	Stronger towards the lower temperature.
10305.3	Stronger towards the lower temperature.
10338.5	Stronger towards the lower temperature.
10387.1	Stronger towards the lower temperature.
10427.3	Stronger towards the lower temperature.
10434.0	There are a couple of contaminating CN lines dominant at $\gtrsim 5000$ K, but this unknown line is stronger towards the higher temperature. It is probably C I 10433.35 listed in KURZ (but not in VALD) which is not seen in the observed spectra at the given wavelength.
10476.5	Synthetic spectra have almost no absorption at $T_{\rm eff} \gtrsim 4500$ K, but there is a clear line whose depth seems to show a peak at ∼5000 K. This line may be a CN line (see text).
10512.8	Stronger towards the lower temperature.
10542.5	Synthetic spectra have almost no absorption at $T_{\rm eff} \gtrsim 4500$ K, but there is a clear line whose depth seems to show a peak at 4500–5000 K.
10549.5	Blended with N I 10549.64 at $T_{\rm eff} \gtrsim 6000$ K and with Cr I 10550.095 at $T_{\rm eff} \lesssim 4500$ K, but there is clearly a line, unexpected in the synthetic spectra, whose depth seems to show a peak at the intermediate $T_{\rm eff}$ range.
10587.1	Strongest at around 4500–5000 K.
10625.4	Stronger towards the lower temperature. Synthetic spectra have almost no absorption at this wavelength at the entire $T_{\rm eff}$ range. The observed absorption resembles Fe I 10622.592 in the synthetic spectra although the latter is not confirmed in the observed spectra.
10657.4	Stronger towards the lower temperature.
10696.5	Observed spectra seem to show two lines not visible in the synthetic spectra. One of them gets stronger towards the lower temperature, while the other is seen at around 6000 K.
11050.3	Stronger towards the lower temperature and seen at only $T_{\rm eff} \lesssim 5000$ K.
11083.7	Stronger towards the lower temperature and seen at only $T_{\rm eff} \lesssim 5000$ K.
	J band
11742.0	Stronger towards the lower temperature and seen at only $T_{\rm eff} < 5000$ K.
11784.9	Stronger towards the lower temperature.
11833.0	Stronger towards the lower temperature.
11910.6	Stronger towards the lower temperature and seen at only $T_{\rm eff} \lesssim 5000$ K. At the higher $T_{\rm eff}$, in contrast, a weak line of C I is visible at 11910.62 Å.
11923.2	Stronger towards the lower temperature.

Table 3 continued

Table 3 *(continued)*

$\lambda_{\rm air}$ (Å)	Comments
12097.5	Stronger towards the lower temperature and seen at only $T_{\rm eff} \lesssim 5000$ K. At the higher $T_{\rm eff}$, in contrast, a weak line of C I is visible at 12097.49 Å.
12290.7	Blended with CN 12291.332, but clearly present in a wide range of $T_{\rm eff}$ and stronger towards the lower temperature.
12351.8	Strongest at around the intermediate temperatures, ∼5000 K.
12357.9	Stronger towards the lower temperature.
12457.0	Seems to be stronger towards the lower temperature, but the $T_{\rm eff}$ dependency is weak.
12476.9	Strongest at around 5000 K.
12499.8	Blended with a couple of CN lines at $T_{\rm eff} \lesssim 5000$ K, but there is a line showing a different trend with a peak at ∼5000 K.
12571.1	The $T_{\rm eff}$ trend seems flat for a wide $T_{\rm eff}$ range, 4000–5500 K.
12635.0	Strongest at around the intermediate temperatures, ∼5000 K.
12658.9	The $T_{\rm eff}$ trend seems consistent with that of the combination of two lines of Ni I at 12655.38 and 12655.60 Å listed in both KURZ and VALD (see text).
12737.8	Blended with Ti I 12738.383 together with other weaker lines, but there is a clear line, at the shoulder of the Ti I line, which is unexpected in the synthetic spectra.
12884.8	Stronger towards the lower temperature.
12916.3	Stronger towards the lower temperature.
13016.4	Stronger towards the lower temperature.
13088.8	There are strong telluric absorption lines around this wavelength, but there is a reasonably strong line which shows a well-behaved trend with the temperature, getting stronger towards the lower temperature.

Table 3 does not include lines which appear both in the observed and synthetic spectra consistently even if the predicted depths are significantly shallower than those in the observed. For example, the observed spectra show a clear line at 10516.1 Å which is almost invisible in the spectra synthesized with KURZ or VALD. This line is probably Ca I 10516.14 (EP=4.74 eV, $\log gf = -0.52$ dex) as listed in MB99. VALD and KURZ also list this line but give a significantly smaller $\log gf$ value, −1.438 dex. If we use the $\log gf$ in MB99 for the spectral synthesis, the line observed is explained reasonably well. Therefore, we do not include this line in Table 3. In fact, inconsistency in line strengths between the observed and synthetic spectra is found in many lines, e.g., Mg I 12456.935 and a pair of N I 12461.25 and CN 12460.83 that give different contribution according to $T_{\rm eff}$, showing much stronger absorption in the observed; they are outside the scope of this paper and not included in Table 3.

As long as one of the three lists (KURZ, VALD, and MB99) gives good identification of the observed feature, Table 3 does not include such a line even if the other two lists cannot explain the feature. For example, we found that Fe I 10452.75 (EP=3.88 eV) is listed in MB99 but not in KURZ and VALD. While warmer stars ($T_{\rm eff} \gtrsim 5000$ K) show a C I line listed in all the line lists almost at the same wavelength, the absorption in low-$T_{\rm eff}$ stars requires the Fe I line in MB99. Moreover, this line was included in the abundance measurements by Kondo et al. (2019) and gave [Fe/H] values within 0.03 dex of the final results based on dozens of Fe I lines. In the case of S I 10635.97 listed in MB99, in contrast, KURZ and VALD list this line with the wavelength of 10633.08 Å. The observed spectra show the absorption at around the wavelength given in MB99. The EP and $\log gf$ of this line are consistent in all the three lists, and the predicted depths as a function of $T_{\rm eff}$ agree with those observed.

For some of the unidentified lines in Table 3, different lines at almost the same wavelength were confirmed in both observed and synthetic ones at a particular $T_{\rm eff}$ range but the observed spectra show unexpected absorption with a completely different trend against the temperature, which indicates the presence of the unidentified lines. At around 10434.0 Å, for example, a CN line is seen at lower temperatures, $T_{\rm eff} \lesssim 5500$ K, and this line appears in both the observed and synthetic spectra. However, we found another line, which is the unidentified line we report, growing with increasing $T_{\rm eff}$.

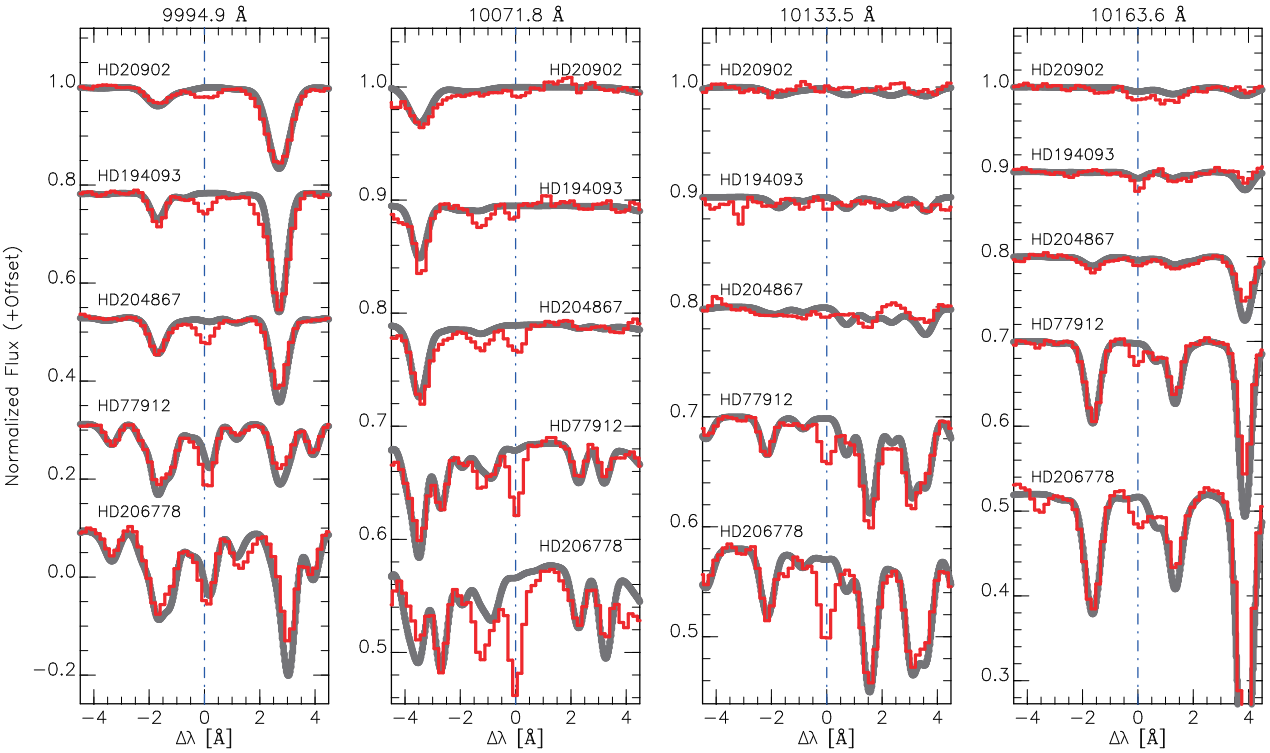

Figure 5. Absorption lines that were not predicted in the synthetic spectra (Table 3). The red and gray curves indicate the observed and synthetic spectra, respectively. The wavelength of each line is indicated by the vertical line and labeled at the top of each panel. The spectra of five stars with different $T_{\rm eff}$ (increasing from top to bottom) are presented, even if the given line is not seen in each star, to show its dependence on $T_{\rm eff}$. The complete figure set (45 panels) is available in the online journal.

Some lines in Table 3 seem to have counterparts in some line lists but at different wavelengths (and no list gives the observed wavelength). In the following, we give remarks on such lines that seem to give the corresponding absorption, in the observed spectra, at shifted wavelengths and show the consistent $T_{\rm eff}$ trends as predicted.

10133.5 Å — The Fe I line listed in KURZ and VALD with the wavelength of 10134.21 Å roughly follows the $T_{\rm eff}$ trend of the absorption at 10133.5 Å in the observed spectra. The observed spectra do not show the absorption at 10134.21 Å. The predicted $T_{\rm eff}$ trend of the Fe I line is slightly different by itself from the observed at the lowest temperatures around 4000 K, but this deviation may be explained by the blend with Ti I 10133.39 and some molecular lines. No line is listed in MB99 around this wavelength.

10476.5 Å — The observed $T_{\rm eff}$ trend may be explained by a CN line. There is, in fact, one CN line at 10475.295 Å, listed in KURZ and VALD, which appears rather shallow in the observed spectra even if it exists. Maybe the wavelength in VALD should be replaced by 10476.5 Å or, instead, there is another CN line which gives the observed wavelength and strengths. No line is listed in MB99 around this wavelength.

12658.9 Å — Interestingly, the feature predicted with two Ni I lines at 12655.38 and 12655.60 Å shows the $T_{\rm eff}$ trend consistent with the observed, but no significant absorption was observed in our 13 targets at the given wavelengths. The two Ni I lines, present in both KURZ and VALD, seem to give similar contributions to the feature, although MB99 lists only one line at 12655.60 Å.

REFERENCES

Abbott, B. P., Abbott, R., Abbott, T. D., et al. 2017, PhRvL, 119, 161101

Adams, W. S., & Joy, A. H. 1926, PASP, 38, 322

Adams, W. S., & Joy, A. H. 1927, Proceedings of the National Academy of Science, 13, 393

Afşar, M., Sneden, C., Wood, M. P., et al. 2018, ApJ, 865, 44

Andreasen, D. T., Sousa, S. G., Delgado Mena, E., et al. 2016, A&A, 585, A143
Andrievsky, S. M., Lépine, J. R. D., Korotin, S. A., et al. 2013, MNRAS, 428, 3252
Andrievsky, S. M., Luck, R. E., & Korotin, S. A. 2014, MNRAS, 437, 2106
Asplund, M., Grevesse, N., Sauval, A. J., & Scott, P. 2009, ARA&A, 47, 481
Battistini, C., & Bensby, T. 2016, A&A, 586, A49
Bensby, T., Feltzing, S., & Oey, M. S., 2014, A&A, 562, A71
Bisterzo, S., Gallino, R., Straniero, O., et al. 2011, MNRAS, 418, 284
Böcek Topcu, G., Afşar, M., Sneden, C., et al. 2019, MNRAS, 485, 4625
Burris, D. L., Pilachowski, C. A., Armandroff, T. E., et al. 2000, ApJ, 544, 302
Burris, D., Lusk, J., & Jones, E. M. 2009, PASP, 121, 111
Busso, M., Gallino, R., & Wasserburg, G. J. 1999, ARA&A, 37, 239
Caffau, E., Andrievsky, S., Korotin, S., et al. 2016, A&A, 585, A16
Chen, X., Wang, S., Deng, L., et al. 2019, Nature Astronomy, 3, 320
Chojnowski, S. D., Hubrig, S., Hasselquist, S., et al. 2019, ApJL, 873, L5
Cunha, K., Smith, V. V., Hasselquist, S., et al. 2017, ApJ, 844, 145
da Silva, R., Lemasle, B., Bono, G., et al. 2016, A&A, 586, A125
Dékány, I., Hajdu, G., Grebel, E. K., & Catelan, M. 2019, ApJ, 883, 58
Delgado Mena, E., Tsantaki, M., Adibekyan, V. Z., et al. 2017, A&A, 606, A94
D'Orazi, V., Magrini, L., Randich, S., et al. 2009, ApJ, 693, L31
Duffau, S., Caffau, E., Sbordone, L., et al. 2017, A&A, 604, A128
Genovali, K., Lemasle, B., Bono, G., et al. 2014, A&A, 566, A37
Gratton, F., Bragaglia, A., Carretta, E., & Tosi, M. 2006, ApJ, 642, 462
Gray, D. F., & Toner, C. G. 1986, ApJ, 310, 277
Gray, R. O., Graham, P. W., & Hoyt, S. R. 2001, AJ, 121, 2159
Hasselquist, S., Shetrone, M., Cunha, K., et al. 2016, ApJ, 833, 81
Hekker, S., & Meléndez, J. 2007, A&A, 475, 1003
Hampel, M., Stancliffe, R. J., Lugaro, M., & Meyer, B. S. 2016, ApJ, 831, 171
Hirai, Y., Saito, T. R., Ishimaru, Y., & Wanajo, S. 2018, ApJ, 855, 63
Hotokezaka, K., Beniamini, P., & Piran, T. 2018, International Journal of Modern Physics D, 27, 1842005
Hubrig, S., Castelli, F., Gonzalez, J. F., et al. 2012, A&A, 542, A31
Ikeda, Y., Kobayashi, N., Kondo, S., et al. 2016, Proc. SPIE, 9908, 99085Z
Ji, A. P., Frebel, A., Chiti, A., et al. 2016, Nature, 531, 610
Ji, A. P., & Frebel, A. 2018, ApJ, 856, 138
Jofré, P., Heiter, U., Worley, C. C., et al. 2017, A&A, 601, A38
Johnson, H. M. 1975, ApJ, 200, 395
Karakas, A. I., & Lattanzio, J. C. 2014, PASA, 31, e030
Kaeufl, H.-U., Ballester, P., Biereichel, P., et al. 2004, Proc. SPIE, 1218
Kondo, S., Fukue, K., Matsunaga, N., et al. 2019, ApJ, 875, 129
Kovtyukh, V. V. 2007, MNRAS, 378, 617
Kovtyukh, V. V., & Andrievsky, S. M. 1999, A&A, 351, 597
Kovtyukh, V. V., Soubiran, C., Belik, S. I., & Gorlova, N. I. 2003, A&A, 411, 559
Kovtyukh, V. V., Soubiran, C., Bienaymé, O., Mishenina, T. V., & Belik, S. I. 2006, MNRAS, 371, 879
Kurucz, R. L., 1993, Kurucz CD-ROM 13, ATLAS 9 Stellar Atmosphere Programs and 2 km/s Grid (Cambridge: SAO)
Lemasle, B., François, P., Genovali, K., et al. 2013, A&A, 558, A31
Lundqvist, M., Wahlgren, G. M., & Hill, V. 2007, A&A, 463, 693
Luck, R. E., & Lambert, D. L. 1985, ApJ, 298, 782
Luck, R. E. 2014, AJ, 147, 137
Luck, R. E. 2018, AJ, 156, 171
Luck, R. E., & Lambert, D. L. 2011, AJ, 142, 136
Luck, R. E., Andrievsky, S. M., Kovtyukh, V. V., et al. 2011, AJ, 142, 51
Lyubimkov, L. S., Lambert, D. L., Korotin, S. A., et al. 2015, MNRAS, 446, 3447
Majewski, S. R., Schiavon, R. P., Frinchaboy, P. M., et al. 2017, AJ, 154, 94
Matsunaga, N., Bono, G., Chen, X., et al. 2018, SSRv, 214, 74
McWilliam, A. 1997, ARA&A, 35, 503
McWilliam, A., Wallerstein, G., & Mottini, M. 2013, ApJ, 778, 149
Meléndez, J., & Barbuy, B. 1999, ApJS, 124, 527
Oliva, E., Origlia, L., Maiolino, R., et al. 2012, Proc. SPIE, 8446, 84463T

Önehag, A., Heiter, U., Gustafsson, B., et al. 2012, A&A, 542, A33
Origlia, L., Oliva, E., Maiolino, R., et al. 2013, A&A, 560, A46
Origlia, L., Oliva, E., Sanna, N., et al. 2016, A&A, 585, A14
Otsubo, S., Ikeda, Y., Kobayashi, N., et al. 2016, Proc. SPIE, 9908, 990879
Park, C., Jaffe, D. T., Yuk, I.-S., et al. 2014, Proc. SPIE, 9147, 91471D
Roach, F. E. 1942, ApJ, 96, 272
Ryabchikova, T., Piskunov, N., Kurucz, R. L., et al. 2015, PhyS, 90, 054005
Ryabchikova, T., Piskunov, N., Pakhomov, Y., et al. 2016, MNRAS, 456, 1221
Sameshima, H., Matsunaga, N., Kobayashi, N., et al. 2018a, PASP, 130, 74502
Sameshima, H., Ikeda, Y., Matsunaga, N., et al. 2018b, ApJS, 239, 19
Schultz, R. H., & Armentrout, P. B. 1991, JChPh, 94, 2262
Sellwood, J. A., Binney, J. J. 2002, MNRAS, 336, 785
Siegel, D. M., Barnes, J., & Metzger, B. D. 2019, Nature, 569, 241
Skowron, D. M., Skowron, J., Mróz, P., et al. 2019, Science, 365, 478
Smartt, S. J., Chen, T.-W., Jerkstrand, A., et al. 2017, Nature, 551, 75
Smith, V. V., Cunha, K., Shetrone, M. D., et al. 2013, ApJ, 765, 16
Sneden, C., Gratton, R.G., & Crocker, D. A. 1991, A&A, 246, 354
Sneden, C., Cowan, J. J., & Gallino, R. 2008, ARA&A, 46, 241
Sneden, C., Bean, J., Ivans, I., et al. 2012, MOOG: LTE line analysis and spectrum synthesis, Astrophysics Source Code Library (ascl:1202.009)
Steel, H. M. 1945, ApJ, 102, 43
Takeda, Y., Kang, D.-I., Han, I., et al. 2013, MNRAS, 432, 769
Tanaka, M., Utsumi, Y., Mazzali, P. A., et al. 2017, PASJ, 69, 102
Taniguchi, D., Matsunaga, N., Kobayashi, N., et al. 2018, MNRAS, 473, 4993
Tody, D. 1986, Proc. SPIE, 733
Tody, D. 1993, Astronomical Data Analysis Software and Systems II, 173
Tsujimoto, T., & Nishimura, N. 2018, ApJL, 863, L27
Tsujimoto, T., & Baba, J. 2019, ApJ, 878, 125
Udalski, A., Soszyński, I., Pietrukowicz, P., et al. 2018, AcA, 68, 315
Wallace, L., Livingston, W., Hinkle, K., & Bernath, P. 1996, ApJS, 106, 165
Zhang, J., Cui, W., & Zhang, B. 2010, MNRAS, 402, 956

タ　イ　ト　ル　：　超低膨張セラミックを用いた回折限界モノシリック反射光学系の開発

担　　当　：　猿楽 祐樹，池田 優二，小林 尚人

関　連　出　版　：　日本赤外線学会誌　第 28 巻 2 号　pp. 56-64

関連学会発表等　：

論文

J. Jpn. Soc. Infrared Science & Technology Vol.28 No.2 (2019)

超低熱膨張セラミックを用いた回折限界モノリシック反射光学系の開発

Diffraction-limited monolithic reflective optical system made entirely of ultra-low thermal expansion ceramics

猿楽祐樹[1]，池田優二[1,2]，小林尚人[1,3]

[1] 京都産業大学 神山天文台 赤外線高分散ラボ

[2] フォトコーディング

[3] 東京大学大学院 理学系研究科附属天文学教育研究センター木曽観測所

Yuki SARUGAKU[1], Yuji IKEDA[1,2], and Naoto KOBAYASHI[1,3]

[1]*Laboratory of Infrared High-resolution spectroscopy (LIH), Koyama Astronomical Observatory, Kyoto Sangyo University*

[2]*Photocoding*

[3]*Kiso Observatory, Institute of Astronomy, University of Tokyo*

日本赤外線学会誌 第28巻2号（2019年）からの転載

論文

超低熱膨張セラミックを用いた回折限界モノリシック反射光学系の開発
Diffraction-limited monolithic reflective optical system made entirely of ultra-low thermal expansion ceramics

猿楽祐樹[1]，池田優二[1,2]，小林尚人[1,3]
[1]京都産業大学 神山天文台 赤外線高分散ラボ
[2]フォトコーディング
[3]東京大学大学院 理学系研究科附属天文学教育研究センター木曽観測所

Yuki SARUGAKU[1], Yuji IKEDA[1,2], and Naoto KOBAYASHI[1,3]
[1]*Laboratory of Infrared High-resolution spectroscopy (LIH), Koyama Astronomical Observatory, Kyoto Sangyo University*
[2]*Photocoding*
[3]*Kiso Observatory, Institute of Astronomy, University of Tokyo*

要旨：反射光学系は一般に理想的な光学設計の実現に適しているが，透過光学系と比較して面形状やアライメントに要求される精度が高いことが実際の装置応用への障壁となっている．これは赤外線観測装置のように冷却を必要とする応用で特に大きな問題となるため，その解決策としてわれわれは，鏡，保持具，定盤のすべてを同一の低熱膨張セラミック材（コージライト）で製作するモノリシック反射光学系を提案している．この系の実証実験として，3 枚の球面から成る試験光学系を製作し，干渉計による可視波長における性能評価を行った．その結果，常温における機械精度の組上げのみで回折限界性能を達成し，それは冷却後も維持されていることを確認した．この新技術は，次世代の赤外線天文観測装置への応用が期待される．

Abstract **:** Although reflective optical system can realize ideal optical design in theory, it is not always the optimum choice compared to refractive optical system because high surface accuracy of the mirrors and complex optical alignment are demanded. This issue tends to be serious, in particular, for cryogenic optics, which are widely used for infrared instruments. Here we propose a monolithic reflective optical system, in which all components including the mirror surfaces, the mirror cell, and the optical bench are made of a ceramic with very low coefficient of thermal expansion (cordierite), to fully overcome the problems of the reflective system. For a demonstration, we fabricated a test optical system, consisting of three spherical mirrors and evaluated its optical performance in the visible wavelength with an interferometer. As the result, we confirmed that the diffraction-limited optical performance is achieved only with a mechanical assembling in the room temperature and that the performance is kept even after the cooldown to 80 K. This new technique may become a key technique for infrared astronomical instruments in the next generation.

Key Words: reflective optics, cryogenic, athermal, ceramic, cordierite, infrared astronomy, high-resolution spectroscopy

日本赤外線学会誌 第28巻2号（2019年）からの転載

1. はじめに

反射光学系は，①原理的に色収差を発生しない，②金属を反射膜にすることで広い波長帯域の光学系が実現できる，③光路を折り曲げることでコンパクトなレイアウトが可能，④軸外し（非）球面鏡を用いるレイアウトによって高度な収差補正が可能，⑤鏡材は面での均一性を出せればよく，メートルサイズ以上の大型光学面でも高い波面精度が実現できる，⑥オプトメカとの親和性がよく，保持具や定盤に同一の素材を用いたアサーマルな設計が容易，といった透過光学系にない利点が多数あり，理想的な光学設計の実現に適している．ところが，著者達の専門とする天文観測用装置のように，広帯域，広視野において回折限界性能（波面収差 PV<λ/4, rms<λ/14）が求められ，ひいては赤外線波長なら極低温環境での使用が必要となるといった要求の高い応用においても，透過光学系が選択されることは少なくない．それは，よく知られているように同じ波面精度を得ようとする場合，反射光学系では透過光学系に比べて 4 倍も高い形状精度（面精度）とアライメント精度が各々の光学面に求められるためである（ガラスの屈折率を 1.5 と仮定）．また，共軸系が基本である透過系に対して，軸外し系が基本である反射光学系のアライメントは調整の自由度が多く，その実現には多大な労力を要する．これらは装置を開発する時間やコストに直に反映されてしまうことも，帯域や視野を犠牲にしてでも透過光学系を選択する理由となっている．いまや天文学の主流の 1 つとなった赤外線観測用の装置では，基本的に光学系は真空低温下で用いられる．クライオスタットにインストールして冷却した後に熱変形によるミスアラインメントや光学素子の面形状の非相似な変形といった予測しがたい問題も発生しうるため，許容できる誤差の大きい透過光学系が好まれる傾向はますます高くなる．

そこで我々は，反射光学系の利点を最大に活かす次世代の光学系として，鏡，保持具，定盤まで光学系の要素すべてを単一の低熱膨張セラミック（コージライト）で製作する"モノリシック反射光学系"を提案している [1]．セラミックはその硬さから光学鏡の基板に用いることが古くから検討されてきたが，多孔質であるため鏡面に多数のボイドが発生することが光学材応用の妨げとなってきた．それが近年ボイドレスの製品が開発されており，例えば京セラ製のコージライト CO720 や黒崎播磨製の NEXCERA などは光学ガラスと同レベルの面精度と面粗さが達成できることが示されている [2,3]．また，セラミック材は焼結前の柔らかく加工が容易な状態（グリーンボディ）で完成品に近い状態に成型加工（ニアネットシェイプ加工）できるため，ブロックから削りだす金属やガラスよりも複雑な形状を実現しやすく，光学系保持具の構造材にも適している．焼結後の仕上げ加工により通常の金属機械加工と同等の高寸法精度の部品も製作可能であるため，近年発展している超高精密多軸加工機などを用いてパーツを製作し，それを機械精度で組上げるのみで，特別な光学調整を行うことなく高精度アライメントを実現できる見込みがある．加えて，光学定盤として十分に大きく平坦な土台も製作可能である．つまり，コージライトは反射光学系を構成する全要素に無理なく適用できるのである．究極的には締結部のない完全一体物として製作することで，組上げ作業さえも無くし，アライメント誤差を気に留める必要すらなくなる可能性もある．

このような単一材料からなるモノリシック光学系のアイデア自体は古くからあり，まずアルミ合金や SiC が，極低温で用いる赤外線装置や打ち上げ後に激しい温度変化を伴う飛翔体用のアサーマル性を必要とする光学系に応用されてきた [4,5]．しかし，これらの材料は線膨張係数（CTE）が大きいため（Table 1）温度変化に起因する内部応力によって高次のアライメントエラーが生じることがあり，また高い研磨性を確保するために表面に異材料のコーティングを施す場合もあり，本来的な意味においてのアサーマル系が実現できていないという指摘もある [13-16]．その点，コージライトは CTE が低熱膨張光学材として広く用いられている ULE，ゼロデュア，クリアセラムと同程度に小さく，研磨性を高めるコーティングの必

Table 1. Physical properties (at room temperature) of typical materials utilized for mirrors for astronomical instruments (CTE at 23±5°C and around 80K are shown for low thermal expansion materials; ULE, Zerodur, Clearceram, and Cordierite).

	CTE: α [10^{-6} K^{-1}]		Thermal conductivity: κ [W m^{-1} K^{-1}]	κ/α [W m^{-1}]	Young's modulus: E [10^3 MPa]	Density: ρ [10^3 kg m^{-3}]	E/ρ [MPa m^3 kg^{-1}]	Ref.
	RT	80K						
Fused silica	0.56		1.37	2.4e6	73	2.20	33	6)
ULE	0.04±0.01	-0.97	1.27	3e7	66	2.20	31	7, 8)
Zerodur	0.05±0.01	-0.18	1.52	3e7	89	2.54	35	7, 9)
Clearceram	0.03±0.03	0.11	1.50	5e7	89	2.55	35	7, 10)
CVD-SiC	2.4		146	6.1e7	466	3.21	145	6)
Cordierite	0.02±0.05	-1.1	4.68	2e8	140	2.55	55	7, 11)
Alminum (6061-T6)	23		171	7.4e6	69	2.71	25	6)
Be (O-30)	11		208	1.9e7	303	1.85	164	12)

日本赤外線学会誌 第28巻2号（2019年）からの転載

要もないためアサーマル光学系の実現において非常に有利であると考えられる. 常温で製作したままの状態が低温環境でも維持されることで，先述の高次の熱歪みがほとんど発生せず，金属材料やSiC では達成されていない高い波面精度を実現できる可能性があるからである.

京都産業大学神山天文台を中心とした我々グループは, 本アイデアの実証実験として，このコージライトを用いた"モノリシック反射光学系"を実際に試作し，性能評価を進めている[1]. 我々は，コージライトの有効性を早くから提案しており, これまでに高い温度安定性（κ/α）を活かした鏡や大型グレーティングホルダー（共に室温用）に応用してきた[17,18]. 我々のグループ以外では，高い比剛性（E/ρ）を活かして大型レンズ保持用のスペーサに応用した例も見られる[19]. しかしながら，これらの例は光学系の一部の部品を置き換えたものであり, 光学系のすべての要素にコージライトを応用する試みは本研究が初となる. 本論文では，モノリシック反射光学系のコンセプト，性能評価を紹介し，さらには赤外線天文観測装置への応用に向けた可能性と将来の展望について述べる.

2. 試験光学系

2. 1 オフナー光学系

コージライト製反射光学系の有効性を検証する試験光学ユニットとして 3 枚球面鏡から成るオフナー光学系を採用した（Fig. 1）. オフナー光学系とは，主鏡と副鏡の曲率半径が 2:1 の 2 枚の同心球面からなる等倍結像光学系であり, 絞りである凸面の副鏡を中心に対称な光学系になっているため, 若干の非点収差は発生するものの軸外収差がほとんど発生しないという特徴を持つ. シンプルな構成ながら回折限界の結像性能を達成できる光学系であり, 光学性能評価において設計と現物との差異や不具合が認められた場合にその原因の特定や切り分けが行いやすいという利点もある. 通常のオフナー光学系ではアライメント誤差の自由度を減らすために主鏡は

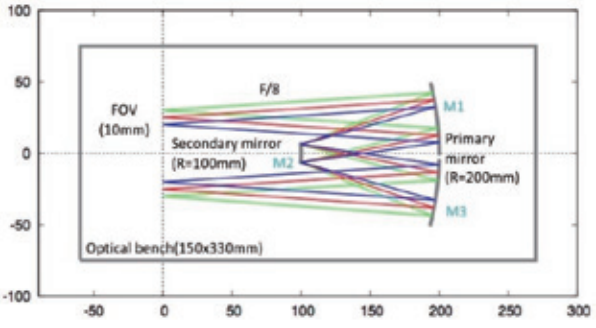

Fig. 1 Optical layout of the test cordierite optical system. Three spherical mirrors (M1, M2, and M3) constitute the Offner relay system.

1 枚で構成される（副鏡の前後で合計 2 回反射する）が，ここではアライメント誤差や冷却によるアライメントへの影響を検証するため，敢えて主鏡を 2 枚に分割し，3 球面から成る光学系とした.

2. 2 試験光学ユニット

実際に製作した試験光学ユニットを Fig. 2 に示す. 主鏡，副鏡の曲率半径 R は，それぞれ 200 mm と 100 mm である. また主鏡，副鏡の有効径は，それぞれϕ36 mm とϕ15 mm であり，口径比 F/8，有効視野 10 mm の光学系を成している. 鏡材にはコージライトの CO720（京セラ）を用いている. すべての鏡には金コートを施しており, 鏡面の面精度と面粗度はそれぞれλ/8 以下（PV 値@ 0.633 μm），数 nm 以下とガラスレベルの性能を達成している. 保持具および光学定盤にはコージライトの CO220（京セラ）を用いた. CO720 と CO220 は同じ CTE を持つが，HIP 処理の有無に違いがある. 前者は HIP 処理によってボイドを減らすことに成功しており，より鏡材に適している. 後者はその処理がない分だけ低コストであり，かつ大型部材の製作が可能であるため光学定盤などの構造材に適している. 締結には，コージライトと同程度の CTE を持つインバー（CTE < 0.8×10^{-6} K^{-1} @10-300 K）製のネジを用いており，ネジの締結によってセラミックが破損しないように綿密なトルク管理を行っている. めねじ側には締結強度を保つためのヘリサートを挿入しているが，製作上の制約からその材質には SUS304（CTE < 16×10^{-6} K^{-1} @10-300 K）を用いている.

一般的に光学系の組上げではレーザーなど制御された光源を用い，その像や波面を見ながらアライメントを調整するが，本試作光学ユニットでは機械的なアライメントのみで組上げを行った. 具体的には，まず位置決めの基準となるブロックを，接触式 3 次元測定器を用いて位置を測定しながら公差±10 μm で光学定盤上に配置する. 次に，鏡と保持具が一体となったミラーユニットを，それに施した基準面が先に配置したブロックの基準面に接するように設置

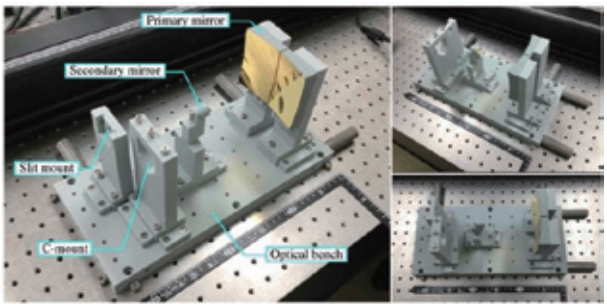

Fig. 2 Test optical system made entirely of cordierite by Kyocera. CO-720 for mirrors and CO220 for other structures. Mirrors are coated with Au. This system was assembled simply with mechanical accuracy. Note that screws and helical coil inserts are made of invar and SUS, respectively.

日本赤外線学会誌 第28巻2号（2019年）からの転載

する．これだけで組みあげた光学系に対して，光学面（表面には金コートが施されているので裏面）を 3 次元測定器で測定することで，光学面が想定通りに公差±30 μm でアライメントされていることも最後に確認した．その後，簡易な光学検査として，コリメートされたレーザー光（0.633 μm）を球面収差が十分補正されてあるアクロマートレンズ（ϕ50 mm，焦点距離 250 mm）を用いて F/8 の集束光に変換して試験ユニットへ入射し，焦点面に設置した CCD カメラで点像分布関数（PSF）の評価を行った．その結果，有効視野全域にわたって回折限界レベルの結像性能が得られていることを確認した．

3. 性能評価

3.1 実験構成

常温から低温までの光学性能を評価するため，オフナー光学系の像面から 100 mm オフフォーカスした位置に曲率半径 100 mm の凸面鏡（面精度λ/20）を設置し，それを折り返し鏡としたフィゾー型干渉計を構成して波面測定を行った（Fig. 3）．この折り返し凸面鏡も CO720 製の特注品である．試験光学ユニット全体を液体窒素冷却式のクライオスタットにインストールし，F/7.1 の球面原器を装着してあるレーザー干渉計（Zygo 社）とともに防振台に設置した．干渉計から射出された集束光をオフナー光学系に正確に導入するため，光軸調整用としてキネマティックマウントホルダに入れた 2 枚の平面鏡をクライオスタットまでの光路間に配し，また距離調整用として直動ステージを取り付けたリニアガイドをクライオスタットの設置治具に設けた（Fig. 4）．干渉計とオフナー光学系の焦点の一致は，試験光学ユニットの焦点にセットした薄板ガラスの反射光によってヌル干渉縞が得られるように調整を行った．なお，オフナー光学系の副鏡が絞りの役目を果たしているため，集束光の F 値を変えるための絞りは設置していない．

次にクライオスタットの内部について説明する．試験光学ユニットは無酸素銅製の支持部品を介してコールドワースサーフェス（CWS）に取り付けた．コージライトと銅の熱収縮差による熱ストレスとそれに伴う破壊を避けるため，ボルト固定は一点のみとし，その固定穴はオフナー光学系の焦点面と光軸の交点の真下に配置してある．この配置は，冷却前後で干渉計側から見た光学レイアウトの変化を最小にするための方策である．また試験光学ユニットの回転ずれを防ぐため，光学定盤の裏側にピンを 2 本設けて，それを支持部品に空けた長穴に通した．長穴は固定穴を基点として光軸方向とそれに直交する方向を長手とした．冷却効率を上げるために，熱パスとして 0.3 mm 厚の銅板を 6 枚重ねたものを 2 セット準備して，CWS から光学定盤へ直接つないでいる．

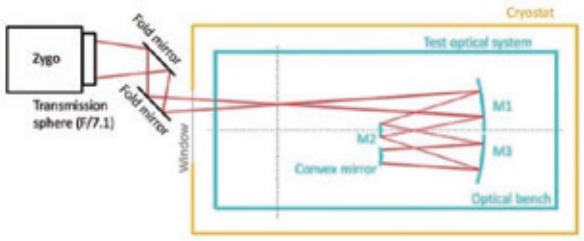

Fig. 3 Scheme of the wavefront error measurement. A convex mirror made of cordierite was added to the test optical system.

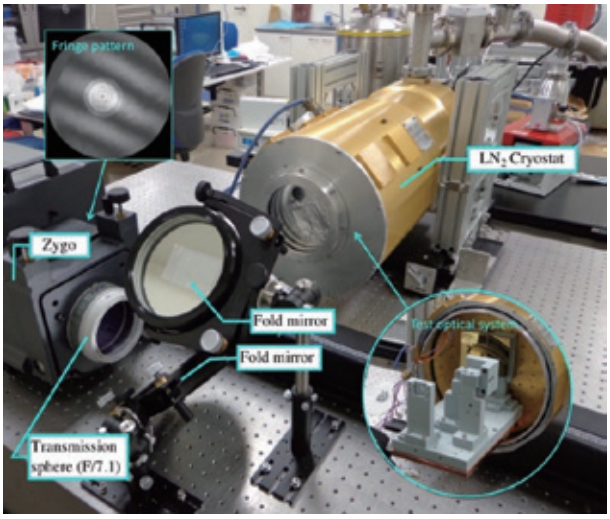

Fig. 4 Experimental set up for measuring the wavefront error at cryogenic temperatures. Note that the bright circular pattern in the fringe, which comes from the cryostat window, was masked out for the analysis (see the top-left inset).

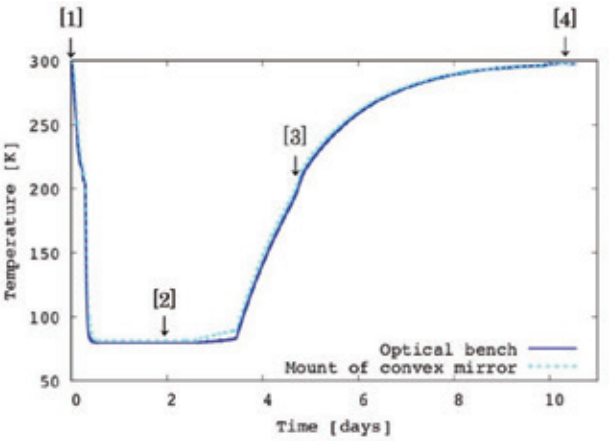

Fig. 5 Temperature change of the test optical system after the start of cooling. Wavefront errors were measured at temperatures indicated by arrows. The numbers [1-4] correspond to those in Fig. 6.

クライオスタットに液体窒素を注入して冷却を開始してから昇温までの光学ユニットの温度変化を Fig. 5 に示す．光学ユニットが十分に冷えてから約 2 日後までは液体窒素の補充を続け，それ以

日本赤外線学会誌 第28巻2号（2019年）からの転載

降は室温で放置して自然に昇温させた. コージライトの熱伝導率は高いとは言えないが（Table 1），装置に応用するうえで現実的な時間内で冷却可能であることが確認できた.

3. 2 結果

冷却前（300 K），冷却状態（80 K），昇温途中（200 K），そして昇温後（300 K）において測定した波面を Fig. 6 に示す. ここで示した波面マップには干渉計，平面鏡，クライオスタット窓の波面誤差も含まれているため注意が必要であるが, いずれの温度においても可視波長におけるいわゆる回折限界の光学性能（PV< λ/4，rms< λ/14）を達成しており，しかも常温（300 K）から低温（80 K）への冷却過程で波面マップのパターンもほとんど変化していないことが分かる. これは期待された「機械精度の組上げのみで高精度アライメント」と「低温環境でも回折限界性能を維持する高いアサーマル性」が見事に実現できていることを意味するものである.

ただし，昇温時に限って波面マップのわずかな変動がみられる. この原因として, 締結部にヘリサートを用いていることが関連していると考えている. コージライトは冷却するとわずかながら膨張し, バネ性をもつヘリサートがそれに追随する. その状態が昇温過程で完全には元に戻らず, 熱サイクル前後で締結状態が変化する可能性がある. 実際，コージライトに同様の締結構成を施して独立に行った冷却実験によって, 昇温後に締結穴付近にサブミクロンオーダーの変形が生じることを確認できている. 波面誤差の変化量は一般的な天文観測用の光学系においては全く無視できるレベルではあるが，今回の結果は 1 回の熱サイクルについてである. 複数回の熱サイクルによるヒステリシスの有無についても調査が必要であり, 引き続いての検証実験を進めている.

4. まとめと展望

我々は, 反射光学系の利点を最大限に活かすことのできる光学系としてコージライト製モノリシック反射光学系を提案し, その開発を進めている. この光学系の有効性を検証する試験ユニットとしてオフナー光学系を成す 3 枚球面系を製作し，まずコンセプト通り常温では機械精度の組上げのみで回折限界光学系が可視波長で達成できていること, 冷却環境においてもその回折限界性能を維持していることを確認した. 引き続いて，経年変化の有無を確認する熱サイクル試験, 冷却によって歪みが生じにくい締結方法の検討なども現在進行中である.

コージライト製モノリシック反射光学系が実用化されれば, 光赤外線観測装置の光学系のあり方が一新されるかもしれない. とくに 1 章で述べたように，冷却が必須である赤外線観測装置や打ち上げによって激しい温度変化を伴う飛翔体用装置の光学系に大きなブレークスルーをもたらすことが期待される. 本稿の主題からは逸れるため詳しく触れなかったが, コージライトには低熱膨張ガラスと比べて比剛性が高い（Table 1），形状の経年変化が小さいという特徴もあり [2], 軽量化が求められる飛翔体や長期に亘って使用される地上望遠鏡の主鏡への応用に利点となる. 我々としては，地上望遠鏡用冷却赤外線装置への応用を第一に目指している. 現在主力の口径 10 m 級の地上望遠鏡では補償光学（AO）技術の進展により近赤外波長まで回折限界の解像度が得られるようになっており, また高感度の大フォーマット赤外線検出器が普及し，より広視野（分光で

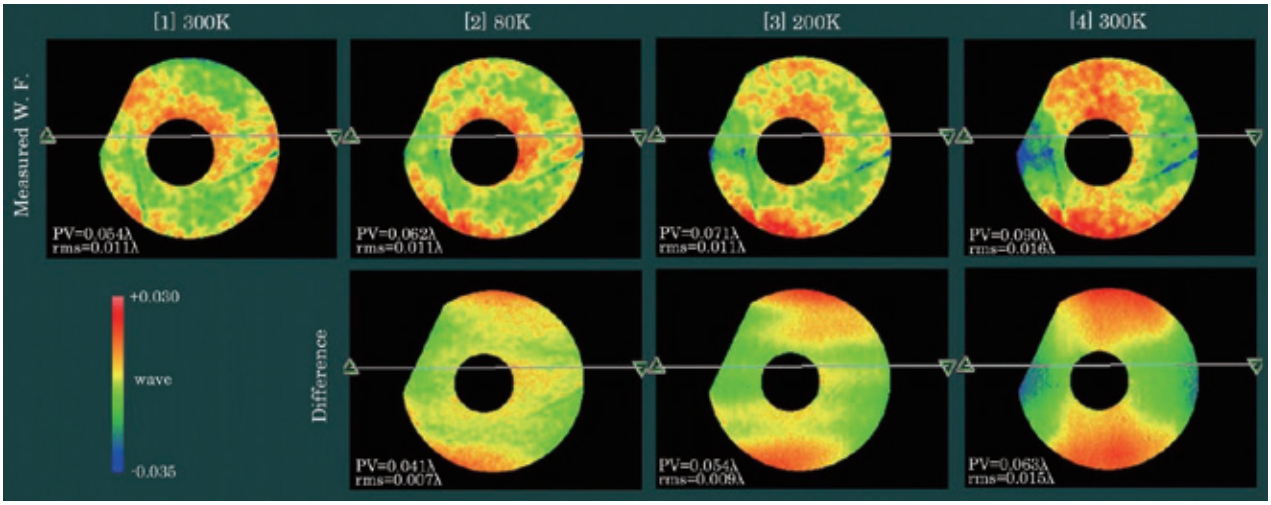

Fig. 6 Upper: Variation of wavefront map (λ = 0.633 μm) of the test optical system through the thermal cycle. The maps include the wavefront errors contributed from other mirrors and lenses in the path. The masked region corresponds to the bright circular fringe pattern (see Fig. 4). The time sequence is same as in Fig. 5. The diffraction-limited performance was kept even at the cryogenic temperature. Lower: Difference of the wavefront maps relative to [1].

日本赤外線学会誌 第28巻2号（2019年）からの転載

は広帯域）の観測が可能となってきている．しかしながら，従来の光学系はそれらを最大限に活用できているとは言えない．コージライト製モノリシック反射光学系を用いれば，高波面精度，広視野，高感度を兼ね備えた装置を，より容易に実現できる．このような光学系は将来の赤外線観測装置の標準技術として幅広く用いられ，次世代の口径 30 m 級超大型望遠鏡用の大型かつ複雑な光学系実現のハードルを下げる，あるいはよりチャレンジングな目標設定を可能にすることが期待される．京都産業大学神山天文台赤外線高分散ラボ（LIH）ではその先駆けとして，近赤外線高分散分光器 VINROUGE（波長 2-5 μm，比波長分解能 λ/Δλ=80,000）への初実用を目指し[20]，本光学系の開発を進めている．

謝辞

コージライト製試験光学ユニットの製作では，京セラ株式会社ファインセラミック事業本部の方々にこれまでの製品開発の知見にもとづいた貴重なアドバイスをいただいている．また各種実験では，京都産業大学のスタッフ・学生のみなさんに諸所でサポートをいただいており，特に岡賢治君には実験部品の設計・製作において多大な貢献をいただいた．紙面の都合ですべての名前をあげることができないが，関係者の皆さまに深くお礼申し上げる．本研究開発は国立天文台の平成 28-29 年度 TMT 戦略基礎開発研究経費の助成を受けて実施されたものである．

参考文献

1) Y. Sarugaku *et al.*：Proc. SPIE **10706** (2018) 107063P.
2) Y. Nakahori *et al.*：Proc. SPIE **10706** (2018) 107060B.
3) T. Kamiya and T. Mizutani：Proc. SPIE **10742** (2018) 1074205.
4) E. F. Erickson *et al.*：Proc. SPIE **0509** (1985) 129.
5) K. Honnen *et al.*：Proc. SPIE **7018** (2008).
6) P. R. Yoder, Jr.：OPTO-MECHANICAL SYSTEMS DESIGN, Second edition (Marcel Dekker, Inc., 1993).
7) T. Kamiya and T. Mizutani：Proc. SPIE **10372** (2017) 1037208.
8) G. K. White：Cryogenics **16** (1976) 487.
9) J. H. Burge *et al.*：Applied Optics **38** (1999) 7161.
10) OHARA corporation catalog, https://www.oharacorp.com/pdf/ccz-2013-nav.pdf
11) Okaji *et al.*：Cryogenics **34** (1994) 163.
12) D. Hashiguchi *et al.*：Advanced Materials & Processes **173** (2015) 20.
13) R. G. Ohl *et al.*：Proc. SPIE **4822** (2002) 51.
14) R. Eng *et al.*：Proc. SPIE **5868** (2005) 58680Q.
15) D. Vukobratovich *et al.*：Proc. SPIE **3435** (1998) 9.
16) J. Rodolfo *et al.*：Proc. SPIE **10563** (2014) 105631Z.
17) T. Kotani *et al.*：Proc. SPIE **9147** (2014) 914714.
18) Y. Ikeda *et al.*：Proc. SPIE **10702** (2018) 107025U.
19) S. Miyazaki *et al.*：Proc. SPIE **8446** (2012) 84460Z.
20) T. Arasaki *et al.*：Proc. SPIE **9908** (2016) 990875.

（論文受付 2018 年 10 月 9 日，論文受理 2018 年 12 月 13 日）

■著者紹介■

氏名　猿楽　祐樹
所属　京都産業大学神山天文台赤外線高分散ラボ
（〒603-8555　京都府京都市北区上賀茂本山）
2007 年，東京大学大学院理学系研究科地球惑星科学専攻博士課程修了．博士（理学）．東京大学大学院理学系研究科附属天文学教育研究センター木曽観測所，宇宙航空研究開発機構宇宙科学研究所の研究員を経て，2017 年より京都産業大学神山天文台主任研究員．専門は惑星科学および天文観測装置開発．
所属学会：日本天文学会
E-mail：sarugaku@cc.kyoto-su.ac.jp

氏名　池田　優二
所属　フォトコーディング
（〒606-0025　京都府京都市左京区岩倉中町 460-102）
2002 年，東北大学理学研究科天文学専攻博士課程後期修了．博士（理学）．2006 年よりフォトコーディング代表，2009 年より京都産業大学理学部准教授を，2013 年より同大学神山天文台客員研究員を併任．専門は恒星物理学，および光学．
所属学会：日本天文学会，応用物理学会
E-mail：ikeda@photocoding.com

氏名　小林　尚人
所属　東京大学大学院理学系研究科附属天文学教育研究センター木曽観測所
（〒397-0101　長野県木曽郡木曽町三岳 10762-30）
1994 年，京都大学大学院理学研究科物理学第二専攻研究指導認定退学，1995 年，博士（理学）．1995 年，国立天文台開発機器実験センター助手，1997 年，国立天文台ハワイ観測所助手，2003 年，東京大学大学院理学系研究科附属天文学教育研究センター准教授．2016 年より同センター木曽観測所所長を兼任．専門は天体物理学および天文観測装置開発．
所属学会：日本天文学会
E-mail：naoto@ioa.s.u-tokyo.ac.jp

日本赤外線学会誌 第28巻2号（2019年）からの転載

研究成果・関連論文リスト

令和元(2019)年度、神山天文台における研究活動にもとづく博士号学位取得者、学術論文雑誌掲載論文（査読有り／無し）および学会・研究会等での発表については、以下のとおりである。令和元（2019）年度は、神山天文台設置後10年目にあたる年度であった。近年、神山天文台の活動に基づく研究成果が数多く出版されており、神山天文台における研究活動のアクティビティが十分なレベルで維持できていると考えている。令和元年（2019）年度の神山天文台における研究活動は、①「赤外線高分散ラボ: Laboratory of Infrared High-resolution spectroscopy」に関連する成果と②「特徴ある独自装置による天体分光学の新展開」に大別される。

赤外線高分散ラボの活動は、波長1ミクロン帯の高感度・高分散分光器WINEREDの開発とそれを用いた観測研究を中心としている。平成29(2017)年度からWINEREDをチリ共和国・欧州南天天文台ラ・シヤ観測所の口径3.6m New Technology 望遠鏡に取り付け、低湿度・高晴天率の観測条件の下で非常に良質の観測データを多く取得できた。これは、高湿度・低晴天率の京都において口径1.3m荒木望遠鏡を用いて数年がかりで得られる情報に匹敵すると考えている。それを受け、近年では荒木望遠鏡によって得られたデータをもとにした研究成果だけでなく、New Technology 望遠鏡での観測データをもとにした研究が進んでいる。また、波長3−5ミクロン帯の高感度・高分散分光器VINROUGEの開発もすすめている。イマージョン回折格子の開発や低膨張セラミックを用いたアサーマル光学系の実現に向けた基礎開発実験も進めてきた。一方、②に相当するものとして、口径1.3m荒木望遠鏡を用いた古典新星の観測研究も着実に進んでいる。可視光低分散分光器 LOSA/F2 や可視光分散偏光分光器 VESPolA を用いた観測が進み、海外との連携もあって、着実に成果が得られ続けている。

以上、神山天文台の研究活動は定常的な状態で推移している。現在、WINEREDをチリ共和国ラス・カンパナス天文台の口径6.5mマゼラン望遠鏡に移設を進めており、更に大口径の望遠鏡を活かし、より遠方の宇宙論的な天体をも観測ターゲットとすることが、将来、可能となる。更に多様な研究テーマが開拓できる状況が整いつつある。神山天文台は、学祖荒木俊馬博士の研究されたセファイド型変光星や「はくちょう座P星」、新星などをテーマとして引継ぎ、世界トップレベルの成果を生み出している。

博士号学位取得者

（該当者無し）

学術論文雑誌掲載論文（2019年４月～2020年３月）

1. 論文名：Unidentified Infrared Emission Features in Mid-infrared Spectrum of Comet 21P/Giacobini-Zinner、著者名：T. Ootsubo, H. Kawakita, Y. Shinnaka, J. Watanabe, M. Honda、掲載誌名：Icarus、査読の有無：有、巻：338、最初と最後の頁：113450、発表年：2020年

2. 論文名：Thermal structure of the Venusian atmosphere from the sub-cloud region to the mesosphere as observed by radio occultation、著者名： Ando, Hiroki; Imamura, Takeshi; Tellmann, Silvia; Pätzold, Martin; Häusler, Bernd; Sugimoto, Norihiko; Takagi, Masahiro; Sagawa, Hideo; Limaye, Sanjay; Matsuda, Yoshihisa; Choudhary, Raj Kumar; Antonita, Maria、掲載誌名：Scientific Reports、査読の有無：有、巻：10、最初と最後の頁：3448(7pp)、発表年：2020 年
3. 論文名：14N/15N Isotopic Ratio in CH3CN of Titan's Atmosphere Measured with ALMA 、著者名： Iino, Takahiro; Sagawa, Hideo; Tsukagoshi, Takashi、掲載誌名：The Astrophysical Journal、査読の有無：有、巻：890、最初と最後の頁：95(6pp)、発表年：2020 年
4. 論文名：An optical search for transients lasting a few seconds 、著者名： Richmond, Michael W.; Tanaka, Masaomi; Morokuma, Tomoki; Sako, Shigeyuki; Ohsawa, Ryou; Arima, Noriaki; Tominaga, Nozomu; Doi, Mamoru; Aoki, Tsutomu; Arimatsu, Ko; Ichiki, Makoto; Ikeda, Shiro; Ita, Yoshifusa; Kasuga, Toshihiro; Kawabata, Koji S.; Kawakita, Hideyo; Kobayashi, Naoto; Kokubo, Mitsuru; Konishi, Masahiro; Maehara, Hiroyuki Mito, Hiroyuki; Miyata, Takashi; Mori, Yuki; Morii, Mikio; Motohara, Kentaro; Nakada, Yoshikazu; Okumura, Shin-Ichiro; Onozato, Hiroki; Sarugaku, Yuki; Sato, Mikiya; Shigeyama, Toshikazu; Soyano, Takao; Takahashi, Hidenori; Tanikawa, Ataru; Tarusawa, Ken'ichi; Urakawa, Seitaro; Usui, Fumihiko; Watanabe, Junichi; Yamashita, Takuya; Yoshikawa, Makoto、掲載誌名：Publications of the Astronomical Society of Japan、査読の有無：有、巻：72、最初と最後の頁：3(14pp)、発表年：2020 年
5. 論文名：Probing the Evolutionary History of Comets: An Investigation of the Hypervolatiles CO, CH4, and C2H6 in the Jupiter-family Comet 21P/Giacobini—Zinner 、著者名： Roth, Nathan X.; Gibb, Erika L.; Bonev, Boncho P.; DiSanti, Michael A.; Dello Russo, Neil; McKay, Adam J.; Vervack, Ronald J., Jr.; Kawakita, Hideyo; Saki, Mohammad; Biver, Nicolas; Bockelée-Morvan, Dominique; Feaga, Lori M.; Fougere, Nicolas; Cochran, Anita L.; Combi, Michael; Shou, Yinsi、掲載誌名：The Astronomical Journal、査読の有無：有、巻：159、最初と最後の頁：42(14pp)、発表年：2020 年
6. 論文名：Post-perihelion volatile production and release from Jupiter-family comet 45P/Honda-Mrkos-Pajdušáková 、著者名： Dello Russo, Neil; Kawakita, Hideyo; Bonev, Boncho P.; Vervack, Ronald J.; Gibb, Erika L.; Shinnaka, Yoshiharu; Roth, Nathan X.; DiSanti, Michael A.; McKay, Adam J.、掲載誌名：Icarus、査読の有無：有、巻：335、最初と最後の頁：113411、発表年：2020 年
7. 論文名：Identification of Absorption Lines of Heavy Metals in the Wavelength Range

0.97―1.32 μm 、著者名: Matsunaga, Noriyuki; Taniguchi, Daisuke; Jian, Mingjie; Ikeda, Yuji; Fukue, Kei; Kondo, Sohei; Hamano, Satoshi; Kawakita, Hideyo; Kobayashi, Naoto; Otsubo, Shogo; Sameshima, Hiroaki; Takenaka, Keiichi; Tsujimoto, Takuji; Watase, Ayaka; Yasui, Chikako; Yoshikawa, Tomohiro、掲載誌名：The Astrophysical Journal Supplement Series、査読の有無：有、巻：246、最初と最後の頁：10(14pp)、発表年：2020 年

8. 論文名：New constraint on the atmosphere of (50000) Quaoar from a stellar occultation 、著者名：Arimatsu, Ko; Ohsawa, Ryou; Hashimoto, George L.; Urakawa, Seitaro; Takahashi, Jun; Tozuka, Miyako; Itoh, Yoichi; Yamashita, Misato; Usui, Fumihiko; Aoki, Tsutomu; Arima, Noriaki; Doi, Mamoru; Ichiki, Makoto; Ikeda, Shiro; Ita, Yoshifusa; Kasuga, Toshihiro; Kobayashi, Naoto; Kokubo, Mitsuru; Konishi, Masahiro; Maehara, Hiroyuki Matsunaga, Noriyuki; Miyata, Takashi; Morii, Mikio; Morokuma, Tomoki; Motohara, Kentaro; Nakada, Yoshikazu; Okumura, Shin-ichiro; Sako, Shigeyuki; Sarugaku, Yuki; Sato, Mikiya; Shigeyama, Toshikazu; Soyano, Takao; Takahashi, Hidenori; Tarusawa, Ken'ichi; Tominaga, Nozomu; Watanabe, Jun-ichi; Yamashita, Takuya; Yoshikawa, Makoto、掲載誌名：The Astronomical Journal、査読の有無：有、巻：158、最初と最後の頁：236(7pp)、発表年：2019 年
9. 論文名：Possible Progression of Mass-flow Processes around Young Intermediate-mass Stars Based on High-resolution Near-infrared Spectroscopy. I. Taurus 、著者名： Yasui, Chikako; Hamano, Satoshi; Fukue, Kei; Kondo, Sohei; Sameshima, Hiroaki; Takenaka, Keiichi; Matsunaga, Noriyuki; Ikeda, Yuji; Kawakita, Hideyo; Otsubo, Shogo; Watase, Ayaka; Taniguchi, Daisuke; Mizumoto, Misaki; Izumi, Natsuko; Kobayashi, Naoto、掲載誌名：The Astrophysical Journal、査読の有無：有、巻：886、最初と最後の頁：115 (20pp)、発表年：2019 年
10. 論文名：Comet 66P/du Toit: not a near Earth main belt comet、著者名：B. Yang, E. Jehin, F. J. Pozuelos, Y. Moulane, Y. Shinnaka, C. Opitom, H. H. Hsieh, D. Hutsemékers, J. Manfroid、掲載誌名：Asronomy and Astrophysics、査読の有無：有、巻：Volume 631、最初と最後の頁：id.A168(9pp)、発表年：2019 年
11. 論文名：Elemental analysis and mixture ratio determination in fine powder metals using microwave-sustained plasma ball spectroscopy 、著者名： Ofosu, Joseph Ampadu; Ikeda, Yuji、掲載誌名：Spectrochimica Acta Part B: Atomic Spectroscopy、査読の有無：有、巻：Volume 160、最初と最後の頁：id. 105693, 5pp、発表年：2019 年
12. ″論文名：The Peculiar Volatile Composition of CO-dominated Comet C/2016 R2 (PanSTARRS) 、著者名：McKay, Adam J.; DiSanti, Michael A.; Kelley, Michael S.

P.；Knight, Matthew M.；Womack, Maria；Wierzchos, Kacper；Harrington Pinto, Olga；Bonev, Boncho；Villanueva, Geronimo L.；Dello Russo, Neil；Cochran, Anita L.；Biver, Nicolas；Bauer, James；Vervack, Ronald J., Jr.；Gibb, Erika；Roth, Nathan；Kawakita, Hideyo、掲載誌名：

13. The Astronomical Journal、査読の有無：有、巻：Volume 158、最初と最後の頁：id. 128, 24 pp、発表年：2019年″
14. ″論文名：First Detection of A—X (0,0) Bands of Interstellar C2 and CN、著者名：Hamano, Satoshi；Kawakita, Hideyo；Kobayashi, Naoto；Takenaka, Keiichi；Ikeda, Yuji；Matsunaga, Noriyuki；Kondo, Sohei；Sameshima, Hiroaki；Fukue, Kei；Yasui, Chikako；Mizumoto, Misaki；Otsubo, Shogo；Watase, Ayaka；Yoshikawa, Tomohiro；Kobayashi, Hitomi、掲載誌名：
15. The Astrophysical Journal、査読の有無：有、巻：Volume 881、最初と最後の頁：id. 143, 13 pp、発表年：2019年″
16. 論文名：Post-perihelion volatile production and release from Jupiter-family comet 45P/Honda-Mrkos-Pajdušáková、著者名：Neil Dello Russoa, Hideyo Kawakita, Boncho P. Bonev, Ronald J. Vervack Jr., Erika L. Gibb, Yoshiharu Shinnaka, Nathan X. Roth, Michael A. DiSanti, Adam J. McKay、掲載誌名：Icarus、査読の有無：有、巻：Volume 335、最初と最後の頁：id. 113411, 14pp、発表年：2019年
17. 論文名：The metallicity effect on line-depth ratios in APOGEE H-band spectra 、著者名：Jian, Mingjie；Matsunaga, Noriyuki；Fukue, Kei、掲載誌名：Monthly Notices of the Royal Astronomical Society、査読の有無：有、巻：Volume 485、最初と最後の頁：pp.1310-1319、発表年：2019年
18. 論文名：Optical spectroscopy of nova ASASSN-17hx at Bosscha Observatory 、著者名：Adhyaqsa, A.；Istiqomah, A. N.；Ramadhan, D. G.；Imaduddin, I.；Malasan, H. L.；Arai, A.；Kawakita, H.、掲載誌名：Journal of Physics: Conference Series、査読の有無：有、巻：Volume 1231、最初と最後の頁：id. 012006, 4pp、発表年：2019年
19. 論文名：Fe I Lines in 0.91—1.33 μm Spectra of Red Giants for Measuring the Microturbulence and Metallicities 、著者名：Kondo, Sohei；Fukue, Kei；Matsunaga, Noriyuki；Ikeda, Yuji；Taniguchi, Daisuke；Kobayashi, Naoto；Sameshima, Hiroaki；Hamano, Satoshi；Arai, Akira；Kawakita, Hideyo；Yasui, Chikako；Izumi, Natsuko；Mizumoto, Misaki；Otsubo, Shogo；Takenaka, Keiichi；Watase, Ayaka；Asano, Akira；Yoshikawa, Tomohiro；Tsujimoto, Takuji、掲載誌名：The Astrophysical Journal、査読の有無：有、巻：Volume 875、最初と最後の頁：id. 129, 13 pp、発表年：2019年

学会・研究会等発表（2019年４月～2020年３月）

1. 学会名：新学術領域「星惑星形成」シンポジウム、発表者：安井千香子、発表標題名：星惑星形成過程の中心星質量依存性の観測的研究：mass-flow processの時間進化、開催地：オンライン、発表年月：2020.3.27
2. 学会名：日本天文学会2020年春季年会、発表者：松永典之、発表標題名：[a講演] 近赤外線YJバンドに存在する中性子捕獲元素の吸収線の同定、開催地：筑波大学、発表年月：2020.3.16-19
3. 学会名：日本天文学会2020年春季年会、発表者：安井千香子、発表標題名：[a講演] 前主系列星における彩層活動由来の HeI λ10830 吸収線の初検出: 近赤外線高分散分光器WINEREDによる Taurus星生成領域中の中質量星の観測、開催地：筑波大学、発表年月：2020.3.16-19
4. 学会名：Subaru Telescope 20th Anniversary、発表者：河北秀世、発表標題名：Cometary Science from the Subaru Telescope、開催地：Hawaii, USA、発表年月：2019.11.17-22
5. 学会名：Subaru Telescope 20th Anniversary、発表者：松永典之、発表標題名：Near-IR windows of precise and detailed chemical measurements、開催地：Hawaii, USA、発表年月：2019.11.17-22
6. 学会名：連星系・変光星研究会 2019、発表者：新中善晴、発表標題名：高分散偏光スペクトルから探る古典新星 V339 Del の爆発放出物、開催地：中京大学,名古屋、発表年月：2019.11.29-12.1
7. 学会名：日本惑星科学会 2019 年秋季講演会、発表者：河北秀世、発表標題名：21P/Giacobini-Zinner 彗星の中間赤外線スペクトルにおける複雑な有機分子の検出、開催地：京都産業大学,京都、発表年月：2019.10.7-9
8. 学会名：日本惑星科学会2019年秋季講演会、発表者：新中善晴、発表標題名：彗星探査計画 Comet Interceptor、開催地：京都産業大学,京都、発表年月：2019.10.7-9
9. 学会名：日本惑星科学会2019年秋季講演会、発表者：有松亘, 津村耕司, 臼井文彦, 新中善晴, 市川幸平, 大坪貴文, 小谷隆行, 和田武彦, 長勢晃一, 渡部潤一、発表標題名：恒星掩蔽観測によって明かされる太陽系外縁天体 、開催地：京都産業大学,京都、発表年月：2019.10.7-9
10. 学会名：EPSC-DPS Joint Meeting 2019、発表者：Hideyo Kawakita、発表標題名：Forbidden oxygen emission lines in optical high-resolution spectrum of 21P/Giacobini-Zinner in 2018 apparition 、開催地：Geneva, Switzerland、発表年月：2019.9.15-20
11. 学会名：EPSC-DPS Joint Meeting 2019、発表者：Adam McKay, Michael DiSanti, Boncho Bonev, Neil Dello Russo, Ronald Vervack Jr., Erika Gibb, Nathan Roth, Mohammad Saki, and Hideyo Kawakita、発表標題名：Hypervolatiles in Jupiter Family Comet 46P/Wirtanen Observed with IRTF iSHELL 、開催地：Geneva, Switzerland、発表年

月：2019.9.15-20

12. 学会名：EPSC-DPS Joint Meeting 2019、発表者：Erika Gibb, Nathan Roth, Boncho Bonev, Michael DiSanti, Neil Dello Russo, Ronald Vervack, Adam McKay, Hideyo Kawakita, Mahammad Saki, Nicholas Biver, Dominique Bockelee-Morvan, Anita Cochran, Michael Combi, Martin Cordiner, Jacques Crovisier, Lori Feaga, Nicolas Fougere, Silva Protopapa, and Yinsi Shou、発表標題名：Volatile Compositions of Short Period Comets 2P/Encke and 21P/Giacobini-Zinner Across Apparitions 、開催地：Geneva, Switzerland、発表年月：2019.9.15-20
13. 学会名：EPSC-DPS Joint Meeting 2019、発表者：Michael DiSanti, Mohamed Saki, Erika Gibb, Boncho Bonev, Neil Dello Russo, Adam McKay, Ronald Vervack, Nathan Roth, and Hideyo Kawakita、発表標題名： C/2018 Y1 (Iwamoto): Measuring the volatile composition of a long-period comet shortly following its discovery 、開催地：Geneva, Switzerland、発表年月：2019.9.15-20
14. 学会名：EPSC-DPS Joint Meeting 2019、発表者：Boncho Bonev, Neil Dello Russo, Michael DiSanti, Emily Martin, Gregory Doppmann, Ronald Vervack Jr., Geronimo Villanueva, Hideyo Kawakita, Erika Gibb, Nathan Roth, Mohammad Saki, Dennis Bodewits, Michael Combi, Adam McKay, Jacques Crovisier, Nicolas Biver, Martin Cordiner, and Anita Cochran、発表標題名：Volatile composition and outgassing in comet 46P/Wirtanen: Keck 2 observations with the newly upgraded NIRSPEC instrument 、開催地：Geneva, Switzerland、発表年月：2019.9.15-20
15. 学会名：EPSC-DPS Joint Meeting 2019、発表者：Neil Dello Russo, Adam McKay, Mohammad Saki, DiSanti Michael, Bonev Boncho, Gibb Erika, Vervack Ronald, Roth Nathan, Kawakita Hideyo, Cochran Anita, Cordiner Martin, Biver Nicolas, Crovisier Jacques, Bockelée-Morvan Dominique, Jehin Emmanuel, Feaga Lori, and Weaver Harold、発表標題名：IRTF/iSHELL campaign for comet 46P/Wirtanen 、開催地：Geneva, Switzerland、発表年月：2019.9.15-20
16. 学会名：EPSC-DPS Joint Meeting 2019、発表者：Nathan Roth, Erika Gibb, Neil Dello Russo, Boncho Bonev, Michael DiSanti, Ronald Vervack, Hideyo Kawakita, Mohammad Saki, Adam McKay, Anita Cochran, Emmanuel Jehin, Martin Cordiner, Harold Weaver, Nicolas Biver, and Jacques Crovisier、発表標題名：Volatile composition and coma spatial associations in 46P/Wirtanen as revealed by iSHELL at the NASA-IRTF 、開催地：Geneva, Switzerland、発表年月：2019.9.15-20
17. 学会名：Study of emission line objects: Tools and Techniques、発表者：Arai, Akira、発表標題名：Science of Novae, Novae observationa network、開催地：Indonesia、発表年月：2019.9.25-10.1
18. 学会名：The Golden Age of Cataclysmic Variables and Related Objects V、発表者：

Shinnaka, Yoshiharu、発表標題名：Spatial Distribution of Nova Ejecta during the Early Phase of Explosion of V339 Del from its high-resolution Optical Spectropolarimetry、開催地：Palermo, Italy、発表年月：2019.9.2-7

19. 学会名：The Golden Age of Cataclysmic Variables and Related Objects V、発表者：Arai, Akira、発表標題名：Spectral Evolution of Novae in the Near-Infrared、開催地：Palermo, Italy、発表年月：2019.9.2-7
20. 学会名：WINERED マゼラン望遠鏡観測検討会、発表者：大坪翔悟、発表標題名：マゼラン移設と装置のステータスと初期エンジニアリング観測、開催地：京都産業大学、発表年月：2019.5.29
21. 学会名：WINERED マゼラン望遠鏡観測検討会、発表者：松永典之、発表標題名：銀河系円盤の未開拓領域および散開星団にあるセファイドの観測、開催地：京都産業大学、発表年月：2019.5.29
22. 学会名：WINERED マゼラン望遠鏡観測検討会、発表者：谷口大輔、発表標題名：RSG で探る銀河系円盤内縁部の金属量、開催地：京都産業大学、発表年月：2019.5.29
23. 学会名:WINERED マゼラン望遠鏡観測検討会、発表者:Mingjie Jian、発表標題名:WINERED observation for bulge red clump stars and/or globular clusters、開催地：京都産業大学、発表年月：2019.5.29
24. 学会名：WINERED マゼラン望遠鏡観測検討会、発表者：辻本拓司、発表標題名：Sagittarius 矮小銀河に見る中性子星合体による r 過程元素組成進化の検証、開催地：京都産業大学、発表年月：2019.5.29
25. 学会名：WINERED マゼラン望遠鏡観測検討会、発表者：安井千香子、発表標題名：YSO の観測検討、開催地：京都産業大学、発表年月：2019.5.29
26. 学会名：WINERED マゼラン望遠鏡観測検討会、発表者：鮫島寛明、発表標題名：WINERED を用いたスペクトルライブラリーの構築、開催地：京都産業大学、発表年月：2019.5.29
27. 学会名：WINERED マゼラン望遠鏡観測検討会、発表者：濱野哲史、発表標題名：クェーサー吸収線系、DIB、開催地：京都産業大学、発表年月：2019.5.29

神山天文台の普及教育活動

１．はじめに

神山天文台は、京都産業大学の創設者である荒木俊馬博士が宇宙物理学者であったことから創立 50 周年を目指した大学のグランドデザインの一環として、平成 22(2010)年度に設立した研究教育組織である。

本天文台では、これまでに望遠鏡をはじめ各種観測装置を整備し、研究教育施設として、その役割を明確化するとともに、公開事業や産学協働など社会貢献も視野に入れて組織運営を行ってきた。その特色の一つとして、社会に開かれた天文台として独自の公開事業を展開し、装置開発のための設備を開放するなど、一般市民の方々や教育現場・産業界の方々と様々な交流を通じて、本学と一般社会・産業界を繋ぐ新たな天文学コミュニティー（人材育成、社会教育、産学協働の推進）を生み出すことを目的として、神山天文台を活用した普及教育活動を行ってきた（図１）。

また、平成 20（2008）年度から平成 24（2012）年度まで文科省・私立大学戦略的研究基盤形成支援事業に採択された「研究教育用天文台の設置および天文学教育研究拠点の形成」の観点からも、神山天文台が行う普及教育活動が社会に向けた「知の情報発信」に繋がるように、その基盤を整備してきた。こうした活動は、同事業の最終評価においても高く評価されており、平成 25（2013）年度以降についても、引き続き本学における「知の情報発信」の一翼を担い、大学と社会との窓口としての役割を果たすべく、上記のような、社会と関連できる活動を継続した。

ここでは、平成 22（2010）年度から本天文台で行ってきた普及教育活動を交えながら、令和元（2019）年度の活動について、以下のとおり記す。

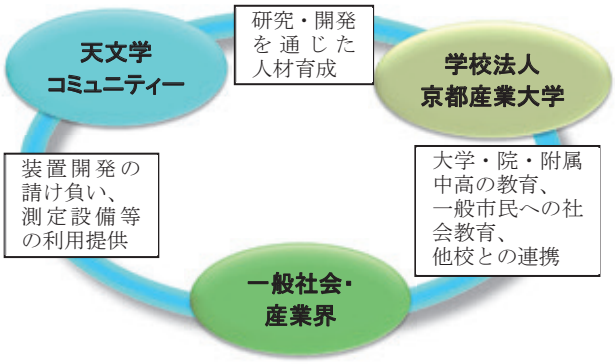

図１　神山天文台の役割

２．大学としての教育活動

神山天文台は、天文学における研究教育を行う組織として、特色ある教育を実践するために、理学部・理学研究科との連携を図ってきた。これまで、神山天文台の施設・設備（望遠鏡・観測装置、各種実験・計測機器）を活用し、神山天文台を利用する学生への教育支援を行ってきた。例えば、神山天文台研究員などが実施する研究会・勉強会・講習会等への学生の参加、さらに、天文台で実施する研究・観測装置の開発プロジェクトを通じた実践的な教育・研究指導を行い、神山天文台としての教育支援の活性化を図っている。

また、平成 20（2008）年度から平成 24（2012）年度にかけては、私立大学戦略的研究基盤形成支援事業の研究プロジェクト「研究教育用天文台の設置および天文学教育研究拠点の形成」の達成のために、様々な教育支援を行ってきた。荒木望遠鏡（大型望遠鏡）を用いた「新星の早期分光確認観測」や「新星における炭素分子の世界初検出」などの学術成果は、学生が主体となって成功している。平成 26（2014）年度には、本学理学研究科・博士後期課程在籍者２名が、神山天文台における研究・開発活動を元にして博士（理学）の学位を取得した。このことからも、神山天文台における教育支援活動が、学位取得に繋がるだけのクオリティを有していることが分かる。

平成 26（2014）年度から平成 30（2018）年度にかけては、私立大学戦略的研究基盤形成支援事業に研究プロジェクト「赤外線高分散分光天文学研究拠点 Infrared Spectroscopy Laboratory の形成」が採択された（神山天文台としては２回目）。本研究プロジェクトにおいて取り組んでいる研究は、当該分野では常に最先端である。当該補助金により複数の神山天文台研究員を雇用し、研究所の活性化を目指してきた。

また、上記研究プロジェクトとは別に「特徴ある独自開発装置による天体分光学の新展開」と題する研究計画の下、学生とともに神山天文台研究員が各種の研究を推し進めている。このように神山天文台における研究の多くは、学生及び神山天文台研究員が主体であり、教育と研究の相乗効果を狙うことも目的の一つである。研究成果の多くはマスメディア等に取り上げられるなど、学生たちの活躍が神山天文台のアクティビティを支える要因となっている。

３．学内公開

本学においては、学生・教職員などの学内者を対象とした天体観望会や宇宙の 3D 映像の上映会を行っている。望遠鏡で宇宙の姿を実際に見ることは、宇宙における地球、そして人類の存在する意味を考えるよい機会となり、本学の創設者である荒木俊馬博士の「建学の精神」の理念を、より多くの学生たちに認識してもらいたいという願いも含んでいる。

４．近隣学校等への天文学習

神山天文台では、小・中・高校生等（附属幼稚園・中高等学校を含む。）が宇宙に対して興味・関心を育み、様々な天文に関する事象を科学的に探求する機会を提供することを目的に講座を実施している。特に高校においては、地学を開講していない学校もあり、天文や宇宙のことを体系的に学習する機会が少なくなっているものの、昨今の宇宙・天文ブームを反映し、これまでにも平成 24（2012）年に金環日食、金星の太陽面通過等についてイベントを実施している。その中で、このような天文現象に関心を示す生徒たちの数が、以前にも増して多くなっていることを実感している。そのような生徒たちも、天文や宇宙について自ら探究的に学ぶことができるのが天文学習である。

昼間は 3D 映像を取り入れた講義と施設見学、夜間は 3D 映像にて 30 分の星空解説、その後 30～60 分の天体観望と合わせて 60～90 分間のプログラムを提供している。

天文学習では、年間で 10～20 校ほどの参加があり、近隣の学校への出前授業等も実施するなど、地域の教育機関との連携強化も視野に入れ、また、京都という土地柄を活かして修学旅行生の受入れも積極的に行うなど、開かれた天文台を目指している。

５．他機関との連携事業

平成 22（2010）年度、平成 23（2011）年度と２年連続で、日本学術振興会のひらめき☆ときめきサイエンス、サイエンス・パートナーシップ・プロジェクトに採択され、補助金を受けてスペクトル観測体験学習講座を実施した。受講生の中には、近畿地区のみならず、遠方からの参加もあった。受講生にとっては、小・中学生を中心に普段の学校の授業では体験できないようなことを学ぶことができ、特に、子どもたちにとっては大学の先生に教わるという機会も持つことができる非常に興味深い内容となった。

また、平成 23（2011）年度には、京都市青少年科学センターと連携し、「未来のサイエンティスト養成講座」（平成 23(2011)年８月実施）、プラネタリウム共同番組「星の虹から宇宙を探る」の共同制作（投影期間：平成 24(2012)年１月～３月実施）などを行った結果、約 4,500 名の参加があり、神山天文台の研究活動をアピールすることができた。

平成 24（2012）年度からは、東京大学大学院理学系研究科と研究協力に関する協定を締結し、近赤外線高分散分光器の世界最高性能を実現するための研究開発に取り組んでいる。

また、平成 27(2015)年度からは、インドネシアのバンドン工科大学と協定を結び、新星爆発の観測研究に取り組んでおり、平成 28（2016）年７月や平成 29（2017）年１月には、研究成果が学術論文雑誌に掲載された。

６．一般の方への普及教育活動

（１）施設見学と天体観望会

毎週土曜日には、神山天文台専門スタッフと学生補助員（以下、補助員という）が協力して無料の一般公開を行っている。国内の私立大学では最大となる、口径 1.3 メートルの荒木望遠鏡（写真１・写真２参照）を用いて天体観望を行っているほか、小型望遠鏡を用いた観望会や宇宙の４次元デジタルシミュレーションソフト「Mitaka」を用いた宇宙の 3D 映像上映会も行っている。来場者は、ファミリー層が多く、好天候時には 100 名を超える方々が天体観望会に訪れる。

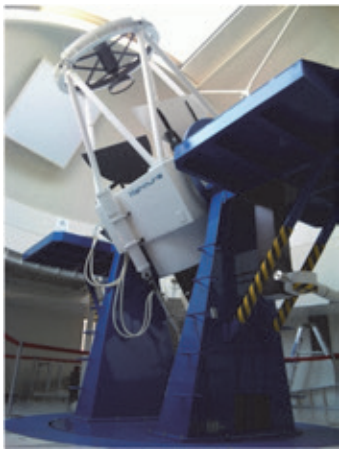

写真１　荒木望遠鏡

写真２　接眼部

天体観望会においては、その日に見た天体のスタンプが押せる「神山天文台スタンプラリー」を実施し、地域に親しまれる天文台として好評を得ている。平成 22（2010）年度から一般公開を実施し、令和元（2019）年度までの 10 年間で、46,000 名を超える方々に来場いただき、地域に根ざした天文台として、認知されるようになってきた（資料１・２参照）。来場者アンケートの結果では、大学という場所柄を反映してか、天文学の基礎知識や神山天文台で行われている研究について聞きたいという声が多い。

天体観望会においても、スタッフの専門分野の話題やサイエンスの紹介、観測装置を開発した学生の話なども取り入れ、神山天文台の研究活動等も紹介するなどして、参加者が興味の持つ話題やニーズなども取り上げながら、満足度の高い公開事業を行っている。

また、平日又は土曜日の昼間に神山天文台を開放し、荒木望遠鏡や荒木俊馬博士のゆかりの品等を自由に見学いただいている。加えて、平成 26（2014）年度と 27（2015）年度には、著名な星景写真家の協力により、館内にて星景写真展（写真３参照）を開催し、来場者から多数の好評を得ている。

写真３　星景写真展の様子

（２）天文学講座

天文学講座は、学内外の研究者を講師とした、普段の天体観望会よりも天文学の深い話題に触れていただける内容（天文学全般の入門に、太陽観察や光の実験、装置開発の現場見学を交えた内容のもの）を、土曜日の午後の時間帯で年間４回程度実施している（写真４・資料３参照）。天体観望会とリンクさせ、昼間の講座で解説した天体を夜間の観望会でも観察することもできる。

受講生の中には、京都府のみならず、府外の近畿圏からも、常連の方々を含む約 20～60 名の参加があった。同講座の終了後には、毎回、多くの質問が飛び交い、受講生の熱心さが伺える。中には、生物や化学、物理を専門とする高校教員の方が、「学校で天文分野を教える必要に迫られたので勉強したい。」という目的で受講されることもある。このことから、同講座に対し、地学を専門としない高校教員からの一定の需要が見込まれる。このように、地域の理科教育の一端を担うという意味においても、神山天文台の役割は大きい。

また、同講座の終了後には、地域の方々と研究者との交流を目的とした「アストロノミー・カフェ」を開設（写真５参照）し、お茶を飲みながら気軽に講師に質問できる場を提供している。これらの取組により、地域の方々に親しまれる天文台として、本学のイメージアップにも繋げている。

写真４　天文学講座の様子

写真５　アストロノミー・カフェの様子

（３）神山天文台マスコットキャラクター「ほしみ～るちゃん®」

子供から大人まで、より多くの方々に神山天文台に親しんでいただくために、マスコットキャラクター「ほしみ～るちゃん®」を平成 25（2013）年に採用した（図２参照）。これは、観望会における解説補助等を務める学生が考案した原案をもとに、本学理学部卒業の職員が学生時代に神山天文台での観測・測定装置開発で培った技術を駆使して 3D 化したもので、学生及び教職員から名前を公募のうえ決定、商標登録したものである。

「ほしみ～るちゃん®」は、神山天文台における各種ポスターや案内チラシへの掲載、天体観望会で実施しているスタンプラリーの景品等のほか、社会貢献活動において広く活用されている。

また、平成 29（2017）年度には、LINE スタンプを作成し、身近な広報ツールとしての役割を担っている。

図２　ほしみ～るちゃん®

７．公開事業を通じた学生の育成

土曜日の一般公開や天文学習等の実施にあたっては、神山天文台スタッフに加えて、補助員として学生の協力を得ている。

補助員は、天体観望会における天体解説、天文学習における説明補助等を主に担っている。

実際に補助員に登録して勤務を始めても、最初は、相手の目を見て話せない学生や自分の持っている精一杯の知識で説明し終えると沈黙してしまう学生、早口で威圧的に話してしまう学生もいる。しかし、経験を重ねていくうちに、話し方や応対マナーが驚くほど向上し、一緒に観望会を運営していくという責任感が育ち、自分で考えて行動・提案できるように成長していく学生も少なくない。こうした学生の中から、公

開天文台などの天文に関わる業種に就職した卒業生も輩出している。

このように、神山天文台の観望会等の場で活躍できることは、学生のキャリア形成にも貴重な経験となると考えられる。こうした学生を対象に、平成 23（2011）年度から神山天文台で活動を行う基盤として、学生プロジェクトチーム（平成 27（2015）年度に神山天文台ボランティアチームから「神山天文台サポートチーム」に改称）を立ち上げている。

８.神山天文台サポートチーム

神山天文台サポートチームは、平成 23（2011）年度に神山天文台ボランティアチームとして、神山天文台をより活性化することを目指し、有志の学生によって結成された学生プロジェクトチームである。文系理系を問わず、神山天文台や天文学に興味があれば参加をすることができ、令和２（2020）年３月現在で、約 45 名の学生が在籍し、活動をしている。

同チームの学生たちは、神山天文台研究員や教員の指導のもと、自分たちで下記のようなイベントを企画し、広く地域の方々に神山天文台の魅力発信に努めている。

・天体観望会

土曜日に開催している天体観望会において、シミュレーションソフト「Mitaka」を用いた宇宙の 3D 映像の上映会を行い、神山天文台前に小型望遠鏡を設置し、時節に応じた様々な天体を解説付きで来場者の方に楽しんでいただく取組をしている。

なお、悪天候時には、光の性質について、実験を通じて体験していただいている。

・学内天体観望会

上記とは異なり、大学関係者（教職員・学生）を対象として、年に数回実施している。

荒木望遠鏡・小型望遠鏡による天体観望（写真６参照）や、シミュレーションソフト「Mitaka」を用いた 3D 映像上映会などを体験していただいている。

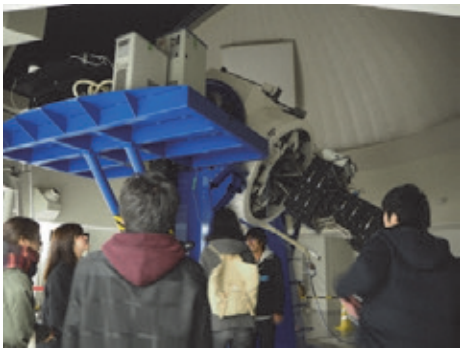

写真６　学内天体観望会の様子

・サタデージャンボリー

サタデージャンボリーは、大学が実施している地域の子供たち向けの大規模イベントである。令和元（2019）年度は、神山天文台を会場とし、「秋の星まつり」と題して、荒木望遠鏡の紹介や宇宙をテーマにした紙芝居、太陽の観察会などを行った。これらを通して、宇宙・天文、ひいては神山天文台への興味の涵養につなげている（写真７参照）。

写真７　サタデージャンボリーの様子

・神山祭（学園祭）

来場する地域・一般の方を対象とし、令和元（2019）年度は、神山天文台を会場とし、「君は一番上まで来たことあるかい？」と題して、荒木望遠鏡の紹介や宇宙の 3D 映像上映会、天体写真やサポートチームの活動写真をまとめたスライドショーなどを実施した。

・その他

上記以外にも、地域の図書館での子ども向けの天体天文教室の実施や、天文同好会などの学内団体との合同イベントなど、日々自主的に神山天文台での活動を続けている。

このように、補助員やサポートチームの一員としての活動による経験を通し、学生たちのコミュニケーション能力や科学に関する知識をより高めることで、本学における人材育成の一端を担っている（資料６参照）。

資料1　各種イベント　来場者数一覧

公開区分	平成22年度（2010）	平成23年度（2011）	平成24年度（2012）	平成25年度（2013）	平成26年度（2014）	平成27年度（2015）	平成28年度（2016）	平成29年度（2017）	平成30年度（2018）
(1) 一般公開（施設見学，天体観望会，3D映像上映会）	2,060	1,762	1,380	973	1,185	1,166	1,584	1,430	1,821
(2) 天文台講座	120	188							
(3) 天文学講座（旧天文学入門講座）		260	303	347	148	114	56	81	145
(4) 特別講演会	77	33	36	64	92	79	64	66	
(5) ひらめき☆ときめきサイエンス（日本学術振興会との共催）	77	30							
(6) 学校・教育機関等利用（小・中・高校等）	484	393	407	204	204	406	499	667	706
(7) オープンキャンパス	960	787	592	510	963	1,614	1,362	1,239	1,105
(8) サタデージャンボリー	547	466	213	316	273	389	500	466	250
(9) 京都産業大学DAY（H28から教育懇談会）	116	156	224	179	217	292	244	295	185
(10) 学内観望会（本学学生、教職員向け3D上映会，天体観望会）	190	417	115	188	122	119	131	74	42
(11) 神山祭	232	557	284	534	509	613	495	870	827
(12) その他（入学式，卒業式等特別公開他）	185	65	162	137	89	150	95	166	105
合計	**5,048**	**5,114**	**3,716**	**3,452**	**3,802**	**4,942**	**5,030**	**5,354**	**5,186**

公開区分	平成31/令和元年度（2019）	平成31/令和元（2019）年度 実施状況（内容・回数等）
(1) 一般公開（施設見学，天体観望会，3D映像上映会）	1,214	年間30回（土曜）実施予定 → 28回実施(2回中止(3/21、3/28))※1
(2) 天文台講座		当初から実施予定なし
(3) 天文学講座（旧天文学入門講座）	131	年間4回実施予定 → 3回実施(1回中止(3/21))※1
(4) 特別講演会		当初から実施予定なし
(5) ひらめき☆ときめきサイエンス（日本学術振興会との共催）		当初から実施予定なし
(6) 学校・教育機関等利用（小・中・高校等）	703	延べ16校利用(幼稚園含む。)
(7) オープンキャンパス	961	年間6回実施予定 → 5回実施(1回中止(3/29))※1
(8) サタデージャンボリー	534	年間1回実施（10月）
(9) 京都産業大学DAY（H28から教育懇談会）	201	年間1回実施(10月)
(10) 学内観望会（本学学生、教職員向け3D上映会，天体観望会）	112	例年、春・冬実施 → 春2回、冬2回実施
(11) 神山祭	817	神山祭期間中実施（3回）
(12) その他（入学式，卒業式等特別公開他）	66	入学式特別開館（4月）実施、入学式・卒業式特別開館（9月）実施 卒業式特別開館（3月）中止※1
合計	**4,739**	

※1　新型コロナウィルス感染拡大防止のため中止

資料2　平成22(2010)年度～平成31/令和元(2019)年度　一般公開来場者数一覧

(注)表記されていない月日は、一般公開やイベントを実施していない。

平成22(2010)年度

	イベント	天候状況	※観望会開催	京都市	京都府	近畿地区	その他府県	小学生以下	中高生	大学生	一般60未満	一般60以上	計
4月3日		晴れ	○	66	6	26	5	10	1	42	47	3	103
4月10日		曇り	×	32	4	3	0	1	0	1	17	20	39
4月17日		晴れ	○	91	16	10	0	21	6	11	61	18	117
4月24日		晴れ	○	69	3	21	3	11	0	32	39	14	96
4月　計			**3**	**258**	**29**	**60**	**8**	**43**	**7**	**86**	**164**	**55**	**355**
5月1日		晴れ時々曇り	○	52	4	22	5	19	1	16	44	3	83
5月8日		晴れ後曇り	○	50	1	7	0	3	2	28	23	2	58
5月15日		晴れ後曇り	○	15	2	22	1	5	1	13	20	1	40
5月22日		曇り	×	5	1	4	5	0	0	1	13	1	15
5月29日		晴れ	○	65	2	13	1	15	1	16	38	11	81
5月　計			**4**	**187**	**10**	**68**	**12**	**42**	**5**	**74**	**138**	**18**	**277**
6月5日		晴れ	○	70	2	24	6	12	2	21	51	16	102
6月12日		晴れ後曇り	○	50	6	13	2	21	2	4	37	7	71
6月19日		曇り	×	6	2	11	1	0	0	3	15	2	20
6月26日	天文台講座	雨	×	9	0	3	0	0	0	1	9	2	12
6月　計			**2**	**135**	**10**	**51**	**9**	**33**	**4**	**29**	**112**	**27**	**205**
7月3日		雨	×	1	4	4	0	0	0	0	8	1	9
7月10日		晴のち曇り	○	28	13	7	4	11	0	6	25	10	52
7月17日		曇り時々晴れ	×	13	1	13	6	5	0	6	20	2	33
7月24日		晴れ時々曇	×	27	4	3	2	11	3	2	14	6	36
7月31日		晴れ時々曇り	△	33	5	15	10	6	20	3	31	3	63
7月　計			**1**	**102**	**27**	**42**	**22**	**33**	**23**	**17**	**98**	**22**	**193**
8月7日		晴れのち曇り	○	126	1	19	8	24	5	1	87	37	154
8月21日		曇り	○	48	1	4	12	14	6	2	38	5	65
8月　計			**2**	**174**	**2**	**23**	**20**	**38**	**11**	**3**	**125**	**42**	**219**
9月4日		曇り後晴れ	○	22	9	10	1	11	0	2	28	1	42
9月11日	天文台講座	晴れ時々曇り	○	21	7	13	1	7	1	16	16	2	42
9月18日		晴れ時々曇り	○	15	7	6	11	4	2	3	26	4	39
9月25日		曇り	○	36	0	30	3	10	1	28	24	6	69
9月　計			**4**	**94**	**23**	**59**	**16**	**32**	**4**	**49**	**94**	**13**	**192**
10月2日	サタデージャンボリー	曇り	○	48	1	5	1	7	1	30	17	0	55
10月9日		雨後曇り	×	3	0	1	0	0	0	0	4	0	4
10月16日		曇り時々晴れ	×	13	5	5	4	6	3	0	15	3	27
10月23日		曇り後晴れ	○	42	0	13	1	12	6	5	25	8	56
10月30日		曇り時々小雨	×	3	0	2	2	1	0	0	3	3	7
10月　計			**2**	**109**	**6**	**26**	**8**	**26**	**10**	**35**	**64**	**14**	**149**
11月6日		晴れ時々曇り	○	19	3	2	0	2	0	2	16	4	24
11月13日		晴れ時々曇り	○	25	14	15	5	2	6	4	40	7	59
11月27日		晴れ時々曇り	○	21	0	2	0	1	0	12	6	4	23
11月　計			**3**	**65**	**17**	**19**	**5**	**5**	**6**	**18**	**62**	**15**	**106**
12月4日		晴れ時々曇り	○	23	0	11	0	8	0	2	21	3	34
12月11日	天文台講座	曇り	△	0	0	2	0	0	0	0	2	0	2
12月18日		曇り	×	3	0	5	3	0	0	2	8	1	11
12月25日	Xmasｽﾍﾟｼｬﾙ講演会	曇り後晴れ	○	2	1	6	5	3	0	2	9	0	14
12月　計			**2**	**28**	**1**	**24**	**8**	**11**	**0**	**6**	**40**	**4**	**61**
1月8日		晴れ時々曇り	○	22	0	6	4	5	1	4	20	2	32
1月22日		晴れ後曇り、小雨	×	12	0	1	0	3	1	3	6	0	13
1月　計			**1**	**34**	**0**	**7**	**4**	**8**	**2**	**7**	**26**	**2**	**45**
2月5日		曇りのち晴れ	○	52	5	14	1	23	2	11	35	1	72
2月12日		曇り一時雪	×	7	2	3	5	1	0	2	13	1	17
2月19日		晴れのち曇り	○	15	0	5	7	4	0	6	13	4	27
2月26日		晴れ	○	29	0	13	15	8	0	12	29	8	57
2月　計			**3**	**103**	**7**	**35**	**28**	**36**	**2**	**31**	**90**	**14**	**173**
3月5日	天文台講座	曇り	○	12	3	4	1	6	0	3	10	1	20
3月12日		曇り	○	8	1	5	3	0	0	8	8	1	17
3月19日		曇り	○	7	2	8	13	1	0	6	22	1	30
3月26日		雪後曇り時々晴れ	○	10	1	2	5	3	0	6	9	0	18
3月　計			**4**	**37**	**7**	**19**	**22**	**10**	**0**	**23**	**49**	**3**	**85**
合　計			**31**	**1,326**	**139**	**433**	**162**	**317**	**74**	**378**	**1,062**	**229**	**2,060**

平成23(2011)年度

	イベント	天候状況	※観望会開催	京都市	京都府	近畿地区	その他府県	小学生以下	中高生	大学生	一般60未満	一般60以上	計
4月2日		曇り	○	12	0	11	2	3	0	3	16	3	25
4月9日		曇り	○	9	4	15	4	5	1	1	24	1	32
4月16日		曇り時々晴れ	○	13	2	1	2	0	1	1	12	4	18
4月23日		曇り	○	3	0	0	0	0	0	1	0	2	3
4月24日		曇り	○	6	0	3	2	1	0	0	9	1	11
4月 計			**5**	**43**	**6**	**30**	**10**	**9**	**2**	**6**	**61**	**11**	**89**
5月7日		曇り時々晴れ	○	15	5	5	0	7	1	5	12	0	25
5月14日	天文学入門講座	晴れ時々曇り	○	49	9	2	1	8	0	8	23	2	61
5月21日	天文学入門講座	曇り	○	26	2	2	3	5	0	3	25	0	33
5月28日		雨天	○	5	0	8	1	0	0	5	7	2	14
5月 計			**4**	**95**	**16**	**17**	**5**	**20**	**1**	**21**	**67**	**4**	**133**
6月4日	サタデージャンボリー	晴れ時々曇り	○	20	3	1	0	6	0	6	9	3	24
6月11日	天文学入門講座	曇り	○	59	2	0	0	18	0	0	43	0	61
6月18日	天文台講座	雨天	×	57	34	4	1	1	4	1	85	5	96
6月25日	天文学入門講座	曇り	○	42	5	16	0	8	1	17	32	5	63
6月 計			**3**	**178**	**44**	**21**	**1**	**33**	**5**	**24**	**169**	**13**	**244**
7月2日	天文学入門講座	曇り	×	22	1	27	2	1	3	1	46	1	52
7月9日	天文学入門講座	晴れのち曇り	○	53	4	13	3	7	0	3	60	3	73
7月16日	天文学入門講座	曇り時々晴れ	○	58	10	11	5	21	0	3	54	6	84
7月23日		曇り時々晴れ	○	25	0	8	0	7	1	3	22	0	33
7月30日		曇り	○	9	1	4	6	5	1	0	11	3	20
7月 計			**4**	**167**	**16**	**63**	**16**	**41**	**5**	**10**	**193**	**13**	**262**
8月6日	オープンキャンパス	曇り時々晴れ	○	40	6	12	6	15	6	2	38	3	64
8月20日	オープンキャンパス	曇り後雨	×	12	4	1	2	5	0	0	12	2	19
8月 計			**1**	**52**	**10**	**13**	**8**	**20**	**6**	**2**	**50**	**5**	**83**
9月3日		台風12号中止	×	0	0	0	0	0	0	0	0	0	0
9月10日	天文台講座	曇り	○	51	9	8	2	16	0	5	45	4	70
9月17日		雨天	×	1	3	5	2	1	0	1	9	0	11
9月24日		晴れ時々曇り	○	55	9	28	1	16	2	14	52	9	93
9月 計			**2**	**107**	**21**	**41**	**5**	**33**	**2**	**20**	**106**	**13**	**174**
10月1日	サタデージャンボリー	曇り時々晴れ	○	14	0	13	0	3	0	4	16	4	27
10月8日	天文学入門講座	曇り時々晴れ	○	54	3	17	6	6	1	23	36	14	80
10月15日		雨天	×	24	3	3	0	0	2	1	24	3	30
10月22日	天文学入門講座	雨天	×	12	1	6	0	0	0	1	12	6	19
10月29日	天文学入門講座	晴れ後曇り	○	33	4	13	0	5	1	9	25	10	50
10月 計			**3**	**137**	**11**	**52**	**6**	**14**	**4**	**38**	**113**	**37**	**206**
11月12日	天文学入門講座	晴れ後曇り	○	68	12	7	2	30	0	7	46	6	89
11月26日	天文学入門講座	晴れ時々曇り	○	57	8	19	6	12	2	3	57	16	90
11月 計			**2**	**125**	**20**	**26**	**8**	**42**	**2**	**10**	**103**	**22**	**179**
12月3日	天文学入門講座	曇り	○	8	1	8	0	0	2	0	12	3	17
12月10日	天文台講座	曇り	○	43	3	12	2	5	5	2	38	10	60
12月17日	天文学入門講座	晴れ時々曇り	○	22	1	11	3	1	0	3	25	8	37
12月24日	Xmasｽﾍﾟｼｬﾙ講演会	曇り	○	32	2	10	6	8	2	8	18	14	50
12月 計			**4**	**105**	**7**	**41**	**11**	**14**	**9**	**13**	**93**	**35**	**164**
1月7日		曇り時々雪	×	2	5	6	6	2	3	0	10	4	19
1月21日		雨天	×	2	0	0	0	0	0	0	2	0	2
1月 計			**0**	**4**	**5**	**6**	**6**	**2**	**3**	**0**	**12**	**4**	**21**
2月4日		晴れ後曇り	○	15	1	11	1	8	0	1	17	2	28
2月18日		雪	○	20	0	3	0	8	1	0	12	2	23
2月25日	科博連ﾌｪｽ	雨天	×	16	1	6	0	8	0	4	10	1	23
2月 計			**2**	**51**	**2**	**20**	**1**	**24**	**1**	**5**	**39**	**5**	**74**
3月3日	天文台講座	晴れ時々曇り	○	23	5	37	1	2	2	3	24	35	66
3月10日		曇り	×	1	0	7	0	2	0	0	5	1	8
3月17日		小雨後曇り	×	6	1	4	9	0	0	8	11	1	20
3月24日		雨後曇り	×	18	0	1	0	0	0	1	18	0	19
3月31日		雨後晴れ時々曇り	○	16	0	3	1	6	3	2	8	1	20
3月 計			**2**	**64**	**6**	**52**	**11**	**10**	**5**	**14**	**66**	**38**	**133**
合 計			**32**	**1,128**	**164**	**382**	**88**	**262**	**45**	**163**	**1,072**	**200**	**1,762**

平成24(2012)年度

	イベント	天候状況	※観望会開催	京都市	京都府	近畿地区	その他府県	小学生以下	中高生	大学生	一般60未満	一般60以上	計
4月7日		曇り時々晴れ	○	10	0	2	2	2	0	5	6	1	14
4月14日		曇り時々晴れ	○	5	1	10	0	5	0	1	8	2	16
4月21日		曇り	×	0	0	0	0	0	0	0	0	0	0
4月28日		晴れ	○	33	5	43	1	20	0	3	49	10	82
4月 計			**3**	**48**	**6**	**55**	**3**	**27**	**0**	**9**	**63**	**13**	**112**
5月12日		晴れ	○	12	5	3	4	4	1	1	17	1	24
5月19日	天文学入門講座	晴れのち曇り	○	31	1	5	4	6	2	3	14	16	41
5月26日		曇り	○	17	5	5	1	5	2	3	12	6	28
5月 計			**3**	**60**	**11**	**13**	**9**	**15**	**5**	**7**	**43**	**23**	**93**
6月2日		曇り	×	12	3	3	2	4	0	3	10	3	20
6月9日	天文学入門講座特別編第1回	曇り時々雨のち晴れ	○	28	2	8	0	4	0	6	13	15	38
6月16日	オープンキャンパス	雨	×	1	0	0	1	1	0	0	1	0	2
6月23日	天文学入門講座	曇り	×	29	1	6	0	2	0	11	15	8	36
6月30日		雨	×	3	2	5	0	1	0	3	5	1	10
6月 計			**1**	**73**	**8**	**22**	**3**	**12**	**0**	**23**	**44**	**27**	**106**
7月7日	七夕講演会	曇りのち晴れ	○	27	4	9	6	11	2	3	24	6	46
7月14日		曇りのち雨	×	4	0	5	0	0	0	4	5	0	9
7月21日		曇り時々雨	×	6	0	12	0	8	1	0	9	0	18
7月28日	天文学入門講座	晴れ時々曇り	○	33	2	17	3	16	2	2	30	5	55
7月 計			**2**	**70**	**6**	**43**	**9**	**35**	**5**	**9**	**68**	**11**	**128**
8月4日	オープンキャンパス	晴れ時々曇り	○	24	4	10	1	4	1	9	19	6	39
8月25日	天文学入門講座	晴れ	○	59	0	32	2	20	0	4	62	7	93
8月 計			**2**	**83**	**4**	**42**	**3**	**24**	**1**	**13**	**81**	**13**	**132**
9月8日	天文学入門講座(池田先生)※中止	曇り時々雨	○	7	0	8	0	0	0	0	12	3	15
9月15日		曇り時々晴れ	○	44	7	31	6	14	1	7	52	14	88
9月29日	天文学入門講座特別編第2回	曇り	×	11	4	9	0	0	1	2	9	12	24
9月 計			**2**	**62**	**11**	**48**	**6**	**14**	**2**	**9**	**73**	**29**	**127**
10月6日		曇りのち雨	×	33	3	14	14	2	8	16	38	0	64
10月13日	サタデージャンボリー	曇り時々晴れ	○	15	0	3	0	3	1	3	8	3	18
10月20日	天文学入門講座	晴れ	○	42	3	10	8	11	2	2	37	11	63
10月27日		曇り	○	21	0	13	2	6	3	3	9	15	36
10月 計			**3**	**111**	**6**	**40**	**24**	**22**	**14**	**24**	**92**	**29**	**181**
11月10日	天文学入門講座	曇り時々晴れ	○	31	4	12	1	4	1	2	26	15	48
11月24日		雲りのち晴れ	○	17	2	2	0	5	0	4	11	1	21
11月 計			**2**	**48**	**6**	**14**	**1**	**9**	**1**	**6**	**37**	**16**	**69**
12月1日		雨	×	1	0	1	1	0	0	1	2	0	3
12月8日	天文学入門講座特別編第3回	曇りのち晴れ	○	14	7	19	0	4	0	5	9	22	40
12月15日		曇りのち雨	×	11	0	5	2	6	2	0	8	2	18
12月22日	天文学入門講座(X'mas特別企画)	曇り時々雨	×	18	2	7	0	5	4	2	8	8	27
12月 計			**1**	**44**	**9**	**32**	**3**	**15**	**6**	**8**	**27**	**32**	**88**
1月12日	天文学入門講座	晴れ	○	15	9	19	2	9	3	3	22	8	45
1月 計			**1**	**15**	**9**	**19**	**2**	**9**	**3**	**3**	**22**	**8**	**45**
2月2日		曇りのち晴れ	○	10	2	2	2	2	1	4	9	0	16
2月9日		曇りのち晴れ	○	9	1	15	3	8	1	1	18	0	28
2月16日	天文学入門講座	晴れ時々雪	○	11	5	20	1	2	7	3	18	7	37
2月23日		晴れ時々曇り	○	9	41	8	0	9	4	5	40	0	58
2月 計			**4**	**39**	**49**	**45**	**6**	**21**	**13**	**13**	**85**	**7**	**139**
3月2日	天文学入門講座特別編第4回・研究成果報告会	雪	×	18	1	21	2	4	3	7	20	8	42
3月9日	天文学入門講座	晴れ	○	17	2	12	7	5	1	3	21	8	38
3月16日		晴れ	○	14	1	2	1	4	0	5	10	0	19
3月23日	卒業式特別開館	曇り時々晴れ	○	21	5	11	8	8	2	10	21	4	45
3月30日		曇り時々晴れ	○	7	0	9	0	1	1	9	4	1	16
3月 計			**4**	**77**	**9**	**55**	**18**	**22**	**7**	**34**	**76**	**21**	**160**
合計			**27**	**730**	**134**	**428**	**87**	**225**	**57**	**158**	**711**	**229**	**1,380**

平成25(2013)年度

	イベント	天候状況	※観望会開催	京都市	京都府	近畿地区	その他府県	小学生以下	中高生	大学生	一般60未満	一般60以上	計
4月6日		雨・嵐	×	0	0	1	0	0	0	0	1	0	1
4月13日		晴れ	○	9	0	2	1	3	0	1	8	0	12
4月20日	天文学入門講座	曇りのち雨	×	29	5	8	0	0	0	11	19	12	42
4月27日		晴れ時々曇り	○	30	3	10	4	11	2	7	26	1	47
4月 計			**2**	**68**	**8**	**21**	**5**	**14**	**2**	**19**	**54**	**13**	**102**
5月11日		雨のち曇り	×	3	0	1	0	1	0	0	3	0	4
5月18日	天文学入門講座	晴れのち曇り	○	23	2	9	2	1	0	13	15	7	36
5月25日		曇り時々晴れ	○	13	0	3	0	5	1	0	10	0	16
5月 計			**2**	**39**	**2**	**13**	**2**	**7**	**1**	**13**	**28**	**7**	**56**
6月1日		曇り	×	0	0	0	0	0	0	0	0	0	0
6月8日	天文学入門講座特別編	曇り時々晴れ	○	44	2	12	2	4	0	16	33	8	61
6月 計			**1**	**44**	**2**	**12**	**2**	**4**	**0**	**16**	**33**	**8**	**61**
7月20日		晴れ	○	32	1	14	1	16	0	0	31	1	48
7月27日	天文学入門講座	曇り時々晴れ	○	49	5	7	7	14	4	7	34	9	68
7月 計			**2**	**81**	**6**	**21**	**8**	**30**	**4**	**7**	**65**	**10**	**116**
8月3日		晴れ時々曇り	○	52	0	15	5	23	2	5	36	6	72
8月24日		曇り時々雨	×	14	0	0	0	7	0	0	7	0	14
8月 計			**1**	**66**	**0**	**15**	**5**	**30**	**2**	**5**	**43**	**6**	**86**
9月7日		雨	×	7	0	0	3	4	0	0	6	0	10
9月14日		曇り	×	4	0	2	0	0	1	2	3	0	6
9月21日		晴れ	○	32	0	11	2	12	1	3	27	2	45
9月28日	天文学入門講座特別編	晴れ	○	41	7	20	2	3	0	9	47	11	70
9月 計			**2**	**84**	**7**	**33**	**7**	**19**	**2**	**14**	**83**	**13**	**131**
10月5日		曇り	×	6	0	5	2	0	0	4	7	2	13
10月12日		晴れのち曇り	○	40	2	7	3	10	0	10	28	4	52
10月19日	天文学入門講座	曇り時々雨	×	16	1	14	1	1	2	1	18	10	32
10月26日		雨のち晴れ	○	4	0	3	0	1	2	0	4	0	7
10月 計			**2**	**66**	**3**	**29**	**6**	**12**	**4**	**15**	**57**	**16**	**104**
11月9日	天文学入門講座	曇りのち晴れ	○	35	3	16	2	8	2	5	34	8	57
11月30日	アイソン彗星講演会	晴れ	○	64	4	13	3	19	2	7	48	8	84
11月 計			**2**	**99**	**7**	**29**	**5**	**27**	**4**	**12**	**82**	**16**	**141**
12月7日	天文学入門講座特別編	雨	×	17	0	16	0	1	2	4	19	7	33
12月14日		曇り時々晴れ	○	7	3	2	11	1	0	0	20	2	23
12月21日	天文学入門講座(X'mas特別企画)	曇りのち雨	×	20	0	12	7	4	0	6	22	8	40
12月 計			**1**	**44**	**3**	**30**	**18**	**6**	**2**	**10**	**61**	**17**	**96**
3月22日		腫れ	○	10	20	6	2	8	4	2	16	8	**38**
3月29日	天文学入門講座特別編	曇り	×	22	3	11	6	2	2	12	19	7	**42**
3月 計			**1**	**32**	**23**	**17**	**8**	**10**	**6**	**14**	**35**	**15**	**80**
合計			**16**	**623**	**61**	**220**	**66**	**159**	**27**	**125**	**541**	**121**	**973**

平成26(2014)年度

	イベント	天候状況	※観望会開催	京都市	京都府	近畿地区	その他府県	小学生以下	中高生	大学生	一般60未満	一般60以上	その他(未記入)	計
4月7日	天体観望会、3D上映会	雨	×	4	0	1	0	0	0	2	3	0	0	5
4月12日	天体観望会	晴れ	○	7	0	2	3	1	0	2	2	0	7	12
4月19日	天体観望会	曇りのち晴れ	○	5	0	0	0	2	0	0	3	0	0	5
4月26日	天体観望会	晴れ	○	26	0	8	7	10	0	6	20	2	3	41
4月 計			**3**	**42**	**0**	**11**	**10**	**13**	**0**	**10**	**28**	**2**	**10**	**63**
5月10日	天体観望会	晴れ	○	23	4	0	0	9	0	3	14	0	1	27
5月17日	施設見学・天文学講座・天体観望会	晴れ	○	30	4	22	3	2	2	17	27	8	3	59
5月24日	天体観望会	晴れ	○	16	1	5	0	4	0	1	14	3	0	22
5月31日	京都産業大学DAY・天体観望会	晴れ	○	27	0	6	7	7	5	3	17	2	6	40
5月 計			**4**	**96**	**9**	**33**	**10**	**22**	**7**	**24**	**72**	**13**	**10**	**148**
6月7日	天体観望会・3D上映会	曇り	△	10	0	0	0	1	0	1	3	4	1	10
6月 計			**0**	**10**	**0**	**0**	**0**	**1**	**0**	**1**	**3**	**4**	**1**	**10**
7月5日	七夕講演会・3D上映会	曇り	×	21	3	15	1	5	1	10	17	5	2	40
7月19日	天体観望会・3D上映会	曇り	×	8	0	0	1	0	0	4	5	0	0	9
7月26日	天体観望会	晴れ	○	26	7	18	0	12	1	3	37	2	0	51
7月 計			**1**	**55**	**10**	**33**	**2**	**17**	**2**	**17**	**59**	**7**	**2**	**100**
8月2日	天文学講座・3D上映会	曇り	×	34	7	25	2	2	5	13	35	7	6	68
8月7日	天体観望会	腫れ	○	14	4	4	19	6	1	5	8	1	4	41
8月23日	3D上映会	曇りのち雨	×	21	4	10	1	6	4	2	17	3	0	36
8月 計			**1**	**69**	**15**	**39**	**22**	**14**	**10**	**20**	**60**	**11**	**10**	**125**
9月6日	3D上映会	雨	×	3	0	1	0	0	0	0	4	0	0	4
9月13日	天体観望会	腫れ	○	48	4	19	15	12	5	12	33	5	19	86
9月20日	天体観望会・3D上映会	曇りのち腫れ	○	17	0	1	1	1	1	5	12	0	0	19
9月27日	天体観望会	晴れ	○	38	4	7	1	11	1	5	24	3	6	50
9月 計			**3**	**106**	**8**	**28**	**17**	**24**	**7**	**22**	**73**	**8**	**25**	**159**
10月4日	天体観望会・3D上映会	曇りのち晴れ	○	13	1	4	0	1	0	4	12	1	0	18
10月8日	皆既月食観望会	晴れ	○	225	12	41	8	41	3	119	99	12	15	286
10月11日	天体観望会	曇りのち晴れ	○	11	0	12	9	1	0	11	12	1	7	32
10月18日	天体観望会・3D上映会	晴れ	○	22	0	9	3	7	1	4	19	4	0	34
10月25日	サタデージャンボリー・天体観望会	晴れ時々曇り	○	13	7	1	4	3	1	5	15	1	0	25
10月 計			**5**	**284**	**20**	**67**	**24**	**53**	**5**	**143**	**157**	**19**	**22**	**399**
11月8日	天体観望会・3D上映会	曇り	△	3	3	3	4	1	1	4	6	1	0	13
11月29日	天体観望会・3D上映会	晴れ時々曇り	○	17	5	5	2	7	2	0	12	0	8	29
11月 計			**1**	**20**	**8**	**8**	**6**	**8**	**3**	**4**	**18**	**1**	**8**	**42**
12月6日	天体観望会・3D上映会	晴れ時々曇り	○	12	0	5	0	4	1	1	9	0	2	17
12月13日	天体観望会	晴れ	○	21	2	9	2	10	2	2	19	0	1	34
12月20日	クリスマス特別講演会・3D上映会	雨のち曇り	×	24	2	13	18	3	0	33	19	1	1	57
12月 計			**2**	**57**	**4**	**27**	**20**	**17**	**3**	**36**	**47**	**1**	**4**	**108**
3月21日	卒業式特別開館・天体観望会	晴れ時々曇り	○	3	0	1	0	0	1	1	1	0	1	4
3月28日	天体観望会・天文学講座	晴れ	○	9	10	7	1	0	5	4	14	3	1	27
3月 計			**2**	**12**	**10**	**8**	**1**	**0**	**6**	**5**	**15**	**3**	**2**	**31**
合計			**22**	**751**	**84**	**254**	**112**	**169**	**43**	**282**	**532**	**69**	**94**	**1,185**

平成27(2015)年度

	イベント	天候状況	※観望会開催	京都市	京都府	近畿地区	その他府県	小学生以下	中高生	大学生	一般60未満	一般60以上	その他(未記入)	計
4月4日	皆既月食解説講座・皆既月食観望会	曇り	△	4	0	4	3	2	1	2	5	1	1	12
4月11日	天体観望会・3D上映会	曇りのち晴れ	○	2	0	0	0	0	0	0	2	0	0	2
4月18日	天体観望会	晴れのち曇り	○	7	2	7	0	5	0	5	5	1	0	16
4月25日	天体観望会	晴れ	○	13	0	0	0	3	1	4	4	1	0	13
4月 計			**3**	**26**	**2**	**11**	**3**	**10**	**2**	**11**	**16**	**3**	**1**	**43**
5月2日	天体観望会	晴れ	○	16	4	20	8	9	2	2	30	2	3	48
5月9日	天体観望会	曇りのち晴れ	○	16	2	4	7	4	1	5	12	2	5	29
5月16日	天文学講座・天体観望会・3D上映会	曇りのち晴れ	○	32	1	11	12	2	1	11	21	13	8	56
5月23日	3D上映会	曇り	×	2	0	3	0	0	1	2	2	0	0	5
5月30日	3D上映会	曇り	×	12	0	0	2	2	1	7	4	0	0	14
5月 計			**3**	**78**	**7**	**38**	**29**	**17**	**6**	**27**	**69**	**17**	**16**	**152**
6月6日	天体観望会	晴れ	○	31	0	13	1	7	5	8	22	1	2	45
6月13日	3D上映会	曇り	×	10	0	9	4	3	2	4	12	2	0	23
6月 計			**1**	**10**	**0**	**9**	**4**	**3**	**2**	**4**	**12**	**2**	**0**	**23**
7月4日	七夕講演会・3D上映会	雨	×	34	2	17	1	1	0	9	26	18	0	54
7月18日	天体観望会・3D上映会	晴れ	○	21	3	4	0	12	2	1	10	1	2	28
7月25日	天体観望会	晴れ	○	53	0	19	3	21	6	2	34	9	3	75
7月 計			**2**	**108**	**5**	**40**	**4**	**34**	**8**	**12**	**70**	**28**	**5**	**157**
8月1日	天体観望会	晴れ	○	39	2	6	3	11	2	2	19	5	11	50
8月22日	天体観望会	晴れ	○	37	3	13	7	17	2	5	30	4	2	60
8月 計			2	**76**	**5**	**19**	**10**	**28**	**4**	**7**	**49**	**9**	**13**	**110**
9月5日	3D上映会	曇り	×	21	0	13	1	14	0	3	13	1	4	35
9月12日	天体観望会・3D上映会	曇りときどき晴れ	△	29	7	7	0	11	3	5	22	1	1	43
9月19日	天体観望会	曇り時々晴れ	○	29	0	11	2	17	0	4	17	1	3	42
9月26日	3D上映会	曇り	×	6	2	9	2	0	2	3	8	3	3	19
9月 計			**1**	**85**	**9**	**40**	**5**	**42**	**5**	**15**	**60**	**6**	**11**	**139**
10月3日	天体観望会	晴れ	○	33	7	6	1	5	1	11	26	1	3	47
10月10日	3D上映会	曇り	×	12	0	0	9	3	0	5	7	4	2	21
10月17日	天体観望会	晴れ	○	35	3	2	0	9	3	8	15	3	2	40
10月24日	天文学講座・天体観望会・3D上映会	晴れ	○	51	0	7	3	9	0	22	14	10	6	61
10月 計			**3**	**131**	**10**	**15**	**13**	**26**	**4**	**46**	**62**	**18**	**13**	**169**
11月7日	3D上映会	雨	×	18	0	9	2	8	0	7	11	2	1	29
11月28日	天体観望会	晴れ	○	31	4	16	1	10	1	4	30	7	0	52
11月 計			**1**	**49**	**4**	**25**	**3**	**18**	**1**	**11**	**41**	**9**	**1**	**81**
12月5日	天体観望会	曇りのち晴れ	○	43	2	10	2	10	0	6	22	4	15	57
12月12日	天体観望会・3D上映会	曇りのち晴れ	○	30	0	17	3	9	8	3	25	1	4	50
12月19日	クリスマス特別講演会・天体観望会	曇りのち晴れ	○	24	5	11	5	7	6	10	18	2	2	45
12月26日	天体観望会	晴れ	○	34	0	7	1	10	2	5	19	4	2	42
12月 計			**4**	**131**	**7**	**45**	**11**	**36**	**16**	**24**	**84**	**11**	**23**	**194**
3月19日	3D上映会	曇り時々晴れ	×	5	0	2	0	1	2	0	4	0	0	7
3月26日	天文学講座・天体観望会	曇りのち晴れ	○	43	19	23	6	22	3	7	43	16	0	91
3月 計			**1**	**48**	**19**	**25**	**6**	**23**	**5**	**7**	**47**	**16**	**0**	**98**
合計			**21**	**742**	**68**	**267**	**88**	**237**	**53**	**164**	**510**	**119**	**83**	**1,166**

平成28(2016)年度

	イベント	天候状況	※観望会開催	京都市	京都府	近畿地区	その他府県	小学生以下	中高生	大学生	一般60未満	一般60以上	その他(未記入)	計
4月2日	入学式特別開館・3D上映会	曇り	×	6	1	24	8	3	2	4	25	2	3	39
4月9日	天体観望会・3D上映会	曇り	△	16	5	7	2	3	3	12	11	1	0	30
4月16日	3D上映会	曇り	×	6	0	0	4	0	0	8	2	0	0	10
4月23日	3D上映会	曇りのち雨	×	6	0	2	0	3	0	0	5	0	0	8
4月30日	天体観望会	晴れ	○	67	5	3	4	22	5	7	11	29	5	79
4月 計			**1**	**101**	**11**	**36**	**18**	**31**	**10**	**31**	**54**	**32**	**8**	**166**
5月7日	天体観望会	曇りのち晴れ	○	18	2	13	1	7	1	0	3	16	7	34
5月14日	天体観望会	曇りのち晴れ	○	38	4	2	6	14	0	1	10	20	5	50
5月21日	天体観望会	晴れ	○	37	1	2	1	9	0	0	12	16	4	41
5月28日	天体観望会	曇りのち晴れ	○	2	2	8	5	2	1	1	11	2	0	17
5月 計			**4**	**95**	**9**	**25**	**13**	**32**	**2**	**2**	**36**	**54**	**16**	**142**
6月4日	3D上映会	曇りのち雨	×	10	1	0	0	3	0	5	2	1	0	11
6月11日	3D上映会	曇り	×	39	3	7	1	9	0	22	12	7	0	50
6月 計			**0**	**49**	**4**	**7**	**1**	**12**	**0**	**27**	**14**	**8**	**0**	**61**
7月9日	七夕講演会・3D上映会	雨のち曇り	×	20	0	7	1	6	0	5	16	1	0	28
7月16日	天体観望会・3D上映会	曇り	△	11	3	4	0	4	2	3	9	0	0	18
7月23日	天体観望会	曇りのち晴れ	○	60	10	31	4	34	3	6	56	2	4	105
7月30日	天体観望会	晴れ	○	52	8	9	23	26	11	8	31	4	12	92
7月 計			**2**	**143**	**21**	**51**	**28**	**70**	**16**	**22**	**112**	**7**	**16**	**243**
8月6日	天体観望会・3D上映会	曇りのち晴れ	○	44	6	8	36	26	3	33	24	2	6	94
8月20日	天体観望会	曇りときどき晴れ	○	48	6	17	16	29	3	7	41	2	5	87
8月 計			**2**	**92**	**12**	**25**	**52**	**55**	**6**	**40**	**65**	**4**	**11**	**181**
9月3日	天体観望会・3D上映会	曇り	△	5	5	5	2	3	0	3	9	2	0	17
9月10日	天体観望会・3D上映会	曇りのち晴れ	○	91	7	12	6	36	2	8	56	9	5	116
9月17日	3D上映会	曇り	×	6	4	1	1	2	3	2	5	0	0	12
9月24日	天体観望会・3D上映会	曇りときどき晴れ	△	12	5	8	7	6	1	1	16	8	0	32
9月 計			**1**	**114**	**21**	**26**	**16**	**47**	**6**	**14**	**86**	**19**	**5**	**177**
10月1日	3D上映会	曇り	×	0	0	1	0	0	0	1	0	0	0	1
10月8日	3D上映会	曇り	×	33	0	17	8	8	1	15	22	8	4	58
10月15日	天体観望会	晴れ	○	61	6	16	7	32	1	7	42	5	3	90
10月22日	3D上映会	曇り	×	9	0	1	1	0	1	4	6	0	0	11
10月29日	天体観望会	曇りのち晴れ	○	23	5	13	1	11	2	4	18	7	0	42
10月 計			**2**	**126**	**11**	**48**	**17**	**51**	**5**	**31**	**88**	**20**	**7**	**202**
11月12日	天体観望会	晴れ	○	67	11	20	0	28	1	11	42	11	5	98
11月 計			**1**	**67**	**11**	**20**	**0**	**28**	**1**	**11**	**42**	**11**	**5**	**98**
12月3日	天体観望会	晴れ	○	51	7	8	8	25	1	2	42	4	0	74
12月10日	天体観望会・3D上映会	曇りのち晴れ	○	30	0	5	4	11	0	6	20	2	0	39
12月17日	天体観望会	曇りのち晴れ	○	27	0	12	0	8	1	6	19	4	1	39
12月24日	クリスマス特別講演会・天体観望会	曇りのち晴れ	○	51	4	23	4	12	7	19	31	10	3	82
12月 計			**4**	**159**	**11**	**48**	**16**	**56**	**9**	**33**	**112**	**20**	**4**	**234**
3月25日	天文学講座・天体観望会	晴れ時々曇り	○	28	28	21	3	20	3	5	32	9	11	80
3月 計			**1**	**28**	**28**	**21**	**3**	**20**	**3**	**5**	**32**	**9**	**11**	**80**
合計			**18**	**974**	**139**	**307**	**164**	**402**	**58**	**216**	**641**	**184**	**83**	**1,584**

平成29(2017)年度 ※平成29(2017)年度より中高生を[中学生][高校生]に分類

	イベント	天候状況	※観望会開催	京都市	京都府	近畿地区	その他府県	小学生以下	中学生※	高校生※	大学生	一般60未満	一般60以上	その他(未記入)	計
4月1日	天体観望会・3D上映会	晴れ	○	26	0	11	2	9	0	1	16	12	1	0	39
4月8日	天体観望会・3D上映会	雨	×	2	0	1	0	0	0	0	3	0	0	0	3
4月15日	天体観望会・3D上映会	曇り時々晴れ	△	1	3	0	0	2	0	0	1	1	0	0	4
4月22日	天体観望会・3D上映会	晴れ	○	50	2	6	2	15	4	2	16	23	0	0	60
4月 計			**2**	**79**	**5**	**18**	**4**	**26**	**4**	**3**	**36**	**36**	**1**	**0**	**106**
5月6日	天体観望会・3D上映会	曇りのち晴れ	○	24	0	0	0	13	0	0	0	11	0	0	24
5月13日	天体観望会・3D上映会	曇り	△	2	3	0	0	2	0	0	0	3	0	0	5
5月20日	天体観望会・3D上映会	晴れ	○	75	4	12	3	30	1	0	5	45	13	0	94
5月27日	天文学講座・天体観望会・3D上映会	晴れ	○	45	3	20	1	14	4	0	13	31	7	0	69
5月 計			**3**	**146**	**10**	**32**	**4**	**59**	**5**	**0**	**18**	**90**	**20**	**0**	**192**
6月3日	天体観望会・3D上映会	晴れのち曇り	○	39	2	4	0	15	0	0	4	24	2	0	45
6月 計			**1**	**39**	**2**	**4**	**0**	**15**	**0**	**0**	**4**	**24**	**2**	**0**	**45**
7月8日	七夕講演会・天体観望会・3D上映会	曇り	△	61	10	20	5	25	0	3	12	35	7	14	96
7月15日	天体観望会・3D上映会	曇り	○	42	21	18	0	33	0	2	1	40	2	3	81
7月22日	天体観望会・3D上映会	曇り時々雨	×	27	6	15	0	17	0	2	6	21	2	0	48
7月29日	天体観望会・3D上映会	曇り時々晴れ	○	42	6	10	3	24	2	3	4	28	0	0	61
7月 計			**2**	**172**	**43**	**63**	**8**	**99**	**2**	**10**	**23**	**124**	**11**	**17**	**286**
8月5日	天体観望会・2D上映会	曇り	○	17	4	1	5	13	0	2	0	11	1	0	27
8月19日	天体観望会・2D上映会	曇り時々晴れ	○	86	14	33	3	44	6	3	3	58	8	14	136
8月 計			**2**	**103**	**18**	**34**	**8**	**57**	**6**	**5**	**3**	**69**	**9**	**14**	**163**
9月2日	天体観望会・2D上映会	晴れ時々曇り	○	70	9	27	0	50	1	1	4	50	0	0	106
9月9日	天体観望会・2D上映会	曇り時々雨	×	51	3	6	0	22	1	0	2	32	3	0	60
9月16日	天体観望会・2D上映会	雨	×	3	0	1	0	0	0	0	3	1	0	0	4
9月30日	天体観望会・3D上映会	晴れ	○	57	12	27	4	25	1	0	2	58	4	10	100
9月 計			**2**	**181**	**24**	**61**	**4**	**97**	**3**	**1**	**11**	**141**	**7**	**10**	**270**
10月7日	天体観望会・3D上映会	雨のち晴れ	○	21	0	2	2	10	0	0	1	12	2	0	25
10月14日	天体観望会(小型望遠鏡のみ)・3D上映会	曇り	○	4	0	2	0	2	0	0	0	2	2	0	6
10月21日	天体観望会・3D上映会	雨	×	1	0	0	0	0	0	0	0	0	1	0	1
10月28日	天体観望会・3D上映会	雨	×	3	0	0	0	1	0	0	0	2	0	0	3
10月 計			**2**	**29**	**0**	**4**	**2**	**13**	**0**	**0**	**1**	**16**	**5**	**0**	**35**
11月11日	天体観望会・3D上映会	曇り時々雨	×	8	1	8	4	10	0	0	1	9	0	1	21
11月18日	天体観望会・3D上映会	曇り時々雨	×	1	0	2	0	0	0	0	3	0	0	0	3
11月25日	天体観望会・3D上映会	晴れ時々曇り	○	65	4	10	6	23	8	0	11	35	8	0	85
11月 計			**1**	**74**	**5**	**20**	**10**	**10**	**0**	**0**	**1**	**9**	**0**	**1**	**109**
12月2日	天文学講座・天体観望会・3D上映会	晴れ時々曇り	○	64	8	13	7	20	2	0	15	44	8	3	92
12月9日	天体観望会・3D上映会	晴れ	○	39	0	5	1	14	3	0	6	19	3	0	45
12月16日	天体観望会・3D上映会	曇りのち晴れ	○	18	0	1	0	5	1	0	4	9	0	0	19
12月 計			**3**	**121**	**8**	**19**	**8**	**39**	**6**	**0**	**25**	**72**	**11**	**3**	**156**
3月24日	天文学講座・天体観望会・3D上映会	晴れのち曇り	○	40	25	19	1	15	3	0	11	42	14	0	85
3月31日	天体観望会・3D上映会	晴れ	○	6	3	11	3	10	0	0	2	9	2	0	23
3月 計			**2**	**46**	**28**	**30**	**4**	**25**	**3**	**0**	**13**	**51**	**16**	**0**	**108**
合計			**20**	**990**	**143**	**285**	**52**	**440**	**29**	**19**	**135**	**632**	**82**	**45**	**1,470**

平成30(2018)年度

	イベント	天候状況	※観望会開催	京都市	京都府	近畿地区	その他府県	小学生以下	中学生	高校生	大学生	一般60未満	一般60以上	その他(未記入)	計
4月7日	天体観望会・3D上映会	雨のち曇り	×	0	3	2	0	1	1	0	0	3	0	0	5
4月14日	天体観望会・3D上映会	雨のち曇り	×	2	0	1	0	1	0	0	1	1	0	0	3
4月21日	天体観望会・3D上映会	晴れ	○	58	1	15	1	23	0	0	17	29	6	0	75
4月28日	天体観望会・3D上映会	晴れ	○	37	1	6	1	10	0	0	14	16	3	2	45
4月 計			**2**	**97**	**5**	**24**	**2**	**35**	**1**	**0**	**32**	**49**	**9**	**2**	**128**
5月12日	天体観望会・3D上映会	曇り	○	52	1	12	2	22	5	1	2	29	8	0	67
5月19日	天文学講座・天体観望会・3D上映会	曇り時々雨	×	36	1	9	1	2	0	0	7	17	21	0	47
5月26日	天体観望会・3D上映会	晴れ	○	48	3	15	0	24	1	1	3	32	1	4	66
5月 計			**2**	**136**	**5**	**36**	**3**	**48**	**6**	**2**	**12**	**78**	**30**	**4**	**180**
6月2日	天体観望会・3D上映会	晴れ	○	95	4	4	0	39	1	0	3	50	10	0	103
6月 計			**1**	**95**	**4**	**4**	**0**	**39**	**1**	**0**	**3**	**50**	**10**	**0**	**103**
7月14日	天体観望会・3D上映会	晴れ	○	86	17	19	4	44	2	9	12	55	4	0	126
7月21日	天文学講座・天体観望会・3D上映会	晴れ	○	100	0	21	0	28	4	4	19	52	14	0	121
7月 計			**2**	**186**	**17**	**40**	**4**	**72**	**6**	**13**	**31**	**107**	**18**	**0**	**247**
8月4日	天体観望会・3D上映会・講演会	晴れ	○	192	21	34	6	93	8	3	11	108	16	14	253
8月18日	天体観望会・3D上映会・講演会	晴れ	○	184	16	30	9	79	10	3	6	123	15	3	239
8月 計			**2**	**376**	**37**	**64**	**15**	**172**	**18**	**6**	**17**	**231**	**31**	**17**	**492**
9月9日	天体観望会・3D上映会	曇り時々雨	×	2	0	0	0	1	0	0	0	1	0	0	2
9月15日	天体観望会・3D上映会	曇り時々雨	×	5	0	3	2	1	0	0	2	3	4	0	10
9月22日	天体観望会・3D上映会	曇り時々晴れ	○	49	8	12	4	24	0	0	9	36	4	0	73
9月29日	天体観望会・3D上映会	雨	×	0	0	0	0	0	0	0	0	0	0	0	0
9月 計			**1**	**56**	**8**	**15**	**6**	**26**	**0**	**0**	**11**	**40**	**8**	**0**	**85**
10月13日	天体観望会・3D上映会	曇り	○	28	0	4	0	11	1	0	3	17	0	0	32
10月20日	天体観望会・3D上映会	曇りのち晴れ	○	42	6	19	3	19	1	9	4	29	8	0	70
10月27日	天体観望会・3D上映会	曇りのち晴れ	○	21	0	31	2	17	7	1	4	18	5	2	54
10月 計			**3**	**91**	**6**	**54**	**5**	**47**	**9**	**10**	**11**	**64**	**13**	**2**	**156**
11月10日	天体観望会・3D上映会	晴れ	○	130	12	4	3	83	0	0	6	49	11	0	149
11月17日	天体観望会・3D上映会	曇りのち晴れ	○	21	7	19	2	25	0	0	0	31	3	0	59
11月24日	天体観望会・3D上映会	晴れ	○	38	10	13	1	22	1	0	4	31	4	0	62
11月 計			**3**	**130**	**12**	**4**	**3**	**83**	**0**	**0**	**6**	**49**	**11**	**0**	**270**
12月1日	天体観望会・3D上映会	曇り時々晴れ	○	16	7	7	2	10	1	0	3	17	1	0	32
12月8日	天体観望会・3D上映会	晴れ時々曇り	○	20	12	8	2	7	0	3	4	20	8	0	42
12月15日	天体観望会・3D上映会	晴れ時々曇り	○	34	4	8	1	13	1	0	13	18	1	0	46
12月22日	天文学講座・天体観望会・3D上映会	曇りのち晴れ	○	43	6	21	9	5	1	7	13	37	16	0	79
12月 計			**4**	**113**	**29**	**44**	**14**	**35**	**3**	**10**	**33**	**92**	**26**	**0**	**199**
3月23日	天文学講座・天体観望会・3D上映会	曇りのち晴れ	○	30	37	19	2	17	0	6	9	43	13	0	88
3月30日	天体観望会・3D上映会	雨	×	3	0	0	3	0	1	0	1	4	0	0	6
3月 計			**1**	**33**	**37**	**19**	**5**	**17**	**1**	**6**	**10**	**47**	**13**	**0**	**94**
合計			**21**	**1,313**	**160**	**304**	**57**	**574**	**45**	**47**	**166**	**807**	**169**	**25**	**1,954**

平成31/令和元(2019)年度

	イベント	天候状況	※観望会開催	京都市	京都府	近畿地区	その他府県	小学生以下	中学生	高校生	大学生	一般60未満	一般60以上	その他(未記入)	計
4月6日	天体観望会・3D上映会	晴れ	○	38	2	8	0	15	0	0	13	17	2	1	48
4月13日	天体観望会・3D上映会	曇り	○	18	3	6	0	7	0	1	5	14	0	0	27
4月20日	天体観望会・3D上映会	晴れ	○	29	0	9	3	12	1	0	3	23	2	0	41
4月27日	天体観望会・3D上映会	小雨のち曇り	×	23	8	12	4	4	0	19	5	17	2	0	47
4月 計			**3**	**85**	**5**	**23**	**3**	**34**	**1**	**1**	**21**	**54**	**4**	**1**	**163**
5月11日	天体観望会・3D上映会	晴れ	○	47	9	7	0	13	1	1	16	26	6	0	63
5月18日	天体観望会・3D上映会	曇り	×	14	3	0	0	4	0	0	3	9	1	0	17
5月25日	天文学講座・天体観望会・3D上映会	曇り	○	59	9	17	7	13	0	11	8	50	10	0	92
5月 計			**2**	**120**	**21**	**24**	**7**	**30**	**1**	**12**	**27**	**85**	**17**	**0**	**172**
6月1日	天体観望会・3D上映会	曇り	○	34	6	2	0	13	0	0	10	12	1	6	42
6月 計			**1**	**34**	**6**	**2**	**0**	**13**	**0**	**0**	**10**	**12**	**1**	**6**	**42**
7月6日	天体観望会・3D上映会	曇り	○	31	3	4	1	14	0	0	9	16	0	0	39
7月13日	天体観望会・3D上映会	雨	×	5	0	0	0	1	1	0	1	2	0	0	5
7月20日	天体観望会・3D上映会	曇り	×	20	0	6	26	5	1	0	31	11	0	4	52
7月27日	天文学講座・天体観望会・3D上映会	曇り	△	40	4	19	3	4	7	2	19	27	7	0	66
7月 計			**1**	**96**	**7**	**29**	**30**	**24**	**9**	**2**	**60**	**56**	**7**	**4**	**162**
8月3日	天体観望会・3D上映会	晴れ	○	62	7	26	2	24	5	2	13	41	5	7	97
8月24日	天体観望会・3D上映会	曇り	×	31	5	3	2	18	0	0	0	19	4	0	41
8月 計			**1**	**93**	**12**	**29**	**4**	**42**	**5**	**2**	**13**	**60**	**9**	**7**	**138**
9月7日	天体観望会・3D上映会	晴れのち曇り	○	68	0	11	2	26	0	2	6	33	4	10	81
9月14日	天体観望会・3D上映会	雲りのち晴れ	○	76	4	26	4	28	4	7	7	49	4	11	110
9月21日	天体観望会・3D上映会	曇り	×	6	0	3	1	0	0	1	5	3	1	0	10
9月28日	天体観望会・3D上映会	曇り	×	7	0	1	0	3	0	0	1	4	0	0	8
9月 計			**2**	**157**	**4**	**41**	**7**	**57**	**4**	**10**	**19**	**89**	**9**	**21**	**209**
10月5日	天体観望会・3D上映会	雲りのち晴れ	○	64	2	4	2	26	0	1	6	33	6	0	72
10月12日	天体観望会・3D上映会【中止】※1	–	–	–	–	–	–	–	–	–	–	–	–	–	0
10月19日	天体観望会・3D上映会	曇り	×	0	1	1	2	0	0	0	0	4	0	0	4
10月26日	天体観望会・3D上映会	曇り時々晴れ	○	28	0	8	2	8	0	0	8	19	3	0	38
10月 計			**2**	**92**	**3**	**13**	**6**	**34**	**0**	**1**	**14**	**56**	**9**	**0**	**114**
11月9日	天体観望会・3D上映会	晴れ	○	49	6	17	4	27	1	1	9	31	3	4	76
11月16日	天体観望会・3D上映会	曇り時々晴れ	×	70	5	15	4	30	1	9	8	38	7	1	94
11月30日	天体観望会・3D上映会	晴れ	○	40	0	4	1	11	0	0	12	22	0	0	45
11月 計			**2**	**49**	**6**	**17**	**4**	**27**	**1**	**1**	**9**	**31**	**3**	**4**	**215**
12月7日	天体観望会・3D上映会	雲りのち晴れ	○	12	0	13	0	6	1	0	2	16	0	0	25
12月14日	天体観望会・3D上映会	曇りのち晴れ	○	12	2	6	2	6	0	1	3	11	1	0	22
12月21日	天文学講座・天体観望会・3D上映会	曇り	×	43	2	18	3	8	0	3	18	34	3	0	66
12月 計			**2**	**67**	**4**	**37**	**5**	**20**	**1**	**4**	**23**	**61**	**4**	**0**	**113**
3月21日	天文学講座・天体観望会・3D上映会【中止】※2	–	–	–	–	–	–	–	–	–	–	–	–	–	0
3月28日	天体観望会・3D上映会【中止】※2	–	–	–	–	–	–	–	–	–	–	–	–	–	0
3月 計			**0**	**0**	**0**	**0**	**0**	**0**	**0**	**0**	**0**	**0**	**0**	**0**	**0**
合計			**16**	**793**	**68**	**215**	**66**	**281**	**22**	**33**	**196**	**504**	**63**	**43**	**1,328**

※1:台風接近のため
※2:新型コロナウイルス感染症の感染拡大の影響のため

資料3　天文台講座・天文学入門講座・天文学講座　開催一覧

平成22(2010)年度　天文台講座

回数	開催日	時間	タイトル	講師
1	6月26日	15:00～16:00	宇宙の秩序と階層構造	中道　晶香　神山天文台専門員
2	9月11日	15:00～16:30	彗星(ほうき星)と私たちの地球	河北　秀世　神山天文台長
3	12月11日	16:00～17:30	銀河の中は、爆発だらけ	新井　彰　神山天文台特定研究員
4	3月5日	16:00～17:30	近赤外線の“目”で宇宙を見る	吉川　智裕　神山天文台専門員

平成23(2011)年度　天文台講座

回数	開催日	時間	タイトル	講師
1	6月18日	15:00～16:30	神山天文台開設1周年記念講演会 第1部　宇宙生命に挑む～天文学からのアプローチ～ 第2部　彗星(ほうき星)とは？研究の最前線	渡部　潤一　国立天文台教授 河北　秀世　神山天文台長
2	9月10日	15:00～16:30	ここまで見えてきた宇宙と地球の歴史	三好　蕃　理学部教授(神山天文台研究員)
3	12月10日	15:00～16:30	宇宙の蜃気楼	米原　厚憲　理学部准教授(神山天文台研究員)
4	3月3日	15:00～16:30	私たちが住む銀河	長尾　透　京都大学白眉プロジェクト 特定准教授

平成23(2011)年度　天文学入門講座

回数	開催日	時間	タイトル	講師
1	5月14日	15:00～16:30	太陽、太陽望遠鏡を用いたプロミネンスと黒点観察	中道　晶香　神山天文台専門員
2	5月21日	15:00～16:30	太陽における核融合反応	中道　晶香　神山天文台専門員
3	6月11日	15:00～16:30	スペクトルの観察	中道　晶香　神山天文台専門員
4	6月25日	15:00～16:30	スペクトル続編	中道　晶香　神山天文台専門員
5	7月2日	15:00～16:30	ドップラー効果	中道　晶香　神山天文台専門員
6	7月9日	15:00～16:30	天体観測技術の発展と銀河の観測	中道　晶香　神山天文台専門員
7	7月16日	15:00～16:30	望遠鏡の仕組み	中道　晶香　神山天文台専門員
8	10月8日	15:00～16:30	天体の運行と月の話	中道　晶香　神山天文台専門員
9	10月15日	15:00～16:30	天王星と海王星	中道　晶香　神山天文台専門員
10	10月22日	15:00～16:30	木星と太陽系概観	中道　晶香　神山天文台専門員
11	10月29日	15:00～16:30	恒星の誕生、太陽系の形成	中道　晶香　神山天文台専門員
12	11月12日	15:00～16:30	恒星の構造と進化	中道　晶香　神山天文台専門員
13	11月26日	15:00～16:30	赤色巨星以降の進化	中道　晶香　神山天文台専門員
14	12月3日	15:00～16:30	中性子星とブラックホール、銀河	中道　晶香　神山天文台専門員
15	12月17日	15:00～16:30	宇宙論	中道　晶香　神山天文台専門員

平成24(2012)年度　天文学入門講座

回数	開催日	時間	タイトル	講師
1	5月19日	15:00～16:30	太陽と金環日食	中道　晶香　神山天文台専門員
2	6月9日 (特別編)	15:00～16:30	天文学の世界史　～四大文明からメソポタミアまで～	廣瀬　匠　京都大学大学院文学研究科　博士後期課程大学院生
3	6月23日	15:00～16:30	空の周期	中道　晶香　神山天文台専門員
4	7月7日	18:00～18:45	織姫星と彦星	河北　秀世　理学部教授／神山天文台長
5	7月28日	15:00～16:30	虹のひみつ	中道　晶香　神山天文台専門員
6	8月25日	15:00～16:30	光と望遠鏡	中道　晶香　神山天文台専門員
＊7	9月10日	15:00～16:30	宇宙の観測	池田　優二　理学部准教授／神山天文台研究員
8	9月29日 (特別編)	15:00～16:30	天文観測装置の最先端　～近赤外線高分散分光器の開発～	近藤　荘平　神山天文台特定研究員
9	10月20日	15:00～16:30	星間物質と星形成	中道　晶香　神山天文台専門員
10	11月10日	15:00～16:30	恒星	中道　晶香　神山天文台専門員
11	12月8日 (特別編)	15:00～16:30	神山天文台の観測研究　～系外惑星と近接連星系の研究～	磯貝　瑞希　神山天文台特定研究員
12	12月22日	15:00～16:30	クリスマスの星	河北　秀世　理学部教授／神山天文台長
13	1月12日	15:00～16:30	太陽系と惑星	中道　晶香　神山天文台専門員
14	2月16日	15:00～16:30	銀河と銀河団	中道　晶香　神山天文台専門員
15	3月2日 (特別編)	15:00～16:30	太陽系外惑星とコロナグラフ	塩谷　圭吾　宇宙航空研究開発機構(JAXA)　助教
16	3月9日	15:00～16:30	宇宙の始まりと進化	中道　晶香　神山天文台専門員

＊第7回は、講師の都合により中止

平成25(2013)年度　天文学入門講座

回数	開催日	時間	タイトル	講師
1	4月20日	15:00～16:30	太陽	中道　晶香　　神山天文台主任研究員
2	5月18日	15:00～16:30	空の周期、望遠鏡	中道　晶香　　神山天文台主任研究員
3	6月8日 (特別編)	15:00～16:30	見えない光で銀河をさぐる	高妻　真次郎　中京大学国際教養学部准教授
4	7月6日 (特別篇)	18:00～18:45	七夕の星と銀河たち	吉川　智裕　　神山天文台博士研究員
5	7月27日	15:00～16:30	虹のひみつ	中道　晶香　　神山天文台主任研究員
6	9月28日 (特別編)	15:00～16:30	金星探査機「あかつき」が解き明かす 大気スーパーローテーションの謎	高木　征弘　　理学部准教授
7	10月19日	14:30～16:00	恒星の一生	中道　晶香　　神山天文台主任研究員
8	11月9日	14:30～16:00	太陽系と惑星	中道　晶香　　神山天文台主任研究員
9	12月7日 (特別編)	14:30～16:00	天体を細かく見るための観測技術	藤代　尚文　　神山天文台専門員
10	12月21日	14:30～16:00	宇宙の過去・現在・未来	中道　晶香　　神山天文台主任研究員
11	3月29日 (特別編)	15:00～16:30	荒木望遠鏡で探る新星の世界	新井　彰　　兵庫県立西はりま天文台　天文科学研究員

平成26(2014)年度　天文学講座

回数	開催日	時間	タイトル	講師
1	5月17日	15:00～16:30	素粒子の質量、宇宙の質量	杉山　弘晃　　益川塾博士研究員
2	7月5日 (特別講座)	17:00～18:00	七夕伝説の星座と天の川	中道　晶香　　神山天文台主任研究員
3	8月2日	16:00～18:00	星空の彼方の大宇宙	大西　浩次　　長野工業高等専門学校教授／天文学者／星景写真家
4	10月18日	14:30～16:00	目に見えない光で観る惑星のすがた	佐川　英夫　　理学部准教授
5	12月20日 (特別講座)	15:00～16:30	はやぶさ2が目指すもの はやぶさ2の開発の裏側―衝突の瞬間を捉えろ	河北　秀世　　理学部教授／神山天文台長 池田　優二　　フォトコーディング代表／神山天文台客員研究員
6	3月28日	15:00～16:30	神山天文台　バックヤードツアー	中道　晶香　　神山天文台主任研究員 中西　賢之　　神山天文台嘱託職員

平成27(2015)年度　天文学講座

回数	開催日	時間	タイトル	講師
1	4月4日	17:30～18:00	皆既月食解説講座	中道　晶香　　神山天文台主任研究員
2	5月16日	15:00～16:30	地球惑星科学振興西田賞　受賞記念講演 「太陽系の起源を求めて」	河北　秀世　　理学部教授／神山天文台長
3	7月5日 (特別講座)	17:00～18:00	世界の星座と七夕の星座	中道　晶香　　神山天文台主任研究員
4	10月24日	14:30～16:00	小型屈折補償光学装置(CRAO)の開発	藤代　尚文　　神山天文台専門員
5	12月19日 (特別講座)	14:30～16:00	星空の多くの地球たちへ	大西　浩次　　長野工業高等専門学校教授／天文学者／星景写真家
6	3月26日	15:00～16:30	星が光るのはなぜ？	加藤　賢一　　岡山理科大学教授／元大阪市立科学館館長

平成28(2016)年度　天文学講座

回数	開催日	時間	タイトル	講師
1	6月11日	15:00～16:30	重力波の直接検出とは？	中道　晶香　　神山天文台主任研究員
2	7月9日 (特別講座)	17:00～18:00	七夕の星々と天の川	河北　秀世　　理学部教授／神山天文台長
3	10月8日	14:30～16:00	太陽フレアと恒星スーパーフレア	野上　大作　　京都大学大学院理学研究科准教授
4	12月24日 (特別講座)	14:30～16:00	古墳天井に星が輝く―キトラ天文図	宮島　一彦　　前・同志社大学教授／中之島科学研究所研究員
5	3月25日	15:00～16:30	南天の星空を目指して	福江　慧　　神山天文台研究員 大坪　翔悟　　理学研究科　修士課程

平成29(2017)年度　天文学講座

回数	開催日	時間	タイトル	講師
1	5月27日	15:00～16:30	探査機が見た太陽系天体たち	小林　仁美　　Estrista　代表
2	7月8日	17:00～17:45	天の川と超巨大質量ブラックホール	中道　晶香　　神山天文台主任研究員
3	12月2日	14:30～16:00	宇宙の果ての銀河地図	市川　隆　　東北大学名誉教授
4	3月24日	15:00～16:30	惑星間ダスト～塵もつもれば〇〇となる!?～	猿楽　祐樹　　神山天文台主任研究員

平成30(2018)年度　天文学講座

回数	開催日	時間	タイトル	講師
1	5月19日	15:00～16:30	彗星と海、そして生命	河北　秀世　　本学理学部長・教授／神山天文台長
2	7月21日	15:00～16:30	火星移住とその先にあるもの	中串　孝志　　和歌山大学観光学部准教授／国際観光学研究センター研究員
3	12月22日	14:30～16:00	宇宙の謎　なぜ私たちはここにいるのか？	谷口　義明　　放送大学教授
4	3月23日	15:00～16:30	望遠鏡で拡大しても見えない星の姿を見るには？	新中　善晴　　神山天文台研究員

平成31/令和元(2019)年度　天文学講座

回数	開催日	時間	タイトル	講師
1	5月25日	15:00～16:30	京都産業大学が明らかにしたいるか座新星	河北　秀世　　本学理学部長・教授／神山天文台長
2	7月27日	15:00～16:30	ブラックホール初撮影の衝撃と今後の展望	嶺重　慎　　京都大学理学研究科教授
3	12月21日	14:30～16:00	ガリレオの冒険　宇宙をめぐる科学と人をめぐる学問	小林　満　　本学外国語学部教授・外国語学部長
＊4	3月21日	15:00～16:30	はやぶさ2の旅　地球のような星は他にある？	亀田　真吾　　立教大学理学部教授

＊第4回は、新型コロナウイルスの状況を踏まえ中止

資料4　平成21(2009)年度～平成31/令和元(2019)年度　新聞等掲載記事一覧

年度(西暦)	No. (年度毎)	日付	広報媒体 (新聞、テレビ等)	広報媒体名 (○○新聞等)	記事名
平成21年度 (2009)	1	12月22日	新聞	MSN産経ニュース	京産大の天文台が完成　口径1.3メートル、国内私立大最大
	2	12月23日	新聞	中日新聞	口径1．3メートル光学望遠鏡を設置　京産大に天文台完成　来春運用へ
	3	12月23日	新聞	京都新聞	私大最大　星空への瞳
	4	12月23日	新聞	毎日新聞	雑記帳
	5	12月23日	新聞	読売新聞	京産大の天文台　完成
	6	12月24日	新聞	朝日新聞	京産大に天文台完成　望遠鏡口径国内6番目
	7	12月27日	新聞	産経新聞	宇宙を望むような大きな挑戦を
	8	3月10日	新聞	産経新聞	京都から銀河を観測
	9	3月14日	新聞	京都新聞	巨大望遠鏡に興味津々
	10	3月27日	新聞	読売新聞	星をたずねて
平成22年度 (2010)	1	4月4日	新聞	読売新聞	京都産業大学神山天文台の一般公開
	2	4月4日	新聞	京都新聞	京の星空「宝石みたい」 京産大「神山天文台」を公開
	3	4月26日	新聞	読売新聞	京産大に大型望遠鏡
	4	5月7日	新聞	京都新聞	神山天文台の開設　モノづくり教育と知の還元
	5	5月16日	新聞	京都新聞	『先生何してるの？』 星の集まりの謎を解き明かす　京都産業大学神山天文台専門員　中道晶香さん
	6	5月25日	新聞	毎日新聞	京都産業大学の真価
	7	6月1日	情報誌	ガクシン	京都産業大学に大型天体望遠鏡を設置した天文台が完成！
	8	6月1日	新聞	THE JUNIOR TIMES	星の集まりの謎を解き明かす　京都産業大学神山天文台専門員
	9	6月2日	新聞	毎日新聞	支局長さんからの手紙　はやぶさ君
	10	6月12日	雑誌	週刊ダイヤモンド	宇宙規模の視点で人間を見つめる天文台
	11	6月15日	新聞	京都新聞	七夕に最新宇宙知ろう
	12	6月19日	情報誌	リビング京都(中央・東南・西南)	天文台＆プラネタリウムで〝星空の旅〟へ出かけよう
	13	7月2日	新聞	産経新聞	全国同時七夕講演会
	14	7月28日	新聞	京都新聞	京産大神山天文台高校生向けに講座(No.27の下に貼付分)
	15	8月2日	新聞	産経新聞	3Dで望遠鏡で・・・〝宇宙の旅〟
	16	8月25日	新聞	毎日新聞	京都産業大学第2回天文台講座「彗星（ほうきぼし）と私たちの地球」
	17	9月1日	新聞	大学新聞71号	中学生、高校生と宇宙を探る
	18	9月13日	Webサイト	Astro Arts 天文ニュース	西山さんと椛島さん、わし座に新星を発見
	19	10月	情報誌	京のみどり　56号	歴史と文化を未来につなぐ　賀茂川周辺のみどりを歩く
	20	10月	情報誌	京阪ニュース　Kプレス　10月号　vol.139	京都産業大学　神山天文台
	21	12月	雑誌	なび①修学旅行フリータイムガイドブック京都奈良	一足お先にキャンパスライフ
	22	12月9日	新聞	京都新聞	京産大天文講座　小学生以上募る
	23	12月22日	新聞	産経新聞	小学生ら対象に天文のイベント
	24	1月1日	その他	進研ゼミ高1講座　高1MyVision　2011.1月号	いざキャンパスジャーニーへ！
	25	2月26日	情報誌	リビング京都中央	子どもも大人も星空の世界へ
平成23年度 (2011)	1	4月24日	新聞	読売新聞	やわらか頭で広がる答え
	2	5月1日	雑誌	週刊ダイヤモンド　2011.5.14号	ダイヤモンド21ｃ　京都産業大学
	3	5月22日	新聞	京都新聞	京都　まなびの系譜　宇宙を見つめて　新設の天文台　膨らむ夢

資料4　平成21(2009)年度～平成31/令和元(2019)年度　新聞等掲載記事一覧

年度(西暦)	No. (年度毎)	日付	広報媒体 (新聞、テレビ等)	広報媒体名 (○○新聞等)	記事名
平成23年度 (2011)	4	6月2日	新聞	京都新聞	最新の天体研究語る
	5	6月6日	新聞	毎日新聞	京都産業大学神山天文台講座
	6	6月7日	新聞	朝日新聞	京都産業大学神山天文台　開設1周年記念講演会
	7	6月10日	新聞	京都新聞	京産大生ら学内天文台超新星確認
	8	7月2日	新聞	京都新聞	天文や七夕テーマ全国同時講演会
	9	7月2日	Webサイト	大学プレスセンター	2011年全国同時七夕講演会「七夕の星と天の川～中国から伝わった星図屏風～」を開催―京都産業大学
	10	7月31日	新聞	読売新聞	星の便り～時空を超えて～
	11	8月9日	新聞	京都新聞	未来の科学者　育ってます
	12	8月30日	新聞	読売新聞	京都産業大学　神山天文台　一般公開のご案内
	13	9月1日	新聞	朝日新聞	星の美しさにウットリ
	14	10月5日	新聞	京都新聞	神山天文台の研究活動紹介
	15	10月8日	新聞	産経新聞	産学連携で観測機器の開発
	16	12月1日	情報誌	日経グローカル　No.185　2011.12.5号	地域内の連携・競争がバネに
	17	12月1日	情報誌	日経グローカル　No.185　2011.12.5号	一押しプロジェクト
	18	12月3日	新聞	産経新聞、朝日新聞、京都新聞	自分たちがつくった観測装置が宇宙の進化を解き明かす
	19	12月9日	新聞	京都新聞	重力レンズ現象解説あす天文学講演会
	20	12月10日	新聞	京都新聞	京都産業大学神山天文台講座「宇宙の蜃気楼」
	21	12月11日	新聞	京都新聞	宇宙の蜃気楼広がる夢
	22	12月17日	新聞	産経新聞	高性能の天体観測装置開発
	23	12月21日	新聞	京都新聞	世界一の観測　星の謎解く
	24	12月23日	新聞	京都新聞	ベツレヘムの星　天文台長が講演
	25	1月11日	新聞	京都新聞	宇宙の魅力発信へ連携
	26	2月1日	新聞	京都新聞	星空を仰いでごらん
	27	3月21日	新聞	毎日新聞	先進望遠鏡で宇宙を解析
平成24年度 (2012)	1	7月23日	Web版新聞	swissinfo.ch web版	最遠の超新星の跡発見
	2	7月23日	Web版新聞	中日新聞web版	119億光年先の超新星の跡発見
	3	7月24日	新聞	京都新聞	119億光年先に最遠超新星跡
	4	8月29日	新聞	京都新聞	ハートレイ彗星ガス分析に成功
	5	8月30日	Webサイト	マイナビニュース	京産大・神山天文台、NASAの「EPOXI彗星探査計画」の地上支援の成果を発表
	6	9月21日	新聞	京都新聞	天文学入門　京産大で講座
	7	9月23日	新聞	読売新聞	嵐山で中秋の名月法輪寺などで催し
	8	9月30日	新聞	京都新聞	京の文化施設学生無料
	9	10月2日	新聞	毎日新聞	最新の超新星跡を発見
	10	11月5日	新聞	京都新聞	私立最大の反射式望遠鏡
	11	2月28日	新聞	日本経済新聞	市民も楽しめる大学のミュージアム「巨大望遠鏡で宇宙を実感」京都産業大学神山天文台
平成25年度 (2013)	1	H25(2013)年度	その他	京都修学旅行パスポート	京都産業大学　神山天文台
	2	H25(2013)年度	Webサイト	JSコーポレーション　日本の学校	夏休み工作教室/天文学入門講座
	3	H25(2013)年度	雑誌	なるほど地図帳　日本2014	京都産業大学　神山天文台

資料4　平成21(2009)年度～平成31/令和元(2019)年度　新聞等掲載記事一覧

年度(西暦)	No. (年度毎)	日付	広報媒体 (新聞、テレビ等)	広報媒体名 (○○新聞等)	記事名
平成25年度 (2013)	4	H25(2013)年度	情報誌	マナビズム　Go to 大学　キャンパス調査隊	神山天文台
	5	H25(2013)年度	その他	student days	京都産業大学　神山天文台
	6	4月11日	新聞	日本経済新聞	近畿特集　天文学入門講座の紹介
	7	4月18日	新聞	京都新聞	天文学入門講座の紹介
	8	5月29日	新聞	京都新聞	「見えない光」で探る銀河研究を学ぼう　8日京産大で
	9	7月26日	新聞	京都新聞	京産大神山天文台　入門講座と観望会
	10	7月26日	新聞	読売新聞	虹の秘密　解き明かせ　京都産業大、あす講座
	11	7月28日	新聞	京都新聞	特殊フィルムで虹の見え方観察
	12	10月15日	情報誌	TOKK 10月15日号	天文台からはるか宇宙の旅へ　京都産業大学　神山天文台
	13	10月23日	新聞	日刊工業新聞	京都産業大学　神山天文台　マスコットキャラクター作製
	14	11月2日	新聞	京都新聞	「大学ツアー」人気上昇
	15	11月8日	雑誌	修学旅行ﾌﾘｰﾀｲﾑｶﾞｲﾄﾞﾌﾞｯｸ「旅なび京都・奈良」	京都産業大学　神山天文台
	16	11月23日	新聞	京都新聞	アイソン彗星の成分分析
	17	11月24日	新聞	日本経済新聞	初期の太陽系、彗星に痕跡
	18	11月27日	新聞	京都新聞	アイソン彗星　催し多数
	19	12月1日	新聞	産経新聞	アイソン彗星　まだ見られる？
	20	12月5日	新聞	京都新聞	天文学入門講座特別編　「天体を細かく見るための観測技術」
	21	12月8日	新聞	読売新聞	彗星の動向　見通す難しさ
	22	12月15日	雑誌	大学ジャーナル　vo.108	京都の街中から世界に挑む　神山天文台
	23	2月20日	Webサイト	Astro　Arts　天文ニュース	アイソン彗星のアンモニアから太陽系誕生の記憶をたどる
	24	2月21日	新聞	京都新聞	アイソン彗星にアンモニア　京産大など分析
	25	2月21日	新聞	赤旗新聞	アイソン彗星崩壊前の観測　太陽系の謎解くヒントに
	26	2月24日	新聞	京都新聞	子ども"科学者"研究発表
	27	2月24日	Webサイト	マイナビニュース	すばる望遠鏡、アイソン彗星から単独彗星では初となる「15NH2」を検出
	28	2月28日	新聞	読売新聞	工作や実験　子供と交流　学生らアドバイス
	29	3月9日	新聞	京都新聞	ソフィアがやってきた　天の川に探る　宇宙の神秘
	30	3月27日	新聞	読売新聞	新星現象　専門家が解説
平成26年度 (2014)	1	H26(2014)年度	その他	student days	京都産業大学　神山天文台
	2	H26(2014)年度	雑誌	なるほど地図帳　日本2015	京都産業大学　神山天文台
	3	H26(2014)年度	雑誌	きょうと修学旅行ナビ	京都産業大学　神山天文台
	4	H26(2014)年度	雑誌	旅なび修学旅行　京都&奈良	京都産業大学　神山天文台
	5	H26(2014)年度	その他	京都修学旅行パスポート	京都産業大学　神山天文台
	6	5月2日	新聞	京都新聞	言葉の力
	7	5月14日	新聞	毎日新聞	京都産業大学神山天文台　天文学講座
	8	6月27日	Webサイト	学研教育出版　進学情報サイト「ガクセイト」	京都産業大「天文学講座　星空の彼方の大宇宙」を開催
	9	7月	情報誌	京都・洛北フリーペーパー　あべきた	天体観望会・第2回天文学講座案内
	10	7月4日	新聞	産経新聞	3000光年の彼方　地球に似た惑星
	11	7月4日	Web版新聞	京都新聞	地球に質量が似た惑星発見　3000光年離れた「連星」で

資料4　平成21(2009)年度～平成31/令和元(2019)年度　新聞等掲載記事一覧

年度(西暦)	No. (年度毎)	日付	広報媒体 (新聞、テレビ等)	広報媒体名 (○○新聞等)	記事名
平成26年度 (2014)	12	7月4日	Web版新聞	北海道新聞	地球に質量が似た惑星発見　3000光年離れた「連星」で
	13	7月4日	Web版新聞	佐賀新聞	地球に質量が似た惑星発見　3000光年離れた「連星」で
	14	7月9日	雑誌	天文ガイド	天体観望会・第2回天文学講座案内
	15	7月10日	雑誌	文藝春秋	星に願いを
	16	7月22日	新聞	読売新聞	宇宙兄弟展　30日、いよいよ開幕
	17	8月7日	新聞	読売新聞	天文台で星空眺めよう
	18	8月7日	情報誌	日経REVIEVE	京阪神の天体観測イベント
	19	8月14日	新聞	読売新聞	「宇宙兄弟」小山さん　高校生と天文台訪問
	20	8月16日	新聞	読売新聞	宇宙兄弟展　体験教室・講座も
	21	8月24日	新聞	京都新聞	夏の大三角形に思いはせ
	22	8月24日	新聞	読売新聞	京産大学生が星の世界案内
	23	8月25日	新聞	読売新聞	太陽系外の微粒子7個
	24	9月27日	新聞	読売新聞	京都産業大学×宇宙兄弟展　失敗恐れず、チャレンジしよう！
	25	10月9日	新聞	京都新聞	赤い月　京にも
	26	10月19日	新聞	日本経済新聞	彗星へ着陸機を放て
	27	10月23日	新聞	毎日新聞	彗星に着陸　新発見期待
	28	11月13日	新聞	毎日新聞	探査機　彗星に初上陸
	29	11月19日	新聞	読売新聞	彗星の気体から有機物
	30	1月10日	Web版新聞	京都新聞	冬の星空の魅力、児童学ぶ
	31	2月14日	情報誌	リビング京都	夜空からのメッセージはふたご星から
	32	2月17日	新聞	京都新聞	銀河に炭素分子多数　京産大などグループ　恒星の光から観測
	33	2月19日	新聞	京都新聞	新星爆発でリチウム　京産大などが初観測　元素増えた過程解明へ
	34	2月28日	新聞	京都新聞	太陽系微量物質の一部、新星爆発に由来　京産大グループ、天体観測で実証
平成27年度 (2015)	1	H27(2015)年度	雑誌	なるほど地図帳　日本2016	京都産業大学　神山天文台
	2	H27(2015)年度	Webサイト	JSコーポレーション　日本の学校	天体観望会、七夕講演会
	3	4月1日	新聞	産経新聞	京産大・河北教授に西田賞
	4	4月23日	新聞	岐阜新聞	宇宙に巨大有機分子か　東大・京産大チーム　新装置で赤外線分析
	5	4月23日	新聞	山陽新聞	宇宙に巨大有機分子
	6	4月23日	新聞	山形新聞	宇宙に巨大有機分子か　東大、京産大　新装置で「吸収線」15本発見
	7	4月23日	新聞	四国新聞	宇宙に巨大有機分子？赤外線分析で新装置
	8	4月23日	新聞	大分合同新聞	宇宙に巨大有機分子か　新装置で赤外線領域分析
	9	4月23日	新聞	中国新聞	宇宙に巨大有機分子か
	10	6月4日	新聞	中日新聞	天文学のきら星　京産大　科学誌掲載私立1位
	11	6月23日	新聞	熊本日日新聞	京都産業大学50周年　宇宙テーマに講演
	12	7月9日	新聞	京都新聞	赤外線の見極め　段違い　京産大　キヤノンなど光学部品開発
	13	7月9日	新聞	日刊工業新聞	赤外線光学素子を開発　京都産業大など
	14	7月14日	新聞	日刊工業新聞	”光の束”期待
	15	7月14日	新聞	日経新聞	西田賞受賞記念講演「太陽系の起源を求めて」

資料4　平成21(2009)年度～平成31/令和元(2019)年度　新聞等掲載記事一覧

年度(西暦)	No. (年度毎)	日付	広報媒体 (新聞、テレビ等)	広報媒体名 (○○新聞等)	記事名
平成27年度 (2015)	16	8月	広報誌	KRP-Week	藤代専門員講演「京都産業大学神山天文台における装置開発と人材育成:補償光学装置の開発事例
	17	8月24日	新聞	読売新聞	飛び出す宇宙　瞳キラリ(神山天文台ｻﾎﾟｰﾄﾁｰﾑ岩倉図書館コラボ)
	18	9月10日	雑誌	エルマガジン社　エコトリップ京都	京都産業大学　神山天文台
平成28年度 (2016)	1	H28(2016)年度	Webサイト	きょうと修学旅行ナビ	天文学習の紹介
	2	H28(2016)年度	Webサイト	JSコーポレーション　日本の学校	天体観望会、七夕観望会
	3	5月26日	雑誌	関西の大学を楽しむ本	京都産業大学　神山天文台
	4	6月8日	新聞	京都新聞	「科学スコープ@キャンパス」暗黒星雲「物作り」で迫る　京産大神山天文台　高精度分光器で内部観測成功
	5	6月17日	Web版新聞	朝日新聞デジタル	京都産業大学神山天文台　世界初！「ぼやけた星間線」の原因となる分子の観測に成功
	6	6月17日	Web版新聞	京都新聞	京都産業大学神山天文台　世界初！「ぼやけた星間線」の原因となる分子の観測に成功
	7	6月17日	Web版新聞	ZDNet Japan	京都産業大学神山天文台　世界初！「ぼやけた星間線」の原因となる分子の観測に成功
	8	6月17日	Web版新聞	共同通信 PR Wire	京都産業大学神山天文台　世界初！「ぼやけた星間線」の原因となる分子の観測に成功
	9	6月17日	Web版新聞	CNET Japan	京都産業大学神山天文台　世界初！「ぼやけた星間線」の原因となる分子の観測に成功
	10	6月17日	Web版新聞	奈良新聞	京都産業大学神山天文台　世界初！「ぼやけた星間線」の原因となる分子の観測に成功
	11	6月17日	Web版新聞	沖縄タイムス	京都産業大学神山天文台　世界初！「ぼやけた星間線」の原因となる分子の観測に成功
	12	6月17日	Web版新聞	OPTRONICS ONLINE	京都産業大学神山天文台　世界初！「ぼやけた星間線」の原因となる分子の観測に成功
	13	6月17日	Web版新聞	zakzak by 夕刊フジ	京都産業大学神山天文台　世界初！「ぼやけた星間線」の原因となる分子の観測に成功
	14	6月30日	情報誌	北区じかん vo.3 2016夏号	神山天文台　天体観望会紹介
	15	7月1日	情報誌	関塾タイムス　8月号	星を観に行こう！－わくわく天体観望のすすめ－
	16	7月3日	新聞	京都新聞	「最前線 京滋ビジネス　西村製作所」(京都産業大学神山天文台 荒木望遠鏡 掲載)
	17	7月12日	TV	NHK　あさいち	神山天文台　天体観望会紹介(テレビ放送)
	18	8月5日	Twitter	twitter(ニッセン)	ニッセンのtwitter(@nissen)にて神山天文台の紹介
	19	9月24日	新聞	京都新聞	京産大グループ　新星での分子生成メカニズムを解明
	20	10月4日	TV	関西テレビ　ワンダー	神山天文台の紹介(テレビ放送)
	21	11月19日	情報誌	リビング京都中央	澄んだ空気の中で楽しむ冬の星座(天体観望会の紹介)
	22	1月24日	Web版新聞	福井新聞	最小探査機が彗星観測に成功　世界初、国立天文台
	23	1月24日	Web版新聞	山形新聞	最小探査機が彗星観測に成功　世界初、国立天文台
	24	1月24日	Web版新聞	岩手日報	最小探査機が彗星観測に成功　世界初、国立天文台
	25	1月24日	Web版新聞	徳島新聞	最小探査機が彗星観測に成功　世界初、国立天文台
	26	1月24日	Web版新聞	中日新聞	最小探査機が彗星観測に成功　世界初、国立天文台
	27	1月24日	Web版新聞	大阪日日新聞	最小探査機が彗星観測に成功　世界初、国立天文台
	28	1月24日	Web版新聞	沖縄タイムズ	最小探査機が彗星観測に成功　世界初、国立天文台
	29	1月24日	Web版新聞	琉球新報	最小探査機が彗星観測に成功　世界初、国立天文台
	30	1月24日	Web版新聞	山陰中央新報	最小探査機が彗星観測に成功　世界初、国立天文台
	31	1月24日	Web版新聞	長崎新聞	最小探査機が彗星観測に成功　世界初、国立天文台
	32	1月24日	Web版新聞	宮崎日日新聞	最小探査機が彗星観測に成功　世界初、国立天文台
	33	1月24日	Web版新聞	神戸新聞	最小探査機が彗星観測に成功　世界初、国立天文台
	34	1月24日	Web版新聞	福島民報	最小探査機が彗星観測に成功　世界初、国立天文台
	35	1月24日	Web版新聞	佐賀新聞	最小探査機が彗星観測に成功　世界初、国立天文台

資料4　平成21(2009)年度～平成31/令和元(2019)年度　新聞等掲載記事一覧

年度(西暦)	No. (年度毎)	日付	広報媒体 (新聞、テレビ等)	広報媒体名 (○○新聞等)	記事名
平成28年度 (2016)	36	1月24日	Web版新聞	静岡新聞	最小探査機が彗星観測に成功　世界初、国立天文台
	37	1月24日	Web版新聞	岐阜新聞	最小探査機が彗星観測に成功　世界初、国立天文台
	38	1月24日	Web版新聞	デーリー東北	最小探査機が彗星観測に成功　世界初、国立天文台
	39	1月24日	Web版新聞	高知新聞	最小探査機が彗星観測に成功　世界初、国立天文台
	40	1月24日	Web版新聞	河北新報	最小探査機が彗星観測に成功　世界初、国立天文台
	41	1月24日	Web版新聞	千葉日報	最小探査機が彗星観測に成功　世界初、国立天文台
	42	1月24日	Web版新聞	東京新聞	最小探査機が彗星観測に成功　世界初、国立天文台
	43	1月24日	Web版新聞	北海道新聞	最小探査機が彗星観測に成功　世界初、国立天文台
	44	1月24日	Web版新聞	南日本新聞	最小探査機が彗星観測に成功　世界初、国立天文台
	45	1月24日	Web版新聞	日本海新聞	最小探査機が彗星観測に成功　世界初、国立天文台
	46	1月24日	Web版新聞	福島民友新聞	最小探査機が彗星観測に成功　世界初、国立天文台
	47	1月24日	Web版新聞	上毛新聞	最小探査機が彗星観測に成功　世界初、国立天文台
	48	1月24日	Web版新聞	山陽新聞	最小探査機が彗星観測に成功　世界初、国立天文台
	49	1月24日	Web版新聞	愛媛新聞	最小探査機が彗星観測に成功　世界初、国立天文台
	50	1月24日	Web版新聞	京都新聞	最小探査機が彗星観測に成功　世界初、国立天文台
	51	1月24日	Web版新聞	共同通信	最小探査機が彗星観測に成功　世界初、国立天文台
	52	1月24日	Web版新聞	産経フォト	最小探査機が彗星観測に成功　世界初、国立天文台
	53	2月2日	新聞	毎日新聞	赤外線でつかめ銀河の謎　京産大が世界最高精度分析装置を開発、南米チリで観測
平成29年度 (2017)	1	H29(2017)年度	Webサイト	JSコーポレーション　日本の学校	天体観望会
	2	H29(2017)年度	雑誌	なるほど地図帳　日本2017	京都産業大学　神山天文台
	3	5月5日	新聞	読売新聞	『サイエンスBOX』研究を続ける情熱が、新たな発見を生む　河北 秀世 京都産業大学神山天文台長
	4	5月25日	新聞	京都新聞	天文学講座「探査機が見た太陽系天体たち」
	5	6月6日	新聞	朝日新聞	『まなビバ！大学編』 京都産業大学　新シンボルは天文台
	6	6月20日	新聞	京都新聞	『いのちとの伴走 iPS細胞誕生10年　第5部 膨らむ夢の陰で③』京都産業大学神山天文台研究員 新井彰
	7	9月16日	新聞	日本経済新聞	『キャンパス新景』京都産業大　巨大な望遠鏡　ロマン追う
	8	10月12日	新聞	京都新聞	神山天文台マスコットキャラクター「ほしみ～るちゃん」無料通信アプリLINEスタンプ
	9	3月20日	雑誌	大学時報 2018年3月号	だいがくのたから　京都産業大学　神山天文台
平成30年度 (2018)	1	H30(2018)年度	その他	京都修学旅行パスポート	京都産業大学神山天文台
	2	H30(2018)年度	Webサイト	JSコーポレーション　日本の学校	体験イベントin大学『天体観望会』
	3	H30(2018)年度	Webサイト	JSコーポレーション　日本の学校	体験イベントin大学『夏の夜空のビッグフェス～七夕の宙に思いを馳せて～』
	4	4月4日	新聞	京都新聞	『情報ワイド　大学講座ガイド』京都産業大学　天体観望会
	5	4月11日	新聞	京都新聞	『情報ワイド　大学講座ガイド』京都産業大学　天体観望会
	6	5月2日	新聞	京都新聞	『情報ワイド　大学講座ガイド』京都産業大学　天体観望会
	7	5月9日	新聞	京都新聞	『情報ワイド　大学講座ガイド』京都産業大学　天体観望会
	8	5月16日	新聞	京都新聞	『情報ワイド　大学講座ガイド』京都産業大学　天文学講座「彗星と海、そして生命」
	9	5月30日	新聞	京都新聞	『情報ワイド　大学講座ガイド』京都産業大学　天体観望会
	10	7月4日	新聞	京都新聞	『情報ワイド　大学講座ガイド』京都産業大学　天体観望会
	11	7月13日	情報誌	サギタリウス7月号(学内冊子)	キャッチアップ・ワールド 「火星大接近」理学部 河北秀世 教授

資料4　平成21(2009)年度～平成31/令和元(2019)年度　新聞等掲載記事一覧

年度(西暦)	No. (年度毎)	日付	広報媒体 (新聞、テレビ等)	広報媒体名 (○○新聞等)	記事名
平成30年度 (2018)	12	7月13日	情報誌	サギタリウス7月号(学内冊子)	おすすめイベントPICK UP『天体観望会』
	13	7月18日	新聞	京都新聞	『情報ワイド　大学講座ガイド』京都産業大学　天文学講座「火星移住とその先にあるもの」
	14	7月23日	雑誌	京阪神エルマガジン社　月刊『SAVY』9月号	『朝・夜イベントカレンダー』天体観望会　京都産業大学内　神山天文台
	15	8月1日	新聞	京都新聞	『情報ワイド　大学講座ガイド』京都産業大学　天体観望会
	16	9月5日	雑誌	京阪神エルマガジン社『ひとりで歩く京都本』	京都産業大学 神山天文台『夜が待ち遠しくなる天文台で天体観測』
	17	9月13日	新聞	日刊工業新聞	ガス放出に伴う衝撃波観測　東大・京都産大
	18	9月14日	Web版新聞	朝日新聞DIGITAL	京都産業大学 神山天文台の新中 善晴 研究員らが、ふたご座流星群の母天体・小惑星フェートンの惑星表面を解明
	19	9月14日	Web版新聞	毎日新聞(デジタル毎日)	京都産業大学 神山天文台の新中 善晴 研究員らが、ふたご座流星群の母天体・小惑星フェートンの惑星表面を解明
	20	9月14日	Web版新聞	AFP通信(AFPBB News)	京都産業大学 神山天文台の新中 善晴 研究員らが、ふたご座流星群の母天体・小惑星フェートンの惑星表面を解明
	21	9月14日	Web版新聞	北海道新聞	京都産業大学 神山天文台の新中 善晴 研究員らが、ふたご座流星群の母天体・小惑星フェートンの惑星表面を解明
	22	9月14日	Web版新聞	中日新聞	京都産業大学 神山天文台の新中 善晴 研究員らが、ふたご座流星群の母天体・小惑星フェートンの惑星表面を解明
	23	9月14日	Web版新聞	河北新聞	京都産業大学 神山天文台の新中 善晴 研究員らが、ふたご座流星群の母天体・小惑星フェートンの惑星表面を解明
	24	9月14日	Web版新聞	新潟日報モア	京都産業大学 神山天文台の新中 善晴 研究員らが、ふたご座流星群の母天体・小惑星フェートンの惑星表面を解明
	25	9月14日	Web版新聞	紀伊民報	京都産業大学 神山天文台の新中 善晴 研究員らが、ふたご座流星群の母天体・小惑星フェートンの惑星表面を解明
	26	9月14日	Web版新聞	OLICON NEWS	京都産業大学 神山天文台の新中 善晴 研究員らが、ふたご座流星群の母天体・小惑星フェートンの惑星表面を解明
	27	9月14日	Web版新聞	Infoseek News	京都産業大学 神山天文台の新中 善晴 研究員らが、ふたご座流星群の母天体・小惑星フェートンの惑星表面を解明
	28	9月14日	Web版新聞	Biglobe ニュース	京都産業大学 神山天文台の新中 善晴 研究員らが、ふたご座流星群の母天体・小惑星フェートンの惑星表面を解明
	29	9月14日	Web版新聞	exciteニュース	京都産業大学 神山天文台の新中 善晴 研究員らが、ふたご座流星群の母天体・小惑星フェートンの惑星表面を解明
	30	9月14日	Web版新聞	@nifty	京都産業大学 神山天文台の新中 善晴 研究員らが、ふたご座流星群の母天体・小惑星フェートンの惑星表面を解明
	31	9月14日	Web版新聞	eltha(OLICON NEWS)	京都産業大学 神山天文台の新中 善晴 研究員らが、ふたご座流星群の母天体・小惑星フェートンの惑星表面を解明
	32	9月14日	Web版新聞	Cnet japan	京都産業大学 神山天文台の新中 善晴 研究員らが、ふたご座流星群の母天体・小惑星フェートンの惑星表面を解明
	33	9月14日	Web版新聞	ZDnet japan	京都産業大学 神山天文台の新中 善晴 研究員らが、ふたご座流星群の母天体・小惑星フェートンの惑星表面を解明
	34	9月14日	Web版新聞	INTERNET COM	京都産業大学 神山天文台の新中 善晴 研究員らが、ふたご座流星群の母天体・小惑星フェートンの惑星表面を解明
	35	9月14日	Web版新聞	とれまがニュース	京都産業大学 神山天文台の新中 善晴 研究員らが、ふたご座流星群の母天体・小惑星フェートンの惑星表面を解明
	36	9月14日	Web版新聞	財経新聞	京都産業大学 神山天文台の新中 善晴 研究員らが、ふたご座流星群の母天体・小惑星フェートンの惑星表面を解明
	37	9月14日	Web版新聞	mapion ニュース	京都産業大学 神山天文台の新中 善晴 研究員らが、ふたご座流星群の母天体・小惑星フェートンの惑星表面を解明
	38	9月21日	雑誌	スタディサプリ『大学の約束』	天文台と観測分析技術で、太陽系や生命誕生の謎に挑戦する　京都産業大学
	39	10月23日	新聞	日本経済新聞	『キャンパス新景』京都産業大学　国内私立最大規模の望遠鏡
	40	10月31日	新聞	京都新聞	『情報ワイド　大学講座ガイド』京都産業大学　天体観望会
	41	11月5日	新聞	日刊工業新聞	ホームズ彗星の起源解明　京都産業大学
	42	11月22日	Web版新聞	朝日新聞DIGITAL	多くの謎に満ちている彗星を解き明かす！ホームズ彗星の起源と増光現象のメカニズムを初めて解明 - 京都産業大学
	43	11月22日	Web版新聞	毎日新聞(デジタル毎日)	多くの謎に満ちている彗星を解き明かす！ホームズ彗星の起源と増光現象のメカニズムを初めて解明 - 京都産業大学
	44	11月22日	Web版新聞	Sankei Biz	多くの謎に満ちている彗星を解き明かす！ホームズ彗星の起源と増光現象のメカニズムを初めて解明 - 京都産業大学
	45	11月22日	Web版新聞	AFP通信(AFPBB News)	多くの謎に満ちている彗星を解き明かす！ホームズ彗星の起源と増光現象のメカニズムを初めて解明 - 京都産業大学
	46	11月22日	Web版新聞	北海道新聞	多くの謎に満ちている彗星を解き明かす！ホームズ彗星の起源と増光現象のメカニズムを初めて解明 - 京都産業大学
	47	11月22日	Web版新聞	中日新聞	多くの謎に満ちている彗星を解き明かす！ホームズ彗星の起源と増光現象のメカニズムを初めて解明 - 京都産業大学
	48	11月22日	Web版新聞	河北新報	多くの謎に満ちている彗星を解き明かす！ホームズ彗星の起源と増光現象のメカニズムを初めて解明 - 京都産業大学
	49	11月22日	Web版新聞	新潟日報	多くの謎に満ちている彗星を解き明かす！ホームズ彗星の起源と増光現象のメカニズムを初めて解明 - 京都産業大学

資料4　平成21(2009)年度～平成31/令和元(2019)年度　新聞等掲載記事一覧

年度(西暦)	No. (年度毎)	日付	広報媒体 (新聞、テレビ等)	広報媒体名 (○○新聞等)	記事名
平成30年度 (2018)	50	11月22日	Web版新聞	紀伊民報	多くの謎に満ちている彗星を解き明かす！ホームズ彗星の起源と増光現象のメカニズムを初めて解明 - 京都産業大学
	51	11月22日	Web版新聞	OLICON NEWS	多くの謎に満ちている彗星を解き明かす！ホームズ彗星の起源と増光現象のメカニズムを初めて解明 - 京都産業大学
	52	11月22日	Web版新聞	Infoseek News	多くの謎に満ちている彗星を解き明かす！ホームズ彗星の起源と増光現象のメカニズムを初めて解明 - 京都産業大学
	53	11月22日	Web版新聞	Biglobe ニュース	多くの謎に満ちている彗星を解き明かす！ホームズ彗星の起源と増光現象のメカニズムを初めて解明 - 京都産業大学
	54	11月22日	Web版新聞	exciteニュース	多くの謎に満ちている彗星を解き明かす！ホームズ彗星の起源と増光現象のメカニズムを初めて解明 - 京都産業大学
	55	11月22日	Web版新聞	@nifty	多くの謎に満ちている彗星を解き明かす！ホームズ彗星の起源と増光現象のメカニズムを初めて解明 - 京都産業大学
	56	11月22日	Web版新聞	eltha(OLICON NEWS)	多くの謎に満ちている彗星を解き明かす！ホームズ彗星の起源と増光現象のメカニズムを初めて解明 - 京都産業大学
	57	11月22日	Web版新聞	Cnet japan	多くの謎に満ちている彗星を解き明かす！ホームズ彗星の起源と増光現象のメカニズムを初めて解明 - 京都産業大学
	58	11月22日	Web版新聞	ZDnet japan	多くの謎に満ちている彗星を解き明かす！ホームズ彗星の起源と増光現象のメカニズムを初めて解明 - 京都産業大学
	59	11月22日	Web版新聞	INTERNET COM	多くの謎に満ちている彗星を解き明かす！ホームズ彗星の起源と増光現象のメカニズムを初めて解明 - 京都産業大学
	60	11月22日	Web版新聞	とれまがニュース	多くの謎に満ちている彗星を解き明かす！ホームズ彗星の起源と増光現象のメカニズムを初めて解明 - 京都産業大学
	61	11月22日	Web版新聞	財経新聞	多くの謎に満ちている彗星を解き明かす！ホームズ彗星の起源と増光現象のメカニズムを初めて解明 - 京都産業大学
	62	11月22日	web版新聞	mapion ニュース	多くの謎に満ちている彗星を解き明かす！ホームズ彗星の起源と増光現象のメカニズムを初めて解明 - 京都産業大学
	63	12月5日	新聞	京都新聞	『情報ワイド　大学講座ガイド』京都産業大学　天文学講座
	64	12月6日	新聞	朝日新聞	京都産業大学　天体観望会
	65	12月11日	web版新聞	YOMIURI ONLINE	京都産業大学 神山天文台・近赤外線高分散ラボ(LiH)が近赤外線波長域での詳細なA型星ライン・カタログを世界で初めて公開
	66	12月11日	web版新聞	朝日新聞DIGITAL	京都産業大学 神山天文台・近赤外線高分散ラボ(LiH)が近赤外線波長域での詳細なA型星ライン・カタログを世界で初めて公開
	67	12月11日	web版新聞	毎日新聞(デジタル毎日)	京都産業大学 神山天文台・近赤外線高分散ラボ(LiH)が近赤外線波長域での詳細なA型星ライン・カタログを世界で初めて公開
	68	12月11日	web版新聞	Sankei Biz	京都産業大学 神山天文台・近赤外線高分散ラボ(LiH)が近赤外線波長域での詳細なA型星ライン・カタログを世界で初めて公開
	69	12月11日	web版新聞	AFP通信(AFPBB News)	京都産業大学 神山天文台・近赤外線高分散ラボ(LiH)が近赤外線波長域での詳細なA型星ライン・カタログを世界で初めて公開
	70	12月11日	web版新聞	北海道新聞	京都産業大学 神山天文台・近赤外線高分散ラボ(LiH)が近赤外線波長域での詳細なA型星ライン・カタログを世界で初めて公開
	71	12月11日	web版新聞	中日新聞	京都産業大学 神山天文台・近赤外線高分散ラボ(LiH)が近赤外線波長域での詳細なA型星ライン・カタログを世界で初めて公開
	72	12月11日	web版新聞	河北新報	京都産業大学 神山天文台・近赤外線高分散ラボ(LiH)が近赤外線波長域での詳細なA型星ライン・カタログを世界で初めて公開
	73	12月11日	web版新聞	新潟日報モア	京都産業大学 神山天文台・近赤外線高分散ラボ(LiH)が近赤外線波長域での詳細なA型星ライン・カタログを世界で初めて公開
	74	12月11日	web版新聞	紀伊民報	京都産業大学 神山天文台・近赤外線高分散ラボ(LiH)が近赤外線波長域での詳細なA型星ライン・カタログを世界で初めて公開
	75	12月11日	web版新聞	OLICON NEWS	京都産業大学 神山天文台・近赤外線高分散ラボ(LiH)が近赤外線波長域での詳細なA型星ライン・カタログを世界で初めて公開
	76	12月11日	web版新聞	Infoseek News	京都産業大学 神山天文台・近赤外線高分散ラボ(LiH)が近赤外線波長域での詳細なA型星ライン・カタログを世界で初めて公開
	77	12月11日	web版新聞	Biglobe ニュース	京都産業大学 神山天文台・近赤外線高分散ラボ(LiH)が近赤外線波長域での詳細なA型星ライン・カタログを世界で初めて公開
	78	12月11日	web版新聞	exciteニュース	京都産業大学 神山天文台・近赤外線高分散ラボ(LiH)が近赤外線波長域での詳細なA型星ライン・カタログを世界で初めて公開
	79	12月11日	web版新聞	@nifty	京都産業大学 神山天文台・近赤外線高分散ラボ(LiH)が近赤外線波長域での詳細なA型星ライン・カタログを世界で初めて公開
	80	12月11日	web版新聞	eltha(OLICON NEWS)	京都産業大学 神山天文台・近赤外線高分散ラボ(LiH)が近赤外線波長域での詳細なA型星ライン・カタログを世界で初めて公開
	81	12月11日	web版新聞	Cnet japan	京都産業大学 神山天文台・近赤外線高分散ラボ(LiH)が近赤外線波長域での詳細なA型星ライン・カタログを世界で初めて公開
	82	12月11日	web版新聞	ZDnet japan	京都産業大学 神山天文台・近赤外線高分散ラボ(LiH)が近赤外線波長域での詳細なA型星ライン・カタログを世界で初めて公開
	83	12月11日	web版新聞	INTERNET COM	京都産業大学 神山天文台・近赤外線高分散ラボ(LiH)が近赤外線波長域での詳細なA型星ライン・カタログを世界で初めて公開
	84	12月11日	web版新聞	とれまがニュース	京都産業大学 神山天文台・近赤外線高分散ラボ(LiH)が近赤外線波長域での詳細なA型星ライン・カタログを世界で初めて公開
	85	12月11日	web版新聞	財経新聞	京都産業大学 神山天文台・近赤外線高分散ラボ(LiH)が近赤外線波長域での詳細なA型星ライン・カタログを世界で初めて公開
	86	12月11日	web版新聞	mapion ニュース	京都産業大学 神山天文台・近赤外線高分散ラボ(LiH)が近赤外線波長域での詳細なA型星ライン・カタログを世界で初めて公開
	87	12月14日	情報誌	サギタリウス12月号(学内冊子)	神山天文台サポートチーム　天文台から観る星の美しさを多くの人に伝えたい

資料4　平成21(2009)年度～平成31/令和元(2019)年度　新聞等掲載記事一覧

年度(西暦)	No. (年度毎)	日付	広報媒体 (新聞、テレビ等)	広報媒体名 (○○新聞等)	記事名
平成30年度 (2018)	88	1月29日	Web版新聞	NHK NEWS WEB	低予算で大発見！太陽系の”最果て”に小天体　日本の研究者
	89	1月30日	Web版新聞	YOMIURI ONLINE	史上初、太陽系の果てに極めて小さな始原天体を発見　―京都産業大学
	90	1月30日	Web版新聞	朝日新聞DIGITAL	史上初、太陽系の果てに極めて小さな始原天体を発見　―京都産業大学
	91	1月30日	Web版新聞	毎日新聞(デジタル毎日)	史上初、太陽系の果てに極めて小さな始原天体を発見　--京都産業大学
	92	1月30日	Web版新聞	AFP通信(AFPBB News)	史上初、太陽系の果てに極めて小さな始原天体を発見　--京都産業大学
	93	1月30日	Web版新聞	北海道新聞	史上初、太陽系の果てに極めて小さな始原天体を発見　―京都産業大学
	94	1月30日	Web版新聞	中日新聞	史上初、太陽系の果てに極めて小さな始原天体を発見　―京都産業大学
	95	1月30日	Web版新聞	河北新報	史上初、太陽系の果てに極めて小さな始原天体を発見　―京都産業大学
	96	1月30日	Web版新聞	新潟日報モア	史上初、太陽系の果てに極めて小さな始原天体を発見　―京都産業大学
	97	1月30日	Web版新聞	紀伊民報	史上初、太陽系の果てに極めて小さな始原天体を発見　―京都産業大学
	98	1月30日	Web版新聞	OLICON NEWS	史上初、太陽系の果てに極めて小さな始原天体を発見　―京都産業大学
	99	1月30日	Web版新聞	Infoseek News	史上初、太陽系の果てに極めて小さな始原天体を発見　―京都産業大学
	100	1月30日	Web版新聞	Biglobe ニュース	史上初、太陽系の果てに極めて小さな始原天体を発見　―京都産業大学
	101	1月30日	Web版新聞	exciteニュース	史上初、太陽系の果てに極めて小さな始原天体を発見　--京都産業大学
	102	1月30日	Web版新聞	@nifty	史上初、太陽系の果てに極めて小さな始原天体を発見　―京都産業大学
	103	1月30日	Web版新聞	eltha(OLICON NEWS)	史上初、太陽系の果てに極めて小さな始原天体を発見　―京都産業大学
	104	1月30日	Web版新聞	Cnet japan	史上初、太陽系の果てに極めて小さな始原天体を発見　―京都産業大学
	105	1月30日	Web版新聞	ZDnet japan	史上初、太陽系の果てに極めて小さな始原天体を発見　―京都産業大学
	106	1月30日	Web版新聞	INTERNET COM	史上初、太陽系の果てに極めて小さな始原天体を発見　--京都産業大学
	107	1月30日	Web版新聞	とれまがニュース	史上初、太陽系の果てに極めて小さな始原天体を発見　--京都産業大学
	108	1月30日	Web版新聞	財経新聞	史上初、太陽系の果てに極めて小さな始原天体を発見　--京都産業大学
	109	1月30日	Web版新聞	mapion ニュース	史上初、太陽系の果てに極めて小さな始原天体を発見　--京都産業大学
	110	2月26日	Web版新聞	YOMIURI ONLINE	世界初、古典新星V339 Delの爆発初期の爆発放出物の空間分布を明らかに -- 京都産業大学
	111	2月26日	Web版新聞	朝日新聞DIGITAL	世界初、古典新星V339 Delの爆発初期の爆発放出物の空間分布を明らかに ― 京都産業大学
	112	2月26日	Web版新聞	毎日新聞(デジタル毎日)	世界初、古典新星V339 Delの爆発初期の爆発放出物の空間分布を明らかに ― 京都産業大学
	113	2月26日	Web版新聞	Sankei Biz	世界初、古典新星V339 Delの爆発初期の爆発放出物の空間分布を明らかに ― 京都産業大学
	114	2月26日	Web版新聞	AFP通信(AFPBB News)	世界初、古典新星V339 Delの爆発初期の爆発放出物の空間分布を明らかに ― 京都産業大学
	115	2月26日	Web版新聞	北海道新聞	世界初、古典新星V339 Delの爆発初期の爆発放出物の空間分布を明らかに ― 京都産業大学
	116	2月26日	Web版新聞	中日新聞	世界初、古典新星V339 Delの爆発初期の爆発放出物の空間分布を明らかに ― 京都産業大学
	117	2月26日	Web版新聞	河北新報	世界初、古典新星V339 Delの爆発初期の爆発放出物の空間分布を明らかに ― 京都産業大学
	118	2月26日	Web版新聞	新潟日報モア	世界初、古典新星V339 Delの爆発初期の爆発放出物の空間分布を明らかに ― 京都産業大学
	119	2月26日	Web版新聞	紀伊民報	世界初、古典新星V339 Delの爆発初期の爆発放出物の空間分布を明らかに ― 京都産業大学
	120	2月26日	Web版新聞	沖縄タイムス	世界初、古典新星V339 Delの爆発初期の爆発放出物の空間分布を明らかに ― 京都産業大学
	121	2月26日	Web版新聞	OLICON NEWS	世界初、古典新星V339 Delの爆発初期の爆発放出物の空間分布を明らかに ― 京都産業大学
	122	2月26日	Web版新聞	Infoseek News	世界初、古典新星V339 Delの爆発初期の爆発放出物の空間分布を明らかに ― 京都産業大学
	123	2月26日	Web版新聞	Biglobe ニュース	世界初、古典新星V339 Delの爆発初期の爆発放出物の空間分布を明らかに ― 京都産業大学
	124	2月26日	Web版新聞	exciteニュース	世界初、古典新星V339 Delの爆発初期の爆発放出物の空間分布を明らかに ― 京都産業大学
	125	2月26日	Web版新聞	@nifty	世界初、古典新星V339 Delの爆発初期の爆発放出物の空間分布を明らかに ― 京都産業大学

資料4　平成21(2009)年度～平成31/令和元(2019)年度　新聞等掲載記事一覧

年度(西暦)	No. (年度毎)	日付	広報媒体 (新聞、テレビ等)	広報媒体名 (○○新聞等)	記事名
平成30年度 (2018)	126	2月26日	Web版新聞	eltha(OLICON NEWS)	世界初、古典新星V339 Delの爆発初期の爆発放出物の空間分布を明らかに ― 京都産業大学
	127	2月26日	Web版新聞	Cnet japan	世界初、古典新星V339 Delの爆発初期の爆発放出物の空間分布を明らかに ― 京都産業大学
	128	2月26日	Web版新聞	ZDnet japan	世界初、古典新星V339 Delの爆発初期の爆発放出物の空間分布を明らかに ― 京都産業大学
	129	2月26日	Web版新聞	INTERNET COM	世界初、古典新星V339 Delの爆発初期の爆発放出物の空間分布を明らかに ― 京都産業大学
	130	2月26日	Web版新聞	とれまがニュース	世界初、古典新星V339 Delの爆発初期の爆発放出物の空間分布を明らかに ― 京都産業大学
	131	2月26日	Web版新聞	財経新聞	世界初、古典新星V339 Delの爆発初期の爆発放出物の空間分布を明らかに ― 京都産業大学
	132	2月26日	Web版新聞	mapion ニュース	世界初、古典新星V339 Delの爆発初期の爆発放出物の空間分布を明らかに ― 京都産業大学
	133	2月27日	新聞	京都新聞	『情報ワイド　大学講座ガイド』京都産業大学　天体観望会
	134	3月14日	新聞	朝日新聞	京都産業大学神山天文台の天文学講座
	135	3月20日	新聞	京都新聞	『情報ワイド　大学講座ガイド』京都産業大学　天文学講座「望遠鏡で拡大しても見えない星の姿を見るには？」
	136	3月27日	新聞	京都新聞	『情報ワイド　大学講座ガイド』京都産業大学　天体観望会
平成31/令和元 年度 (2019)	1	R1(2019)年度	Webサイト	JSコーポレーション　日本の学校	体験イベントin大学『天体観望会』
	2	4月24日	新聞	京都新聞	『情報ワイド　大学講座ガイド』京都産業大学　天体観望会
	3	5月22日	新聞	京都新聞	『情報ワイド　大学講座ガイド』京都産業大学　天文学講座「京都産業大学が明らかにしたいるか座新星」
	4	5月28日	新聞	朝日新聞	新星爆発の様子詳しくわかった　京産大で天文学講座
	5	6月22日	テレビ	KBS京都	「谷口流々」に神山天文台 河北 秀世 台長が出演
	6	7月17日	新聞	京都新聞	『情報ワイド　大学講座ガイド』京都産業大学　天文学講座「ブラックホール初撮影の衝撃と今後の展望」
	7	7月19日	情報誌	サギタリウス7月号(学内冊子)	神山天文台の魅力に潜入！教えて！天体の魅力
	8	8月5日	新聞	朝日新聞	彗星　宇宙で「待ち伏せ」 出現に備え28年にも探査機　京都産業大学、他
	9	8月21日	新聞	読売新聞	京産大参加探査機宇宙へ
	10	8月23日	新聞	日刊工業新聞	星間物質中温度・密度、高精度推定　京産大が成功
	11	8月23日	Webサイト	日刊工業新聞	星間物質中温度・密度、高精度推定　京産大が成功
	12	8月28日	新聞	京都新聞	『情報ワイド　大学講座ガイド』京都産業大学　天体観望会
	13	9月25日	新聞	京都新聞	『情報ワイド　大学講座ガイド』京都産業大学　天体観望会
	14	10月27日	新聞	熊本日日新聞	「ボリゾフ彗星」発見　太陽系外から来た天体
	15	11月19日	新聞	しんぶん赤旗	複雑な有機分子検出　ジャコビニ・ツィナー彗星から
	16	11月22日	新聞	読売新聞	複雑な有機物由来？の光検出　　ジャコビニ・ツィナー彗星
	17	1月4日	雑誌	月刊星ナビ2月号	ブラック星博士のB級天文学研究室
	18	1月5日	雑誌	サンデー毎日	大学プレスセンター　ニュースアクセスランキング3位「新中善晴研究員らが太陽系外縁部に、惑星の形成材料となった始原天体『微惑星』の生き残りと推定される極小天体を史上初めて発見。
	19	1月9日	新聞	しんぶん赤旗	重元素の吸収線同定
	20	1月10日	新聞	日本経済新聞	太陽系外からの天体、何を語る？ボリゾフ彗星最接近
	21	1月10日	Webサイト	日本経済新聞	太陽系外からの天体、何を語る？ボリゾフ彗星最接近
	22	1月12日	新聞	日本経済新聞	彗星に複雑な有機分子
	23	2月5日	雑誌	月刊星ナビ3月号	Observer's NAVI　(取材協力/新井彰　京都産業大学　神山天文台)

資料5　平成25(2013)年度～平成31/令和元(2019)年度　Webサイト等掲載記事一覧

(注)同一年月日・同一タイトルの掲載記事は、ニュース・プレスリリースを行ったため複数載せている

年度(西暦)	No. (年度毎)	日付	Webページ名	タイトル
平成25年度 (2013)	1	9月20日	本学Webサイト	本学学生が荒木望遠鏡により、世界初、新星における炭素分子を発見
	2	11月22日	本学Webサイト	京都産業大学大学院 理学研究科 新中善晴さん(博士後期課程3年次)らが太陽に近づくアイソン彗星の観測に成功
	3	2月5日	本学Webサイト	神山天文台 大型赤外線分光器WINEREDによる高精度な天体分析を開始
	4	2月20日	本学Webサイト	理学研究科 新中 善晴さん(博士課程3年次)らが単独彗星としては世界初の15NH2の検出に成功
平成26年度 (2014)	1	2月16日	本学Webサイト	星間空間に存在する大きな有機分子の吸収線を多数発見
	2	2月19日	本学Webサイト	「神聖爆発は宇宙のリチウム合成工場だった」神山天文台の研究員らのチームが宇宙における爆発的リチウム生成の初観測に成功
	3	2月23日	本学Webサイト	「太陽系の材料は新星爆発で作られた」研究成果が日本天文学会欧文報告誌に掲載
	4	3月31日	本学Webサイト	河北秀世 台長 日本地球惑星科学連合より西田賞を受賞
平成27年度 (2015)	1	7月9日	本学Webサイト	次世代赤外線天文学のための超高感度イマージョン回折格子の開発に成功
	2	10月13日	本学Webサイト	宇宙から彗星の撮影に成功！(神山天文台、JAXA／立教大／東大等と連携)
	3	10月19日	本学Webサイト	理学研究科 大学院生の西岡翼さんらと東京大学の共同研究グループが、系外惑星候補を持つTタウリ星系の新たな力学モデルを構築
平成28年度 (2016)	1	5月23日	本学Webサイト	天文学講座第1回「重力波の直接検出とは？」
	2	5月25日	本学Webサイト	京都産業大学神山天文台　世界初！「ぼやけた星間線」の観測に成功
	3	5月25日	本学Webサイト	京都産業大学神山天文台　世界初！「ぼやけた星間線」の観測に成功
	4	6月3日	本学Webサイト	「関西の大学を楽しむ本」掲載　神山天文台のイベントや公開講座の様子が掲載
	5	6月6日	本学Webサイト	綾部市天文館で公開天文講座「神山天文台が迫る宇宙の不思議」開催
	6	6月9日	本学Webサイト	京都新聞掲載 @キャンパスコーナーで神山天文台 河北 秀世台長が研究を紹介
	7	6月14日	本学Webサイト	全国同時七夕講演会2016「七夕の星々と天の川」
	8	6月20日	本学Webサイト	夏の夜空のビッグフェス!!～遊ぼう、星空のキャンパス～　開催(7/8)
	9	6月27日	本学Webサイト	京都産業大学　神山天文台サポートチーム・天文同好会 共同主催　星空観望会「夏の夜空のビッグフェス!!～遊ぼう、星空のキャンパス～」開催
	10	6月30日	本学Webサイト	フリーペーパー『北区じかん』掲載「北区自慢」コーナーに神山天文台 天体観望会紹介
	11	7月6日	本学Webサイト	京都産業大学神山天文台「新星爆発の内部構造」の謎を明らかに！
	12	7月7日	本学Webサイト	新星爆発によって生じる「火の玉」の内部構造の謎を明らかに －ベールに覆われた新星爆発の内側を探る－
	13	7月8日	本学Webサイト	「夏の夜空のビッグフェス!! ～遊ぼう、星空のキャンパス～」を開催
	14	7月23日	本学Webサイト	京都府綾部市天文館で「天文講座」を開催
	15	9月2日	本学Webサイト	古典新星の「火の玉」における分子生成の謎を解明：一酸化炭素による急激な冷却
	16	9月2日	本学Webサイト	天文台 世界初！古典新星の「火の玉」における分子生成の謎を解明
	17	9月7日	本学Webサイト	天文学講座第2回「太陽フレアと恒星スーパーフレア」
	18	9月18日	本学Webサイト	京都産業大学神山天文台・東京大学大学院 赤外線光学材料の高精度な透過率測定に成功 次世代宇宙望遠鏡による赤外線天文学の実現にむけて前進
	19	9月21日	本学Webサイト	大学院理学系研究科生を含む研究チームが赤外線光学材料の高精度な透過率測定に成功
	20	9月26日	本学Webサイト	京都新聞掲載 新星で分子が生成されるメカニズムを神山天文台 河北 秀世 台長のグループが解明
	21	10月3日	本学Webサイト	関西テレビ「ワンダー」で神山天文台が紹介されます
	22	10月8日	本学Webサイト	天文学講座第2回「太陽フレアと恒星スーパーフレア」開催

資料5　平成25(2013)年度～平成31/令和元(2019)年度　Webサイト等掲載記事一覧

年度(西暦)	No. (年度毎)	日付	Webページ名	タイトル
平成28年度 (2016)	23	11月21日	本学Webサイト	『リビング京都』掲載 冬の星座特集で神山天文台が紹介
	24	12月2日	本学Webサイト	クリスマス特別講演会「古墳天井に星が輝く―キトラ天文図」
	25	12月14日	本学Webサイト	京都産業大学神山天文台　クリスマス特別講演会「古墳天井に星が輝く ― キトラ天文図」のご案内
	26	12月24日	本学Webサイト	神山天文台 クリスマス特別講演会を開催
	27	1月16日	本学Webサイト	新星爆発は煤(すす)だらけ？
	28	1月18日	本学Webサイト	WINEREDが南天へ！―ヨーロッパ南天天文台と神山天文台の間で研究協力に関する覚書―
	29	1月24日	本学Webサイト	超小型探査機が彗星の水のなぞを解明
	30	2月6日	本学Webサイト	神山天文台サポートチームに京都はぐくみ憲章「実践継続推進者部門(10周年特別部門)」で感謝状が贈呈
	31	2月11日	大学プレスセンター	京都産業大学神山天文台「ワインレッド」が南天へ！ヨーロッパ南天天文台ESOの La Silla天文台と研究協力に関する覚書
	32	2月21日	本学Webサイト	理学部×神山天文台 特別企画　天文を学んで働くには？
	33	3月17日	本学Webサイト	天文学講座第3回「南天の星空を目指して～WINERED in Chile～」開催
	34	3月21日	本学Webサイト	京都産業大学神山天文台 天文学講座 第3回「南天の星空を目指して～WINERED in Chile～」開催
	35	3月25日	本学Webサイト	神山天文台 天文学講座第3回を開催
平成29年度 (2017)	1	4月6日	本学Webサイト	インドネシア・国立バンドン工科大学と神山天文台の国際協力で新星爆発に関する研究成果
	2	4月6日	本学Webサイト	インドネシア・国立バンドン工科大学と神山天文台の国際協力で新星爆発に関する研究成果
	3	4月17日	本学Webサイト	京都産業大学卒業生の名前が星の名に！ (11457) Hitomikobayashi／(11809) Shinnaka 国際天文学連合より発表
	4	4月17日	本学Webサイト	本学卒業生の名前が小惑星に！
	5	5月10日	本学Webサイト	天文学講座第1回「探査機が見た太陽系天体たち」開催
	6	5月22日	本学Webサイト	京都産業大学神山天文台 天文学講座 平成29年度第1回「探査機が見た太陽系天体たち」開催
	7	6月13日	本学Webサイト	全国同時七夕講演会2017「天の川と超巨大質量ブラックホール」
	8	7月3日	本学Webサイト	学外・国外からもさまざまな人材が集う神山天文台―京都産業大学生が中心となって、新たな価値を生み出していく
	9	7月3日	本学Webサイト	京都産業大学神山天文台　全国同時七夕講演会2017「天の川と超巨大質量ブラックホール」を開催
	10	7月5日	本学Webサイト	GSC×神サポ～Miracle of Milky way～開催(7月5日)
	11	7月8日	本学Webサイト	神山天文台 全国同時七夕講演会2017「天の川と超巨大質量ブラックホール」を開催
	12	9月1日	本学Webサイト	神山天文台マスコットキャラクター ほしみ～るちゃん®のLINEスタンプができました！
	13	11月7日	本学Webサイト	天文学講座第2回「宇宙の果ての銀河地図」開催
	14	11月24日	本学Webサイト	京都産業大学 神山天文台 天文学講座平成29年度第2回「宇宙の果ての銀河地図」開催
	15	12月2日	本学Webサイト	神山天文台 天文学講座第2回を開催
	16	2月22日	本学Webサイト	第8回天体天文宇宙教室の開催(岩倉冬イベント)
	17	2月22日	本学Webサイト	天文学講座第3回「惑星間ダスト ～塵もつもれば◯◯となる!?～」開催
	18	3月11日	本学Webサイト	「さじアストロパークキャリア実習」実施報告 (理学部生および神山天文台サポートチームの学生研修に参加)
	19	3月19日	本学Webサイト	京都産業大学神山天文台主催 天文学講座 第3回「惑星間ダスト ～塵もつもれば◯◯となる!?～」開催
平成30年度 (2018)	1	4月23日	本学Webサイト	爆発を繰り返す天体「回帰新星」に迫る！
	2	4月24日	本学Webサイト	天文学講座 第1回「彗星と海、そして生命」開催

資料5　平成25(2013)年度～平成31/令和元(2019)年度　Webサイト等掲載記事一覧

年度(西暦)	No. (年度毎)	日付	Webページ名	タイトル
平成30年度 (2018)	3	5月4日	本学Webサイト	堺市教育文化センター「ソフィア・堺」で星空解説を行いました
	4	5月8日	本学Webサイト	バンドン工科大学 × 神山天文台 小型分光器論文を出版
	5	5月10日	本学Webサイト	京都産業大学神山天文台主催 天文学講座 第1回「彗星と海、そして生命」開催
	6	5月19日	本学Webサイト	神山天文台　平成30年度第1回天文学講座を開催
	7	5月25日	本学Webサイト	神山天文台研究員らのチームが「近赤外線波長域における地球大気吸収線の精密補正」を可能に
	8	6月6日	大学プレスセンター	近赤外線波長域における地球大気吸収線の精密補正を可能に　京都産業大学
	9	6月26日	本学Webサイト	第2回 天文学講座 /全国同時七夕講演会「火星移住とその先にあるもの」開催
	10	7月3日	大学プレスセンター	学外・国外からもさまざまな人材が集う神山天文台―京都産業大学生が中心となって、新たな価値を生み出していく
	11	7月5日	本学Webサイト	京都産業大学 神山天文台サポートチーム・天文同好会 共同主催 「夏の夜空のビッグフェス！～七夕の宙に思いを馳せて～」開催
	12	7月13日	本学Webサイト	京都産業大学神山天文台 天文学講座 全国同時七夕講演会 第2回「火星移住とその先にあるもの」開催
	13	7月21日	本学Webサイト	神山天文台 平成30年度第2回天文学講座を開催
	14	9月3日	本学Webサイト	神山天文台の新中 善晴研究員らが、ふたご座流星群の母天体・小惑星フェートンの惑星表面を解明
	15	9月3日	本学Webサイト	ふたご座流星群の母天体・小惑星フェートンの素顔に迫る！
	16	9月12日	本学Webサイト	死にゆく大質量星が星のごく近くに作る衝撃波を発見
	17	9月14日	大学プレスセンター	京都産業大学 神山天文台の新中 善晴 研究員らが、ふたご座流星群の母天体・小惑星フェートンの惑星表面を解明
	18	9月27日	大学プレスセンター	死にゆく大質量星が星のごく近くに作る衝撃波を発見 ― 京都産業大学
	19	10月9日	本学Webサイト	神山天文台が明らかにする新星爆発の姿
	20	11月1日	本学Webサイト	爆発的な増光をしたホームズ彗星は太陽から遠く冷たい場所で誕生した
	21	11月8日	本学Webサイト	第3回天文学講座「宇宙の謎 なぜ私たちはここにいるのか？」開催
	22	11月9日	京都産業大学×ナショナルジオグラフィック『Re:世の中』	Re：宇宙　5500光年も離れた「死にゆく星」からのサイン そのカギは「赤外線高分散分光」。世界最先端の天文観測装置が、星の終焉を受け止める。
	23	11月22日	大学プレスセンター	多くの謎に満ちている彗星を解き明かす！ホームズ彗星の起源と増光現象のメカニズムを初めて解明 ― 京都産業大学
	24	11月27日	本学Webサイト	京都産業大学 神山天文台・近赤外線高分散ラボ(LiH)が近赤外線波長域での詳細なA型星ライン・カタログを世界で初めて公開
	25	12月10日	京都産業大学×ナショナルジオグラフィック『Re:世の中』	Re：スペクトル　星の「七色」から組成物質を突き止めろ追究を阻む「吸収線」が解き明かされた　近赤外線波長域での詳細なA型星ライン・カタログが、世界で初めて公開された
	26	12月11日	大学プレスセンター	京都産業大学 神山天文台・近赤外線高分散ラボ(LiH)が近赤外線波長域での詳細なA型星ライン・カタログを世界で初めて公開
	27	12月22日	本学Webサイト	神山天文台 平成30年度第3回天文学講座を開催
	28	1月10日	京都産業大学×ナショナルジオグラフィック『Re:世の中』	Re：彗星　彗星は、太陽系の過去の情報を内に秘めた化石!? 爆発的な増光をしたホームズ彗星は太陽から遠く冷たい場所で誕生した
	29	1月29日	本学Webサイト	小型望遠鏡で捉えた太陽系最果てにある小天体の影
	30	1月29日	本学Webサイト	史上初、太陽系の果てに極めて小さな始原天体を発見―宮古島の小さな望遠鏡が太陽系誕生の歴史と彗星の起源を明らかに―
	31	2月15日	本学Webサイト	神山天文台、古典新星V339 Del爆発の見えない姿を世界で初めて暴く！
	32	2月26日	大学プレスセンター	世界初、古典新星V339 Delの爆発初期の爆発放出物の空間分布を明らかに ― 京都産業大学
	33	2月27日	本学Webサイト	第4回天文学講座「望遠鏡で拡大しても見えない星の姿を見るには？」開催
	34	3月23日	本学Webサイト	神山天文台 平成30年度第4回天文学講座を開催
平成31/令和元年度 (2019)	1	4月26日	本学Webサイト	第1回天文学講座「京都産業大学が明らかにしたいるか座新星」開催
	2	5月25日	本学Webサイト	神山天文台 令和元年度第1回天文学講座を開催しました

資料5　平成25(2013)年度～平成31/令和元(2019)年度　Webサイト等掲載記事一覧

年度(西暦)	No. (年度毎)	日付	Webページ名	タイトル
平成31/令和元年度 (2019)	3	6月17日	本学Webサイト	KBS京都「谷口流々」に神山天文台 河北 秀世 台長が出演予定
	4	6月21日	本学Webサイト	神山天文台の研究チームが参加するコメット・インターセプター彗星探査計画が欧州宇宙機関の新しい探査計画に選ばれました
	5	6月21日	本学Webサイト	京都産業大学神山天文台の研究チームらが参加する宇宙探査計画が、欧州宇宙機関(ESA)に唯一採択！世界初の探査機待機型の観測により、太陽系の起源の究明を目指す
	6	6月26日	本学Webサイト	第2回天文学講座 /全国同時七夕講演会「ブラックホール初撮影の衝撃と今後の展望」開催
	7	7月1日	本学Webサイト	神山天文台とインドネシア・バンドン工科大学による国際共同研究の成果：特異な爆発を示した古典新星ASASSN-17hx
	8	7月19日	本学Webサイト	史上初めて撮影されたブラックホールの魅力に迫る　神山天文台 天文学講座開催
	9	7月20日	本学Webサイト	オランダの大学の学生達が海外研修で本学理学部、神山天文台を訪れました
	10	7月27日	本学Webサイト	神山天文台 令和元年度第2回天文学講座「ブラックホール初撮影の衝撃と今後の展望」を開催しました
	11	8月9日	京都産業大学×ナショナルジオグラフィック『Re:世の中』	Re:宇宙探査 彗星の飛来を待ち構えろ！彗星、観測大作戦。神山天文台の研究チームが参加するコメット・インターセプター彗星探査計画
	12	8月23日	本学Webサイト	星間分子の近赤外吸収バンドを用いた星間物質の温度・密度の精密測定手法の確立
	13	9月6日	本学Webサイト	神山天文台の新井 彰 研究員と新中 善晴 嘱託職員がイタリアで開催された研究会 “The Golden Age of Cataclysmic Variables and Related Objects V” にて招待講演を行いました
	14	11月11日	本学Webサイト	荒木望遠鏡がとらえたボリソフ彗星
	15	11月19日	本学Webサイト	ジャコビニ・ツィナー彗星から複雑な有機物由来の赤外線輝線バンドを検出
	16	11月19日	本学Webサイト	第3回天文学講座「ガリレオの冒険 －宇宙をめぐる科学と人をめぐる学問－」開催
	17	11月28日	本学Webサイト	星形成過程における質量流出プロセスと原始惑星系円盤進化との関係性を発見
	18	12月13日	本学Webサイト	ガリレオが愛したイタリア文学から宇宙を紐解く！ 神山天文台 天文学講座開催
	19	12月25日	本学Webサイト	神山天文台 令和元年度第3回天文学講座「ガリレオの冒険－宇宙をめぐる科学と人をめぐる学問－」を開催しました
	20	1月9日	本学Webサイト	宇宙の錬金術を観察するためのカギを赤外線域で発見～中性子捕獲元素によって近赤外線に現れる吸収線の多くを観測的に同定～
	21	1月9日	本学Webサイト	宇宙の錬金術を観察するためのカギを赤外線域で発見～中性子捕獲元素によって近赤外線に現れる吸収線の多くを観測的に同定～
	22	3月18日	本学Webサイト	神山天文台 天文台カードを配布開始
	23	3月26日	本学Webサイト	アトラス彗星は大彗星になるか？

資料６ 神山天文台サポートチーム* 学会等発表のあゆみ

＊ 平成 23 年度に「神山天文台ボランティアチーム」として立ち上げ、平成 27 年度から「神山天文台サポートチーム」に改称

平成 23（2011）年度

１．平成 23 年 11 月 27 日(日) 天文教育普及研究会 近畿支部会

(1) 会場：京都産業大学 神山天文台 サギタリウスホール

(2) メインテーマ：大学での天文教育のニューウエーブ

(3) 発表等：

① 台長挨拶
河北 秀世（京都産業大学 神山天文台）

② 「神山天文台における普及教育活動」
中道 晶香（京都産業大学 神山天文台）

③ 「神山天文台ボランティアチーム半年間の歩み」
鈴木 杏那、松崎 玖美（京都産業大学 神山天文台ボランティアチーム）

④ 「神山天文台学生補助員の紹介 ～補助員としての自分～」
小山 直輝（京都産業大学 神山天文台ボランティアチーム）

平成 24（2012）年度

１．平成 24 年８月５日(日) ― ７日(火) 第 26 回天文教育研究会・年会

(1) 会場：和歌山大学

(2) メインテーマ：天文教育の温故知新

(3) 発表等：

① 「誤解だらけの天文学史～古代インドの宇宙観を例に」
廣瀬 匠（京都大学）
※ 廣瀬氏は本学の大学院修士課程修了、それまで２年間を補助員として観望会等で活躍していたため、参考として記載

② 「京都産業大学 神山天文台ボランティアチーム 試行錯誤の１年目を終えて２年目へ」
近本 衛（京都産業大学 神山天文台ボランティアチーム）

２．平成 24 年 11 月 18 日 天文教育普及研究会 近畿支部会

(1) 会場：琵琶湖博物館 セミナー室

(2) メインテーマ：科学館や博物館等と学校教育の連携

(3) 発表等：

① 「京都産業大学神山天文台の『天文を伝える』実践教育」
中道 晶香（京都産業大学 神山天文台）

② 「神山天文台ボランティアチームのあゆみ」
近本 衛、鈴木 杏奈（京都産業大学 神山天文台ボランティアチーム）

平成 25（2013）年度

1．平成 25 年８月 18 日(日) ― 20 日(火)　第 27 回天文教育研究会

(1) 会場：山口県教育会館５階

(2) メインテーマ：学校での天文教育を考える　～連携の時代を迎えて～

(3) 発表等：

① 「大学の天文台で「天文学を伝える」学生を育成する」
吉川 智裕（京都産業大学 神山天文台）

2．平成 25 年 12 月１日(日)　天文教育普及研究会　近畿支部会

(1) 会場：京都大学 理学研究科セミナーハウス

(2) メインテーマ：ＳＮＳとモバイルツールを天文普及に使いこなそう

(3) 発表等：

① 「冒頭のご挨拶」
近畿支部長　中道 晶香（京都産業大学 神山天文台）

② 「140 文字の天文コミュニケーション（基調講演（招待講演））」
廣瀬 匠（京都大学・星のソムリエ京都）

③ 「学生ボランティアによる神山祭向け天文台公開イベント」
竹中 慶一（京都産業大学 神山天文台ボランティアチーム）

④ 「インターネットを使った天文教育～アストロ・アカデミアの事例～」
小林 仁美（LLP 京都虹光房）
※ 小林氏は、本学補助員 OG のため参考として記載

平成 26（2014）年度

1．平成 26 年８月 10 日(日) ― 12 日(火)　第 28 回天文教育研究会

(1) 会場：東京学芸大学

(2) メインテーマ：天文教育普及活動の次の一歩を探る

(3) 発表等：

① 「学生ボランティアによる学内観望会」
塩谷 葵（京都産業大学 神山天文台ボランティアチーム）

② パネルディスカッション パネラー学生代表に選出
竹中 慶一（京都産業大学 神山天文台ボランティアチーム）

平成 27（2015）年度

1．平成 27 年８月 19 日(水) ― 21 日(金)　第 29 回天文教育研究会

(1) 会場：北海道大学 百年記念会館

(2) メインテーマ：地域と育む新しい天文コミュニティーの形　～学び・文化・人～

(3) 発表等：

① 「市民・大学生・大学の３者にメリットをもたらす社会貢献とは」
中道 晶香（京都産業大学 神山天文台）

平成 28（2016）年度

1．平成 28 年８月 21 日(日) ― 23 日(火)　第 30 回天文教育研究会

(1) 会場：東北大学 理学部 青葉サイエンスホール

(2) メインテーマ：天文教育で日本を元気にする～宇宙と親しみ、人とつながる～

(3) 発表等：

① 「神山天文台サポートチーム　～５年間の活動とこれからの展望～」
坂部 健太（京都産業大学 神山天文台サポートチーム）

2．平成 28 年 11 月 20 日(日)　天文教育普及研究会　近畿支部会

(1) 会場：京都教育大学 藤森キャンパス

(2) メインテーマ：ものづくりと天文教育

(3) 発表等：

① 「遊んで学べる天文グッズ　～製作と使用例～」
小坂 美紀、塩谷 葵（京都産業大学 神山天文台サポートチーム）

平成 29（2017）年度

1．平成 29 年８月６日(日) ― ８日(火)　第 31 回天文教育研究会

(1) 会場：西本願寺 聞法会館

(2) メインテーマ：アクティブ・ラーニングで天文教育・普及 ～主体的・対話的で深い学びを目指して～

(3) 発表等：

① 「京都産業大学　神山天文台の学校利用」
中道 晶香（京都産業大学 神山天文台）

② 「神山天文台サポートチームの活動事例紹介」
阪本 麻裕（京都産業大学 神山天文台サポートチーム）

平成 30（2018）年度

1．平成 30 年８月５日(日) ― ７日(火)　2018 年日本天文教育普及研究会年会

(1) 会場：慶応大学 日吉キャンパス

(2) メインテーマ：みんなで楽しむ天文・宇宙

(3) 発表等：

① 「神山天文台天体観望会の観望天体のライブ上映について」
村井 太一（京都産業大学 神山天文台サポートチーム OB）

2．平成 30 年 12 月 15 日(土)　日本天文教育普及研究会 近畿支部会

(1) 会場：東播磨生活創造センター かこむ

(2) メインテーマ：教養と天文

(3) 発表等：

① 「神山天文台サポートチームの活動事例紹介」
阪本 麻裕（京都産業大学 神山天文台サポートチーム）

平成 31/令和元（2019）年度

１．令和元年８月 18 日(日) ― 20 日(火)　第 33 回日本天文教育研究会

(1) 会場：長野県志賀レークホテル

(2) メインテーマ：「若い世代が考える天文教育」

(3) 発表等：

① 「天文台で活動する大学生の意識調査」

阪本 麻裕（京都産業大学 神山天文台サポートチーム）

２．令和元年 11 月 24 日(日)　日本天文教育普及研究会　近畿支部会

(1) 会場：大阪市立科学館

(2) メインテーマ：「若いからできる 社会とつながる天文活動」

(3) 発表等：

① 若手企画グループのメンバーとして企画運営に携わり、第一部の司会進行を担当

阪本 麻裕（京都産業大学 神山天文台サポートチーム）

以　上

京都産業大学　神山天文台
2019 年度　年報

発行者　京都産業大学　神山天文台
住　所　〒603-8555　京都市北区上賀茂本山
TEL.075-705-3001　FAX.075-705-3002
発行日　2021 年３月５日
印　刷　株式会社　北斗プリント社

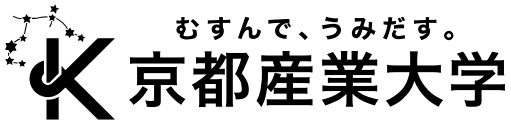
むすんで、うみだす。
京都産業大学